Acceleration of cosmic rays in the outer heliosphere

PL Prinsloo
21696764

Dissertation submitted in partial fulfilment of the requirements
for the degree *Magister Scientiae* in Space Physics at the
Potchefstroom Campus of the North-West University

Supervisor: Prof MS Potgieter
Co-supervisor: Dr RD Strauss

May 2016

NORTH-WEST UNIVERSITY ®
YUNIBESITI YA BOKONE-BOPHIRIMA
NOORDWES-UNIVERSITEIT

It all starts here ™

Dedicated in loving memory
of my grandparents:
****

Paul Jacobus Lategan

(1923-1996)

&

Johanna Elena Lategan *(b. Potgieter)*

(1925-2011)

Gerrit Cornelis Prinsloo

(1926-2012)

&

Freda Prinsloo *(b. Pietersen)*

(1927-2002)

Abstract

Shortly before the Voyager spacecraft crossed the heliospheric termination shock, they encountered narrow, peak-like enhancements in the intensities of low-energy electrons. These enhancements were associated at the time of their observation with diffusive shock acceleration, however it had not been formally confirmed whether this acceleration mechanism can indeed reproduce such intensity increases. This provided the impetus for a study revisiting the features of diffusive shock acceleration, considered within the global context of the heliospheric transport of cosmic rays. The distribution of cosmic rays in two spatial dimensions and energy, and the modulation thereof, are simulated by solving a transport equation using a comprehensive numerical model that also accounts for the effects of diffusive shock acceleration. The model is initially applied to the acceleration of anomalous cosmic rays, using their features to illustrate the characteristics of the acceleration mechanism. The primary focus of the study, however, is to investigate the spectral imprints of diffusive shock acceleration on galactic electron distributions. It is found that in addition to the well-known dependence of the spectral indices of accelerated spectra on the shock compression ratio, the acceleration process is also largely dependent on the form of the energy distribution of particles incident at the termination shock: It is revealed that while energy spectra with large spectral indices are not appreciably affected by diffusive shock acceleration, those with smaller spectral indices are more susceptible to it, with large intensity increases accompanying their acceleration. It follows that the efficiency of diffusive shock acceleration as a re-accelerator of galactic electrons is strongly influenced by any process or characteristic that affects their energy distribution at the termination shock, including their local interstellar energy spectra, the properties of their diffusion, and even the effects of drifts. The diffusion properties following from dissipation-range turbulence yield spectral forms that are particularly conducive to acceleration. It can be inferred from the modelling results that the effects of diffusive shock acceleration on electrons at Voyager-observed energies cannot necessarily be discerned from changes in their spectral slopes across the termination shock. This is because their spectra are already too hard and the compression ratio of the shock too small to induce them. The intensity increases this mechanism induces, however, are not only essential in reproducing radial profiles and energy spectra observed by Voyager 1 in the heliosheath, but are in fact large enough under these observationally constrained conditions to account for the magnitudes of the peak-like intensity enhancements detected near the termination shock. Diffusive shock acceleration emerges in this study as a prominent mechanism for the re-acceleration of galactic electrons.

Keywords:

cosmic rays, termination shock, diffusive shock acceleration, re-acceleration,
galactic electrons, heliosphere, heliosheath, solar modulation, electron spectra.

Opsomming

Kort voordat die Voyager ruimtetuie die heliosferiese terminasieskok oorgesteek het na die helioskede is puntagtige intensiteitverhogings van lae-energie elektrone waargeneem. Hierdie verhogings is toe met diffuseskokversnelling geassosieer, maar dit is nie bevestig of hierdie versnellingsmeganisme sulke intensiteitsverhogings tot stand kan bring nie. Dié aspek is die dryfveer vir 'n studie wat die karakteristieke van diffusieskokversnelling heroorweeg binne die konteks van die heliosferiese transport van kosmiese strale. Die energie- en ruimtelike verdelings van kosmiese strale in twee dimensies, en die modulasie van hierdie verdelings, word gesimuleer deur 'n transportvergelyking op te los deur middel van 'n numeriese model wat voorsiening maak vir die uitwerking van diffuseskokversnelling. Die model word aanvanklik toegepas op die versnelling van anomale kosmiese strale, en hul kenmerke word gebruik om die karakteristieke van die versnellingsmeganisme ten toon te stel. Die primêre fokus van hierdie studie is egter om die spektrale effekte van diffuseskokversnelling op galaktiese elektronverdelings te ondersoek. Bykomend tot die bekende afhanklikheid van die spektrale indeks van versnelde spektra op die skok se kompressieverhouding, word daar bewys dat die versnellingsproses ook grootliks afhanklik is op die vorm van die energieverdelings van invallende deeltjies op die terminasieskok. Daar word verduidelik dat energiespektra met hoë spektraalindekse nie merkwaardig beïnvloed word deur diffuseskokversnelling nie, maar dat die spektra met kleiner spektraalindekse meer gevoelig is daarvoor met groot gepaardgaende intensiteitsverhogings. Dit volg verder dat die doeltreffenheid van diffuseskokversnelling as 'n herversneller van galaktiese elektrone sterk beïnvloed word deur enige proses of kenmerk wat hul energieverdeling affekteer. Dit sluit plaaslike inter-stellêre energiespektra, diffusiekenmerke en dryfeffekte in. Die diffusiekenmerke wat volg vanweë die dissipasiereeks van turbulensie bevorder veral versnelling. Dit word afgelei uit die modelresultate dat die uitwerkings van diffuseskokversnelling op elektrone by die waargenome energieë van Voyager nie noodwendig waargeneem kan word uit die verandering van spektrale hellings oor die terminasieskok nie, omdat die hellings reeds te steil is en die skok se kompressieverhouding te klein is om dit te verander. Die intensiteitsverhogings wat hierdie versnellingsmeganisme veroorsaak, is noodsaaklik vir beide die herproduksie van die radiale profiele en energiespektra wat deur Voyager 1 waargeneem is in die helioskede, en om onder dié waarnemingsgebonde omstandighede die grootte van die puntagtige verhogings wat naby die terminasieskok waargeneem is, na te maak. Diffuseskokversnelling kom na vore in hierdie studie as 'n prominente meganisme vir die herversnelling van galaktiese elektrone.

Sleutelwoorde:

kosmiese strale, terminasieskok, diffuseskokversnelling, herversnelling,
galaktiese elektrone, heliosfeer, helioskede, sonmodulasie, elektronspektra.

Acronyms and Abbreviations

1-D/2-D/3-D	One-, Two- and Three-dimensional
ACR	Anomalous Cosmic Ray
BS	Bow Shock
CIR	Co-rotating Interaction Region
CR	Cosmic Ray
DSA	Diffusive Shock Acceleration
ENA	Energetic Neutral Atom
FLS	Fast Latitude Scan
GALPROP	Galactic Propagation (model)
GCR	Galactic Cosmic Ray
HCS	Heliopsheric Current Sheet
HD	Hydrodynamic
HMF	Heliospheric Magnetic Field
HP	Heliopause
HPS	Heliopause Spectrum
IBEX	Interstellar Boundary Explorer
ISM	Interstellar Medium
ISMF	Interstellar Magnetic Field
LECP	Low-energy Charged Particle (instrument aboard Voyager)
LOD	Locally One-dimensional
LOS	Line-of-sight (model)
MHD	Magnetohydrodynamic
MFP	Mean Free Path
NLGC	Non-linear Guiding Centre (theory)
PAMELA	Payload for Antimatter Matter Exploration and Light-nuclei Astrophysics
PDE	Partial Differential Equation
PUI	Pick-up Ion
QLT	Quasi-linear Theory
RH	Rankine-Hugonoit (equations)
SEP	Solar Energetic Particle
SMF	Solar Magnetic Field
SW	Solar wind
TPE	Transport Equation
TS	Termination Shock
TSP	Termination Shock Particle

Contents

Chapter 1

Introduction

A remarkable milestone of the Voyager space mission was the eventual crossing of the solar wind termination shock by both of the twin spacecraft [*Stone et al.*, 2005, 2008; *Burlaga et al.*, 2005, 2008]. Shortly before the crossing, the spacecraft recorded narrow increases in the intensities of low-energy electrons that were thought to have arisen from the acceleration of particles at the termination shock [e.g. *McDonald et al.*, 2003; *Decker et al.*, 2005; *Stone et al.*, 2005]. These increases, while certainly noticeable, were soon overshadowed by the large and rapidly increasing intensities measured by Voyager 1 in the heliosheath immediately after the crossing of the termination shock [*Webber et al.*, 2012]. Attention was further diverted from the shock when the long-standing paradigm that anomalous cosmic rays originate there through diffusive shock acceleration came under scrutiny, because their intensities were observed to increase away from it [*Webber et al.*, 2007], suggesting a source further into the heliosheath. As such, the aforementioned intensity peaks had gone largely unnoticed and unexplored. This study endeavours to formally establish whether, and to what extent, diffusive shock acceleration can account for these intensity increases.

In addition to the investigation of the intensity peaks, these observations prompted a comprehensive study of the features of diffusive shock acceleration in association with cosmic-ray modulation in the heliosphere. It is aimed that this will in turn reveal the viability of this mechanism as a re-accelerator of cosmic rays. Hence, expanding upon the earlier related study of *Langner* [2004], this study solves the well-known *Parker* [1965b] transport equation using a comprehensive 2-D cosmic-ray modulation model, which also includes the effects of diffusive shock acceleration [see also *Potgieter and Ferreira*, 2002; *Potgieter and Langner*, 2004; *Langner and Potgieter*, 2004, 2008]. Following the approach of *Langner and Potgieter* [2006] and *Strauss et al.* [2010b, 2011a], the classic features of shock-accelerated energy spectra are initially illustrated by modelling the acceleration of anomalous cosmic rays (or more technically, termination shock particles), which display these features explicitly. Applying a similar technique, the spectral imprints of diffusive shock acceleration on electrons are studied, while taking due notice of the peculiarities of this cosmic-ray species such as its small rest mass and distinct response to modulation processes and turbulence [e.g. *Potgieter*, 1996; *Caballero-Lopez et al.*, 2010]. The properties of galactic electrons, specifically their distribution with energy on arrival at the outer heliospheric boundary, the coefficients describing their transport (particularly through diffusion), and how these affect their distributions at the TS, are studied in detail. These energy distribution properties at the termination shock are furthermore studied in terms of their effect on acceleration efficiency. Note that since diffusive shock acceleration essentially entails the migration of particles in energy, this study mostly focusses on the spectral features of cosmic-ray electrons, although the global spatial distribution of electrons re-accelerated at the termination shock is also explored. As a final exercise, transport parameters are configured to reproduce observations from the Voyager 1 and PAMELA spacecraft, and the acceleration features arising from this configuration are discussed. It is consequently inferred whether diffusive shock acceleration, under the conditions constrained by the aforementioned observations, can account for the electron intensity increases observed by the Voyager spacecraft in the vicinity of the termination shock. Note that details on the Voyager mission can be viewed at http://voyager.jpl.nasa.gov/, while *Menn et al.* [2013] provide a review on PAMELA.

The study is constructed as follows: The heliospheric physics essential for the study of cosmic-ray modulation is covered in **Chapter 2**. Applicable cycles of solar variability are introduced, along with the major defining components of the heliosphere, such as the solar wind and its coupled magnetic field, which vary, in turn, according to the aforementioned cycles. It is also conveyed how these heliospheric features are modelled. Moreover, cosmic rays are introduced, and accompanying observations needed for further chapters are presented. In **Chapter 3**, a transport equation is introduced that describes the modulation of cosmic rays subject to the relevant processes in the heliosphere. The essential transport coefficients are given and the incorporation of the effects of diffusive shock acceleration is discussed. The numerical model utilised in this study to solve the transport equation is also briefly reviewed. The general characteristics of diffusive shock acceleration are furthermore illustrated in **Chapter 4** with the application of the model to the acceleration of anomalous cosmic-ray Oxygen. **Chapter 5** introduces the properties of galactic electrons, and reviews general modulation concepts to provide context for subsequent chapters. Drawing on the insights garnered from the previous two chapters, **Chapter 6** illustrates the properties of diffusive shock acceleration applying to electrons. Specifically, the re-acceleration of galactic electrons is considered, and the spatial and energy distributions of particles re-accelerated at the TS are investigated extensively. The interaction of diffusive shock acceleration and modulation processes are also explored. Finally, an optimum configuration of heliospheric and transport parameters is found to reproduce the observed energy spectra and radial intensity profiles. This is illustrated and discussed in **Chapter 7**, where the role of diffusive shock acceleration in the creation of the peak-like intensity enhancements is also considered. An overview of the study is given in **Chapter 8**, where the most noteworthy conclusions are reiterated.

Aspects of this study were presented at the following conferences and workshops:

- Centre for High-Performance Computing Annual Meeting, Cape Town, December 2013.
- International workshop on cosmic rays: "From the Galaxy to the Heliosphere", Potchefstroom, March 2014.
- 40th COSPAR Scientific Assembly, Moscow, August 2014.
- 60th annual conference of the South African Institute of Physics, Port Elizabeth, July 2015.

Chapter 2

On Cosmic Rays and the Heliosphere

2.1 Introduction

The heliosphere is a region of space formed due to the interaction of plasma emanating from the Sun with the local interstellar environment. Energetic charged particles, referred to as comic rays (CRs), move through the heliosphere and are modulated subject to the various processes encountered therein. This chapter aims to introduce the essential background to the study of CR modulation, and discusses the major defining plasma and magnetic field properties of the heliosphere and their responses to solar variability.

Specifically, the chapter begins by identifying the cycles of solar variability of interest to this study. The concept of the solar wind is discussed along with its coupled magnetic field; their mathematical descriptions as utilised in this study are also given. Moreover, the global structure of the heliosphere, largely characterised by the aforementioned plasma and magnetic field properties, is discussed. The types of CRs considered in this study are also introduced along with essential observations of their properties and distributions. Finally, a summary of the heliospheric configuration carried over to next chapters is provided.

2.2 Solar Variability

The Sun influences the properties of the heliosphere and the consequent transport of CRs through this medium according to its own variability. However, without elaborating on the properties of the Sun itself [see e.g. *Stix*, 2012], the current section is focused on the cycles of solar variability that are pertinent to the study of CR modulation; for this study, these are the solar activity and magnetic polarity cycles. The following discussion is also limited to the observable features and consequences of solar activity rather than its physical causes; refer to e.g. *Weiss and Tobias* [2000] for more on the latter.

The solar activity cycle refers to the progression of the Sun between states of intense activity through relatively inactive periods in between; this takes place over roughly 11 years. High solar activity is typically associated with large numbers of sunspots, large solar magnetic field (SMF) magnitudes, and frequent transient events such as coronal mass ejections and solar flares

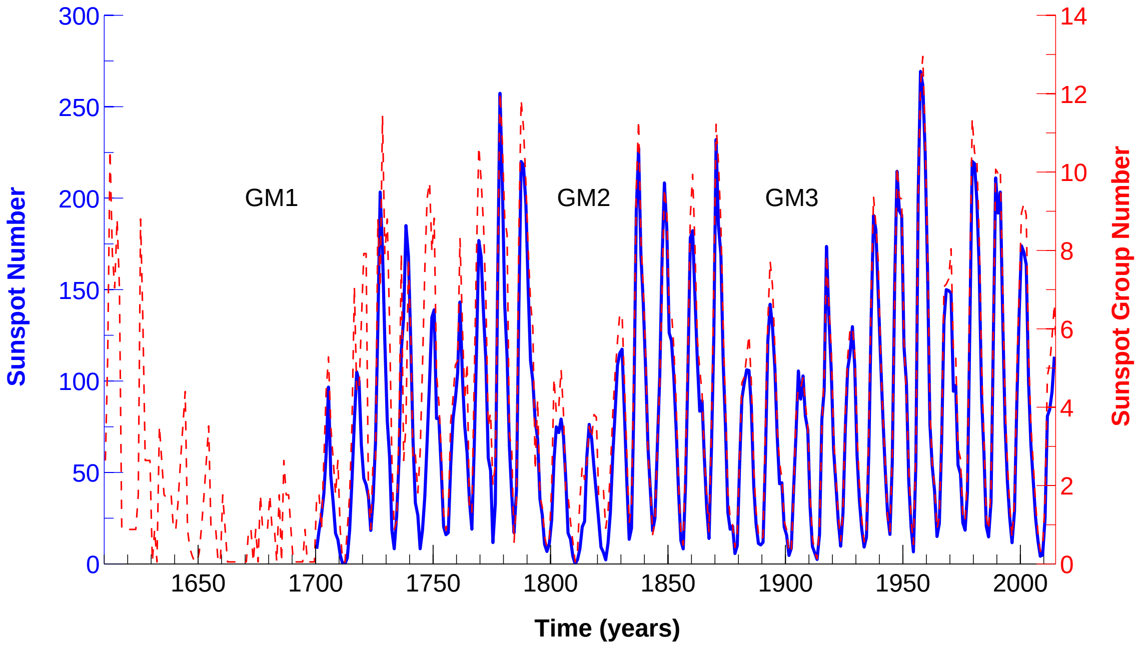

Figure 2.1: Revised yearly averaged international sunspot numbers and sunspot group numbers [of e.g. *Clette et al.*, 2014] respectively shown in solid blue and dashed red lines over the last roughly 400 years. The labels GM1, GM2 and GM3 indicate the Maunder, Dalton and Gleissberg Grand Minima. Sunspot data retrieved from the World Data Center SILSO, Royal Observatory of Belgium, Brussels (url: http://sidc.be/silso/ doa: 9 November 2015).

[note also the features reported by *Smith and Marsden*, 2003]. Solar-quiet conditions, on the other hand, are marked by the appearance of large coronal holes at the polar regions and a well-defined structure of the SMF. Due to the many manifestations of its effects, several indicators of solar activity exist [see *Hathaway*, 2010, for an overview], which range from direct measures such as the total solar irradiance to proxy indicators such as the deposition of radioisotopes in tree rings or ice cores. While the latter example allows for the reconstruction of past solar activity over very long time scales, the sunspot number is perhaps the earliest applied measure of solar activity; sunspots are dark and irregular blemishes that periodically appear upon the photosphere of the Sun. While they were first observed over two millennia ago, and uninterrupted records of their numbers exist from the 17th century, a modern understanding of sunspots only followed after they were respectively linked to solar activity and magnetic fields in the mid 19th and early 20th centuries [see *Vaquero*, 2007, for a historical overview]. Indeed, sunspots are associated with other features of high solar activity: Their darker appearance follows because of the repulsion of surrounding plasma due to strong magnetic fields, while field lines form coronal loops between sunspot groups, which form part of active regions associated with the formation of the aforementioned transient events.

Although the sunspot number is a synthetic index, which differs depending on whether e.g. the Wolf series or the Group Number series is considered [*Hoyt and Schatten*, 1998; *Clette et al.*, 2014], the sunspots themselves are linked to solar activity on a fundamental level. Hence, the periodicity displayed in e.g. Figure 2.1 by sunspot numbers (however they are constructed) provides a compelling indication of solar variability. Figure 2.1 shows a clear 11-year cycle, but also reveals possible cycles on longer time scales, e.g. a hundred-year cycle, and extended or

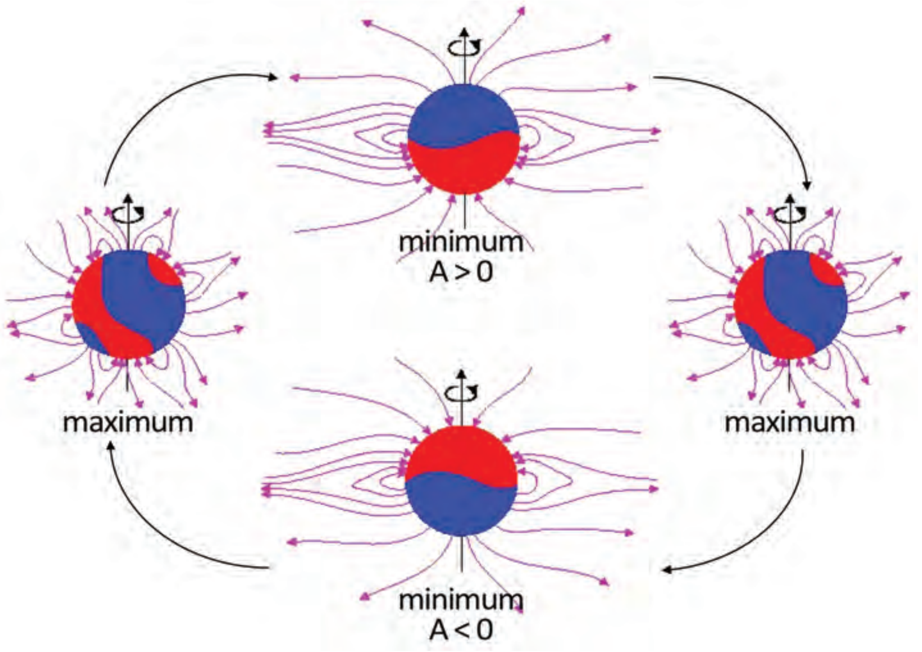

Figure 2.2: A schematic representation [adapted from *Heber and Potgieter*, 2006] of the form of the SMF and the distribution of regions of opposite polarity during different phases of the solar activity cycle. While 11 years elapse between consecutive minima and maxima, 22 years elapse before the Sun returns to its previous state of polarity. The notations of A $>$ 0 and A $<$ 0 refer to positive and negative solar magnetic polarities respectively.

abnormally low periods of solar activity known as the Grand Minima. The consecutive peaks and valleys, respectively separated by ∼11 years, are associated with what is generally known as maximum and minimum solar activity conditions. The 11-year activity cycle is also reflected in the time dependence of many of the quantities introduced in subsequent sections, including ground-based measurements of CR intensities, which not only show an 11-year cycle related to solar activity, but also a 22-year cycle (see Section 2.7). This periodicity stems from changes in the polarity of the SMF.

Figure 2.2 illustrates the form of the SMF during different phases of the solar activity cycle and during opposite magnetic polarities. The convention followed in this study is that the polarity of the Sun is positive (A $>$ 0) when field lines point outward in the northern hemisphere of the Sun and inward in the south, while the opposite applies for a negative polarity (A $<$ 0). Note that during minimum solar activity the SMF somewhat resembles a dipole and two distinct hemispheres of opposite polarity are visible. During these conditions the magnetic and rotational axes, while not aligned, are separated by reasonably small angles. For solar maximum conditions, on the other hand, conditions are evidently different [see e.g. *Smith and Marsden*, 2003; *Heber*, 2011]. Approaching higher levels of activity, the SMF structure becomes more complicated, and no simple boundary is visible between regions of different polarities. It is during this disorderly phase of high solar activity that the polarity of the Sun is reversed; since about 11 years elapse between consecutive solar maxima, the SMF polarity returns to its previous state after roughly 22 years. Therefore, in addition to the 11-year periodicity associated with solar activity, CR intensities display a 22-year periodicity due to the magnetic polarity cycle. The effects of different magnetic polarities have far-reaching consequences in terms of charge-sign dependent CR modulation, and is a recurring theme in this study.

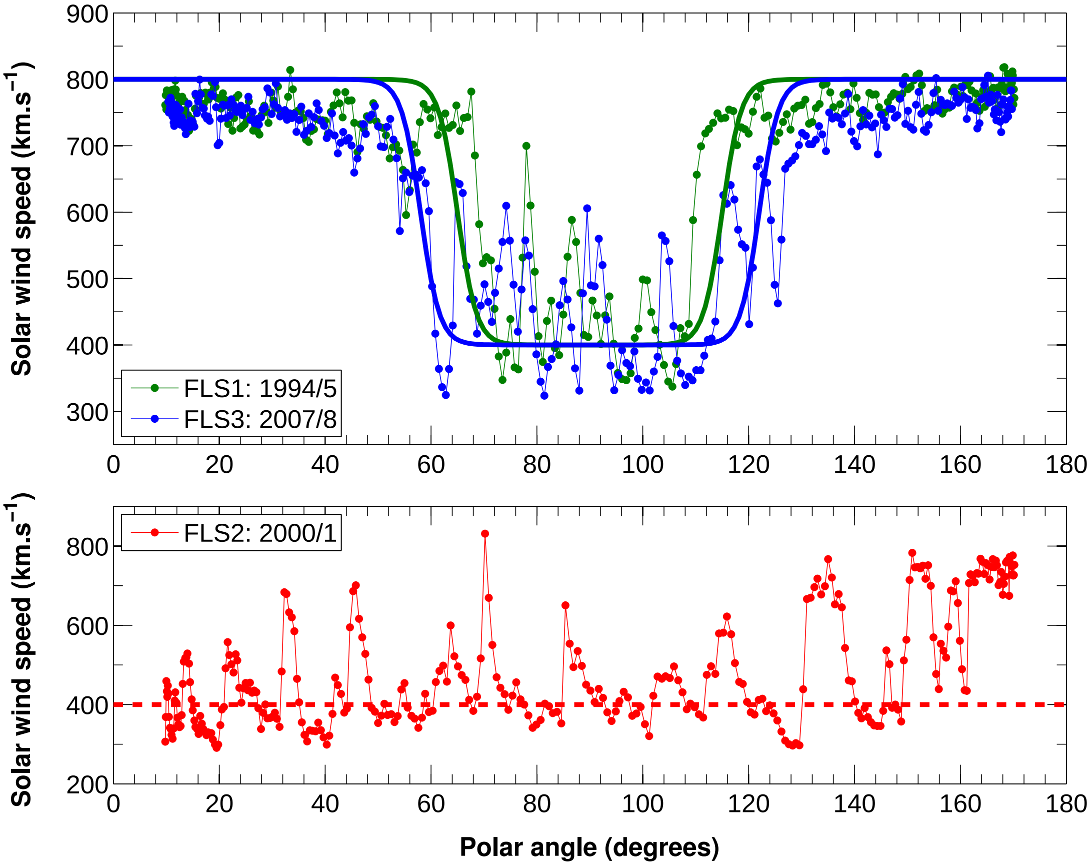

Figure 2.3: SW speed as a function of heliographic latitude. In the top panel, the line-connected markers respectively represent Ulysses measurements during the first and third latitude scans for the solar minimum periods indicated in the legend. The solid-lines profiles are modelled using Eq. 2.2 with α =10° (for FLS1, in green) and 17° (for FLS3, in blue) to emulate appropriate solar activity levels. A clear transition is visible from slow SW speeds near the equator ($\theta = 90°$) to faster speeds toward polar regions ($\theta \to 0°, 180°$). The bottom panel shows measurements concurrent with maximum solar activity, for which Eq. 2.2 yields a horizontal line. No global latitude dependence can be discerned. Data from NASA SPDF COHOWeb (url: http://omniweb.gsfc.nasa.gov/coho/ doa: 11 November 2015).

2.3 The Solar Wind

The Sun is constantly losing mass [e.g. *Tayler*, 1994] in the form of a continuous outflow of charged particles from its outermost atmosphere (or solar corona). This was first inferred from the radial deflection of comet tails away from the Sun [e.g. *Biermann*, 1961], but was later formally derived as a continual hydrodynamic (HD) expansion of the solar corona [*Parker*, 1958]: Due to a large pressure gradient, the corona cannot be in thermodynamic equilibrium with the interplanetary medium unless it is expanding supersonically beyond some critical point. See also *Parker* [1961, 1965a]. This expanding corona would later become known as the solar wind (SW). Indeed, these supersonic flow speeds were confirmed by the Mariner II spacecraft [*Neugebauer and Snyder*, 1962], while the Ulysses spacecraft observed that the SW composition is similar to that of the solar corona [e.g. *von Steiger et al.*, 2000], consisting mostly of protons.

Being of coronal origin, the SW is also affected by solar activity. Section 2.2 mentions that coronal holes form at the polar regions of the Sun during low-activity conditions. Magnetic field lines emanating from these structures are generally open and thus tend to be largely parallel to the SW flow; this facilitates the coronal expansion and gives rise to fast SW streams [see e.g *Krieger et al.*, 1973]. Polar coronal holes occupy greater surfaces as the solar cycle tends toward its minimum and hence the latitudinal extent of the associated fast SW streams also increases. By contrast, magnetic field lines are closed near the solar equator (see Figure 2.2 to aid in visualisation), and because they are directed largely perpendicular to the radial outflow, SW streams emanating from this region are slower [e.g. *Schwenn*, 1983; *Marsch*, 1991]. While no global latitude dependence of the SW is visible during solar maximum conditions, Ulysses confirmed the emergence of the fast SW stream during solar minimum conditions [*Phillips et al.*, 1995].

Figure 2.3 shows observations this spacecraft collected during its three Fast Latitude Scans (FLSs); the first and third of these, coinciding with periods of 1994 to 1995 and 2007 to 2008, show the solar minimum characteristics discussed above with a clear latitude dependence. At higher heliolatitudes, that is, polar angles of $\theta \lesssim 60^\circ$ and $\theta \gtrsim 120^\circ$, the fast SW streams attain speeds of up to 800 km.s^{-1}, while at the more active equatorial regions ($\theta \sim 90^\circ$) the average flow speed is closer to 400 km.s^{-1}. The slower average flow speed is also visible at all latitudes for solar maximum conditions; see FLS2 for the years 2000 to 2001 in the bottom panel of Figure 2.3. Note that at the equatorial regions during minimum solar activity, and quite generally during maximum activity, the SW is more variable with several intermittent spikes of higher speeds - this can be attributed to irregular SMF structures and open field lines from smaller coronal holes. Refer also to the relevant discussions of *Hundhausen* [1972] and the references therein for further reading on these matters.

To model the latitudinal dependence described above, as well as the radial dependence of the SW speed, the approach also used by *Hattingh* [1998] and *Langner* [2004] is applied: Assuming a purely radial outward-directed SW flow, the SW speed may be written as

$$\vec{V}_{sw}\,(r,\theta) = V_{sw}\,(r,\theta)\,\hat{e}_r = V_0\;V_r(r)\;V_\theta(\theta)\;\hat{e}_r\;, \tag{2.1}$$

with r being the radial distance from the Sun, θ the polar angle ($\theta = 0^\circ$: heliospheric north pole; $\theta = 90^\circ$: equatorial plane), $\hat{e}_r$ the unit vector in the radial direction, and $V_0 = 400$ km.s^{-1}. Since the modulation model utilised in the current study is two-dimensional (2-D), other components are not considered. Note that the radial and latitudinal dependences, $V_r(r)$ and $V_\theta(\theta)$, are independent of each other. The latter is given in terms of co-latitude (see also *Moeketsi et al.* [2005]) by

$$V_\theta(\theta) = 1.5 \mp 0.5 \tanh\left[16.0\left(\theta - \frac{\pi}{2} \pm \zeta\right)\right], \tag{2.2}$$

where $\zeta = \alpha + 15\pi/180$, with α the current sheet tilt angle, which is used as a proxy indicator for solar activity; see Section 2.5. The function ζ controls the transition from the slow to the fast solar wind speed, while the top and bottom signs in Eq. 2.2 respectively correspond to the heliospheric quadrants described by $0^\circ \leq \theta \leq 90^\circ$ in the north and $90^\circ < \theta \leq 180^\circ$ in the south; note that a spherically symmetric geometry is assumed. At solar maximum Eq. 2.2 reduces to $V_\theta(\theta) = 1$. The latitudinal profiles of the SW speed are modelled for FLS1 and FLS3 in Figure 2.3 using Eq. 2.2 with $\alpha = 10^\circ$ and 17° respectively.

With regards to the radial dependence, the SW is assumed to be accelerated within the first $\sim$ 0.1 AU and attains a steady flow from about 0.3 AU [*Sheeley et al.*, 1997]. Outward from here,

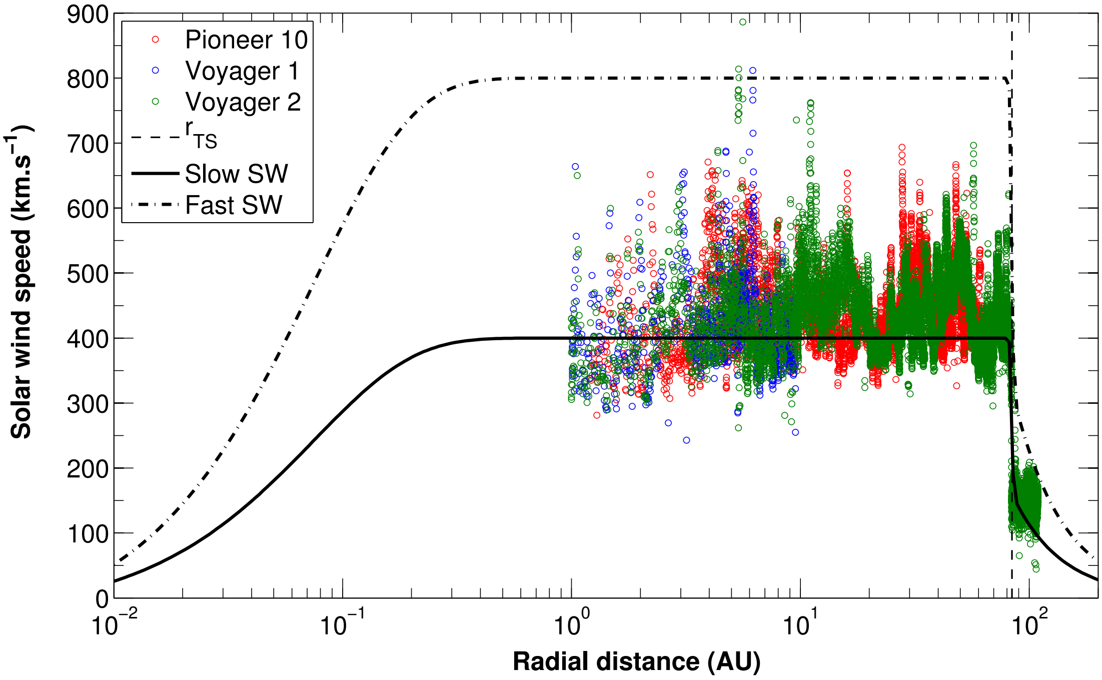

Figure 2.4: Modelled and observed radial SW profiles. The red, blue and green markers represent measurements from Pioneer 10 and Voyager 1 and 2 as indicated in the legend, while profiles modelled using Eq. 2.1–2.4 and 2.7 are shown for the slow and fast SW streams respectively at $\theta = 90°$ and $10°$ for solar minimum conditions ($\alpha = 10°$). The TS position, r_{TS}, as observed by Voyager 2, is shown using a dashed vertical line at $\sim$ 84 AU. Data obtained from NASA SPDF COHOWeb (url: http://omniweb.gsfc.nasa.gov/coho/ doa: 11 November 2015).

the flow remains largely constant along the trajectories of interstellar-bound spacecraft such as Pioneer 10, Voyager 1 and 2 [*Richardson et al.*, 2001]. Measurements from these spacecraft are shown in Figure 2.4. The radial dependence in Eq. 2.1 can be modelled as

$$V_r(r) = 1 - \exp\left[\frac{40}{3}\left(\frac{r_\odot - r}{r_0}\right)\right], \tag{2.3}$$

with $r_\odot = 0.005$ AU the solar radius and $r_0 = 1$ AU the position of Earth. In the near-Sun environment, Eq. 2.3 suffices to describe the SW acceleration observed by *Sheeley et al.* [1997]; see Figure 2.4 for profiles modelled using Eq. 2.3 for both the slow and fast SW streams. Note that e.g. Voyager 2, travelling at $\theta \approx 120°$ (or 30° south of the equatorial plane), can according to Eq. 2.2 detect SW flows with speeds ranging between 400 and 800 km.s^{-1} due to varying solar activity. The variations in the spacecraft measurements from 1 AU to $\sim$ 80 AU can hence be assumed to be mostly temporal. Note also that the SW speed decreases abruptly between 83 and 84 AU, which is emphasised in the bottom panel of Figure 2.5. This semi-discontinuous transition from supersonic to subsonic speeds is the hallmark of the SW termination shock (TS), and is modelled [following *le Roux et al.*, 1996] according to

$$V_{sw}(r,\theta) = V_{sw}(r_{TS},\theta)\frac{s+1}{2s} - V_{sw}(r_{TS},\theta)\frac{s-1}{2s}\tanh\left(\frac{r - r_{TS}}{L}\right), \tag{2.4}$$

in the upstream region, that is, only for $r < r_{TS}$. Here r_{TS} is the position of the TS, whereas s $(= 2.5)$ is the total factor by which the SW speed decreases across the TS and is referred to as

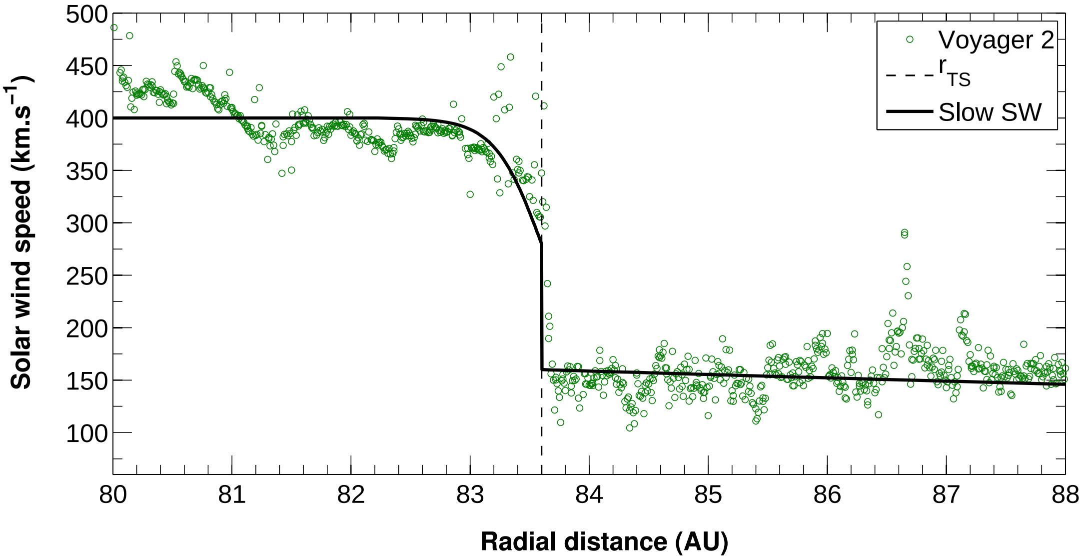

Figure 2.5: Similar to Figure 2.4, but accentuating the region near the TS at 83.6 AU as observed by Voyager 2. As per the discussion in Section 2.6.1, the TS precursor is the continuous decline in SW speed from ∼ 82.4 to 83.6 AU, while the subshock refers to the discontinuous jump at r_{TS}.

the compression ratio. The scale length $L = 1.2$ AU stipulates the extent of the shock precursor, between $r_{TS} - L$ and r_{TS}, across which the SW speed decreases with a factor of $s/2$ before decreasing discontinuously with another $s/2$ factor at r_{TS}. As illustrated in Figure 2.5, this modelled profile simulates the observed decrease in SW speed across the TS satisfactorily. See also *Richardson et al.* [2008] for details on this transition. Further details on the TS and associated precursor events are discussed in Section 2.6.1.

Beyond the TS, in a region called the heliosheath, the SW diminishes to subsonic speeds. Such slow-moving plasmas qualify for the approximation of incompressible flow, that is, the SW density, ρ, can be approximated as being constant in this region. Hence,

$$\frac{d\rho}{dt} = \frac{\partial\rho}{\partial t} + \rho\nabla\cdot\vec{V}_{sw} = 0, \tag{2.5}$$

which, if it is assumed that the slow moving plasma is able to compensate for local density fluctuations so that $\partial\rho/\partial t \ll \rho\,(\nabla\cdot\vec{V}_{sw})$, implies a divergence-free SW velocity ($\nabla\cdot\vec{V}_{sw} = 0$). If the radial component of the SW velocity is furthermore assumed to remain predominant, even though polar and azimuthal components are also observed to develop beyond the TS [*Richardson et al.*, 2009], the assumption that $\vec{V}_{sw} = V_{sw}\,\hat{e}_r$ may be retained. It thus follows as a consequence of incompressible flow in this region that

$$\nabla\cdot\vec{V}_{sw} = \frac{1}{r^2}\frac{\partial}{\partial r}\left(r^2\,V_{sw}\right) = 0, \tag{2.6}$$

$$\Longrightarrow\ V_{sw} \propto \frac{1}{r^2}\,. \tag{2.7}$$

For the purposes of this study, this $1/r^2$ dependence is assumed for the SW speed in the heliosheath and is discussed further in terms of particle acceleration in Section 3.6.1. No consensus yet exists on the velocity profile of the SW in the heliosheath, although compelling

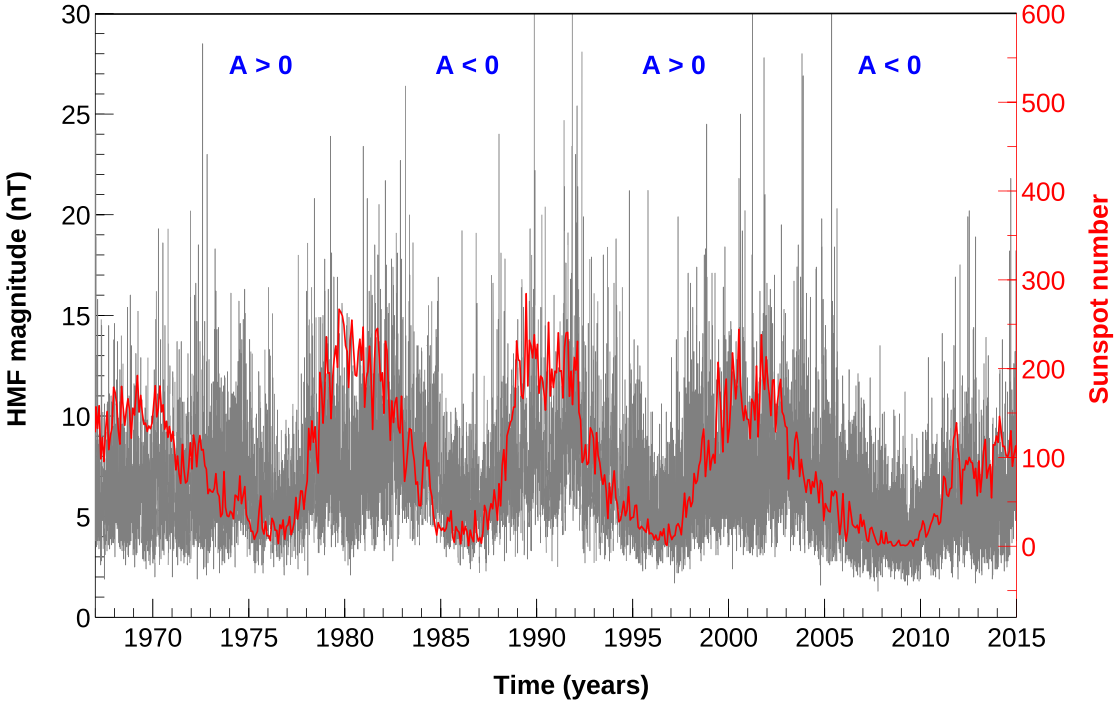

Figure 2.6: The HMF magnitude at Earth (measured by ACE/IMP8) over time. The daily-averaged HMF magnitude is shown (in grey) alongside the monthly sunspot number (shown in red) to demonstrate its adherence to the 11-year solar activity cycle. The HMF polarity epochs in effect during each solar cycle are indicated. HMF data retrieved from NASA SPDF COHOWeb (doa: 11 November 2015), with sunspot data from the source cited in Figure 2.1.

examples may be inferred from the results of HD and magnetohydrodynamic (MHD) modelling [e.g. *Ferreira et al.*, 2007a, b; *Strauss et al.*, 2013b]. Voyager 2 may also yield further insights in this regard when its journey through the heliosheath is complete. Section 2.6.2 continues the discussion on the heliosheath.

2.4 The Heliospheric Magnetic Field

The interaction between the SMF and coronal plasma is not limited to the formation regions of the SW. At a certain distance from the Sun called the Alfvén radius, r_A ($\approx 10r_\odot$), the thermal energy density of the plasma outflow exceeds the magnetic energy density [see e.g. *Choudhuri*, 1998]. Whereas the structure of the SMF dictates the outflow nearer to the Sun (hence giving rise to different flow speeds as discussed in Section 2.3), beyond r_A this interaction is reversed. Due to the high conductivity of the high-temperature coronal plasma, the SMF is embedded in the radially expanding SW and is carried into interplanetary space; see also the treatments of this process as discussed by e.g. *Hundhausen* [1972], *Kallenrode* [2001] or *Smith* [2008]. This embedded field is referred to as the heliospheric magnetic field (HMF). *Parker* [2001] reviewed the early developments in the conception of this field.

The HMF adopts the polarity of its progenitor, the SMF, and adheres to the same 22-year cyclic behaviour, switching between A $>$ 0 and A $<$ 0 during each solar maximum. The change in the HMF magnitude at Earth with time is illustrated in Figure 2.6, with the polarity epochs in effect

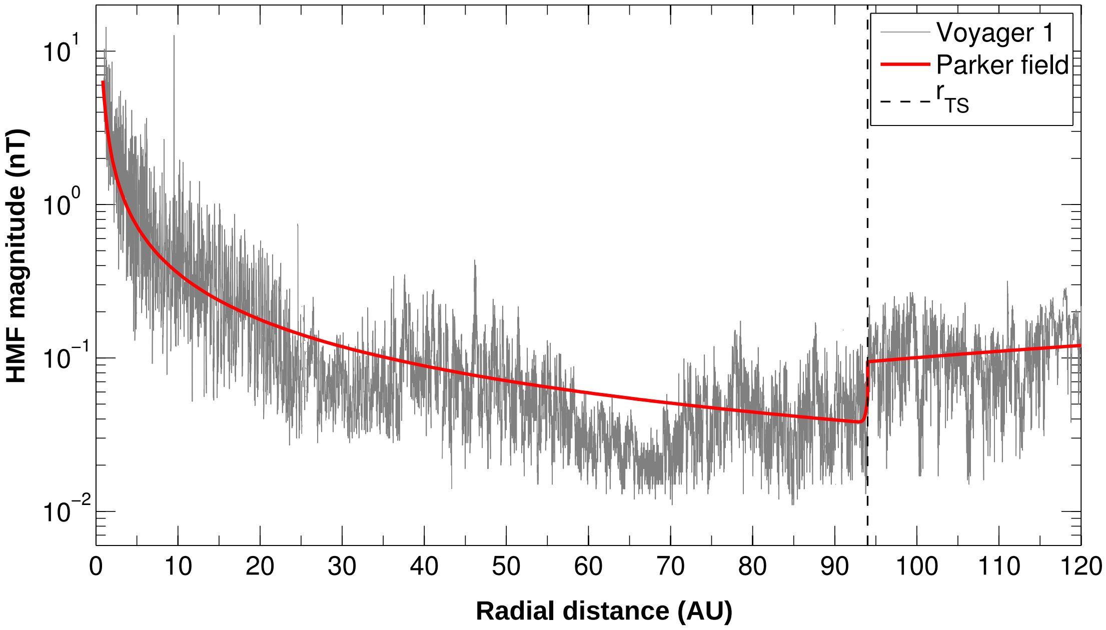

Figure 2.7: The radial profile of the HMF magnitude. The grey fluctuating line represents measurements along the Voyager 1 trajectory, while the red line shows the profile predicted by the Parker HMF model (Eq. 2.10). Note that the Voyager 1 measurements also reflect variations associated with the solar activity cycle. The TS position is indicated with the dashed vertical line. Data obtained from NASA SPDF COHOWeb (url: http://omniweb.gsfc.nasa.gov/coho/ doa: 11 November 2015).

between consecutive maxima indicated. The drift directions of charged particles throughout the heliosphere alternate between these periods of different polarities as discussed in Section 3.4. Moreover, Figure 2.6 illustrates that the HMF magnitude also exhibits the 11-year solar activity dependence as evidenced by its correlation with the sunspot number. The HMF is hence strongest during solar maximum conditions and weakens toward solar minimum, with magnitudes reaching particularly low levels (below 4 nT) during the minimum of 2009. Aside from changing with time, the HMF also exhibits a radial dependence as shown in Figure 2.7. With values at Earth typically measured at around 5 nT, Voyager 1 detected that the HMF magnitude declines with increasing distance until the TS is encountered; Voyager 2 measured a similar profile, but encountered the TS sooner. Note by comparing Figures 2.7 and 2.5 that the HMF magnitude increases across the TS by roughly the same factor by which the SW speed decreases there; also compare the results of *Richardson et al.* [2008] and *Burlaga et al.* [2008]. See *Balogh and Erdös* [2013] for more on the properties of the HMF.

While it can be inferred from observations that an inverse relationship exists between the SW speed and the HMF, the derivation of a mathematical description of the HMF hinges on the geometry of field lines with regards to the radial direction and the rotation of the Sun. *Parker* [1958] was the first to derive such an expression, valid for $r > r_\odot$, and given by

$$\vec{B} = B_e \left(\frac{r_0}{r}\right)^2 \left(\hat{e}_r - \tan\psi\,\hat{e}_\phi\right), \tag{2.8}$$

which is referred to as the Parker HMF, where $\hat{e}_r$ and $\hat{e}_\phi$ are unit vectors in the radial and azimuthal directions respectively, and B_e is the HMF magnitude at Earth ($r_0 = 1$ AU) for which the default value in this study is 5 nT. Note that there is no polar (θ) component for this field.

Also, ψ, known as the spiral angle, denotes the angular separation between the tangent at any point along a Parker field line and the radial direction represented by $\hat{e}_r$; it is given by

$$\psi = \tan^{-1}\left(\frac{\Omega\,(r - r_{\odot})}{V_{sw}}\sin\theta\right), \tag{2.9}$$

where $\Omega = 2.67 \cdot 10^{-6}$ rad.s^{-1} is the average angular rotation speed of the Sun and the rest is as previously defined. The relation in Eq. 2.9 can be inferred geometrically by noting that $V_{sw}\sin\psi = \Omega r\cos\psi$, and adding $\sin\theta$ to incorporate the height above the equatorial plane. The resultant global geometry of the Parker HMF, resembling Archimedean spirals along cones of constant heliographic latitude, is illustrated in Figure 2.8. Its magnitude, following directly from Eq. 2.8 and 2.9, is expressed as

$$B = B_e\left(\frac{r_0}{r}\right)^2\sqrt{1 + \left[\frac{\Omega\,(r - r_{\odot})}{V_{sw}}\sin\theta\right]^2}. \tag{2.10}$$

The density of field lines in Figure 2.8 also serves as an indication of HMF magnitude. The abrupt decrease of the SW speed at the TS, for instance, is reflected by the increased compression of field lines toward larger radial distances. Note from Figure 2.7 that the radial profile of the HMF magnitude predicted by the Parker model shows similar features to the observations.

A number of modifications to the Parker field have been suggested. One such modification was suggested by *Jokipii and Kota* [1989], who argued that the surface where the footpoints of field lines occur is not smooth, but granular and turbulent, especially at the poles. As a result, footpoints wander randomly, leading to the formation of transverse components in the field and highly irregular and compressed field lines. This compression is indicative of a mean magnetic field magnitude that is larger at the poles than predicted by the Parker field. To account for this, *Jokipii and Kota* [1989] introduced a parameter, $\delta(\theta)$, so that the HMF magnitude (Eq. 2.10) is modified as follows to account for the superimposed transverse field components:

$$B = B_e\left(\frac{r_0}{r}\right)^2\sqrt{1 + \left[\frac{\Omega\,(r - r_{\odot})}{V_{sw}}\sin\theta\right]^2 + \left[\frac{r\delta(\theta)}{r_{\odot}}\right]^2}. \tag{2.11}$$

Furthermore, to retain a divergence-free magnetic field ($\nabla \cdot \vec{B} = 0$), it is required that $\delta(\theta) \propto (\sin\theta)^{-1}$, so that

$$\delta(\theta) = \frac{\delta_m}{\sin\theta}, \tag{2.12}$$

is assumed, with $\delta_m = 8.7 \cdot 10^{-5}$ [see *Steenberg*, 1998; *Langner*, 2004]. This yields $\delta(\theta \to 0^{\circ}) \approx 0.002$ and $\delta(\theta \to 90^{\circ}) = 0$. The modified HMF magnitude consequently decreases as $\sim\ 1/r$ instead of $1/r^2$ in the polar regions. *Moraal* [1990] accounts for the same physical effects by incorporating an arbitrary θ-dependent function as a scaling factor. Another modification, though not incorporated in this study, is that by *Smith and Bieber* [1991], which accounts for non-radial magnetic field components up to the Alfvén radius. Finally, there are *Fisk* [1996]-type magnetic fields [discussed in detail by e.g. *Burger*, 2005] that account for the differential rotation of the Sun [e.g. *Snodgrass*, 1983], as well as Fisk-Parker hybrid fields, which reflect the Fisk HMF at the poles, but is Parker-like in the equatorial regions [e.g. *Burger and Hattingh*, 2001; *Burger*

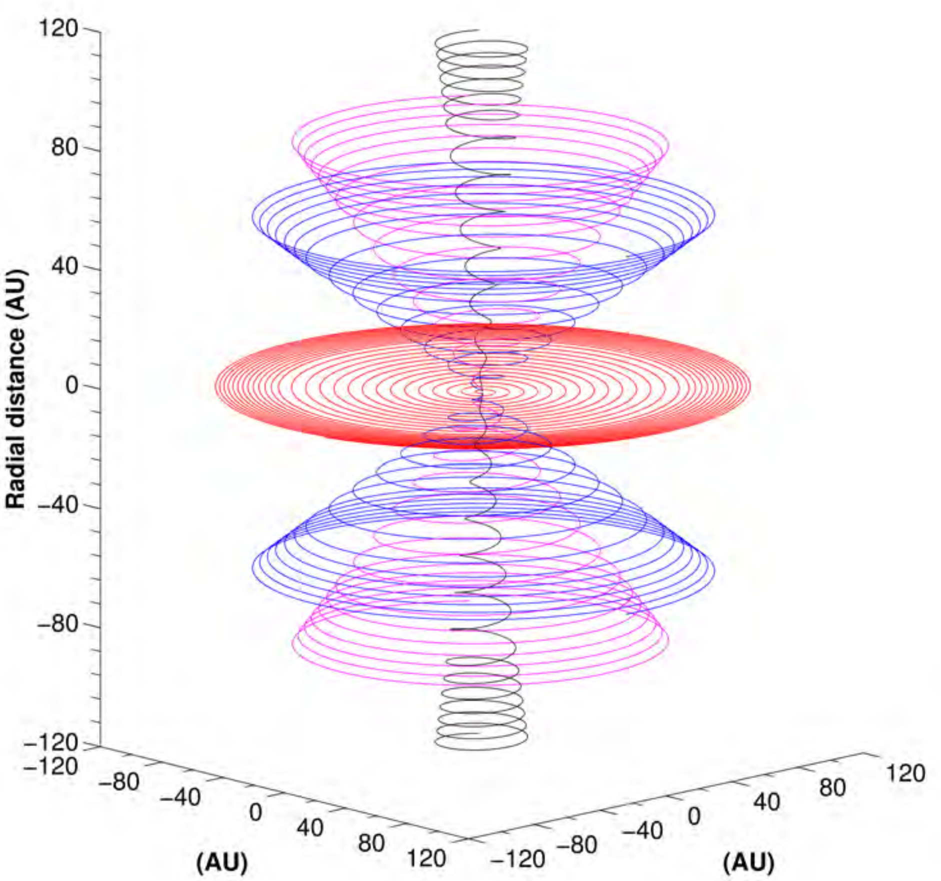

Figure 2.8: A representation of the Parker HMF geometry at co-latitudes of $\theta = 10°$, $170°$ (in black), $\theta = 45°, 135°$ (in magenta), $\theta = 60°, 120°$ (in blue) and at $\theta \approx 90°$ (in red). These field lines are computed by solving $d\phi$ from $d\vec{l} \times \vec{B} = 0$ for a specified step length dr, where $\vec{B}$ is given by Eq. 2.8 and $d\vec{l}$ is the infinitesimal line element in spherical coordinates. Field lines condense at the TS position (at 94 AU) due to the slower SW speed. The Sun is located at the origin.

et al., 2008]. However, since the Fisk HMF is inherently a three-dimensional (3-D) structure, it is not implemented in the current study, which utilises a 2-D CR modulation model. See also the discussions and examples by *Raath* [2015].

2.5 The Heliospheric Current Sheet

Early spacecraft measurements revealed sectors of alternating HMF polarity [*Ness and Wilcox*, 1965; *Wilcox and Ness*, 1965]. These measurements would later be revealed to have sampled the magnetic field on opposite sides of a neutral sheet separating regions of opposite polarity. This structure, like several others, has its origin at the Sun: The open field lines emerging from the high-latitude solar surface eventually extend toward the equatorial regions and run along a surface there (see Figure 2.2); likewise, on the other side of that surface, field lines run inwards and ensue on the solar surface near the polar regions. This dividing surface, called the heliospheric current sheet (HCS), essentially separates the HMF into two hemispheres of opposite polarity, and follows as a requirement of Maxwell's equations [e.g. *Smith*, 2001]. The HCS is neither exactly nor invariantly aligned with the equatorial plane, but is tilted and changes in

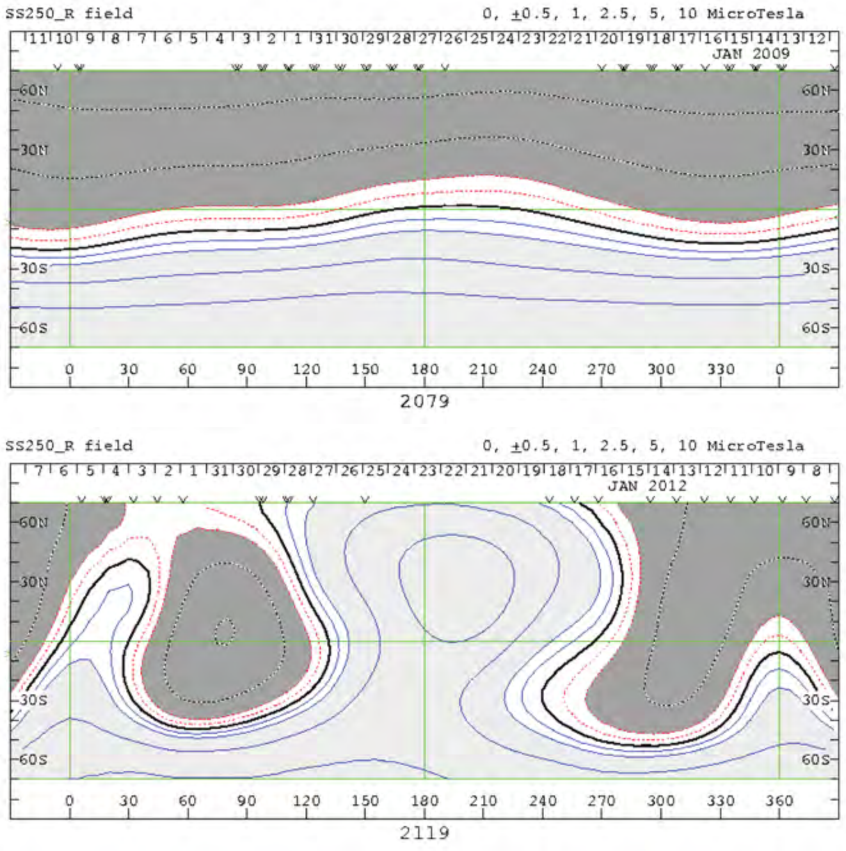

Figure 2.9: Computed solar source surface field maps. The top and bottom panels respectively illustrate magnetic conditions on the Sun during periods of minimum and maximum solar activity. The two shades of grey indicate different polarities and the bold black line represents the HCS. These maps were obtained from the Wilcox Solar Observatory (url: http://wso.stanford.edu/ doa: 29 October 2012).

response to solar activity. Specifically, its form is related to the angular separation between the magnetic and rotational axes of the Sun, denoted by α, the tilt angle, which was already introduced in Section 2.3. During more active solar conditions the tilt angle enlarges, giving rise to a more slanted polarity-dividing boundary on the solar source surface (at $\sim 2.5 r_{\odot}$, where HMF footpoints are anchored) as illustrated in the field maps of Figure 2.9. In these maps, the HCS is visible as a black line separating regions of opposite polarity and is notably more rippled for the map obtained during solar maximum. Together with the Sun's rotation, this dividing boundary creates a wavy sheet when propagated radially outward with the SW, which is illustrated in Figure 2.10 during different stages of solar activity (as emulated by different tilt angles): For more active solar conditions, the HCS is more wavy.

Note that the tilt angle can be computed from observed source surface maps such as those illustrated in Figure 2.9. These computations are done using either one of two existing models, namely the line-of-sight (LOS) model [e.g. *Hoeksema*, 1991], sometimes referred to as the classical model, and the more recent radial model [*Wang and Sheeley*, 1992]. *Burlaga and Ness* [1997] found that the LOS model yields better estimates. From a CR modulation point of view, *Ferreira and Potgieter* [2003] show that the LOS and radial model estimates are better suited as proxies of the solar activity cycle respectively during periods of decreasing and increasing solar activity. Indeed, the tilt angle can be calculated from source surface field maps for every Carrington

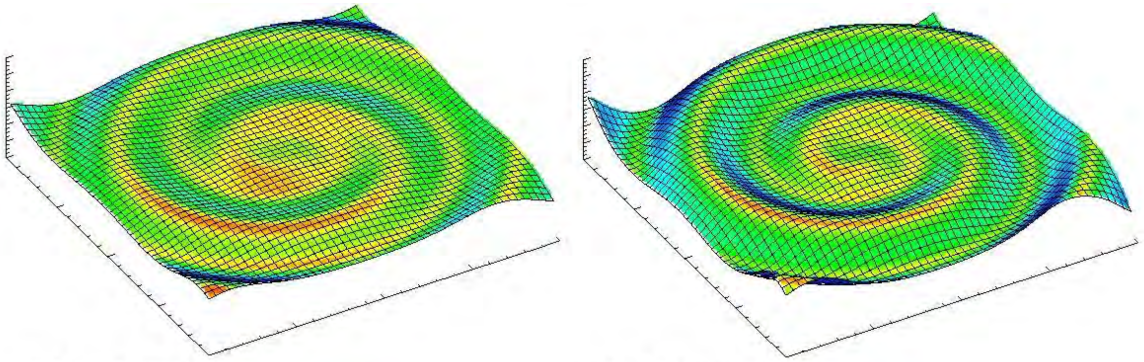

Tilt = 5 degrees

Tilt = 10 degrees

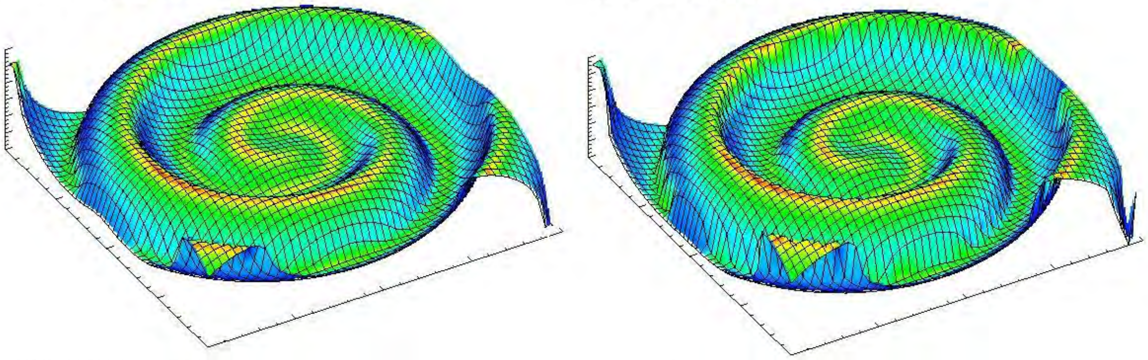

Tilt = 20 degrees

Tilt = 25 degrees

Figure 2.10: Simulations of the HCS at different stages of solar activity as represented by the indicated tilt angles. The simulations are constructed using Eq. 2.14 and extend to a radial distance of 10 AU from the Sun, which position is at the centre of each of the images. Figure obtained from *Strauss* [2010].

rotation[1] for which they are recorded. As such, a time-dependent plot of tilt angles can be constructed as shown in Figure 2.11. The same 11-year solar activity cycle can be deduced from this figure as is seen in Figures 2.1 and 2.6. Indeed, the tilt angle is implemented in this and many other CR modulation studies as an indicator of solar activity levels.

It is a standard practice in solar modulation studies that the tilt angle is used to refer to the latitudinal extent of the HCS, or at least as an indication thereof. The same is done in this study. The latitudinal extent associated with the tilt angle can however be derived as done by *Jokipii and Thomas* [1981]: For tilt angles small enough that $\sin\alpha \approx \tan\alpha$, it follows that

$$\theta' = \frac{\pi}{2} + \sin^{-1}\left\{\sin\alpha\ \sin\left[\phi + \frac{\Omega(r - r_\odot)}{V_{sw}}\right]\right\}, \tag{2.13}$$

which for sufficiently small values of α reduces to

$$\theta' \approx \frac{\pi}{2} + \alpha\sin\left[\phi + \frac{\Omega(r - r_\odot)}{V_{sw}}\right]. \tag{2.14}$$

Here θ' denotes the polar extent of the HCS and ϕ is the azimuthal coordinate. To incorporate

---

[1] Carrington rotations refer to numbered periods of roughly 27.2753 days, which roughly corresponds to the mean duration of a complete solar rotation as observed from Earth. This numbering system begins at 1 on November 9, 1853. At the time of writing Carrington rotation 2170 was in progress.

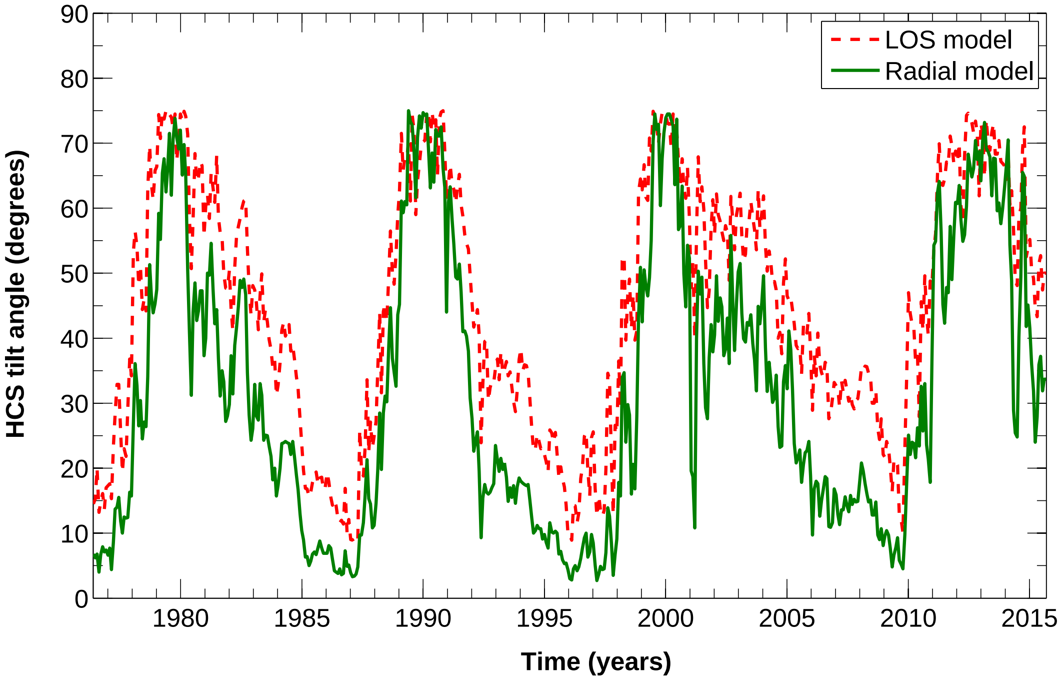

Figure 2.11: The HCS tilt angle as a function of time and computed using the LOS and radial models as indicated in the legend. These tilt angles vary according to the 11-year solar activity cycle, and are largest during solar maximum conditions. Data obtained from the Wilcox Solar Observatory (url: http://wso.stanford.edu/ doa: 11 November 2015).

the HCS into the Parker HMF, Eq. 2.8 is modified as follows:

$$\vec{B} = A_c \, B_e \left(\frac{r_0}{r}\right)^2 (\hat{e}_r - \tan\psi \, \hat{e}_\phi) \left[1 - 2H(\theta - \theta')\right], \tag{2.15}$$

with the HMF polarity stipulated as $A_c = +1$ for A $>$ 0 and $A_c = -1$ for A $<$ 0, and the Heaviside step function given by

$$H(\theta - \theta') = \begin{cases} 0 & \text{for } \theta < \theta' \\ 1 & \text{for } \theta > \theta' \end{cases} \tag{2.16}$$

This simulates the alternation of HMF polarity across the HCS. Although, since discontinuous functions pose some difficulty for numerical models, the Heaviside function is approximated [following e.g. *Hattingh*, 1998] as

$$H(\theta - \theta') \approx \tanh\left[2.75(\theta - \theta')\right]. \tag{2.17}$$

In summary, the HMF switches polarity across the HCS, which becomes increasingly wavy with increased solar activity, which in turn is emulated using the tilt angle. A magnetically sectored region of alternating polarities is created as a result, extending above and below the equatorial plane of the heliosphere by amounts associated with the tilt angle. Note though that the HCS does not necessary extend by equal amounts on either side of the equatorial plane [e.g. *Burlaga and Ness*, 1997]. Observations also suggest that radially the HCS extends throughout the heliosphere and into the heliosheath [*Balogh and Jokipii*, 2009; *Hill et al.*, 2014]. See also *Smith* [2001] for an overview on the HCS.

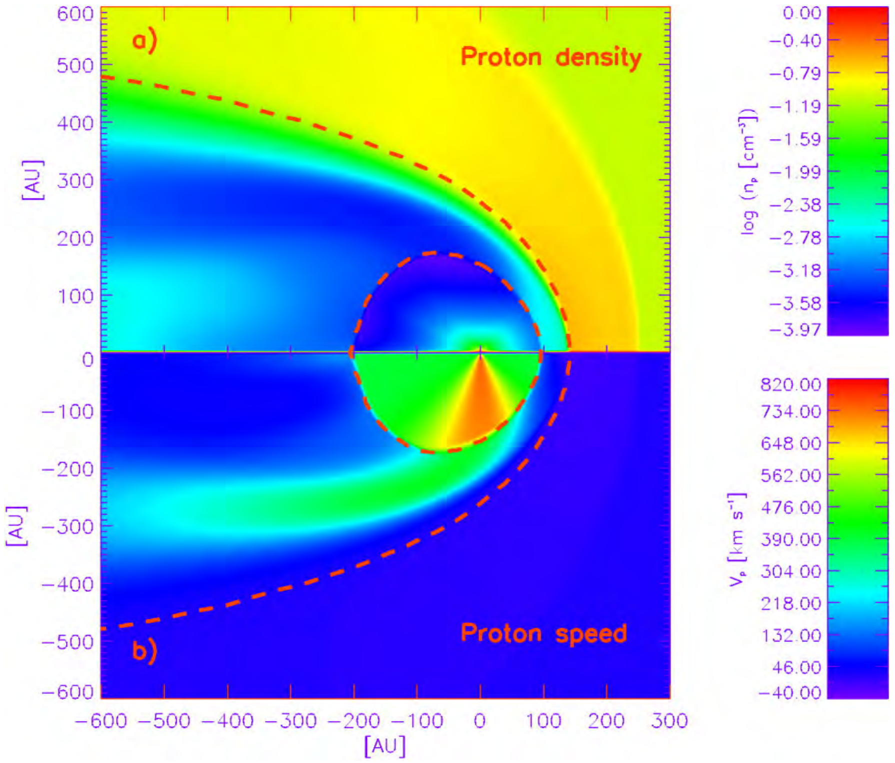

Figure 2.12: HD-modelled SW (proton) number density (top panel) and flow speed (bottom panel) in the meridional plane of the heliosphere. These results are shown in the rest frame of the Sun, which is situated at the origin. The inner and outer dashed lines respectively represent the profiles of the TS and HP. The fast SW stream in the polar regions of the bottom panel is indicative of solar minimum conditions. Figure obtained from *Ferreira and Scherer* [2004].

2.6 Global Features of the Heliosphere

The heliosphere is the region of interstellar space filled with solar material. It is formed and characterised by the SW outflow, its embedded magnetic field, and the movement of the Sun through the interstellar medium (ISM). The result of the SW-ISM interaction is a heliosphere with boundaries separating regions of different flow and magnetic characteristics. These boundaries are the TS, the heliopause (HP), and a possible bow shock (BS). For the purposes of this study, the inner heliosphere refers to regions well inside the TS, characterised by radial supersonic SW flow. The properties of this region is predominantly governed by the Sun itself, its magnetic field structure, and the initial coronal outflow. This is discussed in preceding sections. The regions beyond the TS that are perturbed by the influence of the Sun are collectively referred to as the outer heliosphere and are discussed in greater detail below.

Note that despite their invaluable contribution to the insights garnered of the remote regions of the heliosphere, the Voyager spacecraft only provide observations along two separate trajectories. Discussions on the global features of the heliosphere therefore rely heavily on the results of HD and MHD modelling. Figure 2.12 shows an example of HD modelling, while Figures 2.13 and 2.14 are the results of MHD modelling; see also the references provided in the figure captions. Observations through remote sensing can also inform these discussions, e.g. the Interstellar Boundary Explorer (IBEX) uses energetic neutral atom (ENA) imaging to explore the outer heliosphere [see e.g. *Frisch and McComas*, 2013].

2.6.1 The termination shock

The existence of the TS was first postulated by *Parker* [1961], and occurs where the total SW pressure equals that of the ISM. Following several attempts to estimate its position [e.g. *Steinolfson and Gurnett*, 1995], the TS was traversed by Voyager 1 and 2 at respective radial distances of 94 AU [*Stone et al.*, 2005] and 84 AU [*Burlaga et al.*, 2008]. It is shown in both Figures 2.12 and 2.13 as the innermost lines in dashed red and solid black respectively. The TS was introduced in Section 2.3 as a discontinuous decrease of the SW speed, which decelerated the flow from supersonic to subsonic flow speeds; note that the sonic speeds referred to are those local to the considered regions. This decrease is also visible in Figure 2.12. The transitions of plasma quantities such as the SW speed across the TS can furthermore be described using the Rankine-Hugonoit (RH) equations [see e.g. *Jones and Ellison*, 1991; *Lee et al.*, 2009]: Given that the compression ratio of a shock for non-relativistic flow is defined as $s = V_{sw}^{-}/V_{sw}^{+}$ $(= \rho^{+}/\rho^{-})$, it follows from the RH equations that

$$s = \frac{(\gamma_c + 1)\,(M^{-})^2}{(\gamma_c - 1)\,(M^{-})^2 + 2}\,, \tag{2.18}$$

where γ_c is the ratio of specific heat at constant pressure to that at constant volume, M^{-} is the Mach number, specified as $(V_{sw}/c_s)^{-}$, and V_{sw} and ρ represent the SW speed and mass density as before; c_{sw} is the local speed of sound. The superscripts $-$ and $+$ are introduced to respectively denote upstream (or *unshocked*) and downstream (*shocked*) values. For sonic upstream flow, that is, with Mach number $M^{-} = 1$, Eq. 2.18 reduces to $s = 1$ and no shock is observed. Since the upstream SW flow is supersonic ($M^{-} > 1$), it follows that $s > 1$ for the TS. The maximum value of the compression ratio follows from Eq. 2.18 when $M^{-} \to \infty$ as

$$s = \frac{\gamma_c + 1}{\gamma_c - 1}\,, \tag{2.19}$$

which evaluates to $s = 4$ with $\gamma_c = 5/3$ for a monatomic plasma (as the SW is approximated to be) with non-relativistic flow. The SW speed is however shown by Voyager 2 to suffer a number of step-like decreases near the TS [*Richardson et al.*, 2008], owed to multiple encounters of the spacecraft with the shock due to its relative motion. Each of these encounters reflected a different compression ratio. A summary of empirical estimates for the compression ratio is presented in Section 4.3. Collectively, observations from both Voyager spacecraft suggest a moderately strong shock, and $s = 2.5$ is applied in this study as an approximate value.

Additionally, the upstream SW flow is also decelerated over a length scale of about 1 AU it approaches the TS [*Richardson et al.*, 2008]. This is suggestive of a SW precursor, as shown in Figure 2.5, and is reflected by the measurements of both Voyager spacecraft [*Decker et al.*, 2005; *Richardson et al.*, 2008]. *Florinski et al.* [2009] explains the pre-shock deceleration of the SW as an effect of the back pressure of energetic particles, supported by measurements of high partial pressures of energetic ions [*Decker et al.*, 2008], while *Richardson et al.* [2008] attributes this precursor to magnetic field enhancements associated with transient structures or standing waves. See also *le Roux and Fichtner* [1997] and *Florinski et al.* [2004] for details on particle-modified shocks. In this study, it is not the cause of the SW precursor but its consequences

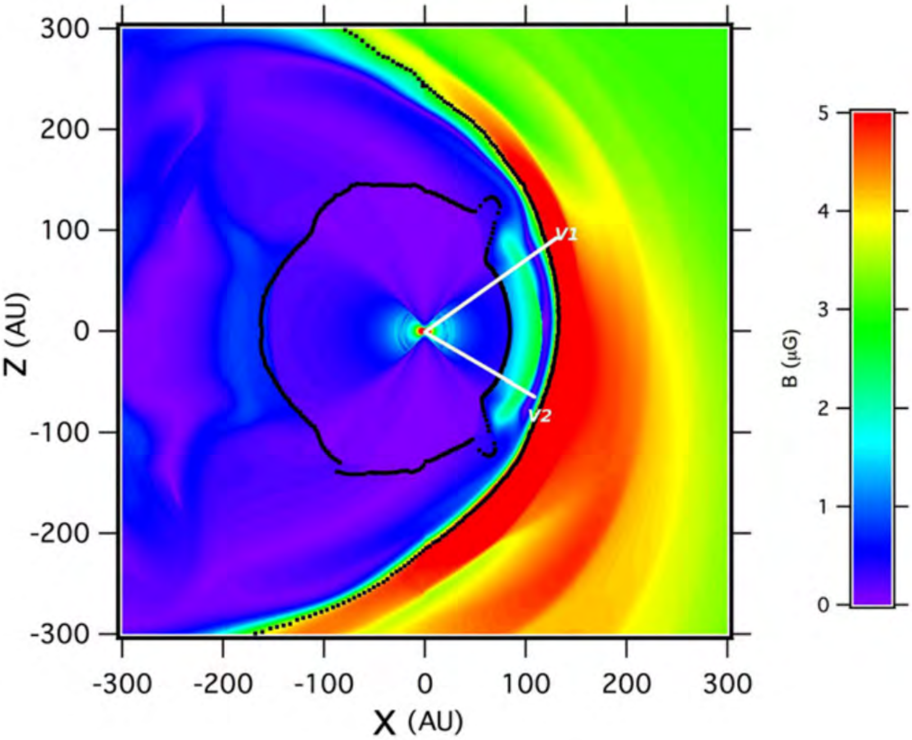

Figure 2.13: MHD-modelled HMF magnitude in the meridional plane of the heliosphere in the rest frame of the Sun, which is situated at the origin. The inner and outer borders shown as black lines respectively represent the profiles of the TS and HP. Also, the projections of the Voyager 1 and 2 trajectories are shown as white lines; note that these spacecraft are actually separated by $\sim 50°$ azimuthally. Figure obtained from *Luo et al.* [2015].

that are of interest. Its effects on e.g. CR acceleration is investigated in Chapter 4. The SW precursor is modelled using Eq. 2.4 and numerical accommodations such as a transformed numerical grid in the vicinity of the TS; see Section 3.7. Note that the SW precursor takes the form of a continuous decrease in the SW speed, and precedes a discontinuous jump referred to in this study as the subshock; see Figure 2.5. These two components form the extended shock structure. Note that the investigation of CR acceleration at the TS is a primary aim of this study, and more on this will follow in later chapters. For further reading on the properties of the TS, see e.g. *Li et al.* [2008] and *Jokipii* [2013].

2.6.2 The heliosheath

The TS lies on the threshold of the heliosheath, which is characterised by slow and increasingly non-radial SW flow [e.g. *Li et al.*, 2008; *Richardson et al.*, 2009]. Due to their relations, the slower SW flow implies larger mass (or number) densities and HMF magnitudes [e.g. *Burlaga and Ness*, 2012] as shown in Figures 2.12 and 2.13 in the regions beyond the TS. See also the reviews by *Balogh and Jokipii* [2009], *Richardson and Stone* [2009] and *Richardson and Burlaga* [2013] for more on the plasma and magnetic properties observed thus far in the heliosheath. Along the Voyager 1 trajectory, the aforementioned conditions persisted until *Decker et al.* [2012] inferred that the radial flow speed at Voyager 1 was virtually zero shortly before crossing of the HP at 122 AU [*Gurnett et al.*, 2013; *Stone et al.*, 2013; *Webber and McDonald*, 2013]. The same feat from Voyager 2 is yet to follow. The HP, a tangential discontinuity, essentially separates the SW from the

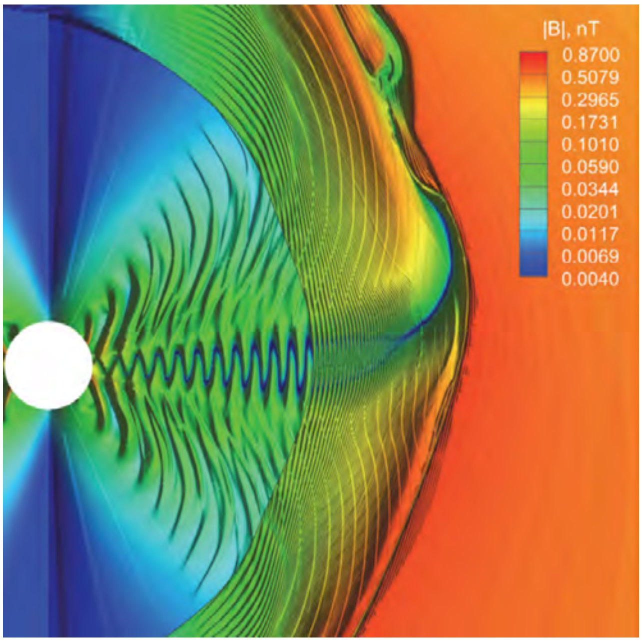

Figure 2.14: MHD-modelled HMF magnitude in the meridional plane of the heliosphere, with the included effects of CIRs. The HCS is shown as a wavy structure with small magnetic field strengths, extending from the Sun to the left of the figure along the equatorial regions and into the heliosheath, where it flips upward into the northern hemisphere. Figure obtained from *Borovikov et al.* [2012].

charged component of the ISM, and is indicated in Figures 2.12 and 2.13 by the outermost lines in dashed red and solid black. In addition to observations, the regions near the HP have been the subject of a great number of studies conducted using MHD models with diverse aims such as investigating the heliospheric structure [e.g. *Pogorelov et al.*, 2009; *Borovikov and Pogorelov*, 2014], flow and magnetic characteristics [e.g. *Opher et al.*, 2012; *Pogorelov et al.*, 2012], and CR modulation [e.g. *Strauss et al.*, 2013b; *Luo et al.*, 2015]. See also the heliosheath configurations as described by *Baranov* [2009] and *Fisk and Gloeckler* [2013]. While the region between the TS and HP is formally known as the inner heliosheath, it is referred to generally in this study as the heliosheath, since the HP is the outermost boundary considered in further chapters.

Some recent developments on the regions beyond the HP are also briefly discussed here. Analogous to the TS, the BS is a boundary where the ISM flow (moving inward with respect to the heliosphere) is reduced in speed. Though faint, it is visible in Figures 2.12 and 2.13 at about 200 to 250 AU. It is thought to be preceded by a high-density region often referred to as the hydrogen wall due to the build-up of neutral hydrogen between the HP and BS [see e.g. *Pogorelov et al.*, 2007; *Zank et al.*, 2013]. *McComas et al.* [2012] however inferred from IBEX observations that the ISM flow at $\sim$ 23.2 km.s^{-1} is slower than previously expected, and argued that what was thought to be a BS rather constitutes an extended bow wave region. The absence of a BS, and by extension the absence of a hydrogen wall, create difficulties in explaining observations of Ly-α emissions in the outer heliosphere [*Zank et al.*, 2013]. *Scherer and Fichtner* [2014], on the other hand, show that by including a helium component in simulations of the ISM the scenario of a BS is still valid. Depending on the outcome of the above controversy, the outer heliosheath may either be defined as the region between the HP and the BS or more generally as the perturbed region of the ISM beyond the HP. It is however not considered in this study.

2.6.3 A dynamic and irregular heliosphere

Due to the dynamical nature of the Sun, the global features of the heliopshere are bound to be transformed according to the same variabilities and in particular the solar activity cycle [*Scherer and Fahr*, 2003]. The fast SW streams appearing during solar minimum conditions, for example, cause the heliosphere to be elongated towards the polar regions [e.g. *Scherer and Ferreira*, 2005]. Moreover, due to solar rotation and the interaction between fast and slow SW streams, co-rotating interaction regions (CIRs) are created, which further interact with each other to give rise to highly complicated plasma structures at large heliospheric distances and in the heliosheath [*Borovikov et al.*, 2012]. This is illustrated in Figure 2.14. Note also from this figure that the HCS, being restricted to the confines set by the HP, extends along a single hemisphere in the heliosheath, which creates an evident north-south asymmetry.

The heliosphere is indeed unlikely to be symmetrical in any plane. The first most obvious suggestion in this regard came with the crossings of the TS at different distances by the two Voyagers [*Stone et al.*, 2005, 2008], although this might also have been due to the motion of the TS in response to the solar activity cycle. This possible asymmetry prompted MHD modelling revealing the potential involvement of the interstellar magnetic field (ISMF): In addition to the inclination of the the ISM flow with the equatorial plane of the heliosphere, the orientation of the ISMF is such that a build-up of magnetic pressure occurs in the southern hemisphere [*Opher et al.*, 2006, 2009; *Pogorelov et al.*, 2007, 2008], essentially compressing that region and accounting for the Voyager 2 crossing of the TS at a smaller distance. Indeed, observations from IBEX corroborate such an ISMF orientation [*McComas et al.*, 2009]. Figure 2.13 also shows a particularly pronounced magnetic field magnitude in the southern region along the Voyager 2 direction of travel. Note also that there are several CR modulation studies probing the effects of an asymmetrical heliosphere [e.g. *Ferreira et al.*, 2004a; *Langner and Potgieter*, 2005; *Ngobeni and Potgieter*, 2011, 2012]. Aside from the north-south asymmetry, the heliosphere is elongated away from its direction of movement, which gives rise to the heliotail [e.g. *Pogorelov et al.*, 2015].

This study is concerned mostly with properties along the Voyager trajectories, and is hence focussed on the nose region of the heliosphere (in its direction of travel), and only within the HP; a spherical-symmetric heliosphere remains a reasonable approximation if the considered region is constrained in this manner.

2.7 Cosmic Rays

In this study, CRs refer to energetic (non-thermal) charged particles either accelerated and transported from astrophysical sites or originating locally in the heliosphere through various acceleration processes. Their existence was initially inferred at the turn of the nineteenth century following the discovery of radioactivity and observations of the spontaneous discharge of electroscopes. This would lead to the postulation of an ionising radiation of extraterrestrial origin that consisted mostly of gamma rays. It was hence before establishing the corpuscular nature of the ionising radiation that the curious name of “cosmic rays” would be coined. See the review by *Carlson* [2012]. The latter-day CRs are categorised according to their origins:

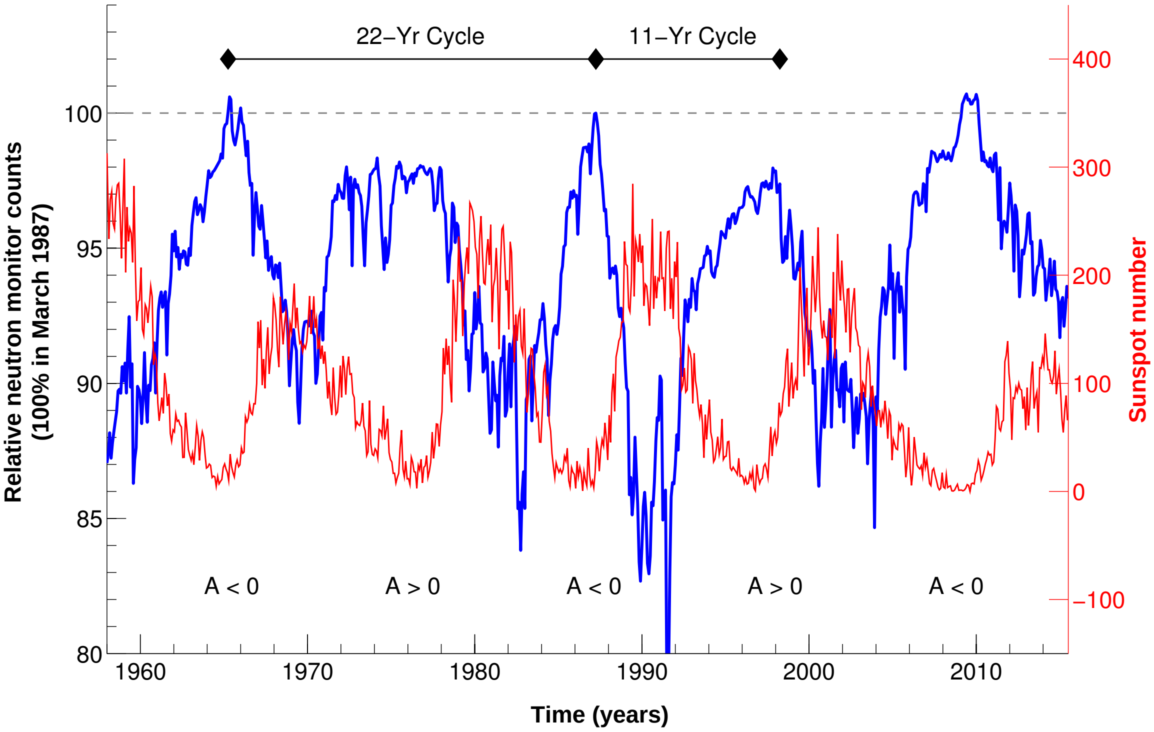

Figure 2.15: CR intensities at Earth (blue line) over time as represented by the count rates registered at the neutron monitor based in Hermanus, South Africa. The counts are normalised to 100% at the level registered in March, 1987. The monthly sunspot number is shown as a red line for comparison. An example of a complete 11- and 22-year cycle is indicated, along with the polarity epoch of each solar cycle. The sunspot data is obtained from the source cited in Figure 2.1 and the neutron monitor counts from http://www.nwu.ac.za/neutron-monitor-data (doa: 11 November 2015).

- Galactic cosmic rays (GCRs) have been observed with energies up to $3 \cdot 10^{20}$ eV [e.g *Fraschetti*, 2008], although their intensity levels measured at Earth generally decline with increasing energy; see also *Moskalenko et al.* [2002] and *Hillas* [2006] for more on their energy spectra. They are fully ionized and originate outside the heliosphere from galactic and extragalactic sources. Among the likely sites for their acceleration are supernovae and their remnants, e.g. pulsars [e.g. *Büsching et al.*, 2008a, b]. Below $\sim$ 30 GeV they become susceptible to solar and heliospheric modulation [*Strauss and Potgieter*, 2014]. See also *Swordy* [2001] for more on the elemental composition of GCRs. Galactic electrons are of particular interest in this study and are discussed further in Section 2.7.2.

- Anomalous cosmic rays (ACRs) are discussed in Section 2.7.1.

- Jovian electrons with energies up to 100 MeV originate from the magnetosphere of Jupiter, as first revealed by the Pioneer 10 spacecraft. These particles dominate CR intensities in the inner heliosphere [e.g. *Strauss et al.*, 2013a]. See also *Ferreira et al.* [2001a, b] and *Potgieter and Nndanganeni* [2013a]. Though occasionally mentioned, Jovian electrons are not formally considered in this study.

- Energetic charged particles also emerge from the Sun [see *Cliver*, 2000; *Dröge*, 2000b], but are not considered in this study.

Whereas the GCR component will be more pronounced in the outer heliosphere, the contribution at Earth is decidedly more heterogeneous. Ground-based observations give an indication of the incident flux of GCRs at Earth, because generally only GCRs have sufficient energy to penetrate through the geomagnetic field instead of being diverted along field lines to the poles. These high-energy CRs hence interact with atmospheric particles to produce cascades of secondary particles [e.g. *Gil et al.*, 2015], which are detected by neutron monitors on the Earth's surface. Figure 2.15 shows the CR flux recorded in this manner over the last few decades. As mentioned in Section 2.2, both an 11-year and a 22-year periodicity is observed. With regards to the 11-year cycle, CR intensities are anti-correlated with solar activity, which is represented in the figure by the sunspot number. During solar maximum conditions the HMF magnitude and associated turbulence increase, which results in impaired diffusion of CRs to Earth and hence lower intensities. Also prevalent during periods of high solar activity (e.g. 1991) are large and sudden discontinuous decreases in CR intensities. These are referred to as Forbush decreases and are associated with transient events such as coronal mass ejections, which form propagating diffusion barriers that sweep incoming GCRs away. See also *le Roux and Potgieter* [1995] and *Haasbroek et al.* [1995]. The 22-year cycle is discernible in Figure 2.15 from the form of consecutive intensity peaks: For $A < 0$ sharp intensity peaks are observed, while these are broader and lower for $A > 0$. This is a consequence of the drift directions of CRs during each HMF polarity [e.g. *Potgieter and Moraal*, 1985], which are introduced in Chapter 3 and illustrated again in the chapters thereafter. The unusual minimum of 2009 has evoked particular interest [e.g. *Moraal and Stoker*, 2010; *Potgieter et al.*, 2014a], as it is associated with especially small HMF magnitudes (see Figure 2.6) and high CR intensities. See *Bazilevskaya et al.* [2014] and *Potgieter* [2008, 2010, 2013, 2014b] for more on CRs and their interaction with the solar cycle.

2.7.1 Anomalous cosmic rays

Garcia-Munoz et al. [1973] and *Hovestadt et al.* [1973] respectively reported enhancements in the fluxes of CR Helium and Oxygen. These enhancements were attributed to the contribution of ACRs, which were named after their relatively high abundances [*McDonald et al.*, 1974]. *Fisk et al.* [1974] explained that these particles arise from a seed population inside the heliosphere: Neutral interstellar particles entering the heliosphere become ionised and are consequently swept up with the SW due to its embedded HMF to form pick-up ions (PUIs). The manner in which these neutrals are ionised depends largely on their location: Nearer to the Sun they may be photo-ionised, while they most likely undergo charge exchange with SW protons in the heliosheath. Indeed, Figure 2.16 confirms the highest densities of PUIs occur near the Sun and in the heliosheath. Note by comparing the top and bottom panels of this figure that their distributions also vary somewhat with the solar cycle.

To attain ACR energies the PUIs must be accelerated further, although how this transpires has been the source of some contention. Originally, PUIs were proposed to be accelerated to ACR energies through diffusive shock acceleration (DSA) at the TS [*Fisk et al.*, 1974; *Pesses et al.*, 1981]. See also the reviews by *Fichtner* [2001] and *Moraal* [2001]. However, with the Voyager spacecraft having explored the outer heliosphere, observations suggest that the source of ACRs is further into the heliosheath [*McDonald et al.*, 2007; *Webber et al.*, 2007]. Following earlier modelling [e.g.

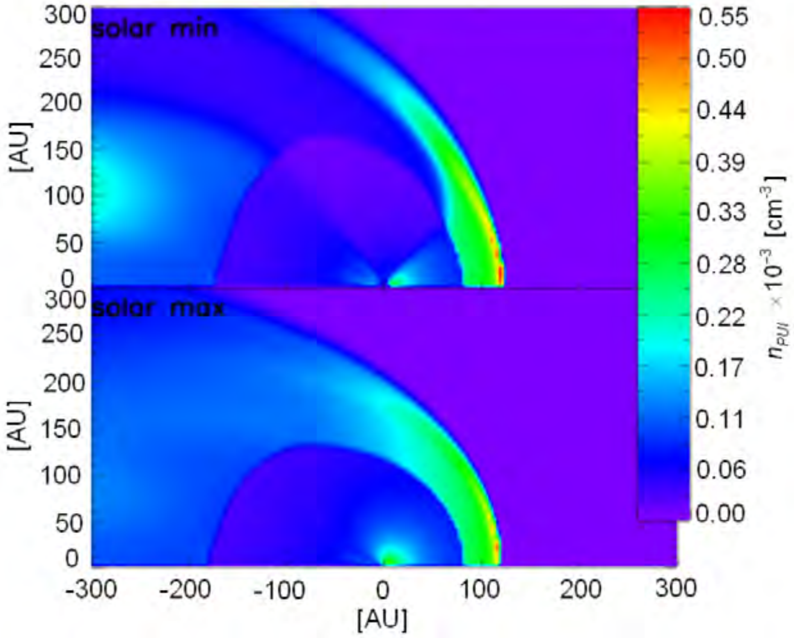

Figure 2.16: HD-modelled PUI densities in the meridional plane of the heliosphere during solar minimum (top panel) and maximum (botttom panel). The Sun is located at the origin and the heliosheath is centred around $\sim$ 100 AU in the nose direction. Figure obtained from *Scherer and Ferreira* [2005].

Zhang, 2006; *Ferreira et al.*, 2007a; *Moraal et al.*, 2008], *Strauss et al.* [2010b] accounted for the observations of ACR Oxygen in the heliosheath through the inclusion of adiabatic heating and stochastic acceleration in their modulation model. Termination shock particles (TSPs), on the other hand, are still thought to arise from DSA of PUIs at the TS. Their energy distributions resemble power laws and are visible at lower energies, preceding the intensity enhancements associated with ACRs [see e.g. *Stone et al.*, 2005]. For more details on the possible acceleration mechanisms involved in the formation of ACRs, see the review by *Giacalone et al.* [2012]. Note that while ACRs are usually singly charged, having lost only one orbital electron, multiply-charged ACRs are also observed [*Mewaldt et al.*, 1996; *Strauss*, 2010; *Strauss et al.*, 2010a].

Note finally that while TSPs and ACRs are often viewed as separate populations [see e.g. *Lee et al.*, 2009], this study, which primarily aims to illustrate the features of DSA, makes no distinction between the two. Hence, references to ACRs in this study imply all particles that arise as a result of the acceleration (including DSA at the TS) of a PUI seed population. The discussion of ACRs continues in Chapter 4, while details of their modelling are provided in Chapter 3.

2.7.2 Galactic electrons

GCR electrons (or simply referred to as galactic electrons) exhibits significantly different behaviour from CR ions. This stems mostly from the fact that they are relativistic down to much smaller energies than their ionic counterparts. The various aspects of their behaviour, and how this behaviour is modelled, are conveyed in subsequent chapters. See also the relevant discussions of *Florinski et al.* [2013]. In this section, the major observational features of electrons are surveyed to provide context for the modelling to follow.

Figure 2.17 illustrates the radial distribution of electrons in the heliosphere. Between 22 AU and

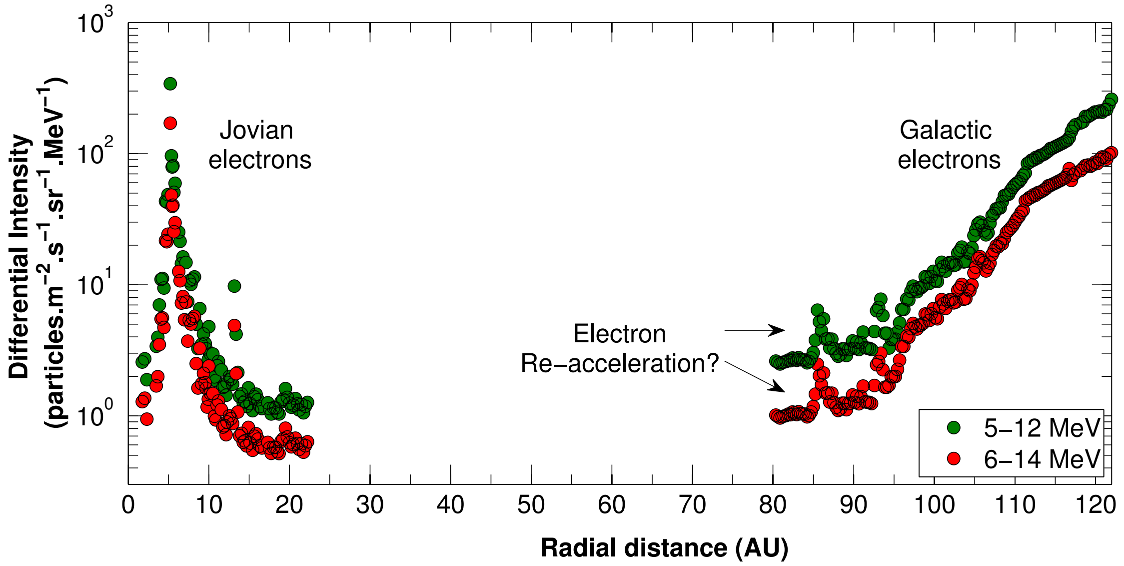

Figure 2.17: Radial intensities of low-energy electrons as observed by Voyager 1 [*Webber*, 2014]. Jovian electrons dominate in the inner heliosphere, with intensities peaking at Jupiter's position at 5 AU. In the outer heliosphere, intensities of galactic electrons are reduced by a large factors from the HP (at 122 AU) to the TS (at ∼ 94 AU), while intensity peaks near the latter possibly emerge as a result of re-acceleration.

80 AU intensities are unfortunately contaminated by background-produced electrons and thus are not displayed [see also *Nndanganeni*, 2015]. As mentioned in the introduction to this section, at smaller radial distances intensities are dominated by the contribution of Jovian electrons, especially at lower energies. Note that the intensities peak at Jupiter's approximate position at 5 AU. This obscures the contribution of the galactic component. See also the modelling of *Potgieter and Nndanganeni* [2013a] in this regard. Of greater interest though to this study are the features in the outer heliosphere. In the vicinity of the TS, which is at roughly 94 AU in Figure 2.17, peak-like increases are visible for low-energy electrons (of 5 to 14 MeV) and to lesser extent at higher energies. These are associated with the acceleration of electrons at the TS [*Stone et al.*, 2005; *Decker et al.*, 2005; *Stone et al.*, 2008]. Note that since galactic electrons were likely accelerated during their formation at astrophysical sites, those electrons that undergo DSA at the TS are referred to in this study as re-accelerated electrons. The features of shock-accelerated electrons are studied in Chapter 6. Another notable feature in Figure 2.17 is the steep intensity gradient between the TS and the HP at 122 AU. This stark decrease of electron intensities from their local interstellar levels follows as a result of large modulation in the heliosheath, which in turn informs the levels of diffusion that ought to be reflected when modelling electron modulation in this region; see Section 3.3.

Further insights on modulation parameters may be derived from the observed electron energy spectra illustrated in Figure 2.18. At energies from about 10 to 100 MeV, distributions appear to remain largely power-law distributed and their spectral indices unchanged from that measured at the HP [*Stone et al.*, 2013]. This suggests that diffusion levels remain largely constant across this range of energies. Furthermore, since the solar modulation of CRs phases out, the intensity levels measured toward higher energies at Earth may provide an indication of local interstellar intensity levels at energies where no *in situ* measurements are available. On the opposite end of the spectrum, at low energies, distinguishing between the contributions of solar

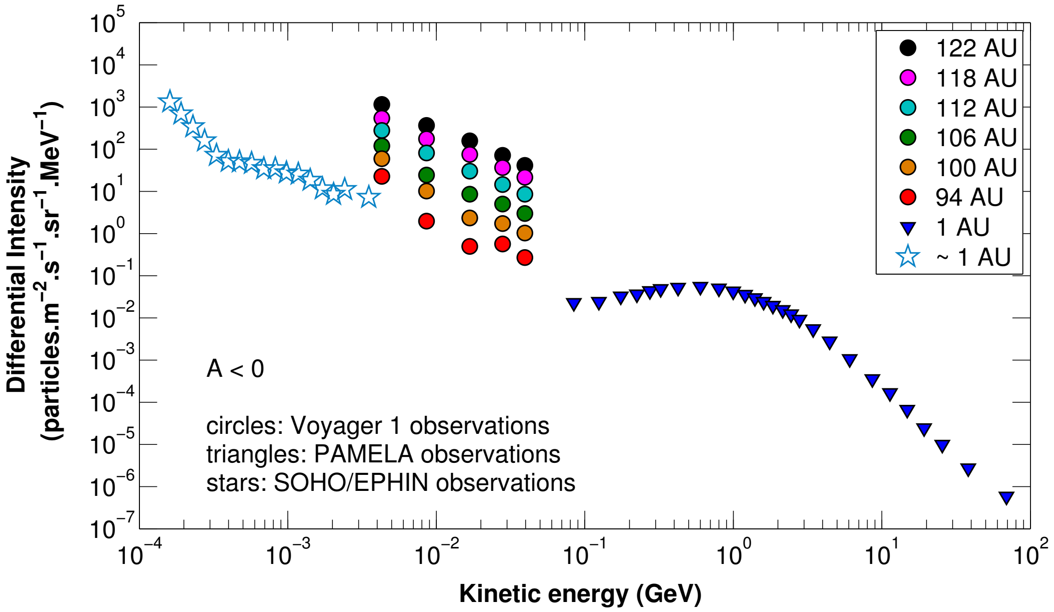

Figure 2.18: Observations of electron energy spectra at Earth (SOHO/EPHIN: 2007/8; PAMELA: 2nd Semester, 2009, *Adriani et al.* [2011]) and at distances along the Voyager 1 trajectory [*Webber*, 2014] from the TS (94 AU) to the HP (122 AU). SOHO data from *Khül et al.* [2013].

energetic particles (SEPs), Jovian and galactic electrons remains problematic. To make meaningful inferences with regards to electron modulation at these energies the more fundamental aspects characterising modulation, e.g. the underlying turbulence, have to be considered. The features of electron modulation, as well as the expected levels of local interstellar intensities, are explored further in Chapter 5, while the basic concepts of their transport are introduced in Chapter 3. Modelling results and observations are compared in Chapter 7.

2.8 Summary

This chapter reviewed the heliospheric physics essential for an adequate contextual background for the rest of this study.

Two pertinent cycles of solar variability are identified, namely the 11-year solar activity cycle and the 22-year magnetic polarity cycle. Furthermore, with regards to the SW, a radial supersonic flow is assumed for the inner heliosheath, which decreases in speed at the TS by a factor equivalent to its compression ratio. A TS precursor region is also incorporated. The SW speed continues to decrease in the heliosheath under the assumption of incompressible flow. A latitude dependence, giving rise to fast SW streams at high latitudes during solar minimum conditions, is also included. Embedded in the SW, the HMF is described according to the *Parker* [1958] model with the modification of *Jokipii and Kota* [1989], and a HCS is introduced that is coupled to the solar activity cycle through its associated tilt angle. This study is furthermore focused on the nose region of the heliosphere, and only as far out as the HP. It is therefore reasonable to assume a spherical heliosphere if the scope is limited in this manner. ACRs are introduced with the aim on the modelling presented in Chapter 4, while observations of galactic electrons are illustrated and discussed to provide context for Chapters 5 through 7.

The transport and modulation of CRs, as subjected to the heliospheric configuration summarised above, are discussed in the next chapter.

Chapter 3

Cosmic Ray Transport and Acceleration Model

3.1 Introduction

Chapter 2 gave an introduction to CRs and the major defining properties of the heliosphere. As CRs are transported through the heliosphere they are subjected to a number of modulating physical processes that cause their distribution function to change as a function of position, time, and energy. It is the purpose of this chapter to characterise these processes mathematically and model the responding CR behaviour by solving a charged-particle transport equation.

The relevant transport equation is firstly introduced and the processes accounted for therein are discussed. Further discussions elaborate on the mathematical representation of these processes in the transport equation and its transformation to a spherical coordinate system. As a result of the complexity of the transport equation and its constituent parts, analytical solutions cannot be attained without simplifying assumptions and hence numerical solutions are sought instead. The details of the numerical model implemented in this study to solve the transport equation are reviewed concisely.

3.2 The Parker Transport Equation

Accounting for the relevant physical processes [*Fisk*, 1999], the *Parker* [1965b] transport equation (TPE) given by

$$\frac{\partial f}{\partial t} = -\left(\vec{V}_{sw} + \langle \vec{v}_D \rangle\right) \cdot \nabla f + \nabla \cdot (\mathbf{K}_s \cdot \nabla f) + \frac{1}{3}\left(\nabla \cdot \vec{V}_{sw}\right) \frac{\partial f}{\partial \ln p} + Q_s \, , \tag{3.1}$$

is used in this study to describe the modulation of CRs in the turbulent heliospheric plasma. See also the re-derivation of this TPE, of which the Fokker-Planck equation is a more general form, by *Gleeson and Axford* [1967]. A review on CR modulation equations is provided by *Moraal* [2013]. Eq. 3.1 is solved for the pitch-angle averaged CR distribution function, $f = f(\vec{r}, p, t)$, with $\vec{r}$, p, and t each denoting position, momentum, and time. With regards to the

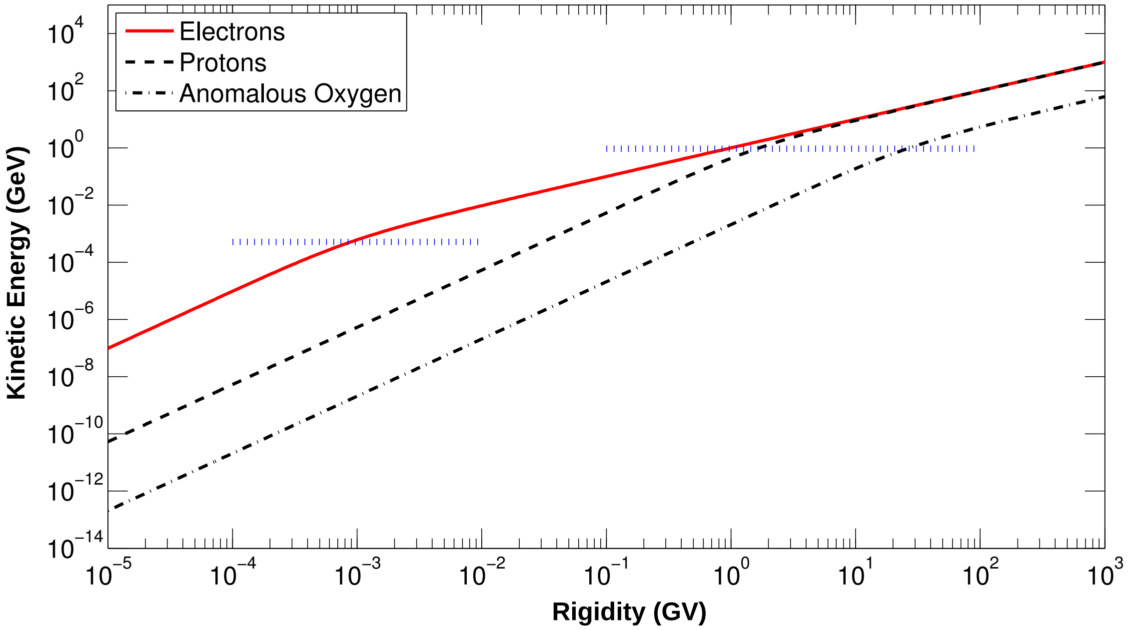

Figure 3.1: The kinetic energy of a particle or nucleon as a function of its rigidity (according to Eq. 3.4) for the CR species indicated in the legend. The electron and proton rest-mass energies, that is, $e_0 = 0.511$ MeV and $E_0 = 938.3$ MeV, are shown as dotted horizontal lines. The electrons and protons both have Θ-values of 1, whereas $\Theta = 16$ for ACR Oxygen.

distribution function, the terms from left to right describe time-dependent changes, convection due to the SW flow at a velocity of $\vec{V}_{sw}$, CR drifts in terms of the pitch-angle averaged guiding centre drift velocity of $\langle\vec{v}_D\rangle$, spatial diffusion as described by the diffusion tensor, $\mathbf{K}_s$, adiabatic energy changes through the divergence of the SW velocity ($\nabla \cdot \vec{V}_{sw}$), and the contribution of CR sources inside the heliosphere. This study only formally considers the transport of GCRs and ACRs, for which the initial distributions are specified as boundary conditions at the HP and TS respectively. The source term denoted $Q_s = Q_s(\vec{r}, p, t)$ in Eq. 3.1 is hence not regarded.

Note that while the TPE is written in terms of momentum, it is solved in terms of rigidity, P, which is related to the former according to

$$P = \frac{pc}{|q|}, \tag{3.2}$$

where p is the particle's relativistic momentum and $|q| = Ze$ its charge, with Z the atomic number, e the elementary charge, and c the speed of light. The relation between a particle's rigidity and its total kinetic energy, E, can furthermore be derived from its total relativistic energy as

$$P = \left(\frac{A}{Ze}\right)\sqrt{E(E + 2E_0)}, \tag{3.3}$$

or conversely

$$E = \sqrt{P^2\left(\frac{Ze}{A}\right)^2 + E_0^2} - E_0\,, \tag{3.4}$$

with A the mass number and E_0 the rest-mass energy of the particle. Note that when considering CR ions, E denotes the total kinetic energy per nucleon. For electrons, $E_0 = e_0 = 0.511$ MeV (the electron rest-mass energy) while for ions the proton rest-mass energy of $\sim$ 938.3 MeV

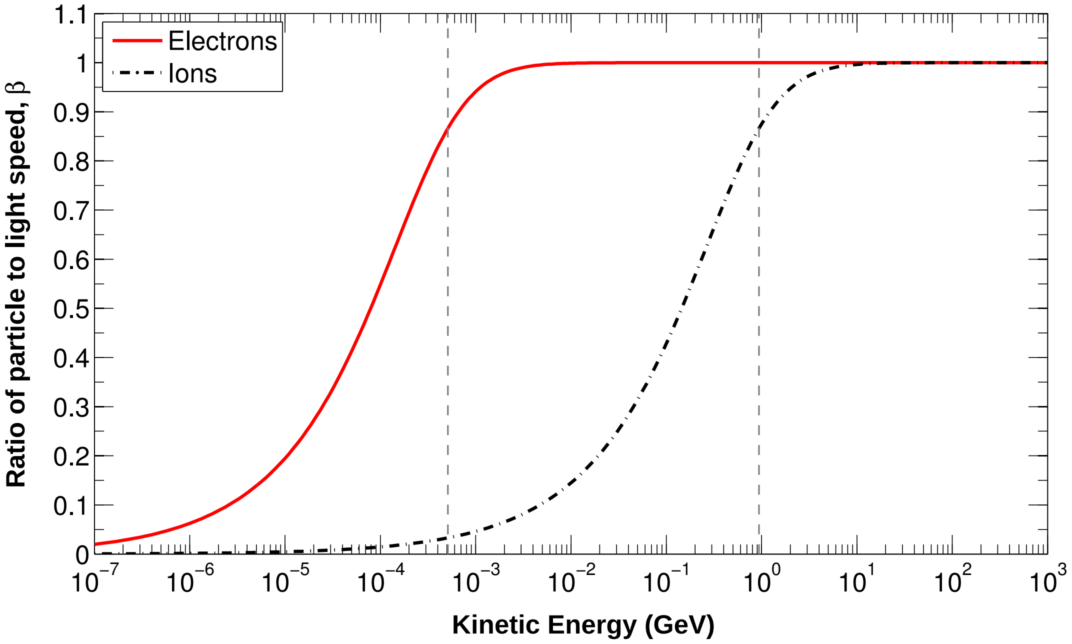

Figure 3.2: The ratio of particle speed to light speed for CR ions and electrons. The electron and proton rest-mass energies are shown as vertical dashed lines at $e_0 = 0.511$ MeV and $E_0 = 938.3$ MeV, at which each profile respectively attains a speed of $\sim 0.87c$. Note that light speed is never fully attained and that β progresses asymptotically to unity above the relevant rest-mass energy.

is applied. Furthermore, the ratio of mass number to charge can used to distinguish between different CR species:

$$\Theta = \frac{A}{Ze}, \tag{3.5}$$

which is 2 for most GCRs (e.g. Helium, Carbon, Oxygen, ...), being fully ionised, except for galactic protons, for which $\Theta = 1$. This quantity is also taken as 1 for electrons. Of course, for singly-charged ACRs it follows that $\Theta = A$. The relation in Eq. 3.4 is demonstrated in Figure 3.1 for different CR species. Note that for each presented species, E is proportional to P^2 and P respectively below and above their rest-mass energies. This may also be inferred from Eq. 3.3 or 3.4 in the limits of $E \ll E_0$ and $E \gg E_0$. Figure 3.4 shows that this proportionality changes at the same kinetic energy ($E \approx E_0$) for protons and ACR Oxygen, since the energy is measured per nucleon, although the rigidities at which this occurs are separated by a factor given by the ratio of their Θ-values. At $E > E_0$, both protons and electrons are relativistic and display identical relationships between E and P, because $\Theta = 1$ for both. Generally, any range of relativistic energies has a corresponding rigidity range encompassing the same values. The difference in the relation between E and P for relativistic and non-relativistic CRs is further reflected in their shock-accelerated energy spectra; see Section 3.6.2.

Another important quantity that can be specified in terms of those introduced above is the ratio of particle speed, v, to light speed, that is,

$$\beta\,(\equiv v/c) = \frac{P}{\sqrt{P^2 + \left(\frac{A}{Ze}\right)^2 E_0^2}} = \frac{\sqrt{E\,(E + 2E_0)}}{E + E_0}\,. \tag{3.6}$$

This quantity is illustrated for CR ions and electrons in Figure 3.2 as a function of E. Ions

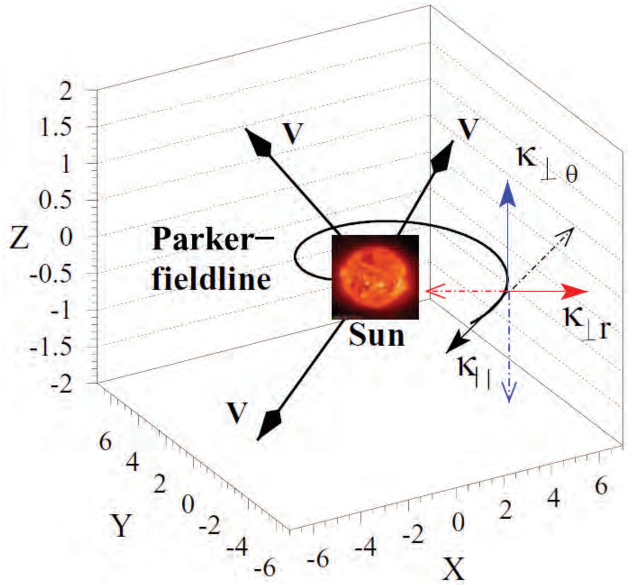

Figure 3.3: A schematic representation of the HMF-aligned diffusion configuration. The directions in which the coefficients $\kappa_{||}$, $\kappa_{\perp r}$ and $\kappa_{\perp\theta}$ govern CR diffusion are indicated with respect to a Parker field line, using black, red and blue arrows respectively. The radial SW outflow is indicated with the bold black arrows labelled **V**. Figure adapted from *Heber and Potgieter* [2006].

and electrons attain speeds near the speed of light above the proton and electron rest-mass energies respectively. Note that different species of CR ions do not show different β-profiles, because Eq. 3.6 in terms of E does not contain an explicit dependence on Θ. The parameter β is an important quantity in CR modulation, since it is contained in the expressions for both the diffusion coefficients and GCR input spectra. Note finally that while the TPE is solved for the distribution function, $f = f(\vec{r}, p, t)$, CR intensities are presented in this study in terms of differential intensity, $j = j(\vec{r}, p, t)$, which is related to f according to

$$j(\vec{r}, p, t) = p^2 f(\vec{r}, p, t), \tag{3.7}$$

with units of particles / unit area / unit time/ unit solid angle / unit kinetic energy (per nucleon, in the case of CR ions). See e.g. *Strauss* [2010] for a full derivation of this quantity.

3.3 Particle Diffusion

The diffusion tensor contained within Eq. 3.1 assumes the form of a symmetrical matrix in HMF-aligned coordinates, that is

$$\mathbf{K}_s = \begin{bmatrix} \kappa_{||} & 0 & 0 \\ 0 & \kappa_{\perp\theta} & 0 \\ 0 & 0 & \kappa_{\perp r} \end{bmatrix} \tag{3.8}$$

where $\kappa_{||}$, $\kappa_{\perp\theta}$, and $\kappa_{\perp r}$ respectively denote diffusion coefficients parallel to the mean HMF, and perpendicular to it in the polar and radial directions. Figure 3.3 aids in the visualisation of these directions. By their relation to the mean free path (MFP), λ, through

$$\kappa = \frac{v}{3}\lambda, \tag{3.9}$$

where v is the particle speed (often written as $c\beta$), each coefficient provides an indication of how far on average a particle can travel along a particular direction before an interaction allows its direction to change significantly. For charged particles such as CRs, these interactions include e.g. encounters with fluctuations of the magnetic field. Indeed, CR diffusion in the heliosphere is generally described in terms of MFPs (in units of length) that are characterised by aspects of magnetic turbulence, of which the essentials are given in the following discussion.

3.3.1 Turbulence

In accordance to the form used in basic perturbation theory, the turbulent Parkerian HMF is written in terms of a uniform background B and fluctuating component $\delta\vec{B}$ as

$$\vec{B} = B\hat{e}_z + \delta\vec{B}(x, y, z), \tag{3.10}$$

with $\langle\delta\vec{B}\rangle = 0$ by an appropriate averaging process [see e.g. *Matthaeus et al.*, 2003]. The perturbation is further characterised by expressing the total turbulence as the sum of the 1-D (slab) and 2-D components thereof [*Bieber et al.*, 1994, 2004; *Matthaeus et al.*, 1995, 2003], so that

$$\delta\vec{B}(x, y, z) = \delta\vec{B}_{slab}(z) + \delta\vec{B}_{2D}(x, y), \tag{3.11}$$

with components $\delta B_{slab,i}(z) + \delta B_{2D,i}(x, y), i = x, y$. This is the form of composite turbulence. Here, the root mean square amplitude and variance of fluctuating components are denoted by δB and δB^2 respectively. The associated total variance of fluctuating field components perpendicular to the background field is given by [e.g. *Engelbrecht*, 2013] as

$$\delta B^2 = \delta B^2_{slab}(z) + \delta B^2_{2D}(x, y). \tag{3.12}$$

Under the further assumption of axisymmetrical turbulence, where

$$\delta B^2_{slab} = 2\delta B^2_{slab,x} = 2\delta B^2_{slab,y} \text{ and } \delta B^2_{2D} = 2\delta B^2_{2D,x} = 2\delta B^2_{2D,y},$$

it follows that

$$\delta B^2 = 2\delta B^2_{slab,x}(z) + 2\delta B^2_{2D,x}(x, y). \tag{3.13}$$

Following *Burger et al.* [2008], an expression for $\delta B^2_{slab,x}$ is modelled as

$$\delta B^2_{slab,x} = \delta B^2_0 \left(\frac{r}{r_0}\right)^{-2.5} \text{ for } r < r_{TS}, \tag{3.14}$$

with δB^2_0 the normalisation constant at Earth ($r_0 = 1$ AU). *Bieber et al.* [1994] presents a value of 13.2 nT^2 for the total variance in one perpendicular component of the HMF. In Chapter 4, $\delta B^2_0 =$ 13.2 nT^2 is employed for the sake of comparability of results with that of *Strauss* [2010], while

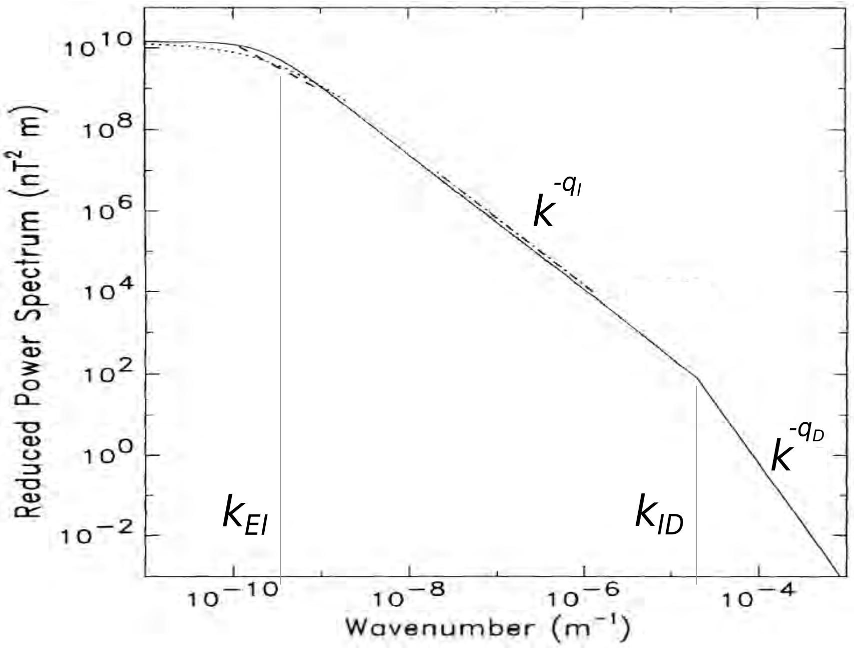

Figure 3.4: An example of a turbulence power spectrum. Three distinct sections are visible from the lowest to the highest wavenumbers, namely the energy range, the inertial range, and the dissipation range, with the transitions between the former and latter two respectively occurring at wavenumbers denoted k_{EI} and k_{ID}. The inertial and dissipation range spectral indices are $-q_I$ and $-q_D$. The fainter dotted, dashed and dash-dotted lines represent observations as discussed by *Bieber et al.* [1994], from where this figure is adapted, and the references therein.

$\delta B_0^2 = 25.0\,\mathrm{nT}^2$ is applied in further chapters [as in *Burger et al.*, 2008]. Observations by *Burlaga et al.* [2014] suggest the fluctuations in the heliosheath may be dominated by compressional (longitudinal) turbulence, requiring a complete revision of turbulence transport and scattering in this region. It is assumed in the meanwhile that $\delta B^2_{slab,x} \sim B^2$ in the heliosheath [see e.g. *le Roux et al.*, 1999, for a similar assumption at Earth]. Assuming 80% 2-D and 20% slab turbulence [*Bieber et al.*, 1994; *Burger et al.*, 2008], it is employed in this study, following *Strauss* [2010], that

$$\delta B^2_{2D,x} = \frac{80}{20}\delta B^2_{slab,x} \,. \tag{3.15}$$

Another aspect important for defining diffusion quantities is the turbulence power spectrum. An example of such a spectrum is shown in Figure 3.4 as a function of wavenumber, k. If turbulence is thought of as a number of eddies of different sizes [see e.g. the treatment of *Choudhuri*, 1998], energy would typically be fed into the turbulent system so as to produce large eddies. This is in the energy range, which extends up to a wavenumber denoted k_{EI}. Above k_{EI}, this energy is cascaded unto a greater number of smaller eddies toward higher wavenumbers, with some energy being dissipated upon each consecutive transferral. Classically, this region, named the inertial range, displays a Kolmogorov-type decay proportional to $k^{-5/3}$. Eventually, when the eddies (or length scales of fluctuations) become too small, energy is rapidly lost to the environment, resulting in the steeper decay seen above k_{ID}, where the inertial range transitions into the dissipation range. For this study, the inertial and dissipation ranges are characterised as k^{-q_I} and k^{-q_D} respectively, with $q_I = 5/3$ and $q_D = 2.6$ [*Smith et al.*, 2006]. See also the comprehensive review by *Shalchi* [2009].

Eq.	**Fit**	a	b
3.17	best fit	0.200	1.760
	through origin	0	3.190
3.18	best fit	0.152	0.451
	through origin	0	0.686

Table 3.1: Linear regression parameters from fits applied by *Leamon et al.* [2000] to observed break-point frequencies (ν_{bp}) as functions of Ω_{ci} and $k_{ii}V_{sw}/2\pi$ for Eq. 3.17 and 3.18 respectively.

The wavenumber of the energy-inertial transition is modelled, following *Burger et al.* [2008], as

$$k_{EI}(r) = \quad k_0 \left[r/r_0\right]^{-0.5} \quad r \leq r_{TS} \tag{3.16}$$

with k_0 = 32.0 AU^{-1} the reciprocal of a correlation length at r_0 of $\sim$ 0.03 AU. It is assumed for comparability with *Strauss* [2010] that k_{EI} stays constant at the value attained at the TS throughout the heliosheath. To characterise k_{ID} for the inertial-dissipation range transition, two expressions are considered here. These are [from *Leamon et al.*, 2000]

$$k_{ID} = \frac{2\pi}{V_{sw}} \left(a + b\Omega_{ci}\right), \tag{3.17}$$

referred to as the proton gyrofrequency model, and

$$k_{ID} = \frac{2\pi}{V_{sw}} \left(a + \frac{b}{2\pi} k_{ii} V_{sw}\right), \tag{3.18}$$

the ion inertial scale model [see also *Engelbrecht and Burger*, 2010, 2013a]. The proton gyrofrequency and ion inertial scale are respectively defined as $\Omega_{ci} = |q|\, B/m$ and $\rho_{ii} = V_A/\Omega_{ci}$, with q and m representing the particle charge and mass and V_A the Alfvén speed. Also, $k_{ii} = (2\pi/p_{ii}) \sin\psi$ with ψ the HMF spiral angle. As usual, V_{sw} denotes the SW speed. Possible choices for the parameters a and b in Eq. 3.17 and 3.18 are given in Table 3.1, where ν_{bp} and k_{ID} are related through $k_{ID} = (2\pi/V_{sw})\nu_{bp}$. Note that $k_{EI} < k_{ID}$ in all circumstances.

3.3.2 Parallel diffusion

CRs undergo diffusive transport in the heliosphere through pitch-angle scattering as a result of HMF fluctuations. The interaction between transported particles and turbulence is related through the Fokker-Planck coefficient, $D_{\mu\mu}$, which essentially specifies the rate of scattering and depends on the turbulence model considered [see *Schlickeiser*, 2002]. The pitch-angle-averaged diffusion of particles parallel to magnetic field lines is in turn related to $D_{\mu\mu}$ through

$$\kappa_{||} = \frac{v^2}{8} \int_{-1}^{1} \frac{\left(1-\mu^2\right)^2}{D_{\mu\mu}(\mu)} d\mu\,, \tag{3.19}$$

where $\mu \in \{-1, 1\}$ is the cosine of the particle's pitch angle. Considered here is the parallel diffusion coefficient of *Burger et al.* [2008], adapted from the random sweeping model for dynamic

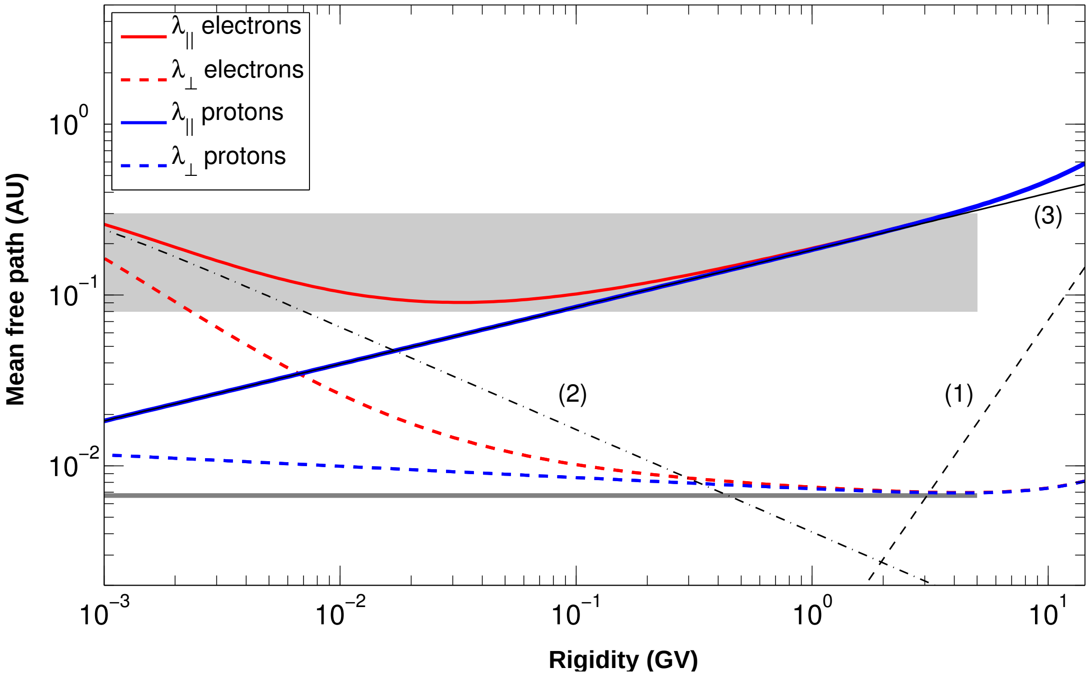

Figure 3.5: Rigidity profiles at Earth ($r = 1$ AU, $\theta = 90°$) for the MFPs of protons and electrons, respectively shown in blue and red lines. The parallel MFPs ($\lambda_{||}$), indicated with solid lines, follow from Eq. 3.20 with Eq. 3.21 and Eq. 3.22 for protons and electrons respectively. The *Palmer* [1982] consensus values for $\lambda_{||}$ are indicated by the shaded region. The contributions of the terms labelled (1) to (3) in Eq. 3.22 are illustrated by the dashed, dashed-dotted, and solid black lines as indicated. The perpendicular MFPs ($\lambda_\perp \equiv \lambda_{\perp r/\theta}$) are shown for $\theta = 90°$ using dashed lines and follow from Eq. 3.26/3.27 with $\xi = \eta = -0.4$. The corresponding *Palmer* [1982] values are shown as a grey line at ~ 0.007 AU.

turbulence of *Teufel and Schlickeiser* [2003], constructed using quasilinear theory (QLT; *Jokipii* [1966]). The corresponding MFP is given by

$$\lambda_{||} = \frac{3q_I}{\sqrt{\pi}(q_I - 1)} \frac{R^2}{bk_{EI}} \left(\frac{B}{\delta B_{slab,x}} \right)^2 K\,, \tag{3.20}$$

where

$$K = \frac{b}{4\sqrt{\pi}} + \frac{2}{\sqrt{\pi}(2-q_I)(4-q_I)} \frac{b}{R^{q_I}}\,, \tag{3.21}$$

for protons, and

$$K = \underbrace{\frac{b}{4\sqrt{\pi}}}_{(1)} + \underbrace{\left(\frac{1}{\Gamma(q_D/2)} + \frac{1}{\sqrt{\pi}(q_D - 2)} \right) \frac{b^{q_D-1}}{Q^{q_D-q_I} R^{q_I}}}_{(2)} + \underbrace{\frac{2}{\sqrt{\pi}(2-q_I)(4-q_I)} \frac{b}{R^{q_I}}}_{(3)}\,, \tag{3.22}$$

for electrons, with dimensionless parameters

$$R = k_{EI}\, r_L \qquad \text{and} \qquad Q = k_{ID}\, r_L \qquad \text{and} \qquad b = \frac{v}{2\alpha_d V_A}\,.$$

The quantities not previously defined are the Larmor radius, $r_L = P/Bc$, and $\alpha_d = 1$, which specifies the strength of dynamical effects [*Bieber et al.*, 1994; *Teufel and Schlickeiser*, 2002]. The

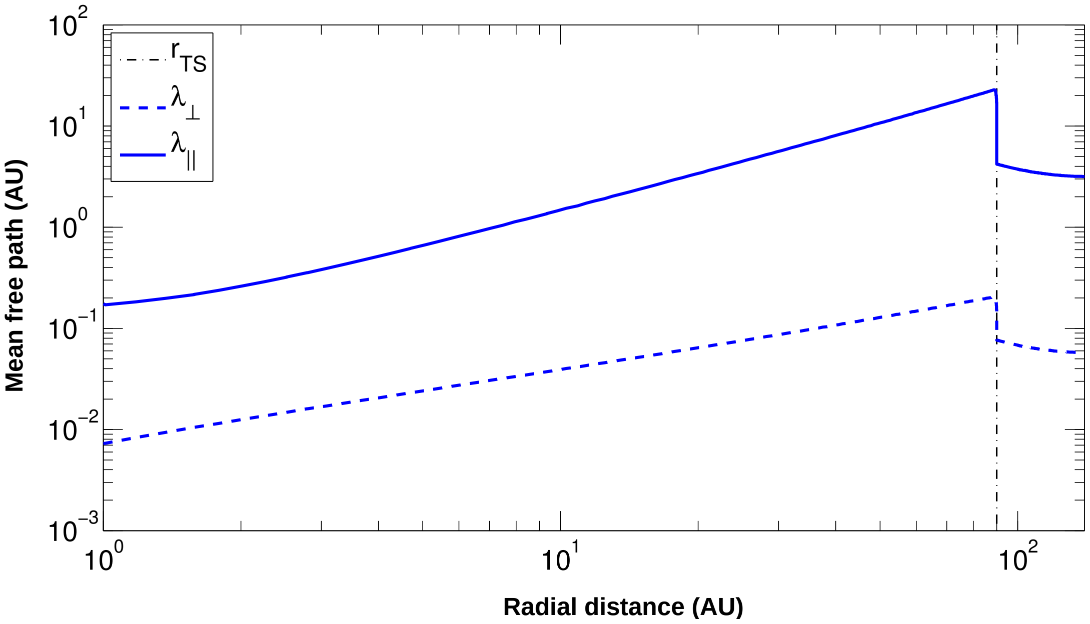

Figure 3.6: MFPs as a function of radial distance in the equatorial plane ($\theta = 90°$) at $P = 1.0$ GV. The parallel ($\lambda_{||}$) and perpendicular ($\lambda_\perp \equiv \lambda_{\perp r/\theta}$) MFPs follow from Eq. 3.20 and 3.26/3.27 with $\xi = \eta = -0.4$. Note from Figure 3.5 that the proton and electron MFPs are equal at 1 GV, and hence these radial profiles are representative of both species. The TS position is indicated using a vertical dash-dotted line at 90 AU, while the HP is at 140 AU; this is only valid for Chapter 4.

Alfvén speed is furthermore expressed as

$$V_A = \frac{B}{\sqrt{\mu_0 \rho_m}}\,, \qquad \rho_m = m_p\, \rho_0 \left(\frac{r_0}{r}\right)^2 \frac{V}{V_{sw}}\,,$$

where ρ_m is the SW mass density [as specified by *Strauss*, 2010], with μ_0 the permeability of free space, m_p the proton mass, ρ_0 the SW proton number density at Earth ($r_0 = 1$ AU, $\theta = 90°$), taken as 5 particles per cm^3, and $V = 400$ km.s^{-1} as before. According to this configuration, V_A remains largely constant at about 35 km.s^{-1} up to the TS, across which it increases with a factor of $s^{1/2}$ and continues to increase proportional to B in the heliosheath; recall that due to the incompressibility assumption discussed in Section 2.3 the SW speed decreases as r^{-2} in the heliosheath, implying that ρ_m remains constant in this region, as expected.

The MFPs described by Eq. 3.20 for both protons (Eq. 3.21) and electrons (Eq. 3.22) are illustrated in Figure 3.5 as functions of rigidity. The contributions of the terms (1) to (3) of Eq. 3.22 are indicated in the figure using black lines. Note that while the proton MFP at the considered rigidities is characterised mostly by the inertial-range contribution (term (3); represented by the solid black line with which it coincides), electrons are also sensitive to dissipation-range turbulence, represented by term (2) of Eq. 3.22. Note that the dissipation-range contribution is negligible for ions and is hence not considered in Eq. 3.21. See *Engelbrecht* [2008]. The result is that the electron MFPs exhibit an up-turn at low rigidities. Toward higher rigidities the proton and electron profiles coincide and the energy-range contribution of term (1) becomes more pronounced. For comparison, the *Palmer* [1982] consensus values are also shown in Figure 3.5. Where the radial profile of the MFPs is concerned, $\lambda_{||}$ increases as $\sim r$ up to the TS, decreases abruptly at the shock, and continues to diminish approximately according to r^{-1} into the heliosheath. This is illustrated in Figure 3.6. The above diffusion configuration along with that following from the damping model for dynamic turbulence [*Teufel and Schlickeiser*, 2003] are revisited by *Engelbrecht and Burger* [2013a, b]. Note that the above diffusion configuration for protons (with Eq. 3.21) is applied in Chapter 4.

In Chapter 5 to 7, where the modulation and shock acceleration of electrons are studied, a different set of expressions are adopted to describe diffusion. While the form of observations presented in Figure 2.18 could be reproduced using Eq. 3.20, this would require substantial adjustment of the considerable amount of parameters contained therein. Such adjustments would furthermore have to be consistent with observational and theoretical constraints on the individual parameters. Hence, to avoid an extended parameter study, a simpler phenomenological MFP expression is assumed [following the similar approaches of *Potgieter and Moraal*, 1988; *Caballero-Lopez et al.*, 2010; *Potgieter and Nndanganeni*, 2013a; *Potgieter et al.*, 2015]:

$$\lambda_{||} = \lambda_r\left(r\right)\lambda_P\left(P\right), \tag{3.23}$$

where an initial rigidity dependence is specified as

$$\lambda_P\left(P\right) = \left[\frac{\left(\frac{P}{P_0}\right)^3 + \left(\frac{P_k}{P_0}\right)^3}{1 + \left(\frac{P_k}{P_0}\right)^3}\right]^{\frac{g_2 - g_1}{3}} \left(\frac{P}{P_0}\right)^{g_1}, \tag{3.24}$$

with $g_1 = 0$, $g_2 = 1.23$, $P_0 = 1$ GV, and $P_k = 0.34$ GV, and where the radial dependence is

$$\lambda_r\left(r\right) = \begin{cases} \lambda_{r,0}\left(\dfrac{B}{\delta B_{slab,x}}\right)^2\left(\dfrac{r}{r_0}\right)^{\Lambda_{IH}} & r \leq r_{TS} \\ \lambda_{r,TS^+}\left(\dfrac{B}{\delta B_{slab,x}}\right)^2\left(\dfrac{r}{r_0}\right)^{\Lambda_{OH}} & r > r_{TS} \end{cases} \tag{3.25}$$

with $\lambda_{r,0} = 0.4$ AU, $\lambda_{r,TS^+} = 0.341$ AU, $\Lambda_{IH} = 0.65$, and $\Lambda_{OH} = 2.0$, as an initial configuration. As a result of earlier assumptions $B/\delta B_{slab,x}$ is constant in the heliosheath. These dependences are illustrated in Figure 3.7. Note that the rigidity dependence reflects two combined power laws, with MFPs that are rigidity-independent up to $\sim$ 0.34 GV and increase according to $P^{1.23}$ at larger rigidities. Comparing Figures 3.7 and 3.5, these two power-law segments roughly reflect the contributions of the inertial and energy ranges of the turbulence spectrum. The modelling of dissipation-range effects is discussed in Section 5.4.3. Similar rigidity dependences are applied by *Potgieter and Nndanganeni* [2013a] and *Potgieter et al.* [2015] in modulation models to reproduce electron observations. The radial dependence of Eq. 3.25 is furthermore similar to that of Eq. 3.20, with $\lambda_{||}$ also increasing as r at $r < r_{TS}$, but with generally larger values. Across the TS, however, the MFPs are required to decrease by a much larger amount than they do according to Eq. 3.20 to account for electron observations. Also, $\lambda_{||}$ is assumed to increase as r^2 in the heliosheath. This is shown in Chapter 7 to reproduce the observed radial distribution of electron intensities in conjunction with an emulated solar cycle dependence in the heliosheath. *Potgieter and Nndanganeni* [2013a] applied a similar profile to reproduce heliosheath observations. A fundamental diffusion theory for the whole heliosphere is yet to be developed.

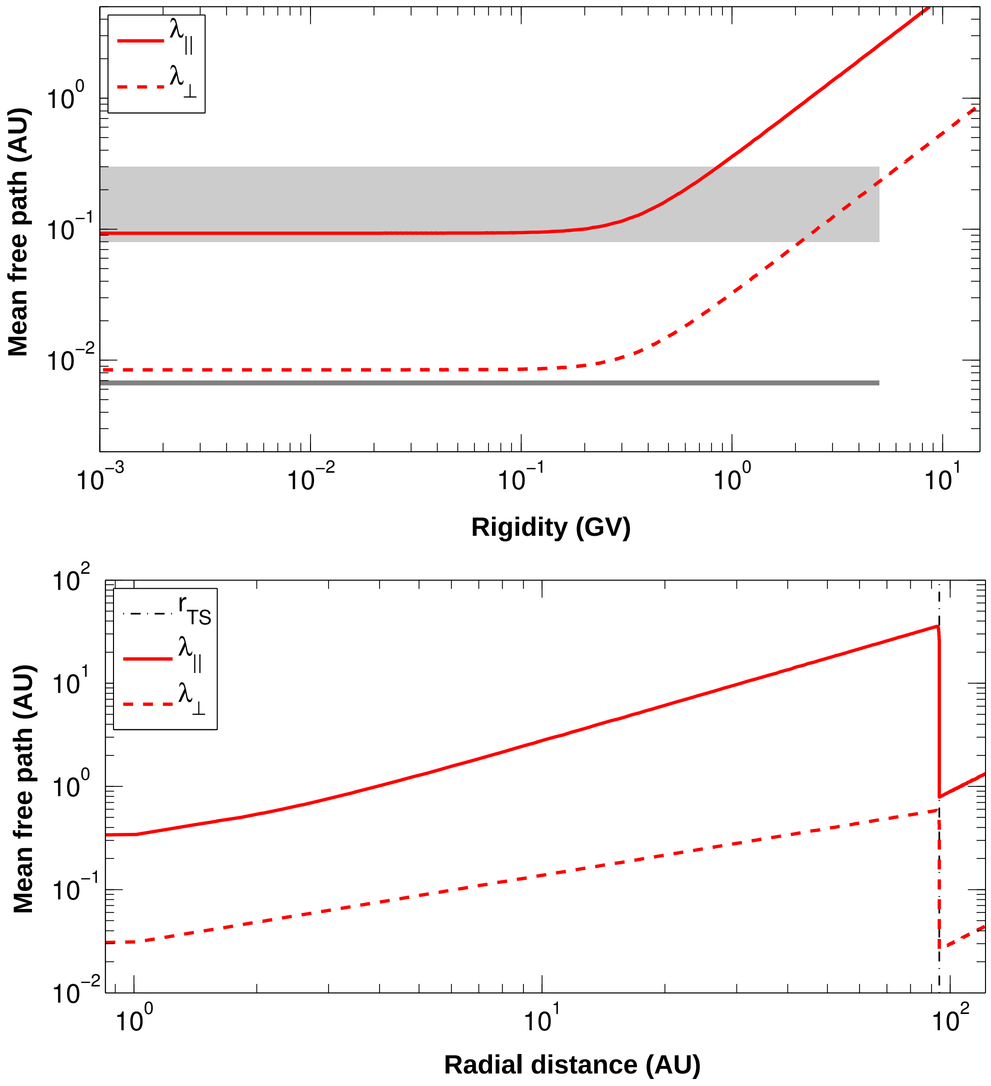

Figure 3.7: The top panel shows the rigidity dependence of electron MFPs at Earth ($r = 1$ AU, $\theta = 90°$). The parallel ($\lambda_{||}$) and perpendicular MFPs ($\lambda_\perp \equiv \lambda_{\perp r/\theta}$) follow from Eq. 3.23 and 3.26/3.27 with $\xi = \eta = 0$. The *Palmer* [1982] values are shown for $\lambda_\perp$ and $\lambda_{||}$ as a grey line and shaded area respectively. The bottom panel shows the corresponding radial profiles of electron MFPs for $\theta = 90°$ at $P = 1.0$ GV. The TS position is indicated using a vertical line at 94 AU. The HP is at 122 AU.

The use of Eq. 3.23 is favourable for the purposes of this study, because any one segment of the rigidity dependence can be readily adjusted without altering another, and without affecting the radial dependence - this is useful when studying the effects of individual features of the diffusion profile. These adjustments can also be implemented explicitly as required by the objective at hand without making possibly erroneous assumptions concerning underlying physical properties. These advantages are exploited further in Chapter 5.

3.3.3 Perpendicular diffusion

Perpendicular diffusion is described by QLT in terms of the random walk of magnetic field lines [*Jokipii*, 1966], however it may also follow due to the scattering of particles in gyro-phase, where particles may transfer from one field line to the next. Collectively, these concepts form part of the non-linear guiding centre (NLGC) theory for diffusion [*Bieber et al.*, 2004; *Shalchi*, 2006]. See also the perpendicular diffusion models constructed from NLGC theory by *Burger et al.* [2008] and *Engelbrecht and Burger* [2013a, b]. *Dosch et al.* [2009] provide an overview of the various cross-field diffusion theories. The perpendicular diffusion coefficients most compatible with the numerical modelling in this study are however those of *Burger et al.* [2000] for enhanced latitudinal transport. Informed by Ulysses observations of HMF variances at high helio-latitudes, these are

$$\kappa_{\perp r} = \kappa_{\perp r,0} \left(\frac{\delta B_{2D,x}}{B} \right)^2 \kappa_{||} \left(\frac{P}{P_0} \right)^{\xi}, \tag{3.26}$$

and

$$\kappa_{\perp \theta} = g(\theta) \left(\frac{\delta B_{2D,x}}{B} \right)^2 \kappa_{||} \left(\frac{P}{P_0} \right)^{\eta}, \tag{3.27}$$

where

$$g(\theta) = \frac{\kappa_p^0 + \kappa_e^0}{2} - \left(\frac{\kappa_p^0 - \kappa_e^0}{2} \right) \tanh\left[8\left(\theta - 90^\circ + \theta_c\right)\right], \tag{3.28}$$

with $P_0 = 1$ GV and $\delta B^2_{2D,x} = 4\ \delta B^2_{slab,x}$, as previously defined, and where $\theta \leq 90^\circ$ and $\theta_c = 35^\circ$ determines the polar extent of the enhancement of $\kappa_{\perp\theta}$. It has become the convention in modulation studies to scale $\kappa_{\perp r/\theta}$ as $\kappa_{||}$, with $\kappa_{\perp r}/\kappa_{||} \in [0.02, 0.04]$ [*Giacalone and Jokipii*, 1999]. Hence, $\kappa_{\perp r,0} = 0.02$ in this study, unless stated otherwise. Furthermore, $\kappa_p^0 = 0.185$ and $\kappa_e^0 = \kappa_{\perp r,0}$, so that perpendicular diffusion is isotropic with $\kappa_\perp = \kappa_{\perp r} = \kappa_{\perp\theta}$ in the equatorial plane ($\theta = 90^\circ$). Note that the constants κ_p^0 and $\kappa_{\perp r,0}$ are scaled according to solar activity through the tilt angle [*Langner*, 2004], e.g. $\kappa_p^0(\alpha) = \kappa_p^0(\alpha/2 + 0.9127)$. Away from the equatorial plane, where the enhancement described in Eq. 3.28 takes effect, anisotropic diffusion ensues. See *Burger et al.* [2000], *Potgieter* [2000] and *Heber and Potgieter* [2006] for the physical substantiation for this enhancement, and *Potgieter* [1996] and *Ferreira et al.* [2000] on the effects of anisotropic perpendicular diffusion. Note finally that Eqs. 3.26 and 3.27 are applied in Chapter 4 with $\xi = \eta = -0.4$, yielding the rigidity dependence for $\kappa_\perp$ illustrated in Figure 3.5. In further chapters however, where electron transport is considered, it is assumed for simplicity that the rigidity dependence of Eq. 3.24 is preserved for the perpendicular coefficients as well, hence $\xi = \eta = 0$. The resultant profiles are shown in Figure 3.7.

3.4 Particle Drifts

Being charged particles, CRs are expected to undergo drifts in response to the large-scale HMF structure as illustrated in Figure 3.8. Specifically, drift motions associated with gradients in the HMF magnitude, the curvature of the field, and with changes in the field direction across the HCS [e.g. *Burger and Potgieter*, 1989], are induced. It is known that drift effects are reduced in the presence of turbulence, although the appropriate characterisation of this turbulence and of the ensuant drift effects is an ongoing endeavour [*Burger and Visser*, 2010; *Engelbrecht and Burger*, 2015]. The significance of drifts in CR modulation was first remarked by *Jokipii et al.* [1977], and indeed, they were later revealed to be necessary to explain dependences of CR observations on the HMF polarity [e.g. *Potgieter and Moraal*, 1985]. See also the review by *Potgieter* [2014b]. In this section, a general discussion on the drift concepts used in this study is provided. Note

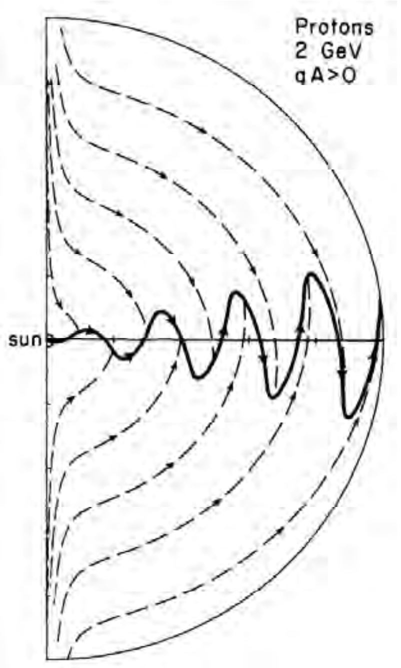

Figure 3.8: Meridional projection of the drift trajectories of positively charged CRs in the inner heliosphere during the A > 0 polarity cycle, with arrows indicating drift directions. The bold line near the equator represents the wavy HCS. See *Strauss* [2013] for a discussion on possible drift patterns in the outer heliosphere. Figure obtained from *Jokipii and Thomas* [1981].

that HCS drifts are emulated in this study using the wavy current sheet model by *Hattingh and Burger* [1995], while its modification and implementation in a 2-D modulation model is discussed thoroughly by *Langner* [2004].

Drifts are represented in the TPE by the pitch-angle-averaged guiding centre drift velocity, which in a very general case is given by

$$\langle \vec{v}_D \rangle = \frac{pv}{3Q}\frac{(\omega\tau_d)^2}{1+(\omega\tau_d)^2}\nabla\times\frac{\vec{B}}{B^2}, \tag{3.29}$$

where the suppression of drifts through scattering is represented by $(\omega\tau_d)^2/(1+(\omega\tau_d)^2)$ [see also *Minnie et al.*, 2007]. Here, ω is the particle's gyro-frequency and τ_d a time scale between scattering events. Eq. 3.29 is written in terms of the maximal Larmor radius ($r_L = P/Bc$) as

$$\begin{aligned} \langle \vec{v}_D \rangle &= \nabla\times\frac{v}{3}r_L\frac{(\omega\tau_d)^2}{1+(\omega\tau_d)^2}\hat{e}_B \\ &\equiv \nabla\times\kappa_D\,\hat{e}_B, \end{aligned} \tag{3.30}$$

with $\hat{e}_B = \vec{B}/B$ a unit vector directed along $\vec{B}$, and where the drift coefficient, κ_D, is preliminarily defined as

$$\kappa_D = \frac{v}{3}r_L\frac{(\omega\tau_d)^2}{1+(\omega\tau_d)^2}. \tag{3.31}$$

The drift coefficient, and hence also the drift velocity, assume maximum values under the assumption of weak scattering, that is, assuming a particle undergoes several gyrations before being scattered. This implies that $\omega\tau_d \gg 1$. On the other hand, the drift coefficient diminishes

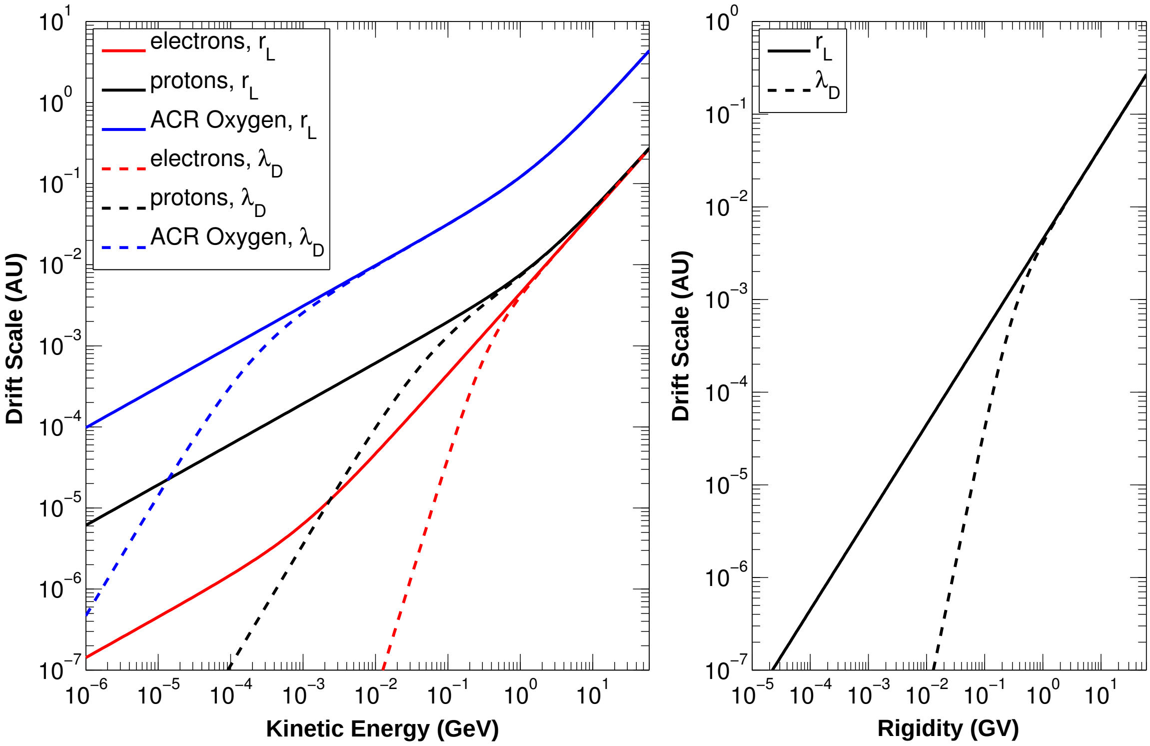

Figure 3.9: CR drift scales (λ_D) as functions of kinetic energy (left panel) and rigidity (right panel) at Earth (1 AU, $\theta = 90°$). Solid lines represent the weak-scattering limit, where drift scales are equal to the Larmor radius, r_L, while dashed lines represent the drift scales following from Eq. 3.33. In the left panel, lines in red, black and blue respectively represent λ_D for electrons, protons and ACR Oxygen.

when $\omega\tau_d \ll 1$. Thus, in these limits it follows that

$$\kappa_D \approxeq \begin{cases} \dfrac{v}{3}r_L & \omega\tau_d \gg 1 \quad \text{weak scattering} \\ 0 & \omega\tau_d \ll 1 \quad \text{strong scattering} \end{cases} \tag{3.32}$$

An intermediate value is likely the more realistic though, and is attained through incorporating a realistic suppression factor to represent the effects of turbulence. Following *Burger et al.* [2000, 2008], it is approximated that $(\omega\tau_d) \sim P$, so that

$$\kappa_D = \kappa_{D,0}\frac{v}{3}r_L\frac{(P/P_D)^2}{1+(P/P_D)^2}, \tag{3.33}$$

with $P_D = 1/\sqrt{10}$ [see also *Langner et al.*, 2003; *Ngobeni and Potgieter*, 2015], and where $\kappa_{D,0} \in [0,1]$ is introduced as a scaling parameter to indicate the drift efficiency. During solar maximum conditions, for instance, when more turbulent conditions are expected, *Ferreira and Potgieter* [2004] employed $\kappa_{D,0} \in [0, 0.1]$ to reproduce observations. This quantity is scaled as needed in the current study, although $\kappa_{D,0} = 0.55$ may be considered a default value [*Langner et al.*, 2003; *Ngobeni*, 2015]. To aid in visualisation, κ_D is represented more intuitively as a length scale, λ_D, similar to how MFPs represent diffusion coefficients (Eq. 3.9). Note that by using this representation, it follows from Eq. 3.32 that $\lambda_D = r_L$ under the weak scattering limit.

The rigidity profile of λ_D is illustrated in the right-hand side panel of Figure 3.9 for full drift efficiency ($\kappa_{D,0} = 1$). The scattering-induced suppression of drifts significantly reduce λ_D at low

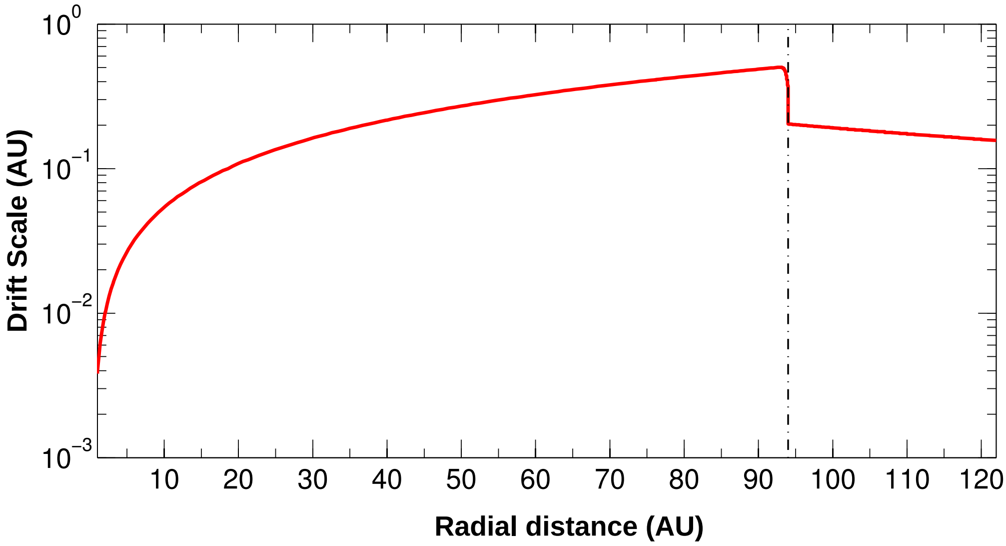

Figure 3.10: Electron drift scale (λ_D) as function of radial distance at $P = 1$ GV, where the weak-scattering limit has already been attained. Note that $\lambda_D \propto 1/B$. The TS position is indicated with a dash-dotted line at 94 AU.

rigidities and become altogether negligible at $P \ll P_D$. The weak scattering limit is attained at $P > P_D$, where the drift scales predicted by Eq. 3.33 converge with the Larmor radius, r_L, and continue increasing proportional to P. In further chapters, drift effects on CR intensities are presented in terms of kinetic energy, in terms of which the drift scales vary appreciably depending on the CR species considered. This is shown in the left panel of Figure 3.9. The drift scales of the heavier species remain significant down to lower energies, whereas those of electrons become negligible quickly below $\sim$ 100 MeV. Indeed, drift effects for electrons are shown in Chapter 5 to be most pronounced in the approximate energy interval of 100 MeV to 1 GeV. See also the comprehensive study on electron modulation by *Nndanganeni* [2015]. Note also that if the rigidity parameters in Eq. 3.33 are expressed in terms of energy according to Eq. 3.3, the dependence of λ_D on E also changes relative to the relevant rest-mass energy; this is reflected in Figure 3.9, where the λ_D-curves of electrons and the heavier species steepen at ~ 0.5 MeV and 1 GeV respectively. The radial dependence of λ_D, as a result of its dependence on r_L, follows as $1/B$, which is evident when comparing Figures 3.10 and 2.7.

With κ_D specified, $\langle \vec{v}_D \rangle$ is also known. The drift directions of CRs can consequently be solved from $d\vec{l} \times \langle \vec{v}_D \rangle = 0$, which would yield streamlines similar to those shown in Figure 3.8. The figure demonstrates that while A > 0 positively charged particles drift downward from the poles to the equator and outward along the HCS. Since the divergence of a curl of a vector is zero, these streamlines are expected to be directed back to the poles at some point in the outer heliosphere, e.g. along the TS. Note that these patterns are shown for qA > 0, which is the notation used in modulation models when solving the TPE. For positively charged particles, $q\text{A} > 0 \implies \text{A} > 0$, since $q > 0$, whereas for negatively charged particles $q\text{A} > 0 \implies \text{A} < 0$, because $q < 0$. The drift directions for electrons are hence reversed from those shown in Figure 3.8. Of course, when the magnetic polarity reverses, and magnetic field lines are directed in the opposite direction, these drift directions are also reversed.

Drifts can be moderated both directly and indirectly in the TPE and the modulation model that solves it. Firstly, the drift coefficient can be scaled explicitly as done in Eq. 3.33 through e.g. $\kappa_{D,0}$ or the rigidity-dependent suppression factor. Implicitly though, any process that acts to decrease intensity gradients and hence the gradient of the CR distribution function, ∇f, in Eq. 3.1, causes the product $\langle \vec{v}_D \rangle \cdot \nabla f$ to be reduced and thereby inhibits drift effects. Note finally that the drift velocity as described by Eq. 3.30 can be rewritten in terms of the asymmetrical drift tensor, $\mathbf{K}_D$. This follows because the curl of a vector may be rewritten as the divergence of a second rank tensor, leading to

$$\langle \vec{v}_D \rangle = \nabla \times \kappa_D \, \hat{e}_B = -\nabla \cdot \mathbf{K}_D, \tag{3.34}$$

with

$$\mathbf{K}_D \equiv \begin{bmatrix} 0 & 0 & 0 \\ 0 & 0 & \kappa_D \\ 0 & -\kappa_D & 0 \end{bmatrix}. \tag{3.35}$$

This identity allows the TPE to be rewritten in a more compact form and facilitates the transformation to spherical coordinates. This is discussed in the next section.

3.5 The Transport Equation in Spherical Coordinates

Combining the drift tensor, $\mathbf{K}_D$, of Eq. 3.35 and the symmetrical diffusion tensor, $\mathbf{K}_s$, introduced in Eq. 3.8, the following asymmetrical tensor is attained:

$$\mathbf{K}_t = \mathbf{K}_s + \mathbf{K}_D = \begin{bmatrix} \kappa_{||} & 0 & 0 \\ 0 & \kappa_{\perp\theta} & \kappa_D \\ 0 & -\kappa_D & \kappa_{\perp r} \end{bmatrix}, \tag{3.36}$$

allowing the TPE of 3.1 to be rewritten in a more compact form as follows:

$$\frac{\partial f}{\partial t} = -\vec{V}_{sw} \cdot \nabla f + \nabla \cdot (\mathbf{K}_t \cdot \nabla f) + \frac{1}{3}\left(\nabla \cdot \vec{V}_{sw}\right) \frac{\partial f}{\partial \ln p} + Q. \tag{3.37}$$

The elements of $\mathbf{K}_t$ are written in terms of HMF-aligned coordinates; see the schematic in Figure 3.3. In this coordinate system, one axis ($\hat{e}_{||}$) is parallel to the mean HMF in the $r\phi$-plane, another is perpendicular to the first in the $\hat{e}_\theta$ direction ($\hat{e}_1$) and the last lies in the $r\theta$-plane ($\hat{e}_2$), completing the right-handed coordinate system. Each of the unit vectors of this HMF-aligned coordinate system ($\hat{e}_{||}$, $\hat{e}_1$, $\hat{e}_2$) are related to those of the spherical coordinate system ($\hat{e}_r$, $\hat{e}_\theta$, $\hat{e}_\phi$) through the HMF spiral angle, ψ, of Eq. 2.9 as follows:

$$\begin{aligned} \hat{e}_{||} &= \cos\psi \, \hat{e}_r - \sin\psi \, \hat{e}_\phi \qquad (3.38) \\ \hat{e}_1 &= \hat{e}_\theta \\ \hat{e}_2 &= \hat{e}_{||} \times \hat{e}_1 \\ &= \sin\psi \, \hat{e}_r + \cos\psi \, \hat{e}_\phi. \end{aligned}$$

Hence, by applying the appropriate transformation matrix, $\mathbf{T}$, the diffusion tensor of Eq. 3.36

may be written in spherical coordinates according to

$$\begin{aligned}
\mathbf{T}\mathbf{K}_t\mathbf{T}^T &= \begin{bmatrix} \kappa_{||}\cos^2\psi + \kappa_{\perp r}\sin^2\psi & -\kappa_D\sin\psi & \left(\kappa_{\perp r} - \kappa_{||}\right)\cos\psi\sin\psi \\ \kappa_D\sin\psi & \kappa_{\perp\theta} & \kappa_D\cos\psi \\ \left(\kappa_{\perp r} - \kappa_{||}\right)\cos\psi\sin\psi & -\kappa_D\cos\psi & \kappa_{||}\sin^2\psi + \kappa_{\perp r}\cos^2\psi \end{bmatrix} \\
&\equiv \begin{bmatrix} \kappa_{rr} & \kappa_{r\theta} & \kappa_{r\phi} \\ \kappa_{\theta r} & \kappa_{\theta\theta} & \kappa_{\theta\phi} \\ \kappa_{\phi r} & \kappa_{\phi\theta} & \kappa_{\phi\phi} \end{bmatrix},
\end{aligned} \tag{3.39}$$

with

$$\mathbf{T} = \begin{bmatrix} \cos\psi & 0 & \sin\psi \\ 0 & 1 & 0 \\ -\sin\psi & 0 & \cos\psi \end{bmatrix} \quad \text{and} \quad \mathbf{T}^T = \begin{bmatrix} \cos\psi & 0 & -\sin\psi \\ 0 & 1 & 0 \\ \sin\psi & 0 & \cos\psi \end{bmatrix}, \tag{3.40}$$

where $\det(\mathbf{T}) = 1$ and the superscript T denotes the transpose of a matrix. The TPE of Eq. 3.37 transformed to spherical coordinates consequently follows as

$$\begin{aligned}
\frac{\partial f}{\partial t} &= \left[\frac{1}{r^2}\frac{\partial}{\partial r}\left(r^2\kappa_{rr}\right) + \frac{1}{r\sin\theta}\frac{\partial}{\partial\theta}\left(\kappa_{\theta r}\sin\theta\right) + \frac{1}{r\sin\theta}\frac{\partial\kappa_{\phi r}}{\partial\phi} - V_{sw}\right]\frac{\partial f}{\partial r} \\
&+ \left[\frac{1}{r^2}\frac{\partial}{\partial r}\left(r\kappa_{r\theta}\right) + \frac{1}{r^2\sin\theta}\frac{\partial}{\partial\theta}\left(\kappa_{\theta\theta}\sin\theta\right) + \frac{1}{r^2\sin\theta}\frac{\partial\kappa_{\phi\theta}}{\partial\phi}\right]\frac{\partial f}{\partial\theta} \\
&+ \left[\frac{1}{r^2\sin\theta}\frac{\partial}{\partial r}\left(r\kappa_{r\phi}\right) + \frac{1}{r^2\sin\theta}\frac{\partial\kappa_{\theta\phi}}{\partial\theta} + \frac{1}{r^2\sin^2\theta}\frac{\partial\kappa_{\phi\phi}}{\partial\phi}\right]\frac{\partial f}{\partial\phi} \\
&+ \kappa_{rr}\frac{\partial^2 f}{\partial r^2} + \frac{\kappa_{\theta\theta}}{r^2}\frac{\partial^2 f}{\partial\theta^2} + \frac{\kappa_{\phi\phi}}{r^2\sin^2\theta}\frac{\partial^2 f}{\partial\phi^2} + \frac{2\kappa_{r\phi}}{r\sin\theta}\frac{\partial^2 f}{\partial r\partial\phi} \\
&+ \frac{1}{3r^2}\frac{\partial}{\partial r}\left(r^2 V_{sw}\right)\frac{\partial f}{\partial\ln p} + Q,
\end{aligned} \tag{3.41}$$

where it is assumed that the SW speed is purely radial, that is, $\vec{V}_{sw} = V_{sw}\hat{e}_r$. Furthermore, if azimuthal symmetry is assumed, Eq. 3.41 reduces to

$$\begin{aligned}
\frac{\partial f}{\partial t} &= \left[\frac{1}{r^2}\frac{\partial}{\partial r}\left(r^2\kappa_{rr}\right) + \frac{1}{r\sin\theta}\frac{\partial}{\partial\theta}\left(\kappa_{\theta r}\sin\theta\right) - V_{sw}\right]\frac{\partial f}{\partial r} \\
&+ \left[\frac{1}{r^2}\frac{\partial}{\partial r}\left(r\kappa_{r\theta}\right) + \frac{1}{r^2\sin\theta}\frac{\partial}{\partial\theta}\left(\kappa_{\theta\theta}\sin\theta\right)\right]\frac{\partial f}{\partial\theta} \\
&+ \kappa_{rr}\frac{\partial^2 f}{\partial r^2} + \frac{\kappa_{\theta\theta}}{r^2}\frac{\partial^2 f}{\partial\theta^2} + \frac{1}{3r^2}\frac{\partial}{\partial r}\left(r^2 V_{sw}\right)\frac{\partial f}{\partial\ln p} + Q,
\end{aligned} \tag{3.42}$$

which is finally solved numerically according to the procedure described in Section 3.7.

3.6 Modelling the Acceleration of Cosmic Rays

There are several instances of particle acceleration within the bounds of the heliosphere, ranging from particles accelerated during transient events on the Sun to acceleration in planetary magnetospheres. Of recent interest is the acceleration of CRs associated with magnetic reconnection, which in the outer heliosphere is thought to occur near the HCS and regions where SW flow has stagnated near the HP [e.g. *Lazarian and Opher*, 2009]. It has also been proposed as a mechanism for the acceleration of ACRs. As discussed in Section 2.7.1, the original paradigm of TS-accelerated ACRs has become further challenged by the concept of stochastic acceleration, which was demonstrated by *Strauss et al.* [2010b] to be able to account for ACR observations in the heliosheath. Stochastic acceleration may be modelled in the TPE with the inclusion of the momentum diffusion term

$$\frac{1}{p^2}\frac{\partial}{\partial p}\left(p^2\kappa_P\frac{\partial f}{\partial p}\right), \tag{3.43}$$

with κ_P the momentum diffusion coefficient. This process, its incorporation in a CR modulation model, and the form of κ_P are discussed in detail by *Strauss* [2010]. This is not the focus of the present study, which aims to investigate the re-acceleration of galactic electrons at the TS for which DSA is still considered the prevalent mechanism. *Tautz et al.* [2013] found that the spectral effects of stochastic acceleration become negligible if particle speeds significantly exceed the local Alfvén speeds. Using this as a guideline, it would be unlikely for CR electrons, which remain relativistic down to very low energies (Figure 3.2), to be accelerated stochastically at any region within the heliosphere. This requires further investigation. It assumed for the purposes of this study that $\kappa_P = 0$.

As stated before, this study endeavours to illustrate DSA as a mechanism for electron re-acceleration, and is also illustrated by surveying the features that emerge from the acceleration of ACRs (or more technically, TSPs). The DSA process is not explicitly contained in the TPE, but is simulated through the SW velocity divergence in the term for adiabatic energy changes, and is further reproduced by specifying the appropriate continuity and streaming conditions for the CR flux across the TS. This section discusses these modelling aspects. See also *Axford et al.* [1977], *Axford* [1981], *Lagage and Cesarsky* [1983], *Drury* [1983], and *Jones and Ellison* [1991] for more on shock acceleration.

3.6.1 Solar wind velocity divergence

The migration of CRs in energy is controlled in the TPE through the term for adiabatic energy changes, which contains the divergence of the SW velocity. It hence depends on the value of $\nabla\cdot\vec{V}_{sw}$ whether particles gain or lose energy in this region. In the inner heliosphere, the radial SW speed remains largely constant, but is rapidly reduced near and at the TS, and continues to decrease as r^{-2} in the heliosheath under the incompressibility assumption. In terms of $\nabla\cdot\vec{V}_{sw}$ this translates to the following:

$$\nabla\cdot\vec{V}_{sw} \equiv: \begin{cases} >0 & r<r_{TS}-L \quad \text{upstream region} \\ <0 & r_{TS}-L\leq r\leq r_{TS} \quad \text{shock region} \\ =0 & r>r_{TS} \quad \text{downstream region} \end{cases} \tag{3.44}$$

Recall that r_{TS} denotes the TS position and L the width of the precursor. Figure 3.11 illustrates the SW profile near the TS and the corresponding divergences of the SW velocity. Note that $\nabla\cdot\vec{V}_{sw}>0$, which occurs upstream of the TS, results in adiabatic cooling. This gives rise to characteristic CR energy spectra in the form of positively distributed power laws, and is dis-

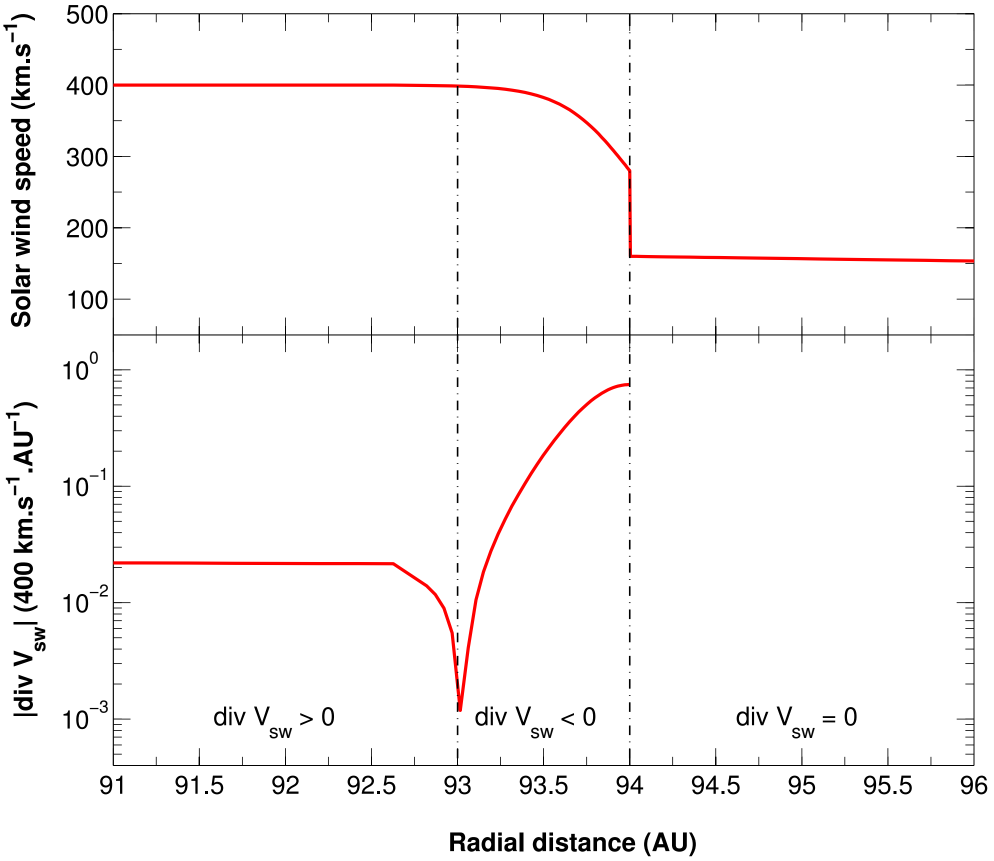

Figure 3.11: The SW speed (V_{sw}; top panel) and the corresponding divergence of the SW velocity ($\nabla \cdot \vec{V}_{sw}$; bottom panel) as functions of radial distance in the equatorial plane ($\theta = 90°$). Note that $\nabla \cdot \vec{V}_{sw}$ is written as div V$_{\text{sw}}$ in this figure, and that it is the absolute value of this quantity plotted in the bottom panel. Regions of different signs of $\nabla \cdot \vec{V}_{sw}$, as indicated, are separated by vertical dash-dotted lines. Note that in the heliosheath the divergence is zero, which is not visible on a logarithmic scale. The TS precursor length scale is specified as $L = 1.2$ AU and the compression ratio is $s = 2.5$.

cussed further in Section 5.4.2. In the shock region, where $\nabla \cdot \vec{V}_{sw} < 0$, the absolute value of the divergence, denoted $|\nabla \cdot \vec{V}_{sw}|$, is particularly large. In the TPE this translates to a large transferral of energy to particles over a relatively narrow radial interval, making the TS a very effective site for CR acceleration. Indeed, Voyager observations near the TS confirmed that the bulk of the SW energy is dissipated into the heating of non-thermal particles [*Richardson et al.*, 2008; *Decker et al.*, 2012]. The SW divergence can hence be exploited to model DSA in the TPE [*Jokipii*, 1992]. Consider finally the SW flow and corresponding velocity divergence in the downstream region of the TS. Section 2.3 explained the implications of assuming incompressible flow in the heliosheath, which included that $\nabla \cdot \vec{V}_{sw} = 0$. Hence, particles are neither heated nor do they incur energy losses in the heliosheath.

Note that should a steeper SW profile than r^{-2} be assumed in the heliosheath [e.g. *Langner et al.*, 2006a, b; *Ferreira et al.*, 2007a, b], particles gain energy through adiabatic heating in this region. These steeper profiles are not substantiated as deviations from the incompressibility assumption, but are modelled instead to account for a hydrodynamically shrunken heliosheath resulting from the loss of SW protons due to charge exchange with interstellar neutrals [e.g. *Fahr et al.*, 2000]. At any rate, incompressibility is assumed in this study with $V_{sw} \propto r^{-2}$ in the heliosheath, not (necessarily) because of its physical viability, but because other forms of heating must be suppressed to study the effects of DSA at the TS alone. Similarly, particle heating at the TS can be suppressed for a control scenario by imposing $\nabla \cdot \vec{V}_{sw} = 0$ when $\nabla \cdot \vec{V}_{sw} < 0$ in the region of $r_{TS} - L \leq r \leq r_{TS}$; this is especially useful to emphasise the effects of DSA by comparing TPE solutions with heating in the shock region to solutions without. The next subsection addresses the continuity conditions at the TS that allows the acceleration to reflect the theoretically expected results of DSA.

3.6.2 Features of diffusive shock acceleration

The hallmark of shock-accelerated CRs is that their energy spectra are power-law distributed, which follows from two conditions respectively concerning the continuity of CR densities and their streaming across the TS. The first of these conditions specifically entails that the differential CR number density, U_p, related to the CR distribution function according to $U_p = 4\pi p^2 f$, is continuous across the TS, which also implies that the distribution function is continuous across this boundary. Hence,

$$f^- = f^+, \tag{3.45}$$

where $f^- = \lim_{r \to r_{TS}} f(r)$ and $f^+ = \lim_{r_{TS} \leftarrow r} f(r)$ respectively represent downstream and upstream values of f with the superscripts $-$ and $+$ as introduced in Section 2.6.1. Secondly, the streaming of particles across the TS from the reference frame of a stationary observer must obey the condition

$$\nabla \cdot \vec{S} = Q, \tag{3.46}$$

with Q the source of particles (not to be confused with Q_s in Eq. 3.1), and where $\vec{S}$ is the differential particle current density, given by

$$\begin{aligned} \vec{S} &= 4\pi \left(C\vec{V}_{sw} j - \mathbf{K}_t \cdot \nabla j \right) \\ &= -4\pi p^2 \left(\frac{\vec{V}_{sw}}{3} \frac{\partial f}{\partial \ln p} + \mathbf{K}_t \cdot \nabla f \right), \end{aligned} \tag{3.47}$$

with C the Compton-Getting factor [*Gleeson and Axford*, 1968] specified as

$$C = 1 - \frac{1}{3j} \frac{\partial}{\partial p}(pj) = -\frac{1}{3} \frac{\partial \ln f}{\partial \ln p}. \tag{3.48}$$

Eq. 3.46 essentially states that the CR flux that diverges from the shock must have its origin at a source on the shock. See also the treatment of the above by *Gleeson and Axford* [1967]. In the case where the particle flux is directed perpendicular to the TS, Eq. 3.46 reduces to

$$S^+ + S^- = \lim_{\epsilon \to 0} \int_{r_{TS}-\epsilon}^{r_{TS}+\epsilon} Q dr. \tag{3.49}$$

Note that solving Eq. 3.49 is simplified by invoking Eq. 3.45, since terms containing the difference between f^- and f^+ may be eliminated, while the product $\mathbf{K}_t \cdot \nabla f$ in Eq. 3.47 may furthermore be expanded in spherical coordinates using the transformed tensor of Eq. 3.39. It

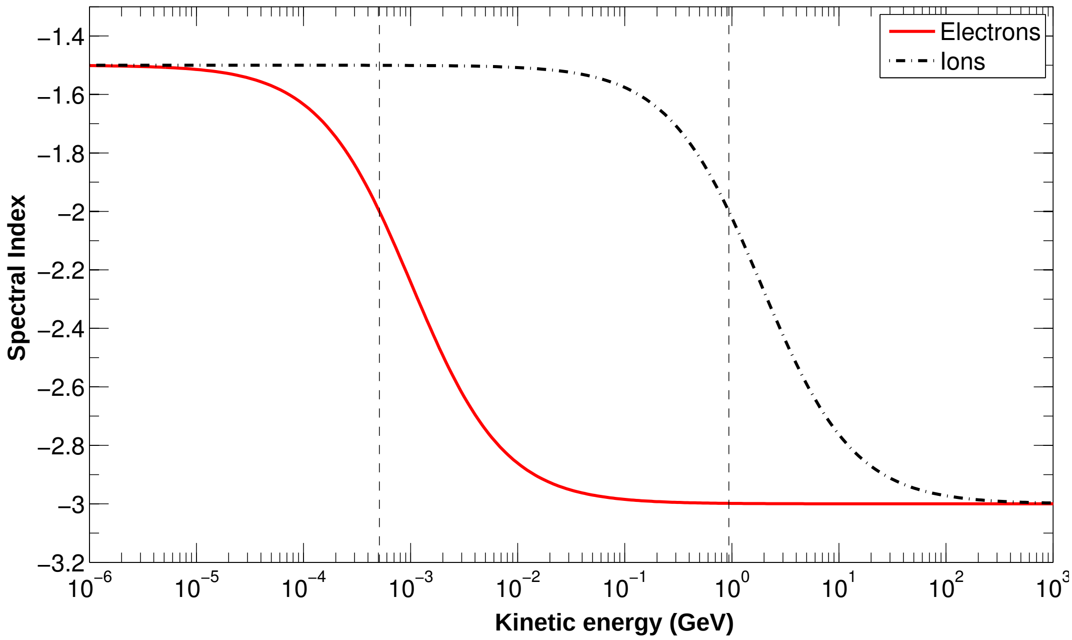

Figure 3.12: The spectral indices, $\gamma(s)$, of Eq. 3.54 as a function of kinetic energy, of CR electron and ion distributions ensuing from the DSA of a monoenergetic source at the TS. A fixed compression ratio of $s = 2.5$ is used so that it follows from Eq. 3.54 that $\gamma(s)$ varies between -1.5 below the rest-mass energy and -3.0 above; the rest-mass energies for electrons and protons are indicated using vertical lines.

consequently follows that

$$\left[\frac{\partial f}{\partial r}\right]^{-} = \frac{\kappa_{rr}^{+}}{\kappa_{rr}^{-}}\left[\frac{\partial f}{\partial r}\right]^{+} - \frac{V_{sw}^{-} - V_{sw}^{+}}{3\kappa_{rr}^{-}}\frac{\partial f}{\partial \ln p} - \frac{\kappa_{r\theta}^{-} - \kappa_{r\theta}^{+}}{r_{TS}\kappa_{rr}^{-}}\frac{\partial f}{\partial \theta} + \frac{Q}{\kappa_{rr}^{-}}, \tag{3.50}$$

which relates the particle flux up- and downstream of the TS, and is referred to as the matching condition [*Langner*, 2004]. This equation and the TPE as written in Eq. 3.42 are solved simultaneously as discussed in Section 3.7.

The source in Eq. 3.46 can be specified as a monoenergetic delta function, representing a seed particle population injected at the TS, according to

$$Q = Q^{*}\,\delta\left(\frac{r - r_{TS}}{r_0}\right)\,\delta\left(\frac{P - P_{\min}}{P_0}\right), \tag{3.51}$$

with $P_0 = 1$ GV and $r_0 = 1$ AU. Here, Q^{*} is of arbitrary magnitude with the units of f, and $P_{\min}$ is the rigidity at which the seed population is injected. When modelling the acceleration of ACRs, $P_{\min}$ essentially represents the rigidity at which PUIs are injected. In a 1-D case, for a source specified as in Eq. 3.51, an analytical solution can be obtained for Eq. 3.46 [*Steenkamp*, 1995; *Langner*, 2004] that yields

$$f \propto P^{-3s/(s-1)}, \tag{3.52}$$

where s is the compression ratio. In differential intensity, this proportionality becomes

$$j = p^2 f \propto P^{(s+2)/(1-s)}. \tag{3.53}$$

To furthermore express this proportionality in terms of kinetic energy, the relation between E

and P, as discussed in Section 3.2, must be considered. At energies respectively much higher and much lower than the rest-mass energy, it follows that $P \propto E$ and $P \propto E^{1/2}$, so that Eq. 3.53 becomes

$$j \propto E^{\gamma(s)} \text{ with } \gamma(s) \in \left[\frac{s+2}{1-s}, \frac{s+2}{2-2s}\right]. \tag{3.54}$$

To demonstrate, $\gamma(s)$ is shown in Figure 3.12 as function of kinetic energy for CR electrons and ions. As a result of the smaller rest-mass energy of electrons, the relationship of their kinetic energy with rigidity becomes linear at lower energies, and hence the transition of their accelerated spectra to the smaller high-energy spectral index also occurs at lower energies than for their heavier CR counterparts. The form of Eq. 3.54, where the spectral index of shock-accelerated spectra arising from a monoenergetic source depends only on s, is encountered repeatedly in further chapters, although the nature of the dependence on s may differ depending on other involved modulation parameters, e.g. those contained in $\mathbf{K}_t$. The idealised solution of Eq. 3.46 given by Eq. 3.54 for an infinite plane shock hence provides a guideline for the forms one can expect numerically computed shock-accelerated spectra to have. A notable deviation (in a 2-D geometry) occurs when the diffusion length scale, κ_{rr}/V_{sw}, of a particle becomes comparable to the shock radius, that is, when

$$\left(\frac{\kappa_{rr}}{V_{sw}}\right)^{-} + \left(\frac{\kappa_{rr}}{V_{sw}}\right)^{+} \gtrsim r_{TS}. \tag{3.55}$$

In such an event particles detect the curvature of the shock and escape, which results in the termination of the accelerated power-law distribution. The establishment of the accelerated spectrum is also time-dependent, since the power law of e.g. Eq. 3.54 can only be achieved up to such an energy as there is time for particles to be accelerated to. Such an acceleration time may be expressed in terms of momentum, p, as

$$\tau_a = \frac{3}{V_{sw}^{-} - V_{sw}^{+}} \int_{p_0}^{p} \left[\left(\frac{\kappa_{rr}}{V_{sw}}\right)^{-} + \left(\frac{\kappa_{rr}}{V_{sw}}\right)^{+}\right] \frac{dp'}{p'}, \tag{3.56}$$

where p_0 ($\equiv P_{\min}(Ze)/c$) denotes the initial momentum. More on these quantities follow in Chapter 4. See also the related discussions by *Jones and Ellison* [1991].

3.7 The Numerical Modulation Model

As mentioned in the introduction of this chapter, analytical solutions for the TPE are not attainable without simplifying assumptions, and hence numerical models are sought. Due to the complexity of the TPE, these numerical solutions are computed using comprehensive numerical models. Of special interest to the present study are those numerical models that account both for general modulation processes and CR acceleration at the TS. Perhaps one of the earliest prototypes of such a model was that of *Jokipii* [1986], which was time-dependent and one-dimensional, while the 1-D steady-state model of *Potgieter and Moraal* [1988] simulated particle acceleration by specifying streaming conditions similar to Eqs. 3.45 and 3.46. The development of 2-D acceleration models followed, with those of *Steenkamp* [1995] and [*Steenberg and Moraal*, 1996, 1999] being notable examples. The progenitor of the 2-D model applied in the present study was initially developed by *le Roux et al.* [1996]. CR drifts were subsequently included [*Haasbroek*, 1997], and variants of this model have been widely applied in CR modulation studies [e.g. *Ferreira*, 2002; *Langner*, 2004; *Ngobeni*, 2006, 2015]. Recently, this model was also applied by *Strauss* [2010] in the study of ACRs, for which the effects of stochastic acceleration (momentum diffusion) had to be included.

The TPE (Eq. 3.42), valid $\forall\theta$, $\forall P$, $r \in [r_\odot, r_{HP}]$, $r \neq r_{TS}$, and the matching condition (Eq. 3.50), valid $\forall\theta$, $\forall P$, $r = r_{TS}$, provide the complete set of equations governing CR transport and acceleration. The TPE is solved using the Locally One-Dimensional (LOD) method [*Steenkamp*, 1995; *Langner*, 2004], which relies on a technique called fractional splitting to write the TPE as separate equations, each dependent only on a single computational dimension. Consider the TPE as written in Eq. 3.42 in the following form:

$$\frac{\partial f}{\partial t} = a_0 \frac{\partial^2 f}{\partial r^2} + b_0 \frac{\partial^2 f}{\partial \theta^2} + c_0 \frac{\partial f}{\partial r} + d_0 \frac{\partial f}{\partial \theta} + e_0 \frac{\partial f}{\partial \ln P}\ , \tag{3.57}$$

which is written in terms of rigidity. Note that since no sources are specified using the source term, Q_s, it is omitted from this discussion. The coefficients are specified as

$$\begin{aligned}
a_0 &= \kappa_{rr} \\
b_0 &= \frac{\kappa_{\theta\theta}}{r^2} \\
c_0 &= \frac{1}{r^2}\frac{\partial}{\partial r}\left(r^2 \kappa_{rr}\right) + \frac{1}{r \sin\theta}\frac{\partial}{\partial \theta}\left(\kappa_{\theta r} \sin\theta\right) - V_{sw} \\
d_0 &= \frac{1}{r^2}\frac{\partial}{\partial r}\left(r \kappa_{r\theta}\right) + \frac{1}{r^2 \sin\theta}\frac{\partial}{\partial \theta}\left(\kappa_{\theta\theta} \sin\theta\right) \\
e_0 &= \frac{1}{3r^2}\frac{\partial}{\partial r}\left(r^2 V_{sw}\right).
\end{aligned} \tag{3.58}$$

The LOD method applied to Eq. 3.57 yields the following set of equations

$$\text{radial equation: } \frac{1}{3}\frac{\partial f}{\partial t} = a_0 \frac{\partial^2 f}{\partial r^2} + c_0 \frac{\partial f}{\partial r} \tag{3.59}$$

$$\text{polar equation: } \frac{1}{3}\frac{\partial f}{\partial t} = b_0 \frac{\partial^2 f}{\partial \theta^2} + d_0 \frac{\partial f}{\partial \theta} \tag{3.60}$$

$$\text{energy equation: } \frac{1}{3}\frac{\partial f}{\partial t} = e_0 \frac{\partial f}{\partial \ln P}. \tag{3.61}$$

Note that each of these equations are only valid on a third of a time step, that is, for $t' < t < t' + \Delta t/3$, $t' + \Delta t/3 < t < t' + 2\Delta t/3$, and $t' + 2\Delta t/3 < t < t' + \Delta t$. Note that the radial and polar equations are second-order parabolic partial differential equations (PDEs) that can be solved using the Crank-Nicholson method. The energy equation is also a second-order parabolic PDE if the momentum diffusion term (Eq. 3.43) is present. Its solution in this form is discussed in greater detail by *Strauss* [2010]. Without the momentum diffusion term, however, it is a first-order hyperbolic PDE, and can either be solved using the method of characteristics [*Langner*, 2004] or the explicit upwind method [*Haasbroek*, 1997]. To be solved simultaneous to the above equations is the matching condition of Eq. 3.50, which is also a first-order hyperbolic PDE in the variables $\ln P$ and θ. It is solved using the Wendroff's implicit method in the direc-

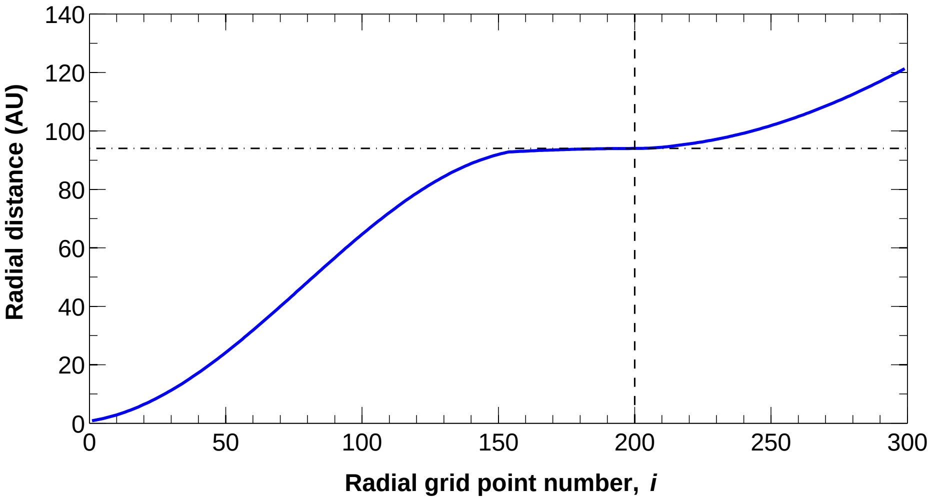

Figure 3.13: Radial distances versus their corresponding grid points. The vertical and horizontal lines denote the TS position at $r_{TS} = 94$ AU and $i = 200$, at which the grid spacing is much finer than elsewhere in the heliosphere. The HP at 122 AU is at $i = 300$.

tion of particle drifts [*Steenkamp*, 1995]. The matching condition and Eqs. 3.59, 3.60 and 3.61 are furthermore expanded using finite difference schemes, which is discussed thoroughly by *Steenkamp* [1995] and *Langner* [2004] and thus not repeated here.

Note finally the boundary conditions and numerical grid sizes applied in the model: The outermost iteration of the numerical scheme is a simple linear time grid, which continues until such a time at which sufficient convergence of the numerical solution is attained; this is usually after some 40000 iterations when heating due to DSA is included, and on average around 23000 if DSA is suppressed. The radial grid $(r_i, i = 1 \rightarrow n_r, n_r = 300)$ is transformed to create an uneven spacing of grid points, which are condensed near the TS, but are further apart away from it, as illustrated and discussed by *Langner* [2004]; see also Figure 3.13. This is for better numerical accommodation of the discontinuous SW speed decrease at the TS. The inner modulation boundary is located at $r_1 \approx 0.8$ AU, and is a reflective boundary, so that

$$\left[\frac{\partial f}{\partial r}\right]_{r=r_1} = 0, \tag{3.62}$$

which implies that no particles enter or leave this boundary. The outer boundary, $r_{n_r} (\equiv r_{HP})$, is a free escape boundary, with

$$f(r_{n_r}, \theta, P, t) = 0, \tag{3.63}$$

for ACRs (Chapter 4), but

$$f(r_{n_r}, \theta, P, t) = j_{\mathrm{HPS}}(r_{n_r}, \theta, P, t)/P^2, \tag{3.64}$$

when GCRs are considered. Here, j_{HPS} represents the differential intensity value associated with the input spectrum, which is specified at the HP in this study, is the same at all polar angles, and does not change with time. These are specified in Chapter 5 for GCR electrons. On the other hand, the polar grid $(\theta_j, j = 1 \rightarrow n_j, n_j = 37)$ is equally spaced, with $\Delta\theta = 2.5^o$. The TPE is solved in this study only for the region $\theta_1 = 0^o \rightarrow \theta_{n_j} = 90^o$ for a spherically symmetrical heliosphere. Hence, it is assumed that

$$\left[\frac{\partial f}{\partial \theta}\right]_{\theta=0,\pi/2} = 0. \tag{3.65}$$

Lastly, the rigidity grid $(P_k, k = 1 \to n_k, n_k = 175)$ is logarithmic, with $P_{\min}$ varied as required; the default values are 30 MV for ACRs and 1 MV for GCR electrons. The maximum rigidity is determined by $P_{\max} = P_{\min}\exp(n_k\ dP)$, with dP varied between 0.040 and 0.062 as required. Zero modulation is assumed to occur at $P_{\max}$, which for GCRs implies that intensities equal those of the input spectrum at all radial distances and latitudes at this rigidity. See *Steenkamp* [1995] for a discussion on numerical stability.

3.8 Summary

This chapter introduced the Parker TPE, which is solved for the CR distribution function, to describe the modulating effects of various processes on CRs travelling through the heliosphere. These processes, including diffusion and drifts, and the behaviour of different CR species in response, were discussed. Their mathematical representations as utilised in this study were also provided. The discussion of the SW velocity divergence and its role in adiabatic energy changes of CRs was particularly important, while the continuity and streaming conditions required to simulate the effects of DSA at the TS were also presented and discussed. The TPE and the matching condition following from the aforementioned conditions constitute the full set of equations required to model the modulation and acceleration of CRs throughout the heliosphere. Since these equations are complex in nature, a numerical model is applied to solve them. An overview of this model, and how it solves the TPE, was presented.

In further chapters, the numerical model introduced in this chapter is used to solve the TPE for a variety of heliospheric conditions, different modulation parameters and CR species. Chapter 4, for instance, demonstrates the acceleration and consequent transport of ACR Oxygen, while Chapters 5 and 6 respectively discuss the modulation and DSA features of galactic electrons.

Chapter 4

Lessons from the Modelling of Anomalous Oxygen

4.1 Introduction

Having arisen from the acceleration of a PUI seed population, ACRs are modelled by allowing a monoenergetic source function, injected at the TS position, to be shocked into the characteristic power-law energy spectrum associated with DSA. This shocked spectrum is then further modulated subject to the processes contained within the TPE. By virtue of their formation from the acceleration processes of interest in this study, ACRs reveal a great deal of information with regards to the features of these processes, and do so more explicitly than their GCR counterparts. To illustrate these features, modelled solutions for ACRs are presented in this chapter, with anomalous oxygen chosen for comparability with recent studies on this species using the same model [*Strauss*, 2010; *Strauss et al.*, 2011a]. See also *Strauss et al.* [2010a] for the transport of multiply-charged ACR Oxygen.

Firstly, the model is set up to yield solutions that may be used as reference when making subsequent changes to modulation parameters. This model configuration, the choices for its constituent parameters, and its resultant solutions are discussed in the first section hereafter. Further sections illustrate the effects of varying key physical processes in the TPE on modelled solutions, while exploring in particular the features of DSA. The parameters investigated include e.g. the TS compression ratio and coefficients of CR drift and diffusion. Finally, some intriguing spectral features at energies roughly below 0.3 MeV. nuc^{-1} are also investigated.

It is aimed that the insights gathered in this chapter inform further application of the model to the re-acceleration of CR electrons at the TS.

4.2 Model Configuration and Reference Solutions

Before illustrating the features of the numerical model as applied to the acceleration of ACR Oxygen, the standard model configuration is summarised here first. Singly-charged anomalous oxygen is assumed, and hence the ratio of mass number to charge is $\Theta = 16$. Also, in this

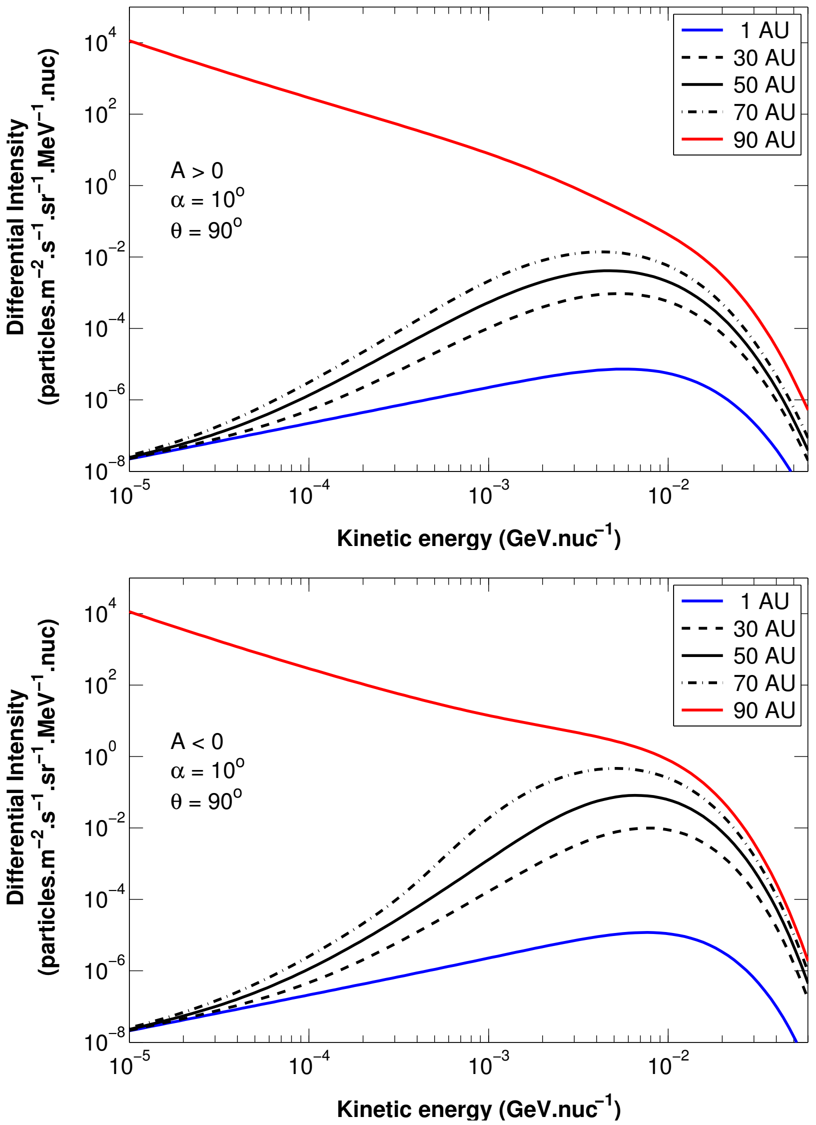

Figure 4.1: Modelled ACR Oxygen energy spectra for the A $>$ 0 (top panel) and A $<$ 0 (bottom panel) magnetic polarity cycles. The spectra are shown for radial distances 1 (Earth), 30, 50, 70 and 90 AU (TS) in the equatorial plane ($\theta = 90°$) for solar minimum conditions ($\alpha = 10°$).

chapter, the respective perpendicular and parallel diffusion coefficients of *Burger et al.* [2000] and *Burger et al.* [2008] are implemented. It is generally assumed here that $\kappa_{||,0} = 0.9$ and $\kappa_{\perp r,0} = \kappa_e^0 = 0.02$ (see Section 3.3), however these scaling factors may vary in subsequent sections. Furthermore, the HCS tilt angle is taken as $\alpha = 10°$ to simulate solar minimum conditions, with CR drift assumed to be 55% effective ($\kappa_{D,0} = 0.55$) in correspondence with previous studies conducted using 2-D models [*Langner*, 2004; *Ngobeni*, 2006, 2015; *Strauss*, 2010]. Furthermore, for this chapter, the positions of the TS and HP are chosen to coincide with that used by *Strauss* [2010] for comparability. The heliocentric position of the TS is thus taken as $r_{TS} = 90$ AU. That of the HP, however, is taken as $r_{HP} = 140$ AU – an overestimate, but similar to that assumed by HD models [e.g. *Ferreira et al.*, 2007a] prior to the Voyager 1 crossing of the HP. Moreover, although estimates for the TS compression ratio vary appreciably (see Section 4.3), a moderately strong shock with s = 2.5 is settled on in this study. Incompressible solar wind flow ($\nabla \cdot \vec{V}_{sw} = 0$) is assumed in the heliosheath, ruling out adiabatic heating, with stochastic acceleration suppressed by setting $\kappa_{P,0} = 0$ (See Section 3.6). Having generated solutions with the above configuration, some care must be taken with their intensities. ACRs are modelled in this study by accelerating a monoenergetic source function, representing a population of injected PUIs, into a power law at the TS [see also *le Roux et al.*, 1996; *Langner*, 2004; *Strauss*, 2010]. Since the intensity of the injected PUI source is chosen arbitrarily (see Section 4.6.2), and by virtue of the linearity of the Parker TPE, the resultant solutions are scaled to fit measured intensity levels. See e.g. *Strauss and Potgieter* [2010], *Strauss et al.* [2010a] or *Strauss et al.* [2011a] for similar modelling approaches, and e.g. *Leske et al.* [2013] and the references therein for ACR Oxygen intensities during recent solar cycles. Although the reproduction of ACR observations is not an objective of this study, the solutions displayed throughout this chapter are nonetheless scaled at the TS to measurements from Voyager 1 and 2 [*Webber et al.*, 2007]. The above model configuration consequently yields the solutions shown in Figures 4.1, 4.2 and 4.3. These may be used as references in subsequent sections, and any departures from this configuration for further solutions in this chapter will be stated explicitly.

The reference solutions already reveal a number of intriguing features with regards to CR acceleration. Figure 4.1 illustrates how the accelerated TS spectrum is modulated from the TS position to Earth for both magnetic polarities in the equatorial plane ($\theta = 90°$). The first notable feature is of course the power-law structure of the TS spectrum – a characteristic of DSA. At energies higher than about 10 MeV. nuc^{-1}, however, this power-law structure diminishes and transitions into an exponential decay. This is referred to as the ACR cut-off or roll-over energy, above which anomalous intensities fall below those of GCRs [*Webber et al.*, 2007]. In the energy region immediately preceding this cut-off, the TS spectrum bulges slightly upward for the A < 0 polarity cycle, while deviating downward for A > 0. This polarity dependence hints at the involvement of CR drifts. The three spectral features identified above form the basis for discussion in following sections. Furthermore, note from Figure 4.2 that the modelled radial intensity profiles attain a maximum at the TS in the equatorial plane (also visible in Figure 4.3). This is however in the absence of any heating mechanisms other than acceleration at the TS, and in apparent contradiction with Voyager observations that show a definitive increase in ACRs from the TS into the heliosheath [*McDonald et al.*, 2007; *Webber et al.*, 2007]. These observations have given rise to some debate on the location of the chief source of ACRs, whether it is indeed at the TS [as argued by *Jokipii and Kota*, 2011] or further into the heliosheath as observations suggest [*Stone et al.*, 2009]. The latter notion was corroborated by *Strauss et al.* [2010b] who modelled ACR intensities in the heliosheath with the inclusion of adiabatic heating and stochastic (second-order Fermi) acceleration. These mechanisms, though summarised briefly in Section 3.6, are not explored further in this study. See *Strauss* [2010] for a comprehensive review.

The omission of alternative acceleration sources does however prove useful to explore some of the more general modulation features in the heliosheath that would otherwise have been obscured. For instance, in the absence of adiabatic energy changes (by virtue of the assumption of incompressible SW flow), Figure 4.2 shows constant intensities throughout the heliosheath for particles with energies below 1.0 MeV. This ensues because ACRs produced at the TS are merely convected outward into the heliosheath with little to no modulation. On the other hand, the intensities of these low-energy particles plummet quickly into the heliospheric interior due

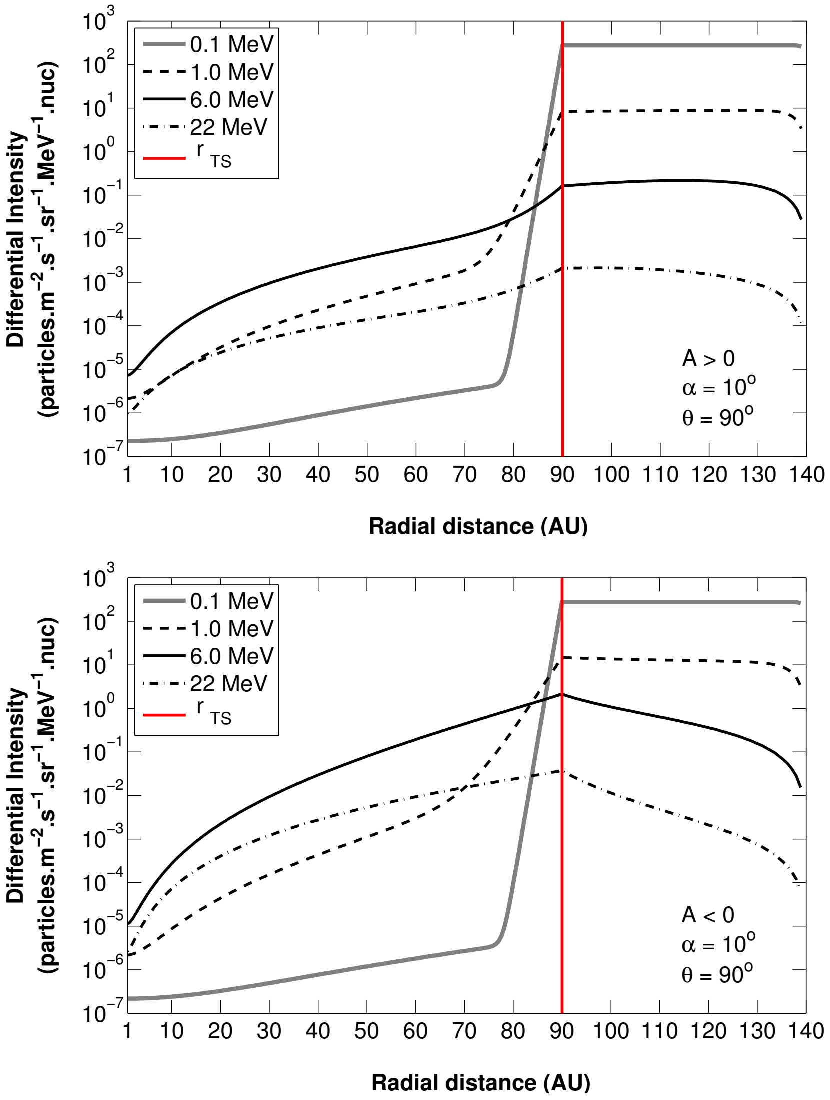

Figure 4.2: Radial profile of modelled ACR Oxygen intensities in the equatorial plane ($\theta = 90^\circ$) for the A $>$ 0 (top panel) and A $<$ 0 (bottom panel) magnetic polarities during solar minimum ($\alpha = 10^\circ$). The intensities are shown for CR energies of 0.1, 1.0, 6.0 and 22 MeV, with the TS at 90 AU (indicated by solid vertical line) and the HP assumed at 140 AU.

to small MFPs (see Figure 3.6), but also due to energy losses. Indeed, Figure 4.1 shows that toward lower energies modulated spectra are forced into the $j \propto E^{+1}$ relation at Earth that is associated with adiabatic cooling [see e.g. *Moraal and Potgieter*, 1982]. For higher-energy particles, however, CR drifts are more pronounced. Figure 4.2 conveys that during the A $<$ 0 polarity, while raising intensities upstream of the TS (see also Figure 4.1), the inward-directed drifts along the HCS serve to diminish intensities of ACRs further into the heliosheath. On the other hand, during the A $>$ 0 cycle, outward drifts and impaired diffusion in the heliosheath collectively yield intensities that are nearly constant across this region. This holds for the equatorial plane as demonstrated in Figure 4.2, while the global drift patterns explained in Section 3.4 are illustrated more clearly with contours in Figure 4.3. Nearer to Earth, however, both diffusion and drift scales become smaller as shown in Figures 3.6 and 3.10, reducing the amount of particles transported here and resulting in similar intensities at Earth for both polarities.

The prevalent qualities of the solutions presented here are consistent with that illustrated by *Strauss* [2010] under the same assumptions. It is however those features discussed above that

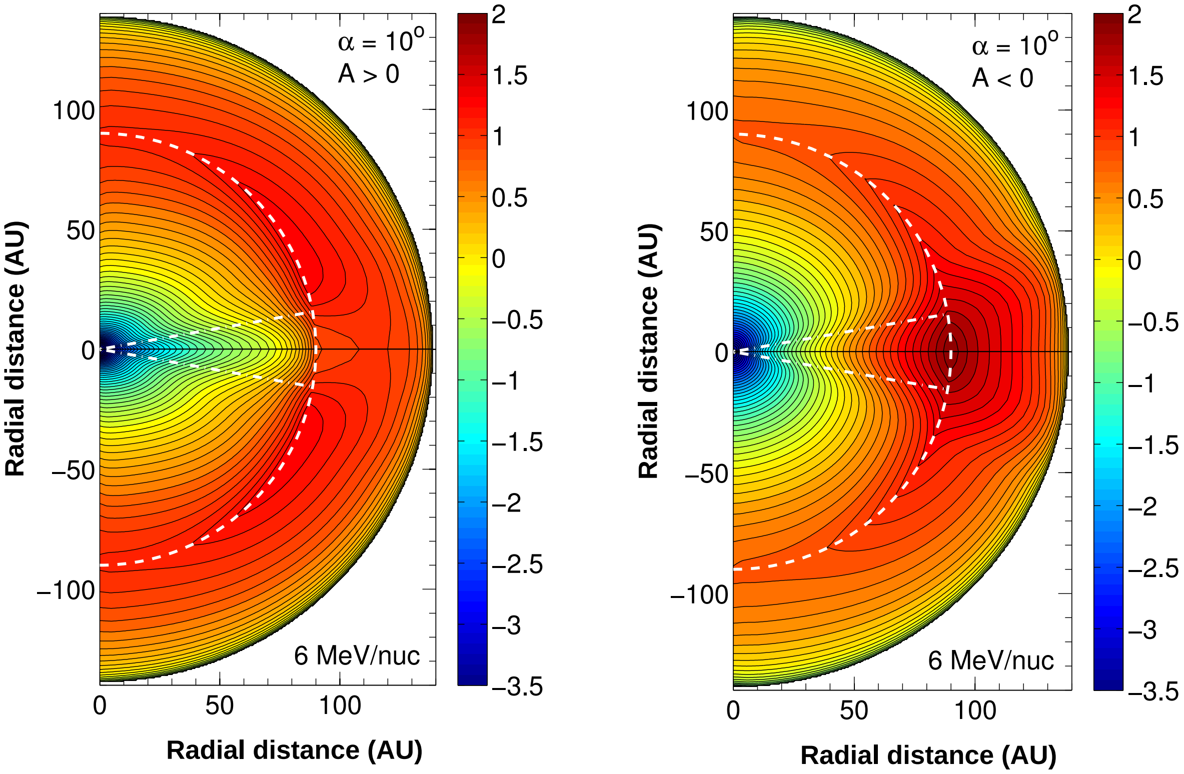

Figure 4.3: Contour plots illustrating 6 MeV. nuc^{-1} ACR Oxygen intensities in the meridional plane of the heliosphere, for A $>$ 0 (left) and A $<$ 0 (right) polarities. The colour bar shows intensities as percentages of the maximum on a logarithmic scale (e.g. $2 \equiv 10^2$ %). The dashed white halfcircle indicates the TS position (at 90 AU), while the dash-dotted white lines indicate the polar extent of the HCS for $\alpha = 10°$. The Sun is located at the origin.

pertain to the acceleration of ACR Oxygen at the TS that are of interest in this study. As mentioned before, these features form the basis for discussion in subsequent sections where they are investigated in greater detail.

4.3 Shock Strength and Solar Wind Compression

Nearly half a century after *Parker* [1961] first postulated the existence of a TS followed its much-lauded detection by the Voyager 1 and 2 spacecraft. During these encounters the first *in situ* measurements were made available to construct a feasible range of values for the compression ratio of the SW at the TS. A summary of these measurements is provided in Table 4.1. Note that there is an appreciable spread in the estimated values, with magnetometer and particle data from Voyager 1 suggesting larger values than plasma experiments aboard Voyager 2. *Arthur and le Roux* [2013] offer an intriguing argument regarding this: They show that the diffusion length scales of the PUIs measured by the Low-energy Charged Particle (LECP) instrument on Voyager 2 are larger than the extended TS structure (that is, including both the subshock and precursor; see Figure 2.5). These particles then experience an effective compression ratio that is greater than that measured by the on-board plasma and magnetic field instruments, which sampled only the subshock. Recall from Section 3.6.2 that the spectral index, γ, of the power-law distribution displayed by shock-accelerated CR ions is a function of the compression ratio

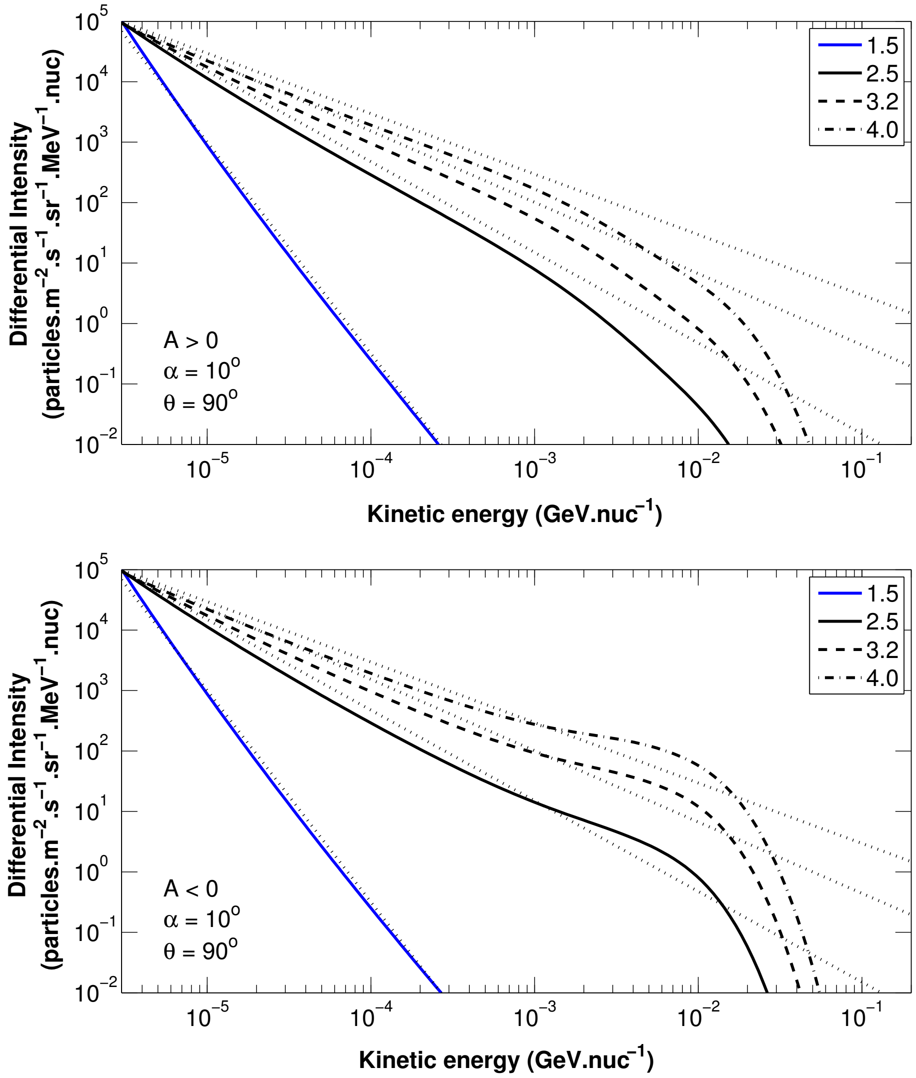

Figure 4.4: Modelled TS spectra for ACR Oxygen in the equatorial plane for varying compression ratios (s) as listed in the figure legend. Each spectrum is accompanied by its corresponding power law (dotted lines) with spectral indices of $-3.50, -1.50, -1.18$ and -1.00 as predicted by $\gamma = (s+2)/(2-2s)$ for $s = 1.5, 2.5, 3.2$ and 4.0 respectively. Solutions are shown for A $>$ 0 (top panel) and A $<$ 0 (bottom panel) during solar minimum conditions.

denoted s. The accelerated spectra are thus of the form $j \propto E^{\gamma}$ with

$$\gamma = \frac{s+2}{2-2s}. \tag{4.1}$$

Although this is derived for a 1-D planar shock, Eq. 4.1 is used in this chapter as an approximation for the expected power-law indices of TS spectra. DSA theory therefore predicts from the form of the energy spectra measured by Voyager 2 a compression ratio of ~ 2.9, which is in closer correspondence to the values measured by Voyager 1 [see *Arthur and le Roux*, 2013, for more details]. Before these spacecraft revelations however, the compression ratio had assumed numerous values in CR modulation studies. Some authors [e.g. *Steenkamp*, 1995; *Steenberg*, 1998; *Ferreira*, 2002] had thought the shock to be stronger, assuming the maximum value of $s = 4$, while e.g. *Langner* [2004] had chosen $s = 3.2$. Others [e.g. *Potgieter*, 1989] were led by observations to assume a weaker shock with compression ratios as small as $s = 2$. The resultant

Spacecraft	Compression Ratio	Method	Reference
V1	$s = 2.6^{+0.4}_{-0.2}$	Particle data	*Stone et al.* [2005]
V1	$s = 3.05 \pm 0.05^{\star}$	Magnetic field	*Burlaga et al.* [2005]
V2	$s \sim 2.5$ (max)†	Magnetic field	*Burlaga et al.* [2008]
V2, TS-3	$s = 1.6 \pm 0.2$	Magnetic field, density	*Burlaga et al.* [2008]
V2, TS-3	$s = 1.6$	Solar wind	*Richardson et al.* [2008]
V2, TS-2	$s = 2.4$	Solar wind	*Richardson et al.* [2008]

Table 4.1: A summary of empirical estimates of the compression ratio as informed by measurements obtained by the Voyager 1 and 2 (V1/2) spacecraft. The labels TS-2/3 refer to sub-structures observed by V2. **Burlaga et al.* [2005] also report $\forall\ s \in [2, 4]$ are admissible. †This is the maximum value for all encounters with substructures as measured by *Burlaga et al.* [2008].

spectra of some of these estimated ratios are shown in Figure 4.4.

As demonstrated in this figure, the various estimates yield significant differences in the form of modelled TS spectra: Higher compression ratios produce harder spectra, essentially stating that a stronger shock yields a larger intensity of high-energy particles than a weak shock. This type of particle distribution, i.e. a power-law function of kinetic energy, is a global characteristic of DSA. Whether at the TS of the heliosphere, that of other astrospheres, or at shocks associated with supernovae and their remnants (where GCRs are thought to originate), the spectral index of the resultant power law is in some manner dependent on the plasma compression ratio. Up until the (ACR) cut-off energy, E_{cut}, the accelerated spectrum is also time-dependent. Formulated differently, the power law distribution can only be obtained up to such an energy as there is time for particles to be accelerated to (see Section 3.6.2). For example, the model used in this study requires a sufficient amount of time iterations of the numerical scheme to avoid the power law terminating prematurely (at too low energies) before a steady-state solution is established. At $E > E_{\text{cut}}$, the power-law distribution is no longer limited by time, but by the curvature of the shock (see Section 4.4).

In this study, for $s = 2.5$, the accelerated TS spectra are expected from Eq. 4.1 to follow a power law with a spectral index of $\gamma = -1.5$. This predicted power law is displayed alongside modelled TS spectra in all subsequent figures within this chapter for reference purposes. It appears that while the power law is arguably the most notable feature of the TS spectrum, varying compression ratios also has some influence on how far particles are accelerated. The solutions here also show polarity-dependent intensity enhancements and depressions. These features are addressed in following sections.

4.4 Dependence on Elements of the Diffusion Tensor

For particles to undergo DSA, it is required that they diffuse across the shock interface. For effective acceleration, CRs must hence be confined to a region local to the TS to allow for repeated crossings. One method by which this can be achieved is by limiting diffusion length scales. There are three modes of diffusion for charged particles with respect to the HMF (see Section 3.3): CRs may diffuse along magnetic field lines as governed by $\kappa_{||}$, or perpendicular to

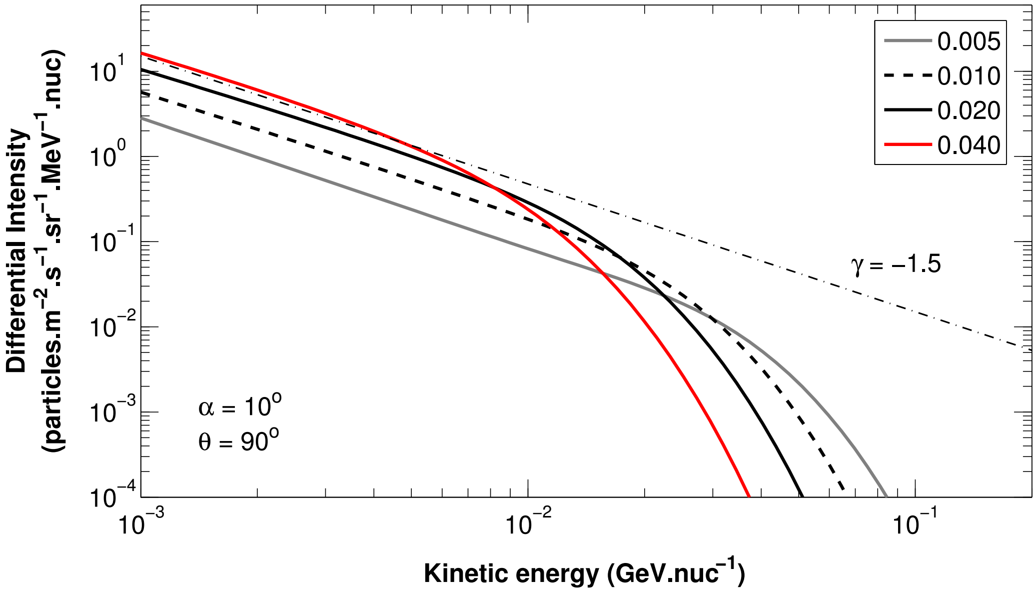

Figure 4.5: Modelled TS spectra for ACR Oxygen for a fixed $\kappa_{||}$ and varying values of $\kappa_{\perp r}$, with legend values corresponding to $\kappa_{\perp r,0}$. Here $\kappa_{\perp r,0} = 0.02$ serves as reference, with the predicted power law indicated with a dash-dotted line. CR drifts are disabled for these solutions, hence $\kappa_{D,0} = 0$.

them in either the polar or radial directions as respectively governed by $\kappa_{\perp\theta}$ and $\kappa_{\perp r}$. These diffusion coefficients have however varying degrees of effectiveness with regards to confinement of particles at the TS [see also *Langner and Potgieter*, 2008]. Consider, for instance, that since the TS extends both in the polar and azimuthal directions, diffusion along these directions is less likely to remove particles from the shock than radial diffusion. Since the model utilised in this study uses a 2-D spherical geometry, only the effective radial and polar coefficients are considered. From Section 3.5, the elements of the diffusion tensor (with drifts neglected) are

$$\kappa_{rr} = \kappa_{||} \cos^2 \psi + \kappa_{\perp r} \sin^2 \psi \tag{4.2}$$

$$\kappa_{\theta\theta} = \kappa_{\perp\theta} \tag{4.3}$$

with ψ the HMF spiral angle. Note that these tensor elements are written in terms of the HMF-aligned coordinates. Each of these are varied in turn in the following subsections, and their effects on the form of the TS spectrum explored.

4.4.1 Effective radial diffusion

The radial diffusion coefficient, κ_{rr}, is significant in CR modulation studies in a number of ways. Classically, using a spherical force-field model approach, the modulation of intensities from some boundary containing a source of particles to an observed point is dependent only on the integral of V_{sw}/κ_{rr} across that region [*Moraal and Potgieter*, 1982]. In acceleration models, however, the role of κ_{rr} is expanded. *Steenberg and Moraal* [1999] identified that the maximum energy attainable by particles accelerated at the TS is subject to energy losses suffered by particles, losses of the particles themselves, and the available acceleration time. Since the model makes no provision for energy losses in the shock region, this study is concerned only with the

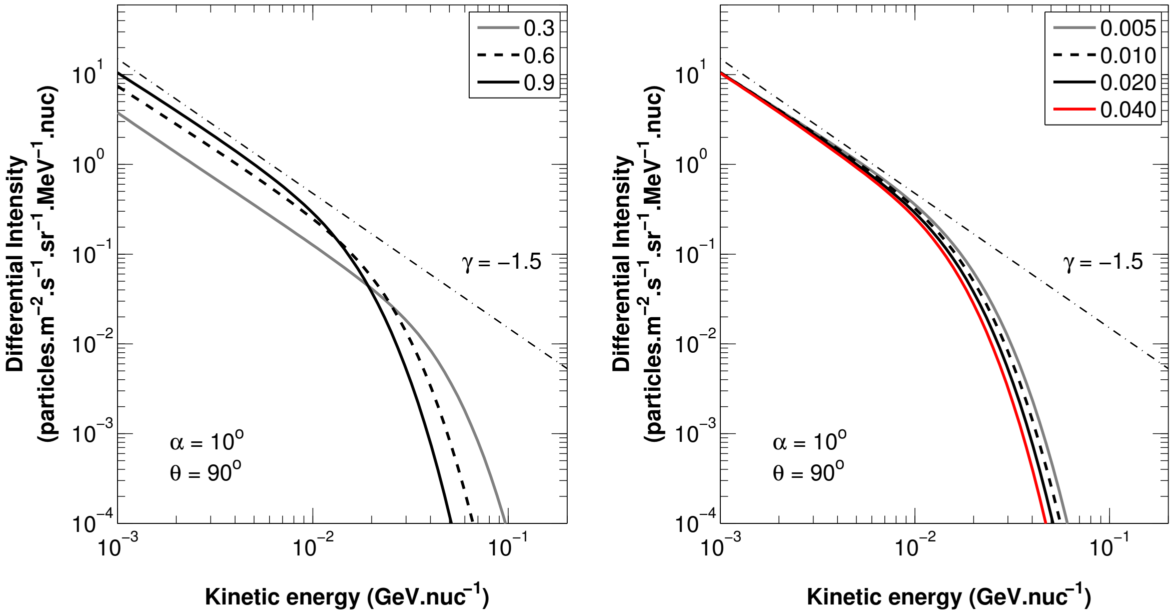

Figure 4.6: Modelled TS spectra for ACR Oxygen for varying values of $\kappa_{||}$ (left panel) and $\kappa_{\perp\theta}$ (right panel), with legend values corresponding to $\kappa_{||,0}$ and κ_e^0 respectively. Here $\kappa_{||,0} = 0.9$ and $\kappa_e^0 = 0.02$ serve as reference solutions, with the predicted power law indicated with a dash-dotted line. Because $\kappa_{\perp r/\theta} \propto \kappa_{||}$, the effects of varying $\kappa_{||}$ as shown in the left panel also implicitly reflect the effects of changing the perpendicular coefficients. CR drifts remain disabled ($\kappa_{D,0} = 0$).

latter two factors. The acceleration time mentioned in Section 4.3 and given by Eq. 3.56 has a lower limit [as shown by *Jokipii*, 1992] of

$$\tau_{\mathrm{acc}} \sim \frac{3s\kappa_{rr}}{V_{sw}^2(s-1)}, \tag{4.4}$$

for a quasi-parallel shock, assuming Bohm diffusion, with κ_{rr} evaluated at r_{TS} and where V_{sw} denotes the solar wind speed. It therefore takes longer to establish the accelerated power-law distribution up to E_{cut} if the effective radial diffusion at the shock is large. When E_{cut} is attained, no added amount of time will allow the spectrum to extend to higher energies [e.g. *Potgieter and Moraal*, 1988]. Its extent then becomes subject to particle losses due to the curvature (or finite dimensions) of the TS, so that the ACR cut-off occurs when the diffusion length scale, κ_{rr}/V_{sw}, becomes comparable to the shock radius (see Section 3.6.2). Assuming that both κ_{rr} and V_{sw} are compressed by a factor s across the TS [e.g. *Steenberg and Moraal*, 1999], this is typically when

$$\frac{\kappa_{rr}}{V_{sw}} \sim 2r_{TS}, \tag{4.5}$$

as reduced from Eq. 3.55. Since diffusion coefficients scale with rigidity, the particular rigidity P_{cut} (or equivalent energy, E_{cut}) where κ_{rr} becomes large enough to achieve the relation in Eq. 4.5 is where the accelerated power-law distribution ultimately terminates. Particles with kinetic energies exceeding this cut-off no longer experience the shock as planar and escape, hence causing the exponential decrease that succeeds the cut-off.

Before illustrating the effects of varying κ_{rr}, consider first its constituents. Recall that the spiral angle, ψ, essentially measures the angular separation of magnetic field lines from the effective radial direction, $\hat{e}_{\vec{r}}$, and that these field lines become increasingly perpendicular to $\hat{e}_{\vec{r}}$ as one moves out to larger radial distances near the equatorial plane. Therefore, at the TS (at $r \gg 1$ AU) it follows that $\psi \rightarrow 90°$ for $\theta \approx 90°$, so that Eq. 4.2 reduces to $\kappa_{rr} \approx \kappa_{\perp r}$. This makes physical sense, since CRs diffusing along magnetic field lines would have to travel great distances along the Parker spiral to be removed an appreciable radial distance from the TS. Note however that this changes toward the polar regions for a Parker HMF, since Eq. 4.2 reduces to $\kappa_{rr} \approx \kappa_{||}$ when $\psi \rightarrow 0°$. When studying the TS spectrum at low heliographic latitudes though, varying $\kappa_{\perp r}$ is sufficient to illustrate the effects of varying the effective radial diffusion. Figure 4.5 demonstrates these effects, showing that smaller values of the scaling factor ($\kappa_{\perp r,0}$) shifts the ACR cut-off to higher energies. This follows because scaling $\kappa_{\perp r}$ downwards necessitates higher energies in order for the relation in Eq. 4.5 to be achieved. Note also that the modelled spectra fall well below the power law in Figure 4.5 for lower values of $\kappa_{\perp r,0}$, though still parallel to it at high energies. A possible explanation for this is offered in Section 4.7. Another interesting result is that varying $\kappa_{||,0}$, as shown in the left-hand side of Figure 4.6, yields effects that are similar to that in Figure 4.5. One would expect that since the contribution of parallel diffusion in Eq. 4.2 is diminished at the TS, the effects would be smaller. However, recall from Section 3.3 that both $\kappa_{\perp r}$ and $\kappa_{\perp \theta}$ scale as $\kappa_{||}$, so that these effects are essentially a combination of varied radial and polar perpendicular diffusion. It is thus well worth noting that any changes made to $\kappa_{||}$ in this study are carried through to other modes of diffusion as well.

4.4.2 Polar diffusion

It was already mentioned in the introduction to this section that varying diffusion along the polar direction, along which the TS also extends, would yield marginal effects in terms of particle acceleration. This is supported in the right-hand side of Figure 4.6. Here $\kappa_{\perp \theta}$ is varied by changing the value of κ_e^0 in Eq. 3.28. Note that for this section diffusion is not necessarily isotropic, since $\kappa_e^0 \neq \kappa_{\perp r,0} \implies \kappa_{\perp r} \neq \kappa_{\perp \theta}$. Qualitatively, varying $\kappa_{\perp \theta}$ produces similar effects to varying $\kappa_{\perp r}$, with the ACR cut-off shifting to higher energies for smaller diffusion, although marginally. Note also, that by virtue of the effects illustrated above and the enhancement of polar diffusion at high latitudes, the energies attained through acceleration would be generally lower away from the equatorial plane. See *Potgieter* [1996, 2000] and *Heber and Potgieter* [2006] for reviews on CR modulation at high latitudes.

It appears that with all of the above taken into account, $\kappa_{\perp r}$ governs the most effective transport away from the TS, and that limiting this parameter contributes a great deal toward particle confinement and improving the acceleration efficiency. It also follows from this section as a general consequence that lower diffusion results in acceleration to higher energies.

4.5 The Effects of Cosmic-ray Drifts

Recall from previous sections the intensity enhancement pointed out in e.g. Figures 4.1 and 4.4 within the energy range preceding the ACR cut-off, that is, between roughly 1 and 10 MeV. nuc^{-1}. This enhancement is visible as a slight upward bulge for the A < 0 epoch, where it deviates from the power law predicted for the TS spectrum. For the A > 0 polarity, this deviation

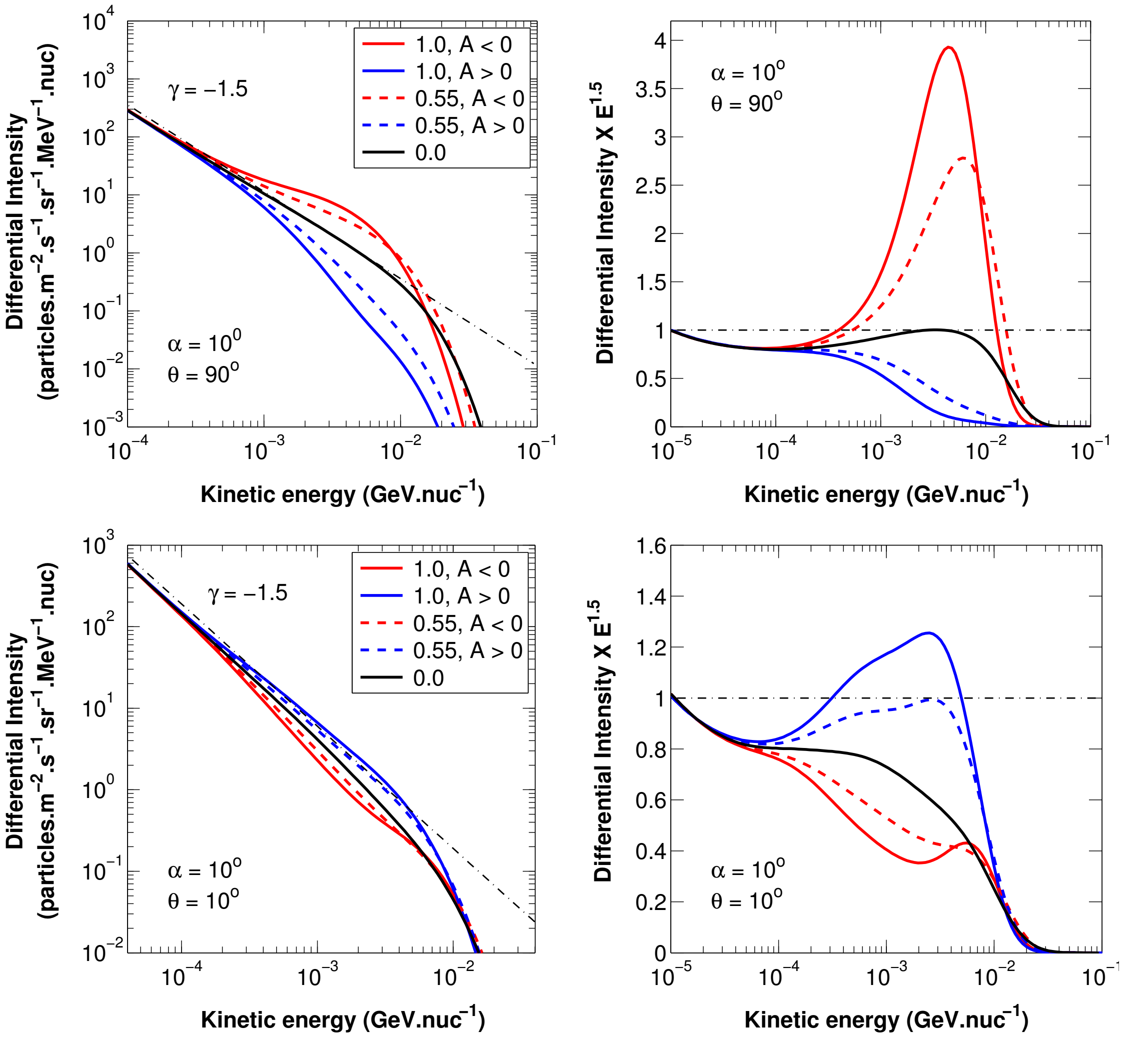

Figure 4.7: On the left, modelled ACR Oxygen spectra are shown at the TS for the equatorial plane (top panel) and polar regions (bottom panel) at $\theta = 90^\circ$ and 10° respectively. The solutions are shown for various levels of drift efficiency ($\kappa_{D,0}$) for both polarities as indicated in the legend. The dashed-dotted line represents the predicted power law with spectral index as labelled. The solutions shown on the right are the same as those on the left, but are multiplied by $E^{1.5}$ and normalised to unity at 10^{-5} GeV. nuc^{-1}. Here the power law is represented as a horizontal line along unity.

seems to be downward and much fainter. Inferring from the fact that the effect varies with magnetic polarity, it is reasonable to expect that drifts are involved.

It is unlikely though that CR drifts are the only cause of this enhancement, because under particular conditions it is also observed in no-drift solutions [see *Potgieter and Moraal*, 1988; *Florinski and Jokipii*, 2003]. It does however seem to be a physical effect rather than a numerical artefact, since this same feature had appeared in previous modulation studies on ACRs using different modelling approaches, e.g. *Potgieter and Moraal* [1988], *Steenkamp* [1995], *le Roux et al.* [1996], *Steenberg and Moraal* [1996] and *Florinski and Jokipii* [2003]. Indeed, there are a number of mechanisms capable of influencing the form of the TS spectrum in this fashion. These not only include current sheet and TS drifts [*Kota and Jokipii*, 1994], but also CR-modified shocks [*le Roux and Fichtner*, 1997] and a (helio)latitude-dependent $\kappa_{\perp r}$ [*Langner and Potgieter*, 2008]. *Florinski and Jokipii* [2003] attributed this feature to the spherical geometry of the heliosphere, proposing that it limits the amount of phase space available to particles so as to increase the efficiency of

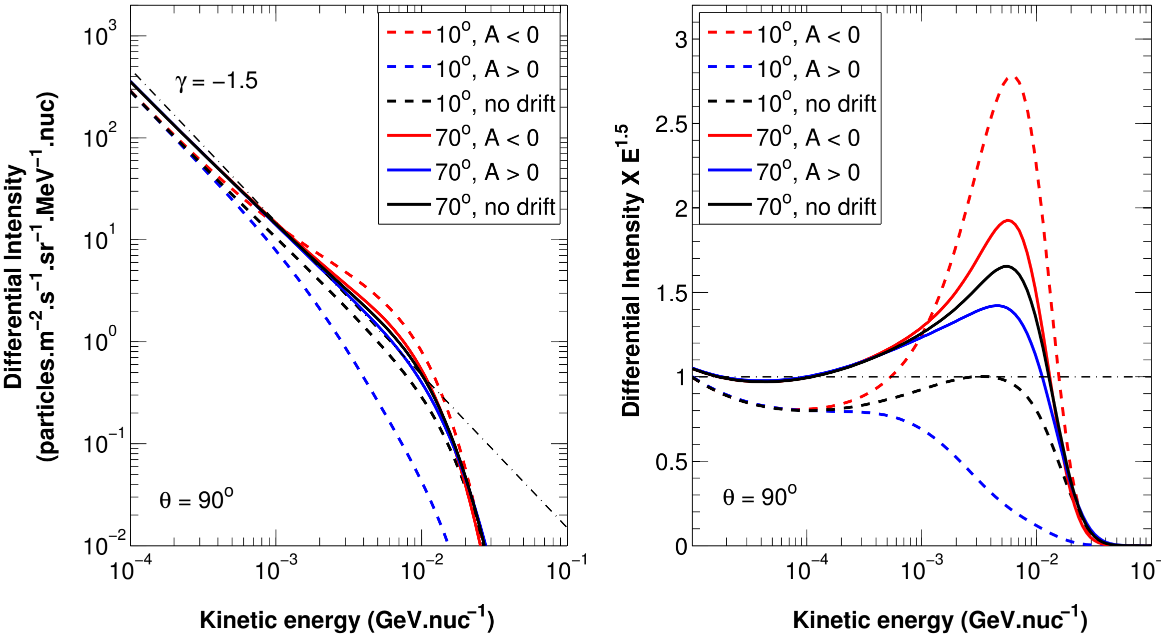

Figure 4.8: Similar to Figure 4.7, but for two different HCS tilt angles (α) as shown in the legend, and for both polarities. Recall that $\alpha = 10°$ and $\alpha = 70°$ respectively represent low and moderately high solar activity conditions. Here, drift efficiencies are taken at the reference value of 55%, except for the no-drift solutions which correspond to $\kappa_{D,0} = 0$.

their acceleration in specific energy regions. However the root cause of this enhancement, if assumed not to be a combination of various processes, remains less obvious, the effects of drift on its prominence are evident.

Figure 4.7 demonstrates the deviation of the modelled TS spectra from the predicted power law for different drift efficiencies during each polarity cycle. These effects are accentuated in the right-hand side of the figure, where the scale is chosen such that protrusions above and below unity respectively signify the hardening or softening of the spectrum from the original power-law distribution. Note that in the equatorial plane, intensity enhancements emerge for A < 0 and intensity depressions for A > 0. Also note the opposite of this effect near the poles. This is explained as a consequence of global CR drift patterns: For A < 0, ACRs produced at the TS near the equatorial plane are unable to escape downstream due to inward drifts along the HCS in the heliosheath. The particles are thus confined and may be injected into the shock repeatedly until they become energetic enough and escape. These intensities are bolstered further, because particles drift along the TS from the polar regions to the equator. For A > 0, on the other hand, these drift patterns are reversed: positive particles drift outward along the HCS and upward along the TS to the poles so that intensities are enhanced at high latitudes. See also the interpretation by *Kota and Jokipii* [1994]. From Figure 4.7, the intensity enhancements and depressions at the poles appear much less pronounced than at the equator. This is likely because HCS drifts are absent from the poles, so that fewer particles are carried to and from the TS in the polar regions as compared to near the equator. This may also be, in part, due to the assumption of enhanced polar diffusion at high latitudes, since it is expected that larger scales of diffusion reduce acceleration efficiency (See Section 4.4).

The prominence of drift effects is also coupled to solar activity. Figure 4.7 is shown for solar minimum conditions, during which the HCS has an inclination from the equator of only 10°, is only marginally wavy, and drifts along this interface are well-defined. As the cycle progresses toward maximum activity conditions, the tilt angle increases and drift effects diminish near the equatorial plane due to an ill-defined HCS structure. Figure 4.8 demonstrates this, showing that for $\alpha = 70^\circ$ the TS spectrum at ~ 6 MeV. nuc^{-1} is only a factor of roughly 1.5 higher for the A < 0 cycle than for A > 0, in contrast to a factor of at least 10 for $\alpha = 10^\circ$. Intriguingly, all of the solutions for solar maximum conditions, including the no-drift solutions, display the intensity enhancement discussed above. This reinforces the notion expressed earlier that CR drifts, subject to magnetic polarity, serve either to obscure or emphasise this enhancement, while it likely arises due to other mechanisms as well. Note that the no-drift solutions for the two tilt angles shown in Figure 4.8 do not coincide. This follows because the scaling factors in the perpendicular diffusion coefficients of Section 3.3.3 are scaled with tilt angle to increase toward maximum solar activity. For recent reviews on drift effects, see *Potgieter* [2013, 2014b].

While the identification of the mechanism responsible for the intensity enhancement still warrants further investigation, the visibility of this enhancement is shown to be drift-dependent. Thereby it is implied that its appearance is also subject to change with solar activity and the magnetic polarity cycle.

4.6 A Latitude-dependent Termination Shock

It emerged from a study by *Scherer et al.* [2006] using HD modelling [*Scherer and Ferreira*, 2005] that both the compression ratio and the ACR injection efficiency harbour a latitudinal dependence, by which these quantities assume their largest values at the equatorial plane and decline toward higher latitudes for solar-quiet conditions. These dependencies are substantiated firstly in that the TS is perpendicular in the equatorial nose region of the heliosphere, and becomes increasingly oblique toward the poles. Secondly, the fast SW streams emanating from coronal holes on the sun during solar minimum conditions, give rise to lower solar wind densities at high latitudes. This is thought to result in diminished SW compression and lowered efficiency of PUI injection at the TS. These effects were incorporated into modulation models by e.g. *Langner and Potgieter* [2006] and *Ngobeni and Potgieter* [2008], and revisited by *Strauss* [2010] and *Ngobeni* [2015]. What follows here is a review of their findings.

4.6.1 The compression ratio

The insights gathered from HD models informed *Ngobeni* [2006] to model a function for the compression ratio that varies with the polar angle θ as follows:

$$s(\theta) = s_{\min} + \frac{s_{\max} - s_{\min}}{1 + \exp\left[\left(\theta_c - \theta\right)/\theta_b\right]}, \tag{4.6}$$

with $s_{\max} = s(90^\circ)$, $s_{\min} = s(0^\circ)$, θ_c the polar angle about which the transition from $s_{\max}$ to $s_{\min}$ is centred and θ_b controlling the steepness of the transition. In this study, the observation-constrained parameter set of *Strauss* [2010] is implemented, so that $s_{\max} = 2.5$, $s_{\min} = 1.5$,

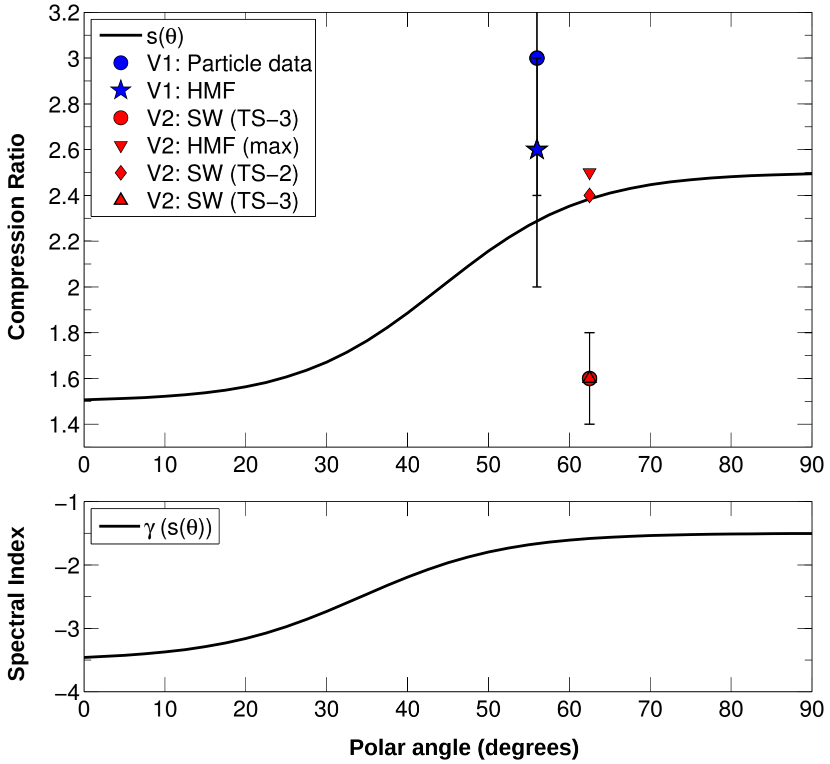

Figure 4.9: A latitude-dependent compression ratio (top panel) with Voyager measurements during TS encounters (Table 4.1), and the corresponding spectral indices of the power laws expected from DSA theory for a 1-D planar shock (bottom panel).

$\theta_c = 45°$ and $\theta_b = 9°$. The corresponding latitude-dependent expression for the spectral indices of the power laws expected for the compression ratios determined by Eq. 4.6, is given by

$$\gamma(\theta) = \frac{s(\theta) + 2}{2 - 2s(\theta)}. \tag{4.7}$$

Figure 4.9 shows $s(\theta)$ and $\gamma(\theta)$ as functions of θ, along with the Voyager measurements listed in Table 4.1. Note that the minimum and maximum values of $s(\theta)$ respectively correspond to spectral indices of $\gamma_{\text{min}} = -3.5$ and $\gamma_{\text{max}} = -1.5$.

Of course, varying the compression ratio in this manner holds implications for the SW flow speed in the heliosheath. Figure 4.10 shows the SW speed in a meridional cross section of the heliosphere for solar minimum conditions, and compares the effects of SW compression varying with latitude with that of a fixed compression ratio at the TS. While the flow in the heliosheath remains unchanged near the equator, the fast SW streams near the poles decrease by a smaller ratio (i.e. 1.5 as opposed to 2.5) across the TS. This results in a SW speed in the heliosheath of ~ 500 km.s^{-1}. It is not unlikely, depending on the local plasma properties, that this flow is still supersonic, or indeed that the SW speed beyond the TS at high latitudes may be supersonic in general. This follows from Voyager 2 measurements confirming supersonic SW flow in the heliosheath [*Li et al.*, 2008; *Chalov and Fahr*, 2011]. Contrarily, Voyager 1 reports much slower SW flow along its trajectory [*Richardson and Burlaga*, 2013]. Of course, if the SW speed in the heliosheath remains fast, it would have run-on effects on all parameters dependent on it as well, e.g. the HMF magnitude.

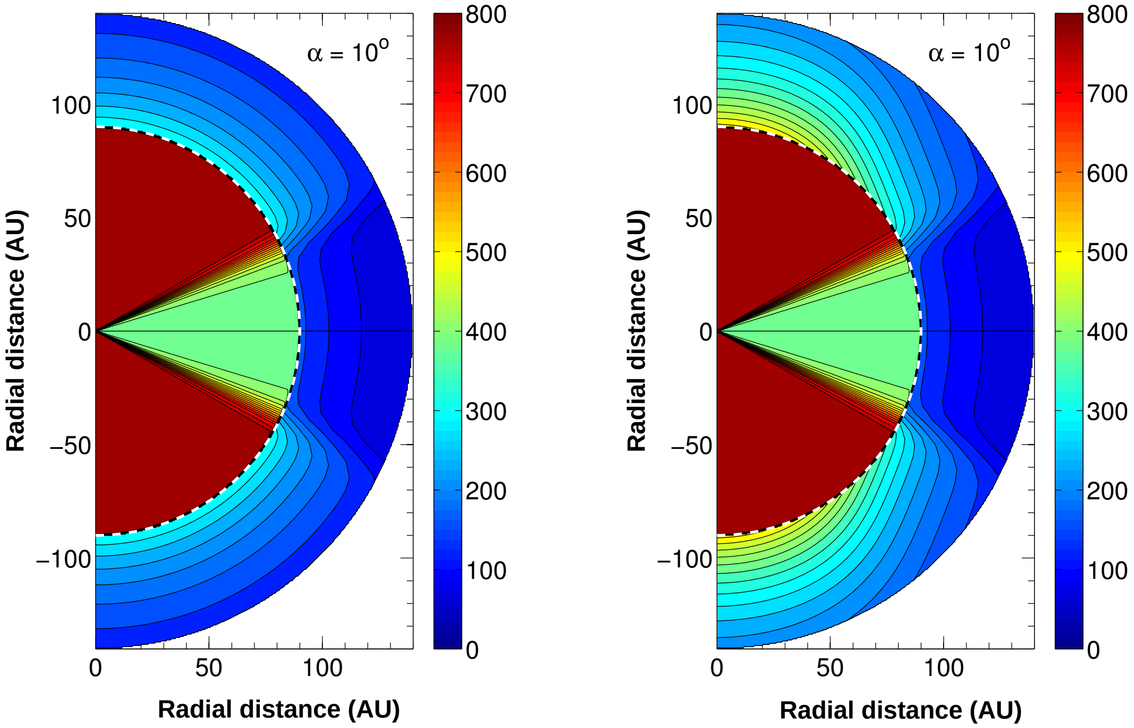

Figure 4.10: Contour plots illustrating the SW speed V_{sw} (according to the scale in the colour bar with units km. s^{-1}) in the meridional cross section of the heliosphere for solar minimum conditions ($\alpha = 10°$). A fixed compression ratio was assumed in the left panel (i.e. $s(\forall\theta) = 2.5$) while it is varied on the right with latitude according to Eq. 4.6. Recall that incompressible flow is assumed for the heliosheath. The TS is shown as a dashed white halfcircle at 90 AU, with the Sun at the origin.

Aside from consequences for heliosheath plasmas however, CR transport is also affected by a varying compression ratio. Plotting the modelled TS spectra for ACR Oxygen at selected polar angles, as illustrated in Figure 4.11, shows harder power laws near the equatorial plane, while the spectra become softer toward the poles. These solutions are shown for both magnetic polarities. As expected, the spectrum at $\theta = 90°$ is similar to the spectrum displayed in Figure 4.4 for a fixed, global compression ratio of $s = 2.5$. This is however not the case for higher latitudes, e.g. $\theta = 10°$, where Figure 4.11 shows a pronounced intensity enhancement developing at energies ranging from roughly 0.1 to 10 MeV. nuc^{-1}, which is not visible for the equivalent $s = 1.5$ spectrum in Figure 4.4. This enhancement is therefore a consequence of a latitude-dependent compression ratio, and arises due to the poleward migration of ACRs produced in the equatorial regions. This migration happens mainly by polar diffusion, especially considering the enhancement included in Eq. 3.27 for high latitudes, but also by drifts along the TS while A > 0. Indeed, since the intensities at $\theta = 10°$ in this enhancement region are higher by a factor of ~ 10 for A > 0 than for A < 0, drifts during the former polarity cycle facilitate the poleward migration while drifts during the latter act to inhibit it. These drift patterns are illustrated for both polarities, with $s = s(\theta)$, using contour plots in Figure 4.12, and are consistent with the patterns described in Section 4.5.

Figure 4.12 also shows that implementing a latitude-dependent compression ratio generally lowers the global ACR Oxygen intensities from what is observed when $s(\forall\theta) = 2.5$ (compare with e.g. Figure 4.3). Since fewer ACRs are produced near the polar regions, as is also visible from the flattened contours for the A < 0 cycle, large latitudinal gradients are observed. What

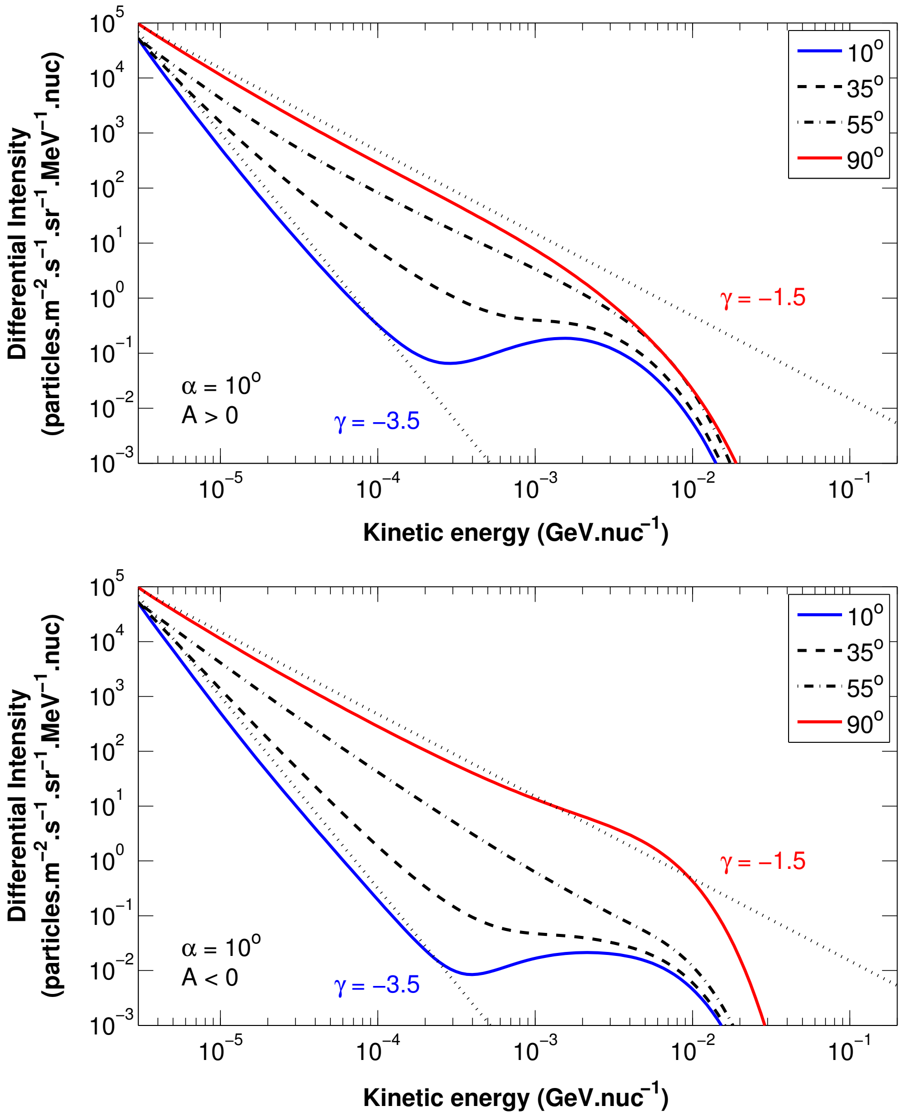

Figure 4.11: Modelled ACR Oxygen TS spectra at varying polar angles (as shown in the figure legend) with a latitudinal-dependent compression ratio for both the A $>$ 0 (top panel) and A $<$ 0 (bottom panel) magnetic polarities. The expected power laws (dotted lines) and their spectral indices are shown for the maximum and minimum compression ratios at $\theta = 90°$ and $\theta = 10°$ respectively

emerges is a region of preferred acceleration near the equatorial nose region, and from Figure 4.12, at the interface where the TS meets the HCS during the A $>$ 0 cycle. Similar results are reported by *Strauss* [2010], although with the inclusion of a latitude-dependent injection efficiency as well (see Section 4.6.2). Consensus had however not yet been reached on where the predominant region for acceleration at the TS resides. Early studies [*Jokipii*, 1986] suggest, in stark contrast to the above, that ACRs are accelerated chiefly at the poles, while the model by *McComas and Schwadron* [2006] favours the flanks of the heliosphere.

While this latitude-dependent compression ratio is well-substantiated and was shown to have yielded satisfactory results when modelling ACR intensities [*Strauss*, 2010], it also makes the model increasingly layered if implemented. To study the effects of individual processes and parameters, a fixed compression ratio is assumed in the following chapters, especially since these chapters are more concerned with the study of electrons at a single latitude along the Voyager 1 trajectory, where estimates for the compression ratio are available.

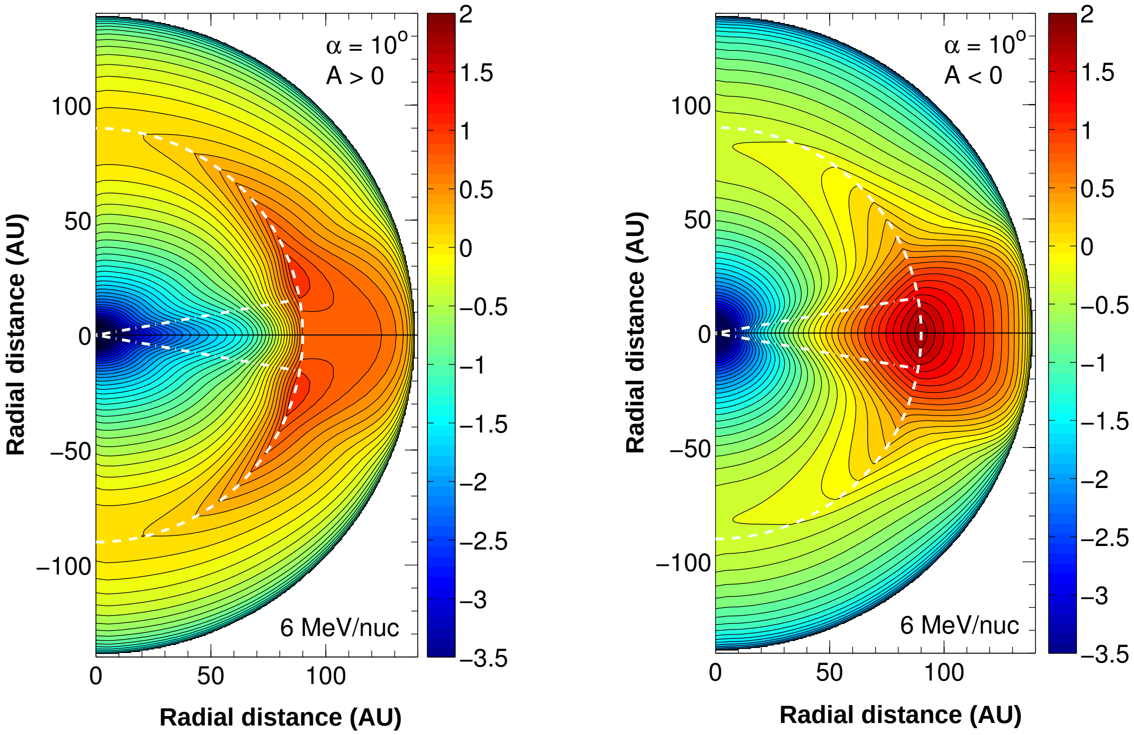

Figure 4.12: Contour plots illustrating 6 MeV. nuc^{-1} ACR Oxygen intensities in the meridional plane of the heliosphere, for A $>$ 0 (left) and A $<$ 0 (right) polarities and a latitude-dependent compression ratio. The colour bar shows intensities as percentages of the maximum on a logarithmic scale. The dashed white halfcircle indicates the TS position (at 90 AU), while the dash-dotted white lines indicate the polar extent of the HCS for $\alpha = 10^{\circ}$. The Sun is located at the origin.

4.6.2 The pick-up ion source strength

Since the quantitative details of the PUI seed population, from which ACRs arise, are not generally known, the intensity of the PUI source function is chosen arbitrarily and the accelerated solutions are normalised to observations (or on some generally approved reference value). Studies have been conducted from which the spatial distribution of PUIs and their rate of injection at the TS are inferred. These include those by e.g. *Fahr et al.* [2008] and *Scherer and Fahr* [2009], which confirm a longitudinal dependence of the PUI injection efficiency and predict a maximum injection rate at the cross-wind (or flank) regions of the heliosphere. Earlier work by *Scherer et al.* [2006] had also found a latitudinal dependence for PUI injection. This was consequently modelled by *Ngobeni* [2006] by specifying the source strength, denoted as $I(\theta)$, in the expression for the PUI source function. That is,

$$Q(\theta) = Q^{*}\, I(\theta)\, \delta\left(\frac{r - r_{TS}}{r_0}\right)\, \delta\left(\frac{P - P_{\min}}{P_0}\right), \tag{4.8}$$

which is just a modified form of Eq. 3.51. The source strength acts as a scaling constant that varies with polar angle, similar to Eq. 4.6, as follows:

$$I(\theta) = I_{\min} + \frac{I_{\max} - I_{\min}}{1 + \exp\left[(\theta_c - \theta)/\theta_b\right]}, \tag{4.9}$$

with θ_c and θ_b as previously defined, $I_{\max} = I(90^{\circ}) = 1.0$, and $I_{\min} = I(0^{\circ}) = 0.1$.

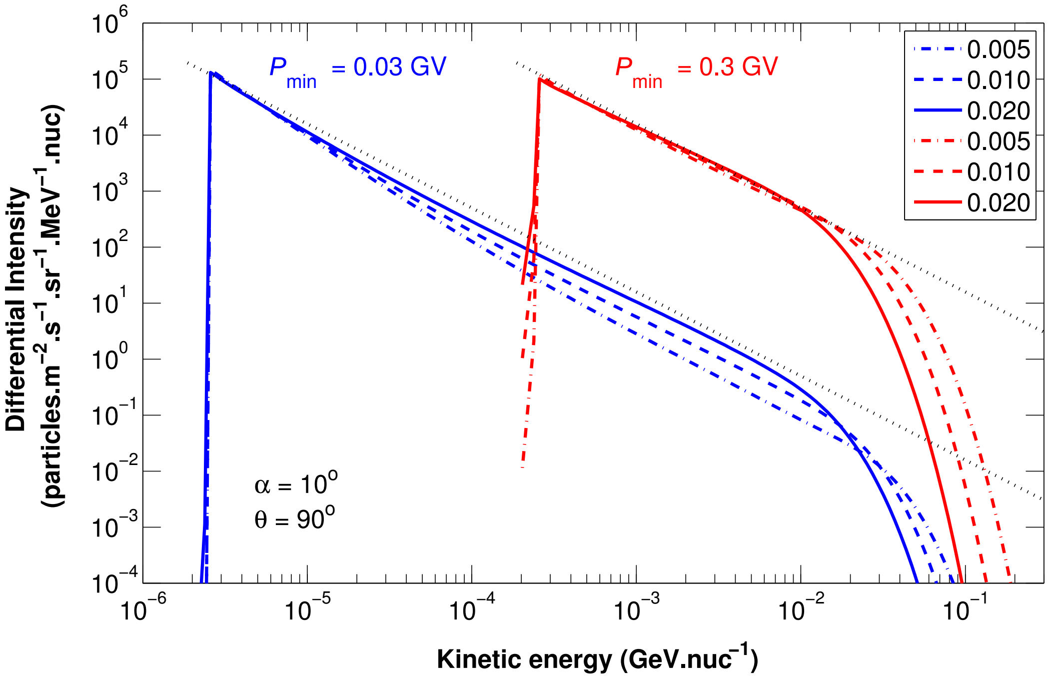

Figure 4.13: Modelled TS spectra for ACR Oxygen in the equatorial plane for varying values of $\kappa_{\perp r,0}$ and source functions representing the PUI seed population injected at $P_{\mathrm{min}} = 0.03$ GV (in blue) and $P_{\mathrm{min}} = 0.3$ GV (in red) respectively. Here, drifts are disabled ($\kappa_{D,0} = 0$), and the expected power laws (with $\gamma = -1.5$ for $s = 2.5$) for each set of solutions indicated with dotted lines.

Physically, this means that all the PUIs injected at the TS in the equatorial plane are accelerated to ACRs, while ten times less are injected at the poles. *Strauss* [2010] reports that this generally results in solutions that are a factor of $\sim I(\theta)$ lower than those shown in Figure 4.11, with slight spectral changes occurring at high energies due to a modified intensity gradient, ∇f. For similar reasons to that stated for refraining from the use of the latitude-dependent compression ratio, the injection efficiency is considered fixed for all polar angles in subsequent chapters.

4.7 Low-energy Features of the ACR Spectrum

In the following discussion, several aspects from previous sections resurface. Firstly, recall from Section 4.3 that the predominant form of the accelerated TS spectrum is predicted to be a power law with spectral index as given by Eq. 4.1. Furthermore, it is gathered from the discussion on the findings of *Arthur and le Roux* [2013] in Section 4.3, that particles with MFPs smaller than the length scale of the TS precursor will experience a smaller effective compression ratio. This is shown in the following discussion to have bearing on the deviations from the expected power law for lower diffusion coefficients, which are pointed out in Section 4.4 and illustrated in e.g. Figure 4.5. While it has been reported that the form of accelerated TS spectra is independent of the energy at which the PUI source function is injected [*Steenkamp*, 1995; *Steenberg and Moraal*, 1999], it is shown here that under certain conditions the value of this injection energy becomes significant.

Figure 4.13 shows two sets of ACR Oxygen TS spectra for varying values of $\kappa_{\perp r}$, with the PUI source function respectively injected at rigidities of $P_{\mathrm{min}} = 0.03$ GV ($\equiv E = 1.9$ keV. nuc^{-1})

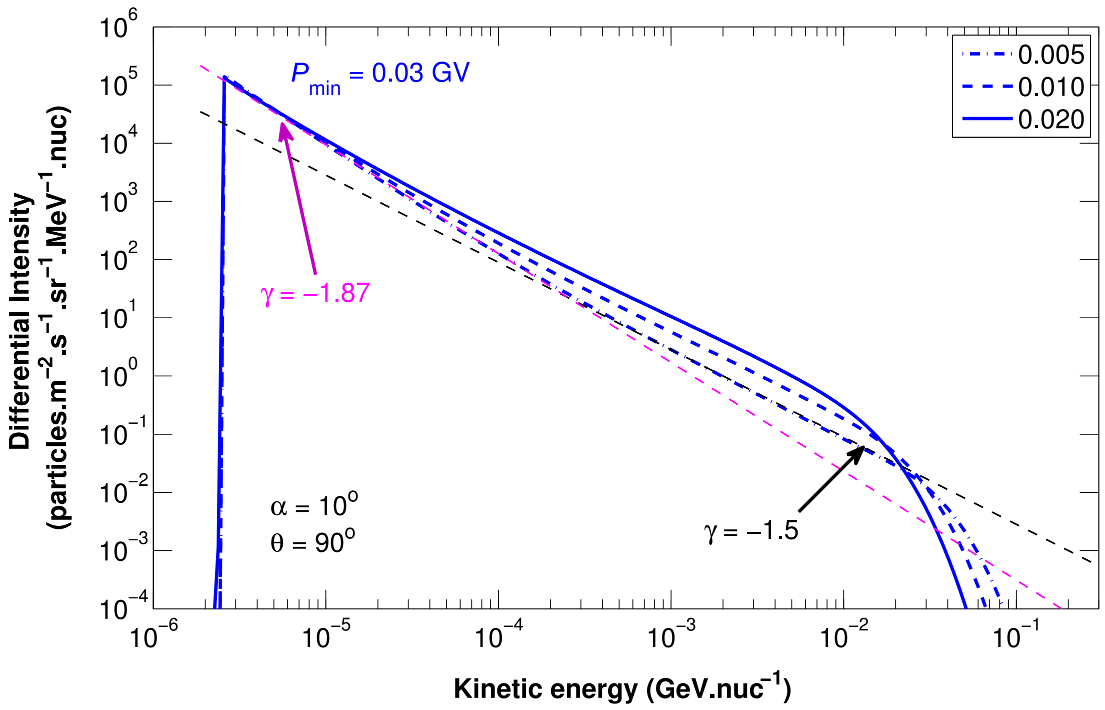

Figure 4.14: Similar to Figure 4.13, but with only the solutions with $P_{\min} = 0.03$ GV shown. Also illustrated here are the two power laws with $\gamma = -1.87$ and $\gamma = -1.5$ fitted to the $\kappa_{\perp r,0} = 0.005$ spectrum respectively below and above $\sim$ 0.3 MeV. nuc^{-1}.

and $P_{\min} = 0.3$ GV ($\equiv E = 190$ keV. nuc^{-1}). Note that the deviations from the power law are pronounced for the lower injection energy (similar to Figure 4.5), but suppressed for the higher-energy injection. The latter solutions thus display accelerated spectra following a power law with $\gamma = -1.5$ as expected for $s = 2.5$, while the former appear not to. It is necessary to comment though that an injection energy of 190 keV exceeds what may reasonably be expected from PUIs, since their maximum energies are predicted to be no more than four times the energy of SW ions [*Moebius et al.*, 1988], i.e. $\sim$ 6 to 40 keV. These solutions are presented though merely as a case for comparison. At any rate, the solutions with the more realistic lower injection energy do not immediately follow the expected -1.15 power law at low energies. Upon closer inspection however, the lowered intensities turn out not to be mere deviations from the expected power law, but a structured consequence of the effective compression ratio observed by low-energy particles.

Figure 4.14 reveals that toward high energies TS spectra for all diffusion levels are parallel to the expected power law, albeit at a lower intensity. Below $\sim$ 0.3 MeV. nuc^{-1} the spectra become softer. The bottommost spectrum, for instance, with $\kappa_{\perp r,0} = 0.005$, displays a power law with $\gamma \sim -1.87$. This spectral index corresponds to a SW compression at the TS of $s = 2.1$, which implies that if $V_2 = 0.4V$, the maximum SW flow speed observed by ACRs in this energy region is $2.1 \cdot V_2 = 0.84V$, with V_2 and $V = 400$ km.s^{-1} respectively representing the downstream and unshocked upstream SW speeds. One may infer from either Figure 3.11 or 4.16 that $V_{sw} = 0.84V^*$ is attained within the precursor structure at $r \sim 89.8$ AU, i.e. 0.2 AU from the (sub)shock. One thus expects that particles with diffusion length scales at the TS of roughly less than 0.2 AU will experience an effective compression ratio of no more than $s = 2.1$. Indeed, such length scales correspond to energies lower than $\sim$ 0.3 MeV. nuc^{-1}, as indicated in Figure

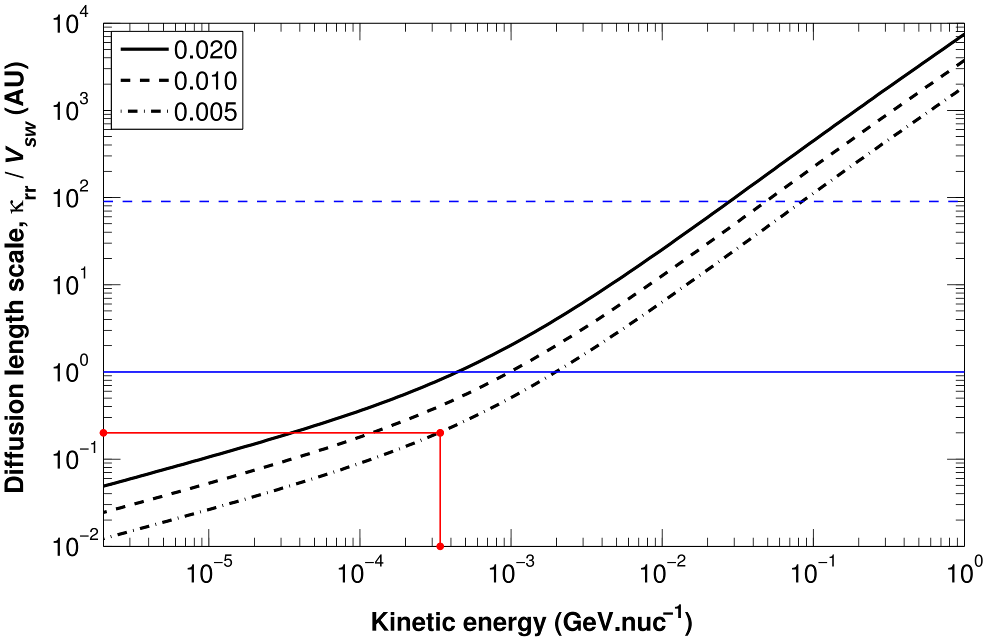

Figure 4.15: The diffusion length scale (κ_{rr}/V_{sw}) of ACR Oxygen at the TS (90 AU, $\theta = 90°$) as function of kinetic energy for varying values of $\kappa_{\perp r,0}$ as shown in the legend. Here $\kappa_{rr}/V_{sw} = (\kappa_{rr}/V_{sw})^- + (\kappa_{rr}/V_{sw})^+$ where the superscripts $-$ and $+$ respectively denote up- and downstream values as introduced in Section 2.6.1. The red lines indicate the length scale observed for the energy at which the power laws indicated in Figure 4.14 intersect. The solid and dashed horizontal blue lines respectively represent the width of the TS precursor and the length scale at which the ACR cut-off is expected to occur.

4.15, which is also roughly where the transition between the power laws shown in Figure 4.14 occurs. Above this energy, length scales increase so as to eventually exceed 1 AU (the width of the modelled TS-precursor structure) and particles experience the full compression ratio of $s = 2.5$. This explains why the solutions injected above this energy in Figure 4.13 follow the expected $\gamma = -1.5$ power law. A lower limit on the compression ratio also exists: Since the SW speed decreases discontinuously across the subshock with a factor of $s = 0.7V^*/0.4V^* = 1.75$, the softest spectral index one might expect is $\gamma = -2.5$. A more refined study of these features may therefore include fitting TS spectra with multiple power laws corresponding to the range of $s = 1.75 \rightarrow 2.5$ constrained above.

The above analysis demonstrates that should a precursor as shown in e.g. Figure 4.16 be present, CRs with small diffusion length scales, typically at low energies, will experience only a fraction of the total compression ratio and be accelerated accordingly. Similar effects are reported by *Kruells and Achterberg* [1994]. Should the precursor be widened as in Figure 4.16, and the energy gains from SW compression hence distributed over a larger interval, the TS spectrum will only display the expected power-law structure at larger energies, i.e from $\sim$ 10 MeV. nuc^{-1} for a precursor width of 2.0 AU. However, if the precursor is diminished, Figure 4.16 shows that the expected power law is already obtained at lower energies, although obscured by the intensity enhancement seen in earlier sections preceding the cut-off. It is therefore the expectation that should the precursor width tend toward zero so as to obtain a fully discontinuous shock, no deviations from the theoretically expected power law will be visible. Indeed, studies where a TS precursor is absent [*Potgieter and Moraal*, 1988; *Steenkamp*, 1995; *Steenberg*

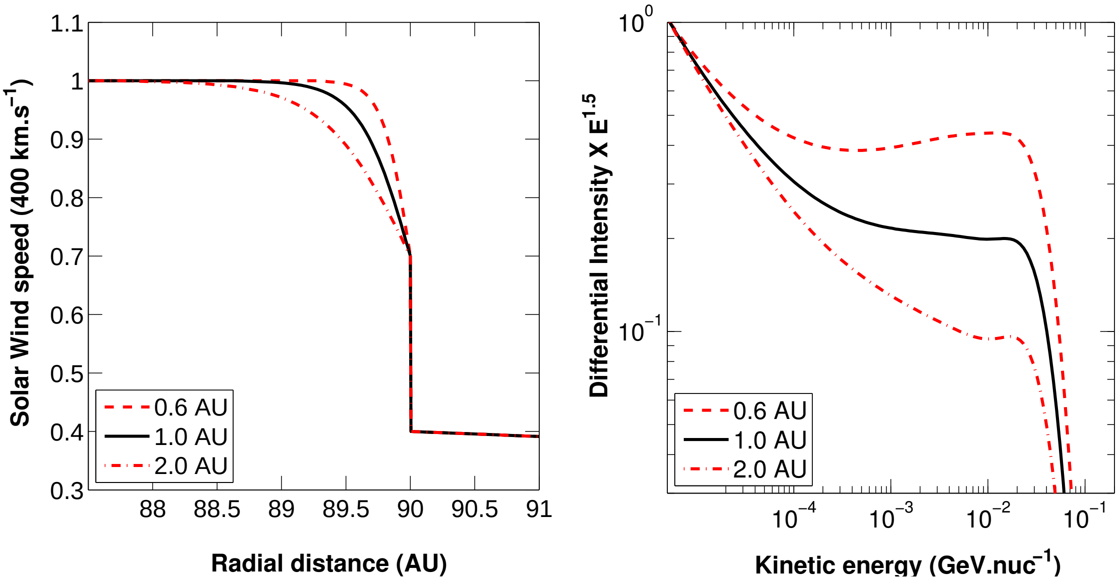

Figure 4.16: The radial profile of the SW speed in the TS region is shown on the left for varying precursor widths as indicated in the legend. The discontinuous jump at 90 AU represents the subshock. On the right are the modelled ACR Oxygen TS spectra for varying precursor widths corresponding to those shown on the left, with $\kappa_{\perp r,0} = 0.005$ and $\kappa_{D,0} = 0$. These solutions are multiplied by $E^{1.5}$ and normalised to unity at $0.5 \cdot 10^{-6}$ GeV. nuc^{-1}. This scale is such that flattening out of spectra to a constant value signifies alignment with the expected power law.

and Moraal, 1999] report no such deviations, and hence their solutions show no sensitivity at low energies to the choice of the injection energy either.

4.8 Summary and Conclusions

This chapter endeavoured to explore the features of the model as applied to the acceleration of ACR Oxygen at the TS. This species serves well in this purpose, since by virtue of their formation from the acceleration processes involved, the features of these processes are exhibited more explicitly. CR heating as well stochastic acceleration in the heliosheath are neglected for the purposes of this study.

From the reference solutions presented in Section 4.2, three main features are identified : The first of these is the power-law form of accelerated TS spectra. It is shown in Section 4.3 that their spectral indices may be approximated as a function of the TS compression ratio, and that larger compression ratios generally result in harder spectra at the TS. The second feature occurs where the former terminates in an exponential decrease, which occurs because high-energy CRs begin to observe the TS curvature and escape. This curvature (or ACR) cut-off is shown in Section 4.4 to shift to higher energies particularly for smaller radial diffusion, which serves to increase acceleration efficiency. In the energy region immediately preceding the cut-off of the power-law spectrum, a third feature, embodying either an intensity enhancement or depression, is observed. The prominence of this feature is illustrated in Section 4.5 to be drift-dependent and is therefore subject to change with solar activity and the magnetic polarity cycle.

Furthermore, the implications of a latitude-dependent TS, with compression ratio and injection efficiency decreasing toward high latitudes, are reviewed in Section 4.6. This is found to localise ACR acceleration at the TS to the equatorial regions of the heliosphere. These latitude dependencies are omitted from subsequent chapters to avoid excessive layering of the model and obscuring other modulation features. Finally, it emerged that assuming smaller diffusion results in deviations from the power-law form predicted by DSA theory. This is demonstrated in Section 4.7 to be a consequence of low-energy particles experiencing a smaller effective compression ratio due to their diffusion length scales being smaller than the width of the TS precursor. This results in TS spectra with softer power laws at low energies, while converging to the expected power law at higher energies. Modelled solutions tend toward their theoretically predicted form as the SW transition becomes increasingly discontinuous at the TS.

The modelling presented here is not intended to explain any ACR observations, but merely to highlight the characteristics of DSA. The insights gathered from the features of accelerated ACRs are carried forth to subsequent chapters to inform further application of the model to the re-acceleration of galactic electrons at the TS.

Chapter 5

General Modulation Features of Galactic Electrons

5.1 Introduction

The previous chapter opened the discussion on DSA by presenting numerical modelling results for the acceleration of ACR Oxygen. The current chapter aims to provide the contextual stage on which the study of DSA is set to continue in following chapters, where the model will instead be applied to simulate the transport and acceleration of galactic electrons. Unlike ACRs, GCRs originate from well beyond the heliosphere and are already distributed with energy upon arrival. Such modelling considerations, along with species-specific aspects in the treatment of electrons as opposed to ions, are taken into account in this chapter. Initial distributions are hence identified, and the major transport processes and structural characteristics of the heliosphere influencing electron intensities are explored so as to demonstrate the general modulation features of galactic electrons.

The model is firstly configured for electron transport, and solutions are shown to illustrate the main features of modulated electron energy spectra and spatial distributions that may later be used as reference. Existing input spectra are surveyed and their expansion to lower energies explored. The processes of drift and diffusion, which are considered to be predominant in electron transport, are discussed, with an especially comprehensive section devoted to investigating the rigidity profile of the latter process. This chapter, aside from aiming to produce general insights on electron modulation, presents cases for consideration in Chapter 6, where the impact of the above transport processes on the DSA of electrons will be investigated.

5.2 Configuring the Model for Electron Transport

Electrons - negatively charged, less massive and generally faster than their ionic CR counterparts - are modelled with a ratio of mass number to charge of $\Theta = 1$ and have a rest-mass energy of $e_0 = 5.11 \cdot 10^{-4}$ GeV. Indeed, much of the desired electron behaviour follows naturally in the model if the rest-mass energy is correctly specified. For example, electrons become

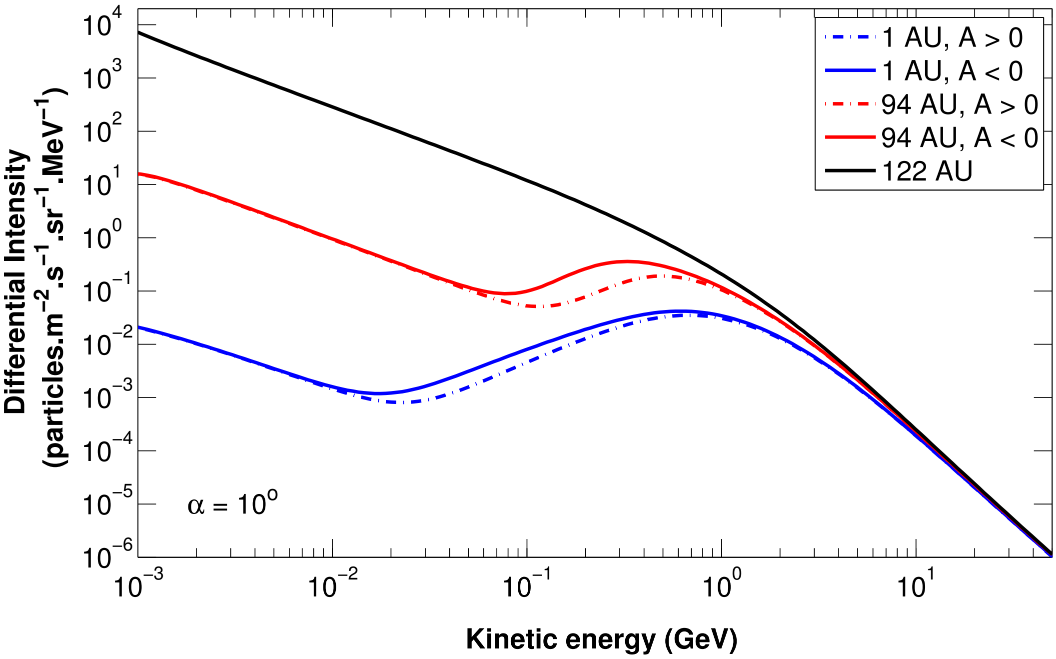

Figure 5.1: Modelled energy spectra for galactic electrons at the TS (94 AU, $\theta = 55°$) and at Earth (1 AU, $\theta = 90°$) as modulated from the reference HPS (black line) at 122 AU. Line styles and colours respectively represent the magnetic polarities and radial distances as indicated in the legend. These solutions are shown without the effects of DSA and for solar minimum conditions ($\alpha = 10°$).

relativistic with particle speeds attaining significant fractions of light speed at an energy of roughly a factor of E_0/e_0 lower than for nuclei (Figure 3.2), with E_0 the rest-mass energy for protons. These same attributes result in electrons having smaller radii of gyration than other heavier CR species at most energies, while displaying the same gyroradius and length scales of drift as protons at $E > E_0$; see Figure 3.9. Their negative charge naturally implies that the drift patterns expected for positive particles are reversed for electrons during both solar polarity cycles. Furthermore, the relationship between a particle's kinetic energy and its rigidity is also shown in Figure 3.1 to differ above and below the rest-mass energy, which is demonstrated in Section 3.6.2 to affect the form of accelerated energy spectra. This is further explored in Section 6.2. See also *Moraal and Potgieter* [1982], *Langner and Potgieter* [2004], and *Caballero-Lopez et al.* [2010] for more on the species-specific differences that are of interest in CR modulation studies.

Further revisions to the model follow from the revelations of the Voyager 1 spacecraft, and pertains mostly to the form of electron energy spectra in the heliosheath. The measurements presented in Figure 2.18 suggest a power-law distributed energy spectrum for 4 to 40 MeV electrons at the HP, with a yet steeper distribution following at $E \gtrsim 1$ GeV as inferred from data collected by the PAMELA detector at Earth. The heliopause spectrum (HPS) of *Potgieter et al.* [2014b], which is discussed further in Section 5.3, displays these features and is implemented in this study as the reference input spectrum for galactic electrons. Although CRs are likely to undergo modulation in the outer heliosheath as well [*Scherer et al.*, 2011; *Strauss et al.*, 2013b; *Luo et al.*, 2015], the HP is the outermost boundary considered in the current model so that an input spectrum specified here suffices. The Voyager observations also prompt revision of the coefficients describing electron diffusion. Note from Figure 2.18 that the power-law distribution of the measured intensities is preserved at radial distances throughout most of the inner

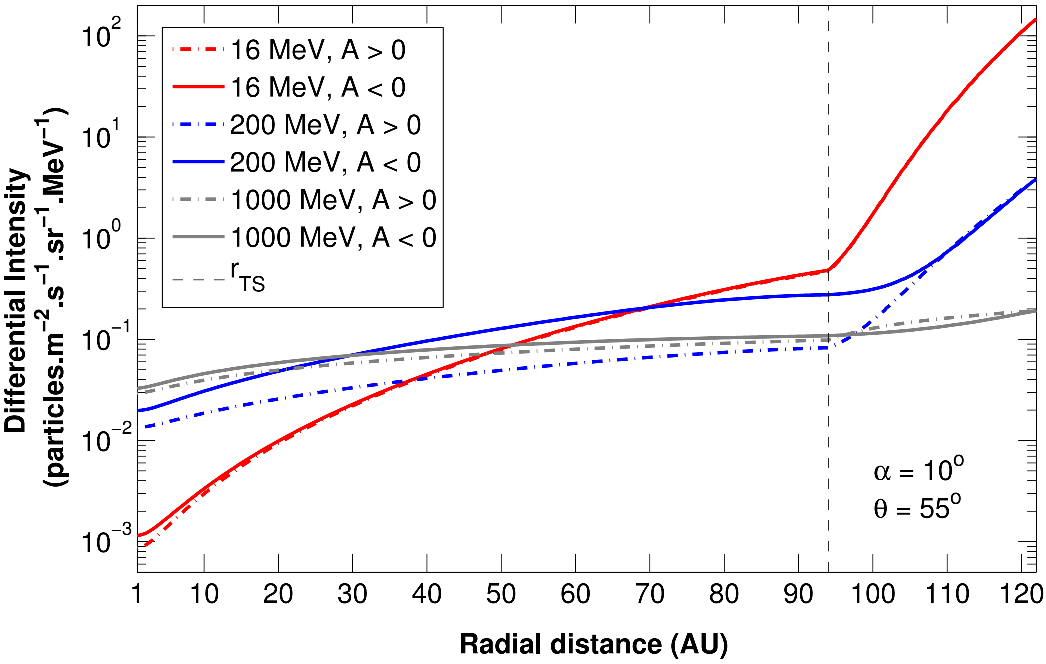

Figure 5.2: Modelled radial intensity profiles for galactic electrons at sample energies of 16 MeV, 200 MeV and 1 GeV, represented by different line colours as indicated in the legend. Solutions are shown along $\theta = 55°$ for solar minimum conditions ($\alpha = 10°$) and both magnetic polarities as also indicated in the legend. The position of the TS is marked with the vertical dashed line at 94 AU and the HP is situated at 122 AU.

heliosheath, which suggests rigidity-independent diffusion across the energy range where this occurs [see also *Potgieter and Nndanganeni*, 2013a]. The intensities also decrease from the HP to the TS with a factor of a few hundred at these energies. To model these features, the use of the parallel diffusion coefficient by *Burger et al.* [2008] is discontinued in favour of the phenomenologically informed coefficient described by Eqs. 3.23 to 3.25. The full motivation for this is discussed in Section 3.3.2. The perpendicular diffusion coefficients of *Burger et al.* [2000] are however still implemented, but are adapted to retain the rigidity dependence of the parallel coefficient (see Section 3.3.3). The rigidity profiles of the selected coefficients are revisited in Section 5.4. Finally, and more generally, the heliosheath is assumed to be less vast in the current and subsequent chapters than in Chapter 4, with the TS and HP positions respectively specified as $r_{TS} = 94$ AU and $r_{HP} = 122$ AU to reflect the Voyager 1 detection of these boundaries. See *Ferreira et al.* [2004b] for a study on electron modulation where the positions of these boundaries are varied. While the TS compression ratio is retained as $s = 2.5$, the effects of DSA are suppressed in this chapter by setting $\nabla \cdot \vec{V}_{sw} = 0$ in the shock region (See Section 3.6.1). No source functions are specified at the TS or elsewhere; all solutions are merely modulated forms of the HPS. For illustrative purposes, full drift efficiency is assumed (i.e. $\kappa_{D,0} = 1.0$). Other modulation parameters that are not mentioned here remain unchanged from those specified in Section 4.2, while any departures are pointed out explicitly in the following sections.

The above model configuration yields the solutions shown in Figures 5.1, 5.2 and 5.3, which serve as standard references for comparison for subsequent solutions. The first of these shows electron energy spectra at the TS along the approximate Voyager 1 trajectory at a polar angle of $\theta = 55^o$, and at Earth in the equatorial plane at $\theta = 90°$, for solar minimum conditions and both

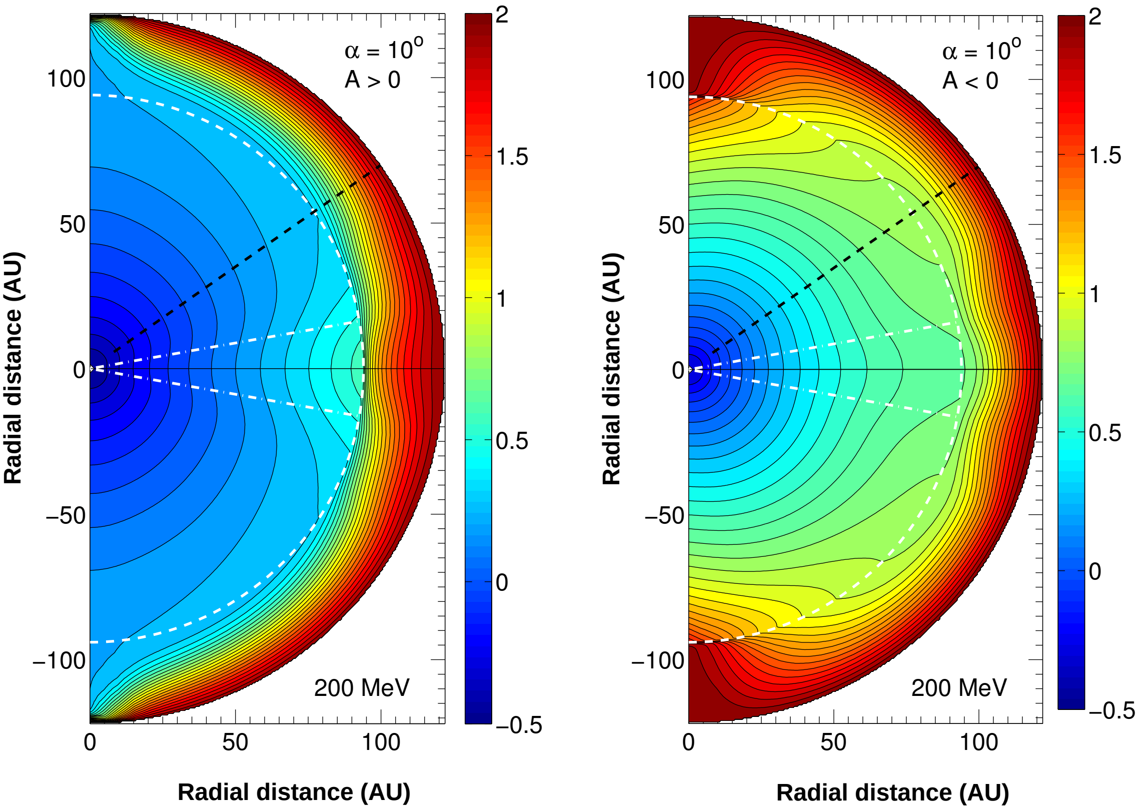

Figure 5.3: Contour plots illustrating 200 MeV galactic electron intensities in the meridional plane of the heliosphere for A > 0 (left) and A < 0 (right). The colour bars show intensities as percentages of the maximum on a logarithmic scale. The dashed white halfcircle indicates the TS position at 94 AU, while the dash-dotted lines indicate the polar extent of the HCS for $\alpha = 10°$. The Voyager 1 trajectory is approximated by the dashed black line along $\theta = 55°$, while the Sun is located at the origin.

magnetic polarities. Note how the TS spectrum retains the power law that the HPS exhibits at lower energies. This follows because of the rigidity-independent MFP chosen for electrons for $P < 0.34$ GV (see Section 3.3.2). *Caballero-Lopez et al.* [2010] and *Potgieter and Nndanganeni* [2013a] show similar results. From the form of the spectrum at Earth, it appears that adiabatic energy losses, which force ion spectra into characteristic E^{+1}-distributed power laws (as in Section 4.2), are absent for electrons in the energy range considered here. This, too, is shown to be a result of rigidity-independent diffusion; see Section 5.4. Furthermore, both the energy spectra in Figure 5.1 and the spatial distributions of Figures 5.2 and 5.3 demonstrate substantial decreases in intensities from the HP to the TS, creating a prominent modulation barrier. This effect, particularly visible toward lower energies, is the result of the impaired diffusion brought about by the small MFPs specified for particles in this region and had been anticipated before its detection by the Voyager spacecraft [*Potgieter and Le Roux*, 1989]. See also the modelling results of *Ferreira and Potgieter* [2002], *Ferreira et al.* [2004b], *Nkosi et al.* [2011] and *Potgieter and Nndanganeni* [2013a] for similarly large electron modulation in the heliosheath. This barrier is also modelled by *Langner et al.* [2004] for protons. The more complicated problem, however, is predicting the contribution of galactic electrons to the intensity at Earth. See e.g. *Potgieter and Nndanganeni* [2013a] and *Nndanganeni* [2015] for comment on this matter.

While electron transport appears to be generally sensitive to diffusion properties, the effects of electron drifts are confined to a narrow domain in energy under the current model configuration. Figure 5.1 shows that polarity-dependent modulation is most prominent for electrons of 0.1 to 1 GeV. Their spatial distributions (as seen in Figures 5.2 and 5.3) may be explained at the hand of the expected electron drift patterns: Recall that their movement along the HCS is outward during the $A < 0$ polarity cycle, poleward in the outer heliosphere, and back downward from the poles toward the equatorial regions in the heliospheric interior. Of course, these directions are reversed during the $A > 0$ cycle. Figure 5.3 illustrates these patterns for 200 MeV electrons, with contours assuming a convex (or outward bulging) shape in their direction of travel. During the $A < 0$ cycle, enhanced polar diffusion at high latitudes facilitates poleward movement of electrons through the heliosheath. Likewise, this also encourages transport from these electron-rich polar regions to the HCS in the interior, from where electrons drift outward. This collectively serves to supplement intensities up to the TS and a short way beyond. This can also be discerned from Figure 5.2. For $A > 0$, the drift patterns in the heliosheath tend to carry electrons toward the equatorial regions, from where the passage of electrons inward along the HCS is stifled by the low-diffusion barrier. The inward drifts along the HCS still manage to carry electrons across the TS and hence supplement intensities in the interior, however not to the extent achieved during the negative polarity cycle. This discussion is expanded in Section 5.5. As for the rest of the chapter, the features and processes earmarked in the text above for further comment form the basis of discussion in following sections.

5.3 Modelling the Electron Input Spectrum

For the modelling of GCRs, the source of particles is specified as an energy distribution at the outer boundary up until where one intends to study their modulation. The HP is typically such a boundary. An input spectrum specified here represents a very local interstellar spectrum, which *Potgieter* [2014a] describes as a CR distribution specified within $\sim$ 150 AU from the Sun in its direction of movement. Before the availability of direct measurements of electron intensities in the remote regions of the heliosphere [e.g. *Webber et al.*, 2012; *Stone et al.*, 2013], several approaches were followed in an attempt to construct realistic spectra that may be used as input in CR modulation models. These include radio data surveys (to constrain electron densities from the synchrotron radiation these particles emit as they travel along magnetic field lines) and galactic propagation modelling. A combination of these methods allowed e.g. *Langner et al.* [2001], *Ptuskin et al.* [2006], *Webber and Higbie* [2008] and *Strong et al.* [2011] to estimate interstellar electron spectra, providing valuable constraints on the intensities of more locally specified spectra such as the HPS. For examples, see Figure 5.4. While its form and intensity levels may presently be inferred more directly from spacecraft data, it is demonstrated by *Bisschoff and Potgieter* [2014] that the HPS can indeed be reproduced under suitable parameter configurations using the GALPROP code [see e.g. *Strong et al.*, 2007, and the references therein], while *Webber and Higbie* [2013] employs a Monte Carlo diffusion model for galactic propagation in a similar demonstration. The galactic spectra computed using these models cannot generally be considered local interstellar spectra though, since the contribution of local sources (within parsecs from the heliosphere; e.g. *Büsching et al.* [2008a, b]) is not necessarily accounted for. *Büsching et al.* [2008b] shows, for instance, that the nearest millisecond pulsars

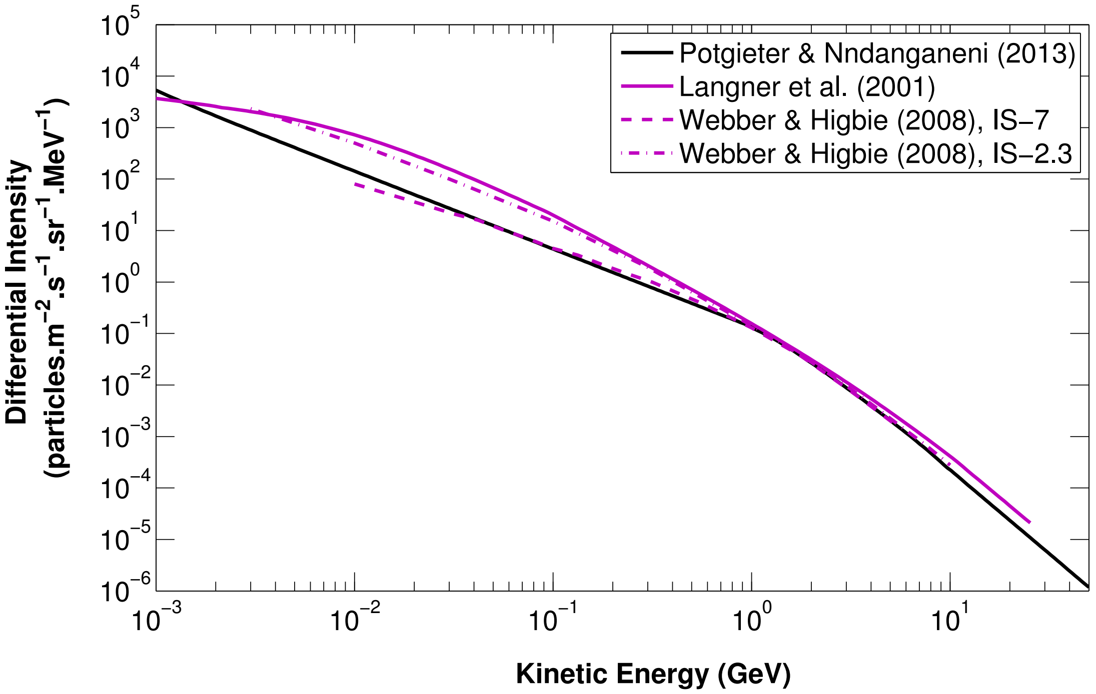

Figure 5.4: Examples of very local interstellar spectra for electrons, which are constructed for use as input in CR modulation models. See the studies referenced in the legend [*Langner et al.*, 2001; *Webber and Higbie*, 2008; *Potgieter and Nndanganeni*, 2013b] for further details on each.

make a non-negligible contribution to local electron spectra. The reference HPS, as specified in Section 5.2 and discussed in the subsection below, is however not computed from an astrophysical point of view, but instead derived from the modelling results of CR modulation within the heliosphere and with the aid of available spacecraft measurements.

5.3.1 A heliopause spectrum for galactic electrons

Potgieter et al. [2014b] presents a HPS for galactic electrons that is proposed to be valid at energies exceeding the lowest energy measurable by the Voyager detectors (i.e. at $E \gtrsim 1$ MeV) and up to about 50 GeV. It is characterised, as mentioned before, by two power laws – the first, at lower energies, displays a larger spectral index than the second, which follows roughly at energies above 1 GeV. This forms a transition that is indicative of different processes dominating at energies on either side of it: Toward lower energies electron propagation through the interstellar medium is diffusion-dominated, whereas energy losses through e.g. synchrotron radiation and inverse-Compton scattering yield the softer distribution at high energies [see e.g. *Webber and Higbie*, 2008]. The soft high-energy spectrum is chiefly informed by measurements at Earth. Since solar modulation effects begin to phase out roughly above 10 GeV and is considered altogether negligible at $E > 30$ GeV [*Strauss and Potgieter*, 2014], it becomes feasible at these energies to infer HPS intensities from electron measurements at Earth. The HPS is hence assumed from PAMELA observations [*Adriani et al.*, 2011; *Menn et al.*, 2013] to exhibit a spectral index of -3.18 ± 0.05 at high energies. Below 1 GeV, where the HPS hardens, Voyager 1 observations at ~ 112 AU in the heliosheath prompted *Potgieter and Nndanganeni* [2013b] to compute a demodulated spectrum at the estimated HP position that displayed a power-

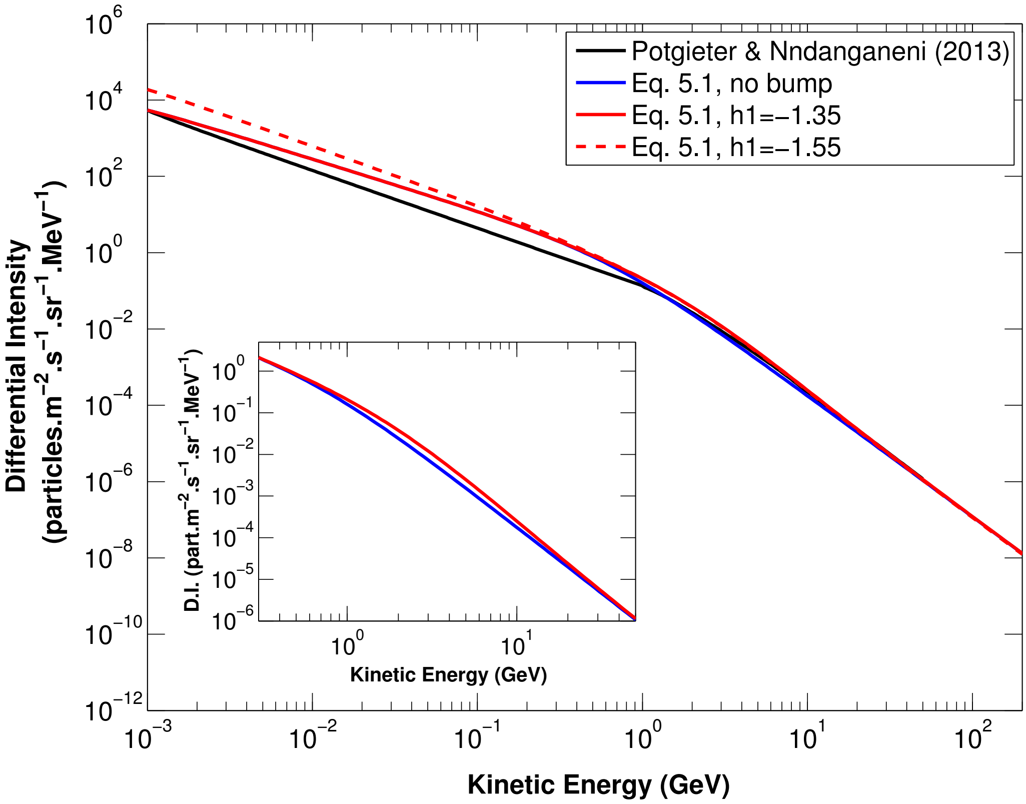

Figure 5.5: Different configurations of the HPS utilised as input spectrum for galactic electrons in this study and as described by Eq. 5.1 and 5.2. The case with $h_1 = -1.35$ serves as reference HPS, while the spectrum by *Potgieter and Nndanganeni* [2013b] is included for comparative purposes. The inset accentuates the contribution of the intensity enhancement described by Eq. 5.2 between 0.5 and 20 GeV.

law index of -1.55 ± 0.05. It is shown in Figures 5.4 and 5.5 for comparative purposes. The Voyager 1 encounter of the HP revealed this spectrum to be quite accurate: *Stone et al.* [2013] report that electron intensities at the HP are indeed power-law distributed with energy, and provides a spectral index of -1.45 ± 0.09, with the lower and upper limits respectively based on a GEANT4 simulation and a pre-launch accelerator calibration.

These empirical insights, along with the antecedent spectrum of *Potgieter and Nndanganeni* [2013b], underlie the form of the HPS implemented in this study. Following *Vos* [2012] and *Potgieter et al.* [2014b], the HPS is expressed in differential intensity as function of kinetic energy according to

$$j_{\mathrm{HPS}} = \frac{0.16}{\beta^2}\left[\frac{\left(\frac{E}{E_N}\right)^{1.5} + \left(\frac{E_b}{E_N}\right)^{1.5}}{1 + \left(\frac{E_b}{E_N}\right)^{1.5}}\right]^{\frac{h_2 - h_1}{1.5}} \left(\frac{E}{E_N}\right)^{h_1}, \tag{5.1}$$

in units of electrons m^{-2} s^{-1} sr^{-1} MeV^{-1}, with $E_N = 1$ GeV, and where $E_b = 0.67$ GeV denotes the energy about which the transition between power laws occurs; the constant valued at 1.5 stipulates the smoothness of this transition. The quantities h_1 and h_2 refer to the power-law indices at energies respectively below and above E_b. The latter is taken as $h_2 = -3.18$ to reflect the reported value of the PAMELA experiment. For the lower-energy index, values on either side of that proposed by *Stone et al.* [2013] are considered, namely $h_1 = -1.35$ and -1.55, while the HPS with the former serves as reference input spectrum. Both these indices are illustrated in Figure 5.5. Another peculiar feature is an intensity enhancement between roughly 0.5 and 20 GeV, where PAMELA electron measurements are slightly offset above the data aligned with the power law. This is accounted for in this study by adding the term

$$j_{\text{bump}} = b_1 \exp\left[b_2 + b_3 \log\left(\frac{E}{E_N}\right) + b_4 \left(\frac{E}{E_N}\right)^{b_5}\right] \tag{5.2}$$

to the differential intensity in Eq. 5.1, with $b_1 = 1.55$ electrons m^{-2} s^{-1} sr^{-1} MeV^{-1}, $b_2 = 4.67$, $b_3 = -5.24$, $b_4 = -8.17$, and $b_5 = -0.5$ specified phenomenologically [see also *Potgieter et al.*, 2013; *Potgieter*, 2014a], and where $E_N = 1$ GeV. Its contribution is also illustrated in the inset of Figure 5.5. It is remarked by e.g. *Vos* [2012] that no acceleration processes are thought to exist within the heliosphere that can account for this enhancement, and that it is likely the effect of a local source or process in the interstellar medium. The HPS collectively described by Eqs. 5.1 and 5.2 is regarded in this study to be valid on the energy interval of 10^{-3} to 50 GeV. The HPS at $E \lesssim 5$ MeV, henceforth referred to as *very low* energies with regards to electrons, is revisited in the next subsection.

5.3.2 Electron intensities at very low energies

Recall from Figure 2.17 the peak-like increases in the radial intensity profiles recorded by Voyager 1 near the TS for electron energies of 2.5 to 14 MeV. In the accompanying text DSA is mentioned as a mechanism that might be at least partially responsible for these features. Should this indeed be the case, it must be borne in mind that the particles that constitute these narrow increases must have migrated from lower energies during acceleration. Section 6.5.1 demonstrates that the efficiency of electron re-acceleration at Voyager-observed energies is in fact sensitive to the features of the HPS below 1 MeV. The intensity levels and spectral shape of the very local interstellar spectrum are however unknown below 1 MeV from both an observational and modelling perspective. It is hence necessary that the form of the HPS is investigated at these very low energies. Figure 5.6 demonstrates that electron intensities continue to grow should Eq. 5.1 be extended below 1 MeV. It also happens more rapidly with decreasing energy because of the decrease of β from unity. This behaviour is however unlikely to be accurate. Consider firstly that most studies on turbulence in the heliosphere predict an up-turn in the MFPs of electrons at low energies (Section 5.4.3), which would imply that should the HPS intensities be allowed to increase indefinitely toward lower energies, the intensities registered at Earth would be largely unaltered from that. This contribution, which would be in the order of 10^5 electrons m^{-2} s^{-1} sr^{-1} MeV^{-1} at 0.1 MeV if Eq. 5.1 is assumed valid there, exceeds the intensities recorded near Earth for electrons at these low energies; see e.g. Figure 2.18. The greatest contribution to these measured intensities is furthermore attributed to particles emanating from the Sun or planetary magnetospheres [e.g. *Ferreira et al.*, 2001a, b], which constrains the galactic electron contribution even further. The differential flux profile reported for 50 keV electrons in the heliosheath by *Hill et al.* [2014] suggests that intensities may be as low as $3 \cdot 10^{-2}$ electrons m^{-2} s^{-1} sr^{-1} MeV^{-1} near the HP along Voyager 1's direction of travel. This implies a HPS with diminishing intensity toward lower energies. However, since published data cov-

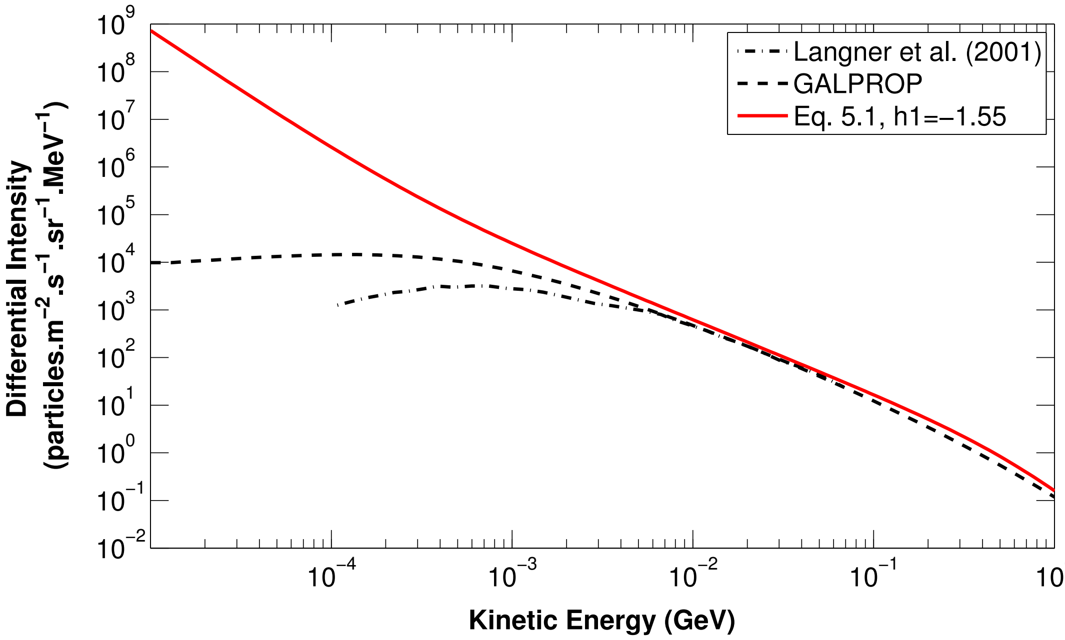

Figure 5.6: Plausible scenarios from galactic CR propagation modelling for electron intensities at the HP (122 AU) for low ($E < 100$ MeV) to very low energies ($E < 1$ MeV). The dash-dotted line represents a 'polar approach' model solution by *Langner et al.* [2001] and the dashed line a GALPROP solution [*Bisschoff*, 2014, *private communication*], while the HPS of Eq. 5.1 (in solid red) is included for comparison.

erage for electrons at these very low energies remains quite sparse, the predictions of galactic propagation models are also considered again. For example, the interstellar spectra calculated using the polar approach of *Langner et al.* [2001] yield 10^3 electrons m^{-2} s^{-1} sr^{-1} MeV^{-1} at 0.1 MeV, signifying that the intensities flatten out and diminish with decreasing energy. The spectra by *Strong et al.* [1994, 2000] appear similar [see also *Strong et al.*, 2011], while GALPROP yields flattened spectra from 1 MeV to as low as 0.01 MeV for rigidity-independent diffusion within this energy range [*Bisschoff*, 2014, *private communication*]. See also *Bisschoff and Potgieter* [2014] for more details on the instance of the GALPROP model referenced here.

With model predictions as illustrated in Figure 5.6 and available data considered, a number of mostly speculative scenarios are explored. It can be conjectured that the HPS flattens toward energies below 1 MeV, or at least decreases slow enough to appear so. This may be simulated by adapting Eq. 5.1 to reflect a convenient triple power-law form according to

$$j_{\mathrm{HPS}} = \frac{0.16}{\beta^2}\left[\frac{\left(\frac{E}{E_N}\right)^{1.5}+\left(\frac{E_{b2}}{E_N}\right)^{1.5}}{1+\left(\frac{E_{b2}}{E_N}\right)^{1.5}}\right]^{\frac{h_2-h_1}{1.5}}\left[\frac{\left(\frac{E}{E_N}\right)^{1.5}+\left(\frac{E_{b1}}{E_N}\right)^{1.5}}{1+\left(\frac{E_{b1}}{E_N}\right)^{1.5}}\right]^{\frac{h_1-h_0}{1.5}}\left(\frac{E}{E_N}\right)^{h_0}, \qquad (5.3)$$

in units of electrons m^{-2} s^{-1} sr^{-1} MeV^{-1}. Here h_0 represents the spectral index of the lowest energy segment of the HPS, and E_{b1} and E_{b2} respectively represent the energies about which power laws transition from h_0 to h_1 and h_1 to h_2. The value of E_{b2} is retained from E_b in Eq. 5.1 as 0.67 GeV, while it is assumed that $E_{b1} = 10^{-3}E_{b2}$. The roles and values of earlier specified quantities remain unchanged. The spectra resulting from Eq. 5.3 for different values of h_0 are illustrated in the left panel of Figure 5.7. The first and second of these, with $h_0 = 1.0$ and 1.5, are in reasonable agreement with GALPROP and *Langner et al.* [2001] estimates respec-

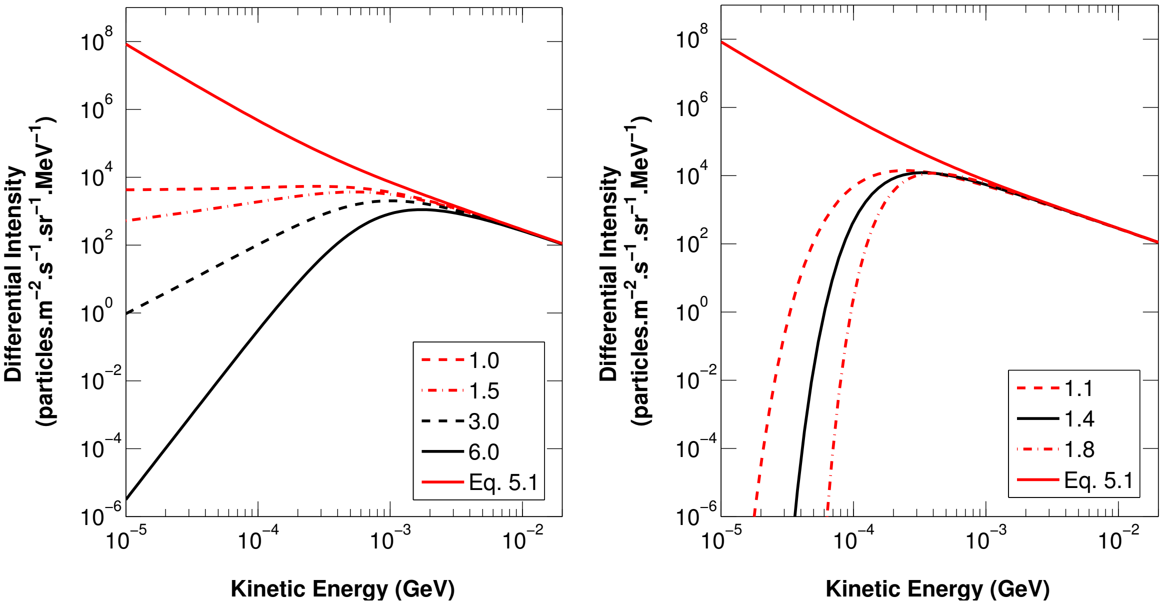

Figure 5.7: Modifications to the HPS described by Eq. 5.1 (solid red line) for $E \lesssim 1$ MeV. In the left panel, the legend values correspond to different values of h_0, representing the power-law indices of the lowest-energy segment of the HPS as described by Eq. 5.3. Simulating an exponential decrease of intensities toward lower energies as described by Eq. 5.4, the spectra on the right are presented for different values of Φ as shown in the legend.

tively, while the spectrum for $h_0 = 6.0$ intercepts the 50-keV observed intensity of *Hill et al.* [2014]. While none can be ruled out given the very limited available data, the forms of the last two spectra, with $h_0 = 3.0$ and 6.0, are less preferable due to their more pronounced deviation from the relatively well-established power law above 1 MeV. This deviation may be avoided by shifting E_{b1} to lower energies, but this would require larger values of h_0 to yield the above correspondences. There may also be more suitable forms than power laws to describe the HPS at these very low energies, since these types of distributions may be erroneously associated with the spectral imprints of energy changes that are not necessarily involved here, e.g. adiabatic cooling. Hence, a second scenario to consider is a HPS with an exponential intensity decrease toward lower energies, which is more reasonable than a power law. This is modelled by modifying Eq. 5.1 as follows:

$$j_{\mathrm{HPS}} = \frac{0.16}{\beta^2}\left[\frac{\left(\frac{E}{E_N}\right)^{1.5} + \left(\frac{E_{b2}}{E_N}\right)^{1.5}}{1 + \left(\frac{E_{b2}}{E_N}\right)^{1.5}}\right]^{\frac{h_2 - h_1}{1.5}} \left(\frac{E}{E_N}\right)^{h_1} \exp\left(-\left(\frac{E_c}{E}\right)^{\Phi}\right), \tag{5.4}$$

in units of electrons m^{-2} s^{-1} sr^{-1} MeV^{-1}, with the energy at which the low-energy intensity decrease ensues taken as $E_c = 0.4$ MeV, Φ denoting the strength of this decrease, and other quantities as already defined. The values of Φ are varied and the resultant spectra shown in the right panel of Figure 5.7. This HPS intercepts the observed 50-keV electron profile for $\Phi = 1.4$, while deviations from the Voyager-observed power law above 1 MeV are small for all Φ-values considered. The scenarios presented in Figure 5.7 for the HPS are utilised in subsequent sections, where their influence will be considered in conjunction with that of the properties governing modulation processes and DSA as discussed in the current and next chapters respec-

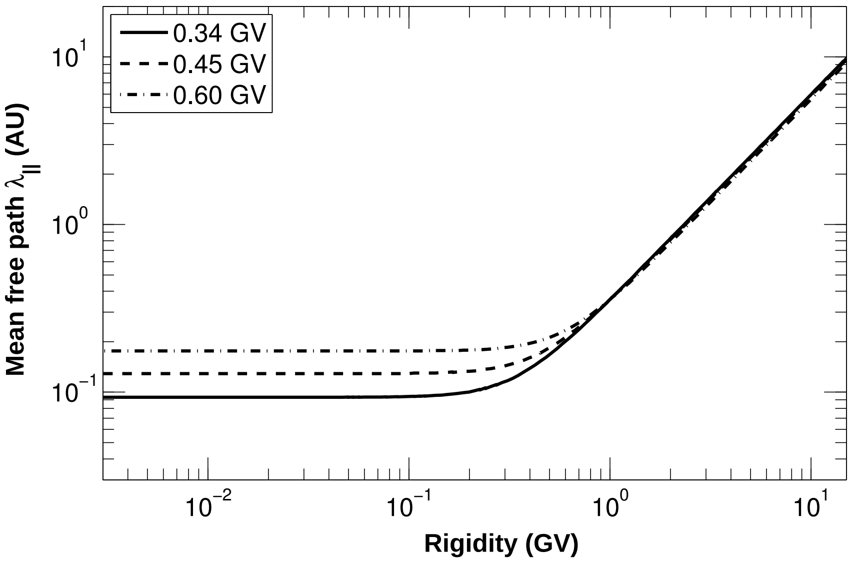

Figure 5.8: The rigidity profile of the parallel MFP for electrons at Earth for different values of P_k in Eq. 3.24 as indicated in the legend.

tively. At any rate, the findings presented above, revealing the form of the very low-energy HPS, are mostly speculative and as such not conclusive. These features may only be inferred upon further investigation.

5.4 The Rigidity Dependence of Electron Diffusion

Following the introduction of possible input energy spectra for galactic electrons, it is explored how these spectra are expected to change as particles are transported through the heliosphere. Diffusion is of course a dominant process governing CR transport, and the rigidity (or equivalent energy) dependence of the coefficients describing this process dictate to a large extent how energy spectra are modulated. This dependence is consequently explored for each of the energy ranges in which the structure of the HPS is also considered. Toward higher energies, global modulation features are better constrained, and the dependence described by Eq. 3.24 has been successfully employed to reproduce electron intensities measured at Earth over several semesters of observation [*Vos*, 2012; *Potgieter et al.*, 2015]. The high-energy rigidity dependence of diffusion is therefore only briefly reviewed in this section. These coefficients must however be re-evaluated for energy domains in which they have not been previously utilised, e.g. below roughly 5 MeV, where the effects of other modulation processes are also shown within this section to emerge under certain conditions.

5.4.1 Electron diffusion at high energies

Diffusion at energies exceeding 5 MeV is fundamentally characterised by the inertial and energy ranges of the turbulence power spectrum. Though constructed phenomenologically, and perhaps over-simplified, the rigidity dependence of the coefficients applied here, and described by Eqs. 3.23 to 3.25, yields a reasonable approximation to that derived from turbulence theory;

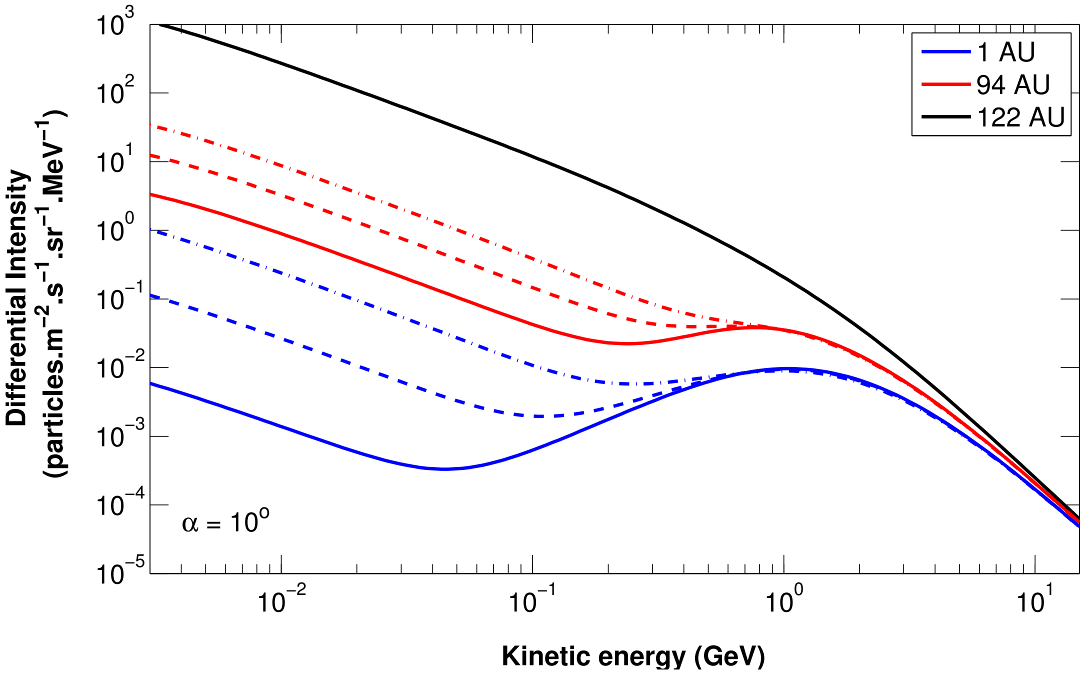

Figure 5.9: Modelled energy spectra for galactic electrons at the TS (94 AU, $\theta = 55°$) and Earth (1 AU, $\theta = 90°$) for varying rigidity dependences of diffusion, with respect to the HPS at 122 AU. Line colours represent radial distances as indicated in the legend. The solutions correspond to the MFP profiles displayed in the same line styles in Figure 5.8 and $P_k = 0.34$, 0.45 and 0.60 GV according to that figure's legend. Electron drifts are disabled for these solutions ($\kappa_{D,0} = 0$).

see Section 3.3. All the parameters contained within Eq. 3.24 are developed in the parameter study by *Vos* [2012], however this study is concerned mostly with P_k at which the rigidity dependence of the coefficient changes. The MFP of electrons are assumed in the standard configuration (based on PAMELA observations from the year 2006) to be rigidity-independent up to $P_k = 0.34$ GV, from where an increase proportional to $P^{1.23}$ eventually ensues. A similar form is adopted by *Caballero-Lopez et al.* [2010] and *Potgieter and Nndanganeni* [2013a] for coefficients describing electron diffusion; see also *Potgieter* [1984]. *Vos* [2012] modifies the standard profile and its defining parameters for consecutive years up to 2009 in order to fit modelled spectra to observations, based on changes in HMF magnitude and HCS tilt angle over the same period. The value of P_k is shown to vary between 0.34 and 0.45 GV during this time. In this study, P_k is arbitrarily varied to demonstrate the modulation effects following from the resulting rigidity dependence; the MFPs and corresponding energy spectra are respectively shown in Figures 5.8 and 5.9. Note that as a result of increasing P_k, the rigidity-independent segment of the MFPs is translated upward according to $P^{1.23}$.

The resultant spectra in Figure 5.9 display higher intensities below the energy equivalent to P_k for larger values of this parameter. This follows since modulation is reduced by the smaller intensity gradients that ensue because of the consequent increase in the rigidity-independent MFPs preceding P_k. However, just as the profiles presented in Figure 5.8 converge above P_k, the energy spectra of Figure 5.9 also converge above the corresponding energy at both the TS and Earth. Varying the rigidity dependence in this manner illustrates another method, aside from modifying the radial dependence of diffusion coefficients directly, by which desired intensities can be attained at lower energies throughout the heliosphere. This ability to alter the radial and

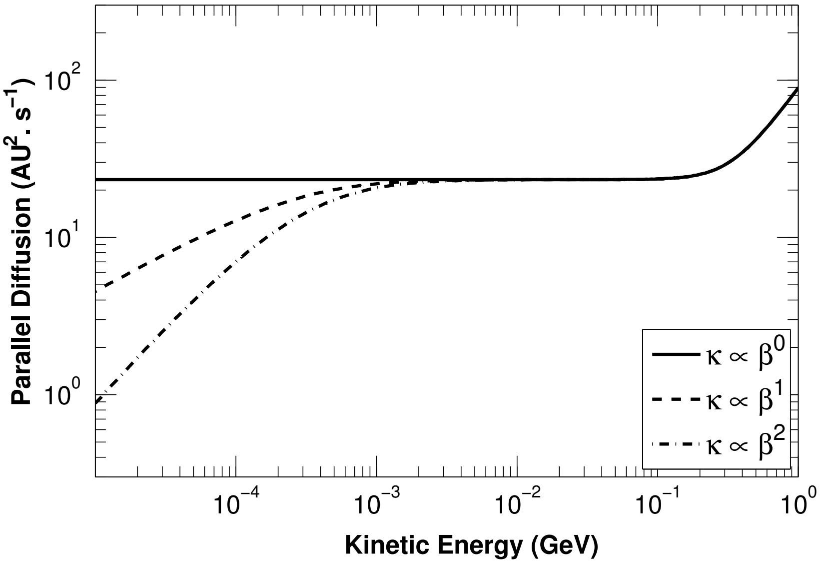

Figure 5.10: The parallel diffusion coefficient displayed at Earth as a function of kinetic energy. The MFP has been changed only for illustrative purposes such that the coefficient exhibits the proportionality displayed in the legend for $E \lesssim$ 100 MeV. Note that $\beta \approx 1$ above about 1 MeV. See Figure 3.2.

rigidity dependences independently is an example of the advantages discussed in Section 3.3 of the employed coefficients. Furthermore, attention is drawn to how the slopes of distributions change between 0.1 and 1 GeV in Figure 5.9. For larger values of P_k, the TS spectrum transitions almost directly from the power law inherited from the HPS below 1 GeV to the softer power law at higher energies, where modulation is eventually phased out due to large MFPs. On the other hand, the intensities of TS spectra following from P_k =0.45 and 0.60 GV respectively flatten out or even increase slightly before adopting the soft high-energy power law. Note that the distributions in these cases are as a result harder across this transition. Since the segment along which MFPs increase according to $P^{1.23}$ is larger for smaller values of P_k, it appears that MFPs increasing with rigidity generally tend to harden distributions from the original form of input spectra - that is at least until MFPs become large enough for modulation effects to phase out completely. These cases are considered again in Chapter 6, where the forms of these spectra are revealed to dictate how efficiently they are accelerated at the TS. The effects of these diffusion profiles on drift-related modulation are also investigated and discussed in Section 5.5.

5.4.2 Implications of rigidity-independent diffusion

As already discussed in Section 5.2, spectra at the TS inherit the power-law distributed form of the HPS at low energies up to a few hundred MeV. This follows as an obvious result of the rigidity independence of the MFPs specified at these energies. However, when spectra are considered at energies as low as the electron rest-mass energy (and lower), more intricate conditions apply. Since the particle speed of electrons become less comparable with light speed at these low energies, β (implicitly contained within Eq. 3.9) forces diffusion coefficients to deviate from the flat rigidity profile assumed for MFPs below P_k. Hence, under such a configuration, modulated spectra do not retain the form of the HPS at very low energies. To study the implications of rigidity-independent diffusion however, the governing coefficients should remain

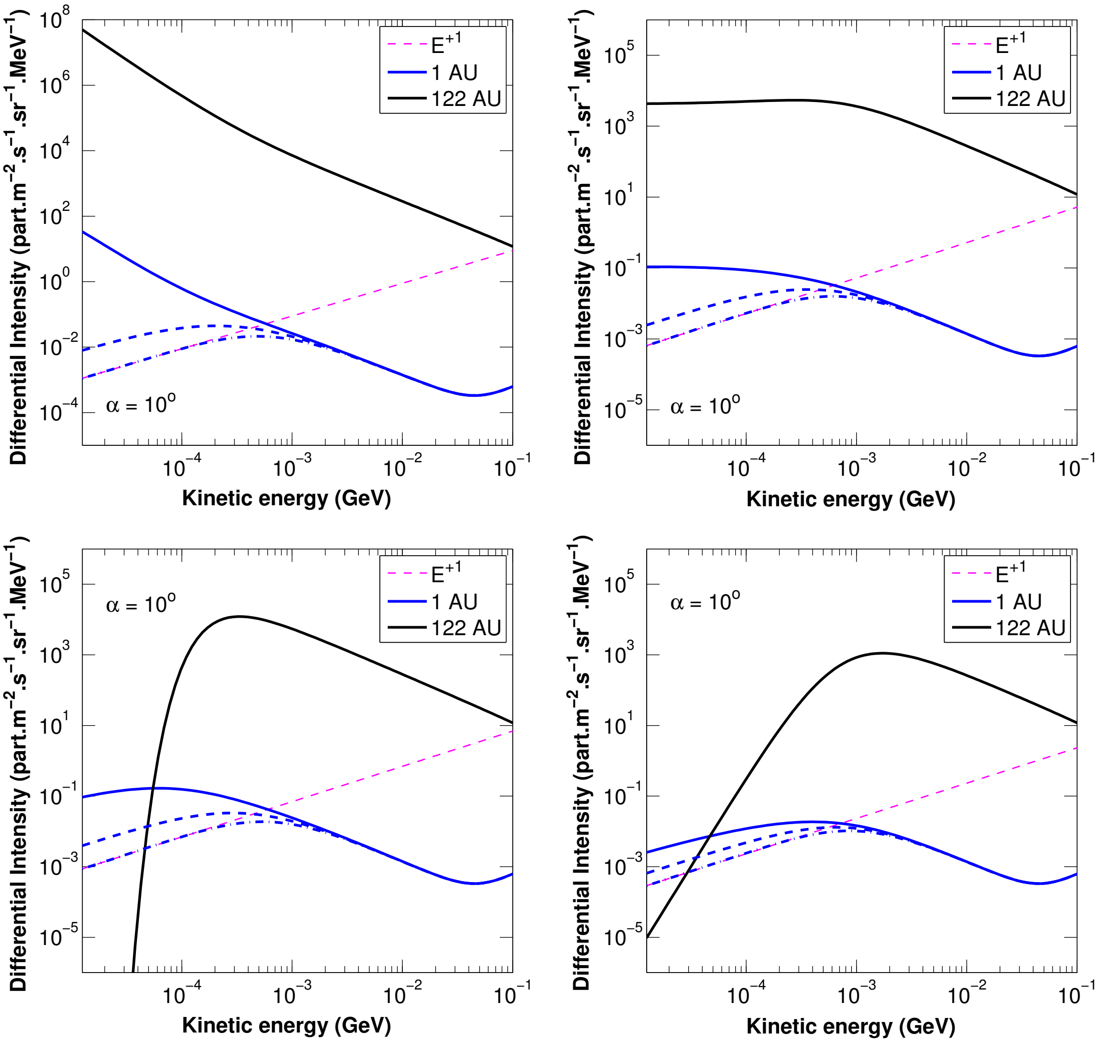

Figure 5.11: Modelled energy spectra at Earth (1 AU, $\theta = 90°$) for various diffusion configurations and with respect to different input spectra (black lines) at 122 AU. In the top-left panel the reference HPS is employed as input, in the bottom left Eq. 5.4 with $\Phi = 1.4$ is applied, while Eq. 5.3 is applied on the right with $h_0 = 1.0$ and 6.0 for the top and bottom panels respectively. Solutions correspond to the profiles with the same line styles in Figure 5.10. The spectra at Earth (all in blue) under the most rapidly declining diffusion scenario (dash-dotted lines) invariantly follow a E^{+1}-distributed power law (dashed magenta line). Drifts are disabled for these solutions.

constant down to the lowest energy considered. This may be achieved by incorporating a $1/\beta$ factor into the diffusion coefficient to suppress the existing dependence on the particle-to-light-speed ratio. The diminishing of low-energy diffusion may also be exaggerated for illustrative purposes by strengthening the dependence on β. Figure 5.10 illustrates these scenarios, which respectively represent a rigidity-independent diffusion configuration with $\kappa \propto \beta^0$, the standard configuration of Section 5.2 with $\kappa \propto \beta^1$, and an exaggerated configuration where $\kappa \propto \beta^2$. It should be stressed however that these cases are presented purely for illustrative purposes, and that they are by no means proposed to be physically valid. Since the parallel and perpendicular diffusion coefficients are assumed to share the same rigidity dependence, κ is used here to denote diffusion coefficients in general and is thus interchangeable with both $\kappa_{||}$ and $\kappa_{\perp,r/\theta}$. Note that while it is the convention to illustrate diffusion properties in terms of MFP versus rigidity (e.g. Figure 5.8), it is more beneficial to the end of demonstrating the dependences on β to show

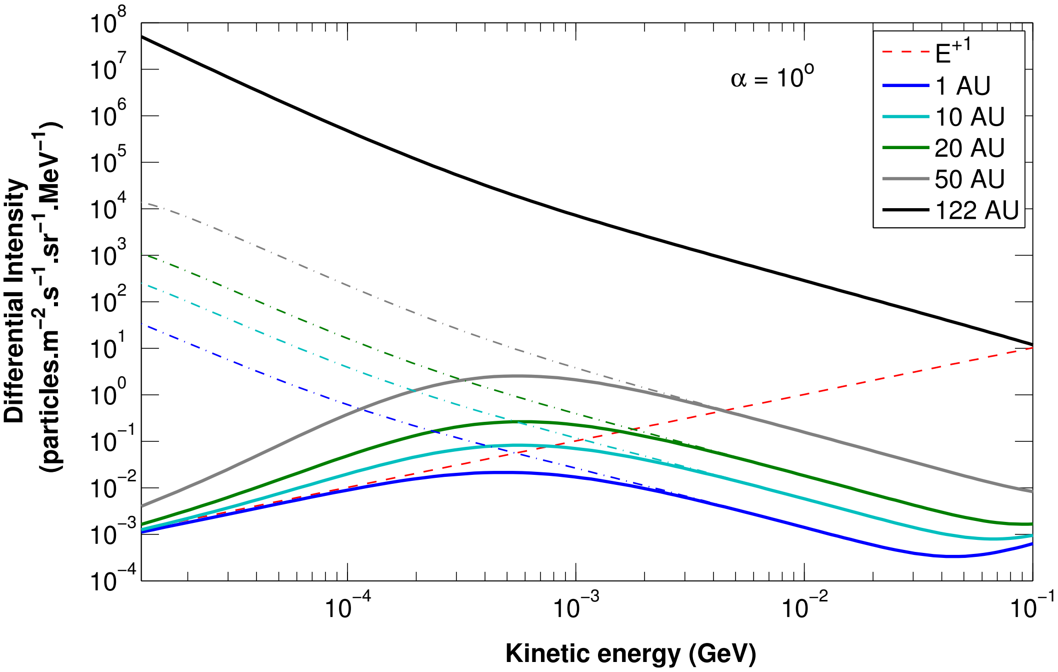

Figure 5.12: Modelled energy spectra at the radial distances indicated in the legend and shown in different colours. The spectra are displayed at $\theta = 55°$, except for that at Earth (1 AU), which is shown at $\theta = 90°$. The input spectrum at 122 AU is the reference HPS of Eq. 5.1. Spectra in solid lines are shown for the $\kappa \propto \beta^2$ configuration, while dashed-dotted lines represent spectra resulting from rigidity-independent diffusion. The dashed red line shows the characteristic E^{+1} power law followed by adiabatically cooled distributions. Drifts are disabled.

the corresponding diffusion coefficient. The coefficient is furthermore rather expressed as function of kinetic energy so that corresponding features in the accompanying energy spectra are more readily identifiable.

Selecting a representative sample of the input spectra introduced in Section 5.3.2, the resultant modulated spectra at Earth are shown in Figure 5.11 for each of the aforementioned diffusion configurations. For diffusion coefficients with a flat rigidity profile the modulated spectra, shown as solid lines in Figure 5.11, mostly retain the form of the HPS . Also, not surprisingly, for $\kappa \propto \beta^1$ and $\kappa \propto \beta^2$ modulation increases toward lower energies, causing greater deviations from the form and intensity of the HPS. However, for the latter configurations where diffusion is allowed to decrease toward lower energies, the modulated spectra at Earth follow a E^{+1}-distributed power law regardless of the form of the input spectrum employed. This spectral characteristic is indicative of the involvement of adiabatic energy losses. This process plays a well-established role in the modulation of ions [see e.g. *Moraal and Potgieter*, 1982; *Potgieter and Moraal*, 1988; *Caballero-Lopez et al.*, 2010; *Strauss et al.*, 2011b], where this E^{+1} power law is also shown to emerge for non-relativistic particles. Indeed, spectra are only aligned to this characteristic distribution below the electron rest-mass energy in Figure 5.9. In most modulation studies, however, electrons are relativistic in the typical energy ranges considered, and had diffusion been allowed to decline sufficiently above the rest-mass energy, they would instead display E^{+2}-distributed spectra at these energies [see *Caballero-Lopez et al.*, 2010; *Strauss et al.*, 2011b]. Unlike for protons though, electron MFPs are not known to decline so rapidly until much lower energies [*Teufel and Schlickeiser*, 2003] that are typically smaller than that considered in this study; electrons are therefore not naturally observed to attain the adiabatic cooling limit. Aside from requiring diminished diffusion, these energy losses are incurred only when $\nabla \cdot \vec{V}_{sw} > 0$, which is only achieved at $r < r_{TS}$. The spectral effects of this process in the inner heliosphere are demonstrated in Figure 5.12: Note that when diffusion declines sharply toward lower energies (according to e.g. $\kappa \propto \beta^2$), spectra indeed follow the E^{+1} power law, while the form of the HPS is retained for rigidity-independent diffusion. Moreover, it appears from Figure 5.12 that radial gradients are extinguished in the adiabatic limit so that cooled spectra throughout the inner heliosphere eventually converge at low-enough energies; recall that κ also grows with r so that spectra at larger radial distances will attain the adiabatic limit at lower energies.

In summary, the assumption of rigidity-independent diffusion firstly allows the intensities of modulated spectra to be reduced in such a manner that the general form of the HPS is retained. It also follows that since diffusion coefficients are not permitted under this assumption to attain sufficiently small values, other modulating processes such as adiabatic energy losses do not manifest in the inner heliosphere. While it is reasonable to assume that the diffusion coefficients of electrons do not diminish toward lower energies (or at least not too drastically), there may nevertheless be more likely scenarios than rigidity-independent diffusion at these very low energies. This is investigated further in the next subsection.

5.4.3 Modelling dissipation-range turbulence effects

Adiabatic energy changes play an appreciable role in ion modulation, and their diffusion coefficients diminish with decreasing rigidity so as to allow this, while electron modulation is conceivably different on a fundamental level [see *Potgieter*, 1996, 2000]. One aspect in which this is portrayed is the sensitivity of electrons to the dissipation range of the turbulence spectrum, which manifests as an increase in electron MFPs toward lower energies according to e.g. models for dynamical turbulence [*Bieber et al.*, 1994]. See also the work of *Teufel and Schlickeiser* [2003]. Due to this enhanced diffusion the adiabatic limit becomes unattainable. Indeed, instances of the random sweeping model predict a pronounced up-turn in low-energy MFPs, while the damping model yields MFPs that very nearly level out toward lower energies [*Dröge*, 2000a, b; *Teufel and Schlickeiser*, 2003; *Engelbrecht and Burger*, 2013a]. The latter model presents a case for which the rigidity-independent diffusion explored in Section 5.4.2 may serve as an approximation. The contribution of the dissipation range is also shown in Figure 3.5 for the electron coefficients of *Burger et al.* [2008] to yield larger length scales at small rigidities. Observations presented by *Bieber et al.* [1994] similarly demonstrate that MFPs would in fact be too small and the rigidity-dependence thereof incorrect should this contribution be neglected. See also *Langner* [2004] for a thorough discussion on the theoretical development of diffusion properties that follow from the dissipation range.

As explained in Section 3.3.2 however, the diffusion coefficients applied in this study for electrons do not follow self-consistently from underlying turbulence-related quantities as e.g. the *Burger et al.* [2008] coefficients do. Instead, diffusion coefficients are modelled to convey certain characteristics predicted by turbulence-based diffusion theory while their dependences are

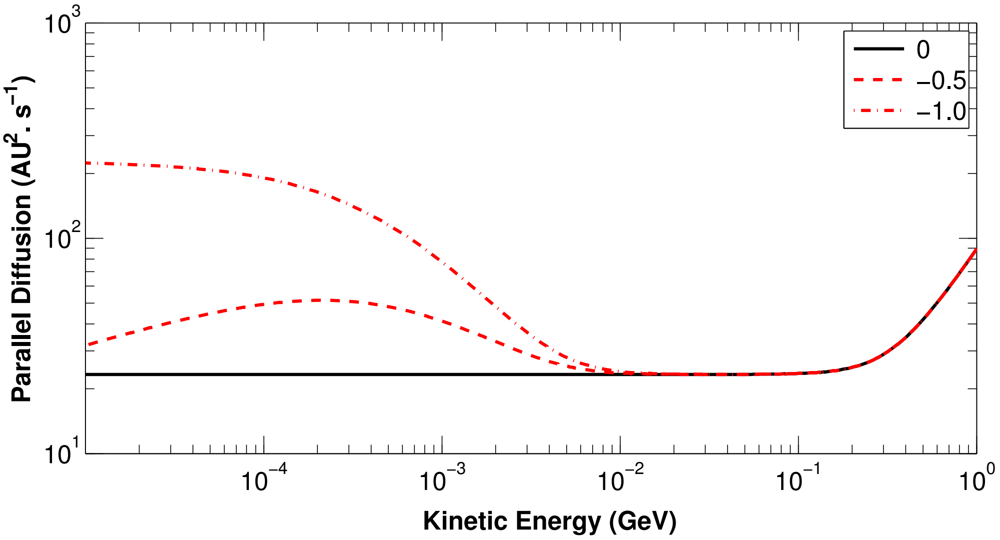

Figure 5.13: The parallel diffusion coefficient at Earth as function of kinetic energy for different configurations of Eq. 5.5 associated with the legend values for g_0. The $g_0 = 0$ profile (black line) is identical to the $\kappa \propto \beta^0$ profile of Figure 5.10, while the standard β-dependence holds for the other two profiles.

configured explicitly. The effects of the dissipation range are hence illustratively modelled by allowing the MFP to increase toward lower energies as shown in Figure 5.13. This is achieved by modifying the rigidity dependence of the electron MFPs described by Eq. 3.24 as follows,

$$\lambda_P(P) = \left[\frac{\left(\frac{P}{P_0}\right)^3 + \left(\frac{P_{k2}}{P_0}\right)^3}{1 + \left(\frac{P_{k2}}{P_0}\right)^3} \right]^{\frac{g_2 - g_1}{3}} \left[\frac{\left(\frac{P}{P_0}\right)^3 + \left(\frac{P_{k1}}{P_0}\right)^3}{1 + \left(\frac{P_{k1}}{P_0}\right)^3} \right]^{\frac{g_1 - g_0}{3}} \left(\frac{P}{P_0}\right)^{g_0} . \tag{5.5}$$

Here P_{k1} and P_{k2} represent the rigidities about which the dependence changes; $P_{k1} = 5$ MV whereas P_{k2} retains its value from P_k in Eq. 3.24. The quantity valued at 3 in the exponents stipulates the smoothness of the transitions in rigidity dependence. Finally, the parameters g_1 and g_2 specify spectral indices of the segments as previously defined, while g_0 is introduced to represent the index of the lowest rigidity segment. The diffusion profiles in Figure 5.13 are shown for different values of g_0. For $g_0 = 0$, Eq. 5.5 above reduces to Eq. 3.24, and the β-dependence of the corresponding diffusion coefficient is once more suppressed (as explained in Section 5.4.2) to provide a rigidity-independent profile as reference. For the other profiles shown, i.e. for $g_0 = -0.5$ and -1.0, coefficients retain the standard linear dependence on β. Hence, as β begins to decrease, the coefficients do not simply grow unperturbed toward lower energies according to the power laws Eq. 5.5 specifies for the MFPs, but flattens out and eventually decreases again.

The modulation following from the inclusion of these dissipation-range features in the diffusion configuration is illustrated in Figure 5.14. As seen before, rigidity-independent diffusion ($g_0 = 0$; $\kappa \propto \beta^0$) conserves the form of the input spectra throughout the heliosphere. However, if an up-turn is included in the MFPs of low-energy electrons, modulation is drastically reduced. For $g_0 = -0.5$ (dashed lines in Figures 5.13 and 5.14), the spectra at the TS and Earth are modulated less downward from 10 MeV to roughly 0.2 MeV, from where modulation (slightly) increases again. The larger MFP turn-up brought about when $g_0 = -1.0$ yields con-

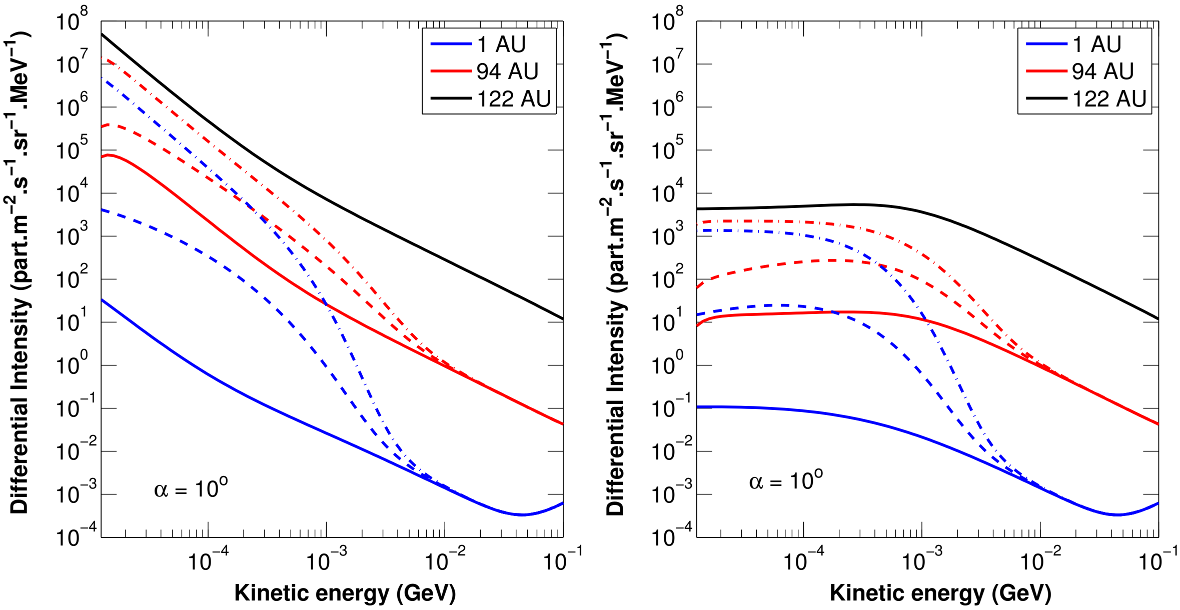

Figure 5.14: Energy spectra at the TS (94 AU, $\theta = 55°$) and Earth (1 AU, $\theta = 90°$) for different diffusion configurations as shown in Figure 5.13. The reference HPS and Eq. 5.3 with $h_0 = 1.0$ are respectively employed as input spectra in the left and right panels. Line colours represent radial distances as indicated in the legend, while solutions correspond to the profiles with the same line styles in Figure 5.13. Drifts remain disabled.

sistently less modulation with decreasing energies, with modulated spectra not only retaining the form of the HPS below $\sim$ 0.2 MeV, but also nearly coinciding with it. As also observed at the high-energy end of the spectrum, very large MFPs phase out modulation at low energies as well. Consider now the decline of the $g_0 = -1.0$ profile in Figure 5.13 between roughly 0.1 MeV to 10 MeV. Note that the resultant modulated spectra in Figure 5.14 have softened from the form of the HPS in this energy range. This is the opposite of the effect observed in Section 5.4.1, where MFPs that increase with rigidity are shown to yield modulated spectra that have hardened. Within certain limits, the forms of modulated energy distributions thus reflect the rigidity dependence of diffusion directly.

5.5 Drift-related Electron Transport and Modulation

The effects of electron drifts on modulation are apparently limited to a relatively narrow energy domain (see Figure 5.1), and constitute another major process involved in the modulation of these particles and their energy distributions. The details of this process and how it is modelled are provided in Section 3.4, whereas the effects of varying drift efficiencies and solar activity on drift-related transport, as well as its latitudinal dependence, are illustrated in Section 4.5 by application of the model to anomalous ions. While Section 5.2 highlights some differences in the modulation and transport of galactic electrons during opposite magnetic polarities, it does not quantify the actual contribution of drifts to electron intensities at different energies or spatial regions. The interplay between electron drifts and diffusion also remains to be explored. It is endeavoured in the current section to comment on these matters.

Consider first Figure 5.15, where modulated spectra at the Earth and TS are shown, both with

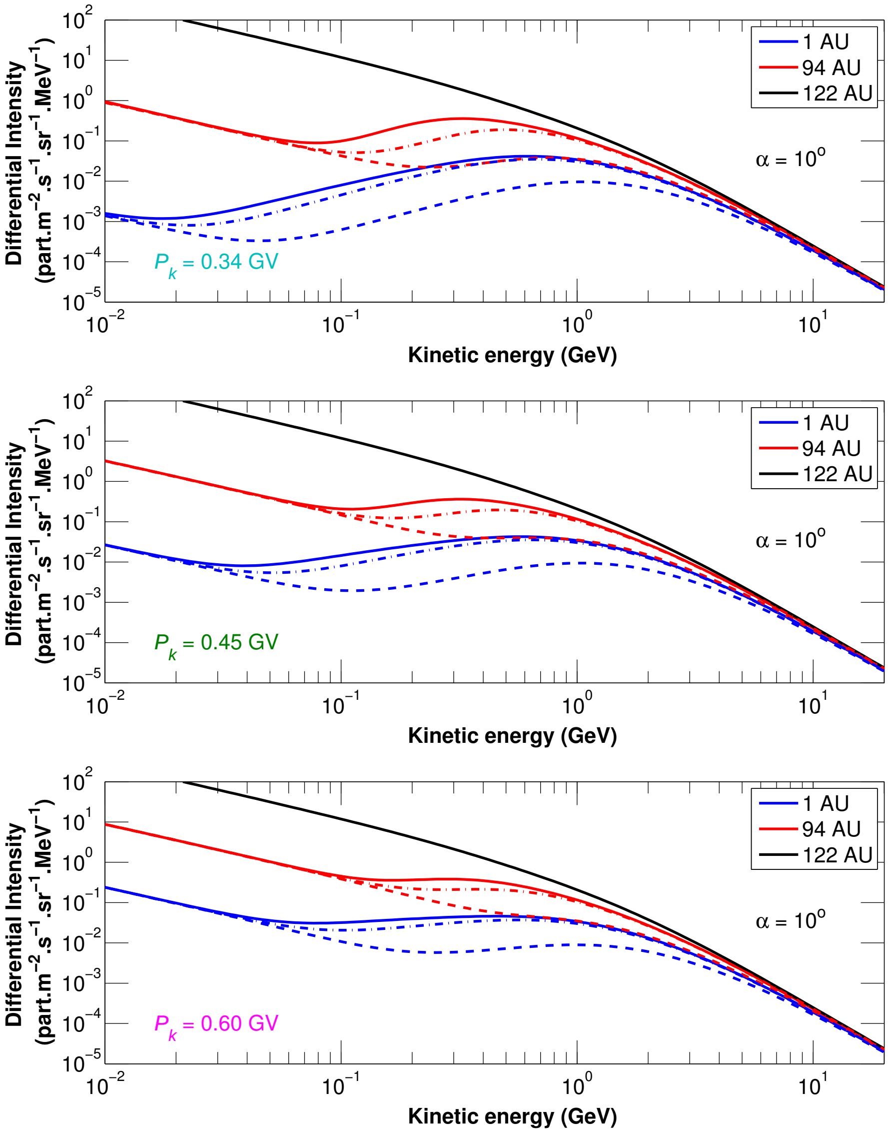

Figure 5.15: Modelled spectra at the TS (94 AU, $\theta = 55°$) and Earth (1 AU, $\theta = 90°$), respectively shown in red and blue, modulated from the HPS at 122 AU in black. Solid and dash-dotted lines respectively represent full-drift solutions for A $<$ 0 and A $>$ 0, whereas dashed lines represent no-drift solutions. Each panel corresponds to a configuration in Figure 5.8 for the indicated values of P_k (of Eq. 3.24).

drift effects (for A $>$ 0 and A $<$ 0) and without, for the three high-energy diffusion scenarios presented in Figure 5.8. It is immediately noticeable that drift effects dramatically raise spectral intensities at energies up to a few GeV and from as low as 100 MeV at the TS and 10 MeV at Earth, whereas the difference between drift solutions during opposite polarities, while significant, is not as spectacular. As far as drifts are affected by diffusion, it follows from the ratios presented in Figures 5.16 and 5.17 that larger MFPs inhibit drift effects and reduce the total contribution of drifts to electron intensities. Recall that increasing P_k (of Eq. 3.24) in Section 5.4.1 shifted the MFPs at lower rigidities upward. Hence, of the cases presented, MFPs are generally lowest for P_k = 0.34 GV, which inhibits diffusion while enhancing drift effects. This follows since the increased modulation brought about by smaller diffusion increases intensity gradients, and because the product of the drift term with ∇f is contained within the TPE. See also *Strauss et al.* [2012] for illustrative examples of how increased diffusion can inhibit drift effects.

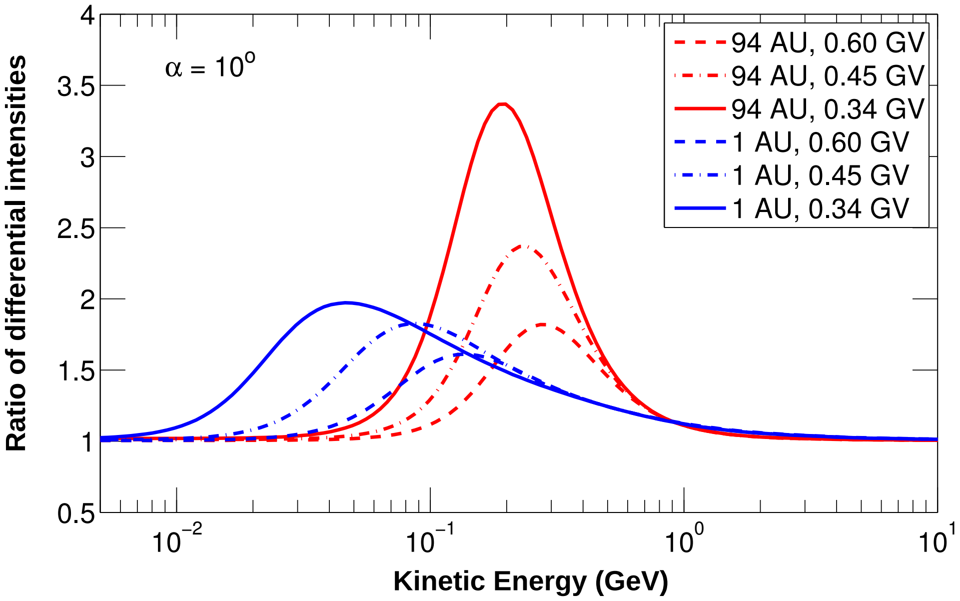

Figure 5.16: Ratios of the drift-enabled model solutions shown in Figure 5.15 with A $<$ 0 to that for which A $>$ 0. Solutions are shown for different values of P_k corresponding to the configurations illustrated in Figure 5.8 and as indicated in the legend. The ratios are shown at Earth (1 AU, $\theta = 90°$) in blue, and the TS (94 AU, $\theta = 55°$) in red.

These effects, quantified as the ratio of intensities during the negative magnetic polarity cycle to that during the positive cycle, are demonstrated in Figure 5.16 to be more pronounced at the TS than at Earth; intensities during the A $<$ 0 cycle are higher with factors of up to nearly 3.5 at the TS than for A $>$ 0, whereas at Earth these intensities are doubled at most. The increases at Earth are also more pronounced at lower energies, peaking at roughly 40 to 50 MeV, while the effects at the TS are centred around 200 MeV. For larger values of P_k these drift effects become consistently smaller and are confined to larger energies.

The total contribution of drifts during both magnetic polarities are represented by ratios of intensities predicted by model solutions for which full drifts ($\kappa_{D,0} = 1.0$) are assumed to those for which drifts are neglected ($\kappa_{D,0} = 0$); these are displayed in Figure 5.17. These ratios display the same qualitative features as discussed above for the ratios illustrated in Figure 5.16: The contributions are confined to higher energies and become smaller for larger values of P_k, and are greater at the TS than at Earth, albeit limited to a narrower energy interval. For P_k = 0.34 GV, for instance, it is illustrated in Figure 5.17 that intensities would have been up to 13 times smaller at Earth during the negative polarity cycle, and up to 15 times smaller at the TS, if there were no drifts. Also note that these contributions are consistently smaller for A $>$ 0 than for A $<$ 0; this is likely a result of the associated drift patterns. The global drift patterns of electrons and their consequences for intensities in different regions are qualitatively discussed in Section 5.2. Figure 5.18, accompanying Figure 5.3, compliments that discussion; it demonstrates for both polarities, and the standard configuration of Section 5.2, the factors by which drifts increase intensities across the heliosphere from the levels of the corresponding configuration where drifts are disabled. Via the drift patterns explained in Section 5.2 for A $>$ 0, intensities are raised inside the heliosphere at all latitudes by factors ranging from roughly $10^{0.9}$ ($\approx$ 8) near the Sun to as low as $10^{0.6}$ ($\approx$ 4) just inside the TS. Intensities are raised in this region by a much

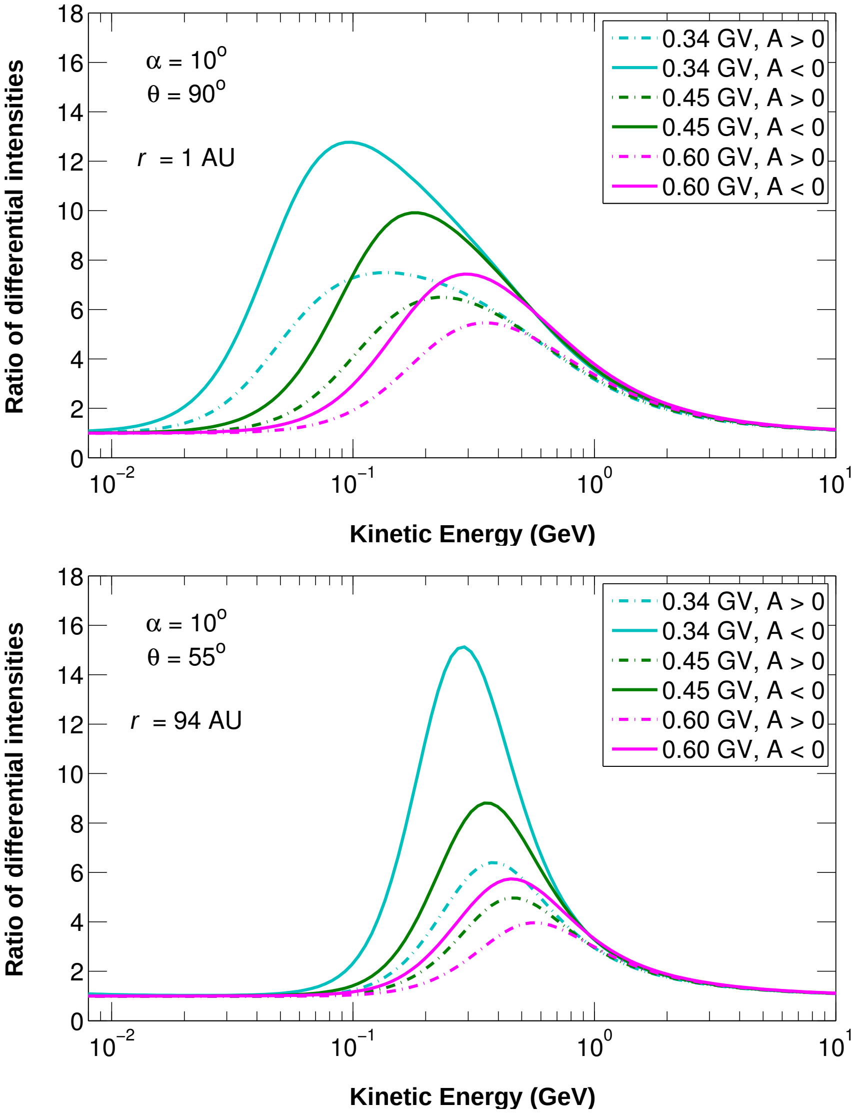

Figure 5.17: Ratios of the model solutions shown in Figure 5.15 with full drift efficiency to that for which drifts are disabled. Solutions are shown for both polarities and different values of P_k (corresponding to the configurations illustrated in Figure 5.8) as indicated in the legend. The top and bottom panels respectively show the ratios at Earth (1 AU, $\theta = 90°$) and the TS (94 AU, $\theta = 55°$).

larger average factor of about $10^{1.25}$ (≈ 18) when A < 0, hence displaying the same tendency seen earlier of the negative polarity cycle yielding larger drift contributions for electrons. It also appears from Figure 5.18 that drifts bolster heliosheath intensities somewhat in the equatorial region and reduces them at the poles for A > 0, while the converse is observed for A < 0. The reductions are represented by colours for which the quantity shown on the logarithmic colour scale is negative, i.e. for factors in the order of 10^x with $x < 0$. In general though, intensities in the heliosheath seem largely unchanged from no-drift conditions for both polarities, with an average factor change of more or less 10^0 (≈ 1) in this region.

It is important to note that the drift-related features outlined above are subject to change should the spatial configuration of other processes such as diffusion also change. Consider e.g. that the drift contribution to intensities near Earth may be larger than at some further distance inside the TS (see e.g. Figure 5.18; A > 0), because electrons transported to Earth via e.g. drifts are confined there due to smaller diffusion coefficients. Moreover, the enhanced polar diffusion

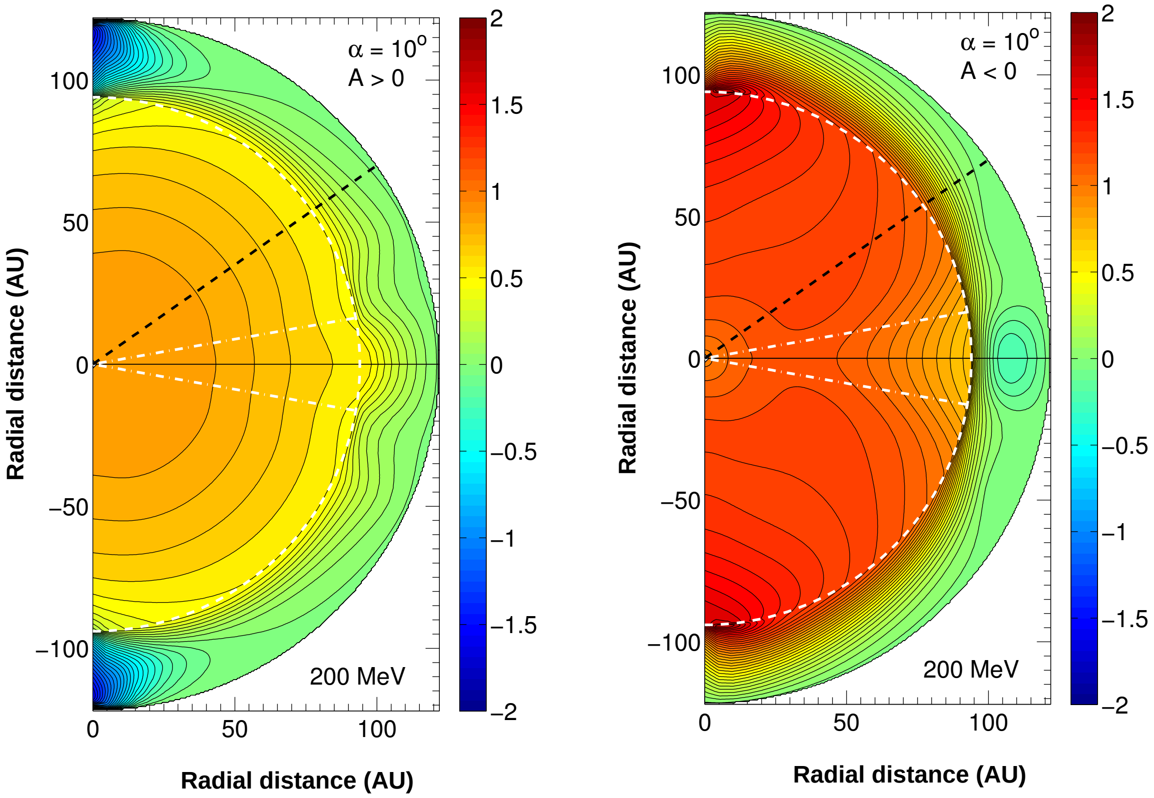

Figure 5.18: Contour plots for 200 MeV electron intensity ratios, illustrating the factor by which solutions with full drift efficiency is larger (or smaller) than corresponding solutions without drifts in the meridional plane of the heliosphere for A > 0 (left) and A < 0 (right). The colour bars follow a logarithmic scale (e.g. $1.5 \equiv 10^{1.5}$). The dashed white halfcircle indicates the TS position at 94 AU, the dash-dotted lines indicate the polar extent of the HCS for $\alpha = 10°$, and the dashed black line shows the trajectory along $\theta = 55°$ at which the corresponding ratios in Figures 5.16 and 5.17 are shown. The Sun is located at the origin.

at high latitudes facilitates particle transport through those regions, while the low-diffusion barrier in the heliosheath may hinder transport - this is touched on in the discussion on drift patterns in Section 5.2. It should also be noted that the drift features discussed above, although indicative of basic trends also predicted by 3-D models [e.g. *Strauss et al.*, 2012], are presented within the context of the 2-D model utilised in this study. While CR modulation studies conducted using 2-D models with drift capabilities usually scale down the drift efficiency based on scattering assumptions (see Section 3.4), full drift efficiency ($\kappa_{D,0} = 1.0$) is assumed for the illustrations in this section. See also the work of *Nndanganeni* [2012, 2015]. Recently, *Ngobeni* [2015] and *Ngobeni and Potgieter* [2015], also using a 2-D model, questioned if drifts could be large in the outer heliosphere - an issue that requires further investigation with full 3-D models.

5.6 Summary and Conclusions

Chapter 5 is presented to provide the necessary context for the study of the DSA of electrons in the next chapter. It outlines the relevant species-specific differences between electrons and ions that come to the fore in modulation studies as well as the modelling aspects encountered when studying GCRs - this eases the transition from the paradigms of Chapter 4. This chapter introduces and details the various major processes involved in the transport and modulation of galactic electrons that may also later influence their re-acceleration.

Section 5.2 highlights the attributes of electrons and conveys how these are accounted for in the model; the model configuration for the study of electron transport is summarised and solutions are presented as reference for subsequent sections. These solutions also convey the standard features of the modulation of galactic electrons as also reported in earlier studies. As a first step in modelling galactic electrons, various possibilities for an input spectrum is considered in Section 5.3. The reference input spectrum specified at the HP (subsequently referred to as the HPS) is discussed, and its features, especially at very low energies ($E \lesssim 5$ MeV), are surveyed. Several possible modifications to the very-low-energy HPS are suggested and evaluated by application in subsequent sections. Section 5.4 investigates the rigidity dependence of electron diffusion. A number of variations of the rigidity profiles for diffusion coefficients (and their associated MFPs) in different energy regions are discussed; these scenarios, along with some of the input spectra introduced in the previous section, will surface again in Chapter 6 to have their influence on the features of re-accelerated electrons gauged. The most probable configuration consists of a low-energy ($E \lesssim 5$ MeV) up-turn in MFPs attributed to dissipation-range turbulence effects, followed by a rigidity-independent segment at intermediate energies up to a few hundred MeV, from where MFPs increase again at higher energies.

It follows as general conclusions from Section 5.4 that sufficiently small diffusion cedes dominance to the effects of other processes such as adiabatic energy changes, while very large diffusion negates modulation altogether. Furthermore, MFPs that decrease with increasing rigidity are shown to soften distributions from the form of the input spectrum in that energy region, while harder spectra are obtained when MFPs increase with rigidity. This observation is important with regards to the acceleration of these electron distributions; see Chapter 6. Section 5.5 reveals the value of MFPs also affect electron drifts: If diffusion is impaired, drift effects and their contribution to intensities are enhanced, while drift effects are subdued for the smaller intensity gradients brought about by enhanced diffusion. Also, pertaining to more global transport, the levels of diffusion largely dictate the extent to which drifts may affect the spatial distributions of electrons.

These general modulation features of galactic electrons are revisited in the next chapter, where the interaction between the transport processes reviewed here and DSA will be drawn into focus.

Chapter 6

Diffusive Shock Acceleration of Electrons at the Termination Shock

6.1 Introduction

Galactic electrons, after having travelled through interstellar space and the heliosheath, may be accelerated upon their arrival at the TS. These locally accelerated electrons are henceforth referred to as re-accelerated electrons and it is aimed in this chapter to survey their features. The insights of the previous two chapters are hence combined, firstly to study how the acceleration of electrons at the TS is influenced by major modulating processes in the heliosphere, and also to ascertain the dependence of the DSA mechanism on the spectral properties of incident electrons. It is furthermore aimed to illustrate the contribution of re-accelerated electrons to global intensities and how this affects other processes accounted for in the TPE. A particular emphasis is placed on spectral features in this chapter, since DSA is characterised by changes in energy distributions.

As an introduction, the spectral features arising from the acceleration of strategically specified electron source functions are presented to convey the imprint of DSA on energy distributions more directly. Thereafter, the standard features of re-accelerated galactic electrons emerging under the reference model configuration are reviewed, followed by in-depth discussions of their spectral properties in subsequent sections. Due to the distinct nature of electrons and their modulation at different energies, the influence of input spectra and diffusion properties on acceleration are considered separately at low and high energies, with the effects of drifts also regarded at the latter. The spatial distributions of re-accelerated electrons are also discussed.

6.2 Spectral Properties of Shock-accelerated Electrons

Galactic electrons exhibit spectral features that were adopted both during their formation at astrophysical sites and due to modulation on their journey towards sites of re-acceleration. Consequently, the energy distribution properties electrons attain due to local acceleration at the TS are not always readily distinguishable from features priorly attained during formation

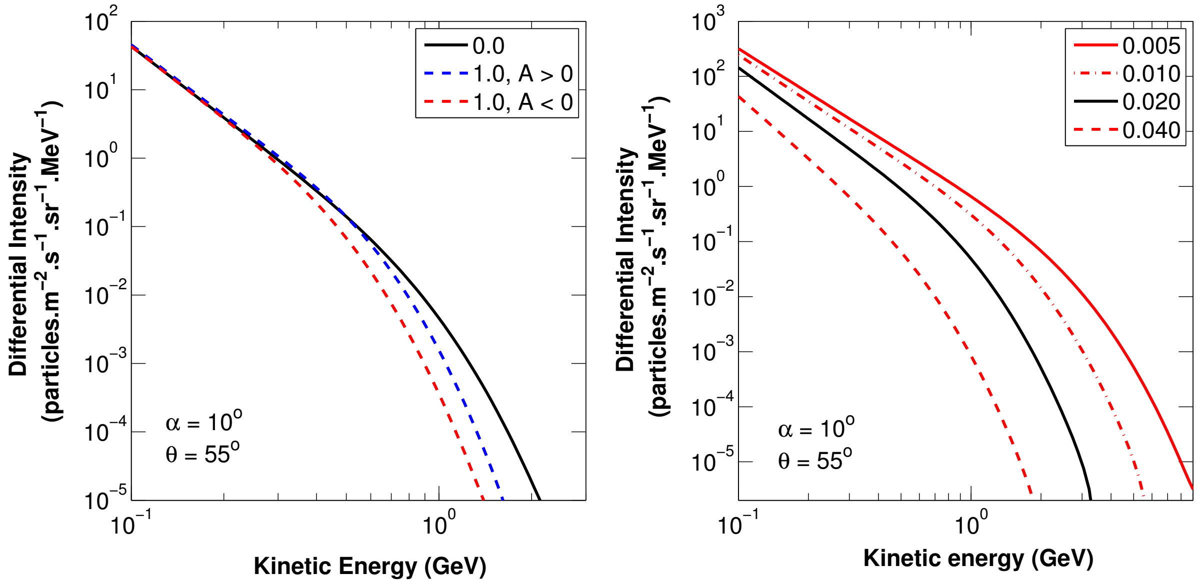

Figure 6.1: Cut-off structures of electron TS spectra modelled for a monoenergetic source injected at $P_{\text{min}} = 1.0$ MV. Legend values in the left panel correspond to $\kappa_{D,0} = 0$ and $\kappa_{D,0} = 1.0$, with the latter shown for both magnetic polarities. Spectra for different levels of radial perpendicular diffusion are shown on the right, with legend values corresponding to $\kappa_{\perp r,0}$. Here drifts are disabled, hence $\kappa_{D,0} = 0$.

and transport. To study DSA effects on electrons at the TS, it would be insightful to consider the local acceleration features initially in isolation. This may be achieved by accelerating electrons that are injected directly at the TS and modelled (as in Chapter 4) by means of a source function. The ensuing power-law spectra emerge solely as a result of DSA at the TS. Their features may vary according to the modulation conditions specified, which in turn may reveal the dependence of the DSA mechanism on the transport processes involved. Important characteristics of accelerated electron distributions are subsequently discussed for different configurations of the source function. Modelled solutions are considered along the approximate Voyager 1 trajectory at a polar angle of $\theta = 55°$ for solar minimum conditions. Note that, unless stated otherwise, the model configuration described in Section 5.2 is also applied for the solutions presented in this chapter, although the HPS is implemented only as from Section 6.3.

6.2.1 Insights from accelerating a monoenergetic electron population

Analogous to the modelling of ACRs in Chapter 4, one may specify the electron source function as a monoenergetic population of particles at the TS using Eq. 3.51. Note that this is merely an academic exercise intended to illustrate the spectral features of shock-accelerated electrons more explicitly. It is unknown whether local electrons serve as seed particles for acceleration at the TS as PUIs do; the intensities of e.g. Jovian electrons are estimated to be small at the TS [see *Ferreira et al.*, 2001a, b; *Potgieter and Ferreira*, 2002], while it is unclear what influence SEPs may have. The features of the accelerated TS spectra attained when specifying the source function in this manner have already been described for ACR Oxygen: A single power-law distribution emerges, with an intensity enhancement (or depression, depending on the magnetic polarity) preceding an exponential decrease; see e.g. Figures 4.1, 4.4 and 4.7. The latter features are demonstrated in Sections 4.4 and 4.5 to be respectively dependent on drift and radial perpen-

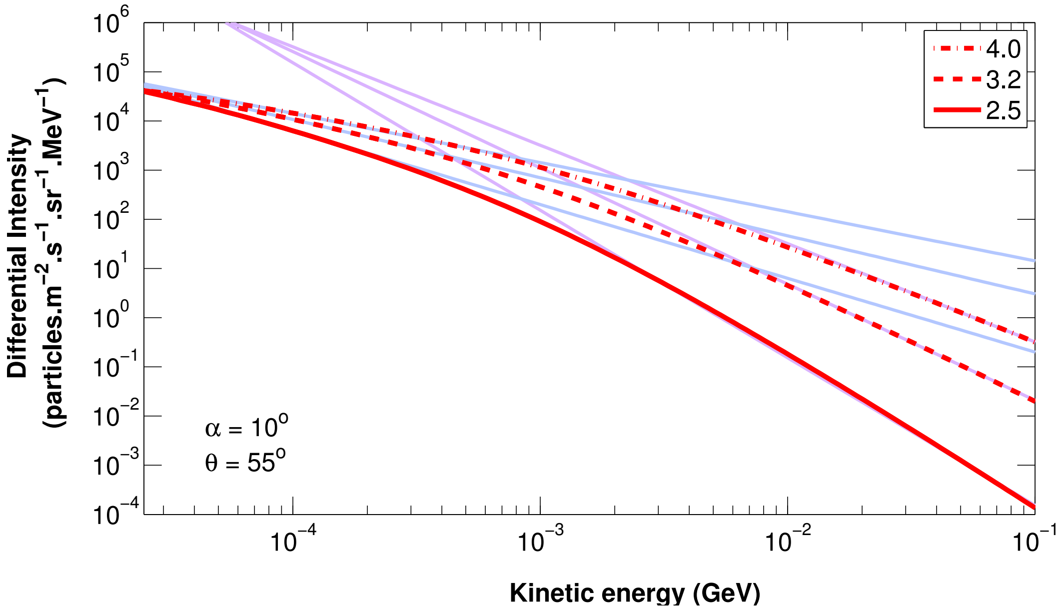

Figure 6.2: Electron TS spectra modelled for a monoenergetic source for different values of the compression ratio as indicated in the legend. The lavender and light blue lines are power laws with spectral indices as shown in Table 6.1 that correspond to each compression ratio respectively above and below the electron rest-mass energy at $5.11 \cdot 10^{-4}$ GeV.

dicular diffusion, while Section 4.3 shows that the spectral index of the power law is a function of the shock compression ratio alone. For electrons however, no significant drift-dependent intensity enhancements or depressions precede the cut-off, but Figure 6.1 (left) does show that the power law extends to slightly higher energies in the absence of drifts (as is also shown in Section 4.5). Furthermore, accelerated electron distributions are shown in Figure 6.1 (right) to terminate at higher energies for smaller diffusion coefficients (similar to ACR Oxygen in Figure 4.5; see also *Potgieter and Moraal* [1988]). Indeed, the hardening of accelerated spectra is also associated with impaired diffusion [e.g. *Axford*, 1981]. Collectively, these cut-off features do resemble that of the ACR spectra referenced above.

The power-law distribution itself, however, manifests differently as a function of kinetic energy for electrons than for ACR Oxygen or indeed any other CR ions. This is one of the consequences of the electron's smaller rest-mass energy. Section 3.6.2 demonstrates that at energies large enough for the rest-mass energy to become comparably negligible, the spectral index associated with the shock compression ratio becomes twice as steep than at energies much smaller than the rest-mass energy. That is,

$$\gamma\left(s\right)=\begin{cases}\left(s+2\right)/\left(2-2s\right), & E\ll E_0\\ \left(s+2\right)/\left(1-s\right), & E\gg E_0,\end{cases}\tag{6.1}$$

where $\gamma(s)$ represents the spectral index as a function of the compression ratio, s, of the accelerated power-law spectrum of the form $j\propto E^{\gamma}$, and E_0 is the rest-mass energy that may be interchanged with e_0 when considering electrons. Eq. 4.1 suffices to describe the indices of the accelerated spectra in Chapter 4, since those spectra terminate well before attaining the proton rest-mass energy. The accelerated distributions of electrons, on the other hand, may extend to energies larger than 1 GeV (see Figure 6.1), which is roughly two thousand times larger than

s	2.5	3.2	4.0
$E \ll e_0$	-1.50	-1.18	-1.00
$E \gg e_0$	-3.00	-2.36	-2.00

Table 6.1: Values for $\gamma(s)$ calculated from Eq. 6.1 for the energies and compression ratios as indicated.

the electron rest-mass energy. Electrons therefore straddle the transition from a non-relativistic to a relativistic regime across the range of energies considered in this study, and their accelerated distributions exhibit both power laws described by Eq. 6.1 across this range. Figure 6.2 illustrates this. The figure shows TS spectra for different compression ratios, with the larger ratios yielding harder spectra as expected. A transition occurs in the proximity of e_0, where the distributions steepen from that also encountered in Figure 4.4 into the softer power laws predicted by Eq. 6.1 for $E \gg e_0$. The spectral indices of the power laws observed for each compression ratio in both energy regions are listed in Table 6.1. At transitional energies the spectral index may adopt any value in the interval between the limits provided in the table, e.g. $\gamma = [-1.50, -3.00]$ for $s = 2.5$. Should Figure 6.2 be extended to lower energies, where the ratio, β, of particle to light speed begins to approach zero, the effect discussed in Section 4.7 will come into play and cause spectra to deviate from the expected power laws due to diminished length scales of diffusion. However, at the energies considered, diffusion length scales remain constant (due to the rigidity independence of the MFP) and in excess of the TS width so that the electrons observe the full compression ratio. For fully relativistic electrons, the hardest distribution that DSA is typically expected to yield for $s = 2.5$ has a spectral index of $\gamma = -3.0$, while the largest index obtainable at any shock in a monoatomic medium is $\gamma = -2.0$ (for $s = 4$; see Section 2.6.1). These upper limits also apply in subsequent discussions.

6.2.2 The imprint of DSA on electron distributions

Another useful exploit of the source function when studying shock-accelerated spectra is to specify it as an electron population that is already distributed with energy, and analysing how this distribution is altered after being subjected to DSA. In this way one may directly study the imprint of this acceleration mechanism on spectral structures that are typically expected to be encountered at the TS; power laws are likely specimens, since they are contained in the HPS and mostly preserved during modulation in case of rigidity-independent diffusion (see Chapter 5). To model the source function as a power-law distribution, Eq. 3.51 is adapted to

$$Q = Q^{*}\delta\left(\frac{r - r_{TS}}{r_0}\right)\left(\frac{E}{E^{*}}\right)^{\chi}, \tag{6.2}$$

where $Q^{*} = Q\left(E^{*}\right)$ is arbitrarily chosen, χ is the spectral index of the initial distribution, and the rest is as previously defined. The accelerated TS spectra emerging from different initial distributions are illustrated in Figures 6.3 and 6.4 for each of the compression ratios considered in Section 6.2.1. The panels on the right-hand side of these figures accentuate deviations from the injected power law. For a hard initial spectrum, such as for $\chi = -1.5$, the accelerated TS spectra retain the slope of the injected power law and the electrons are merely shifted upward

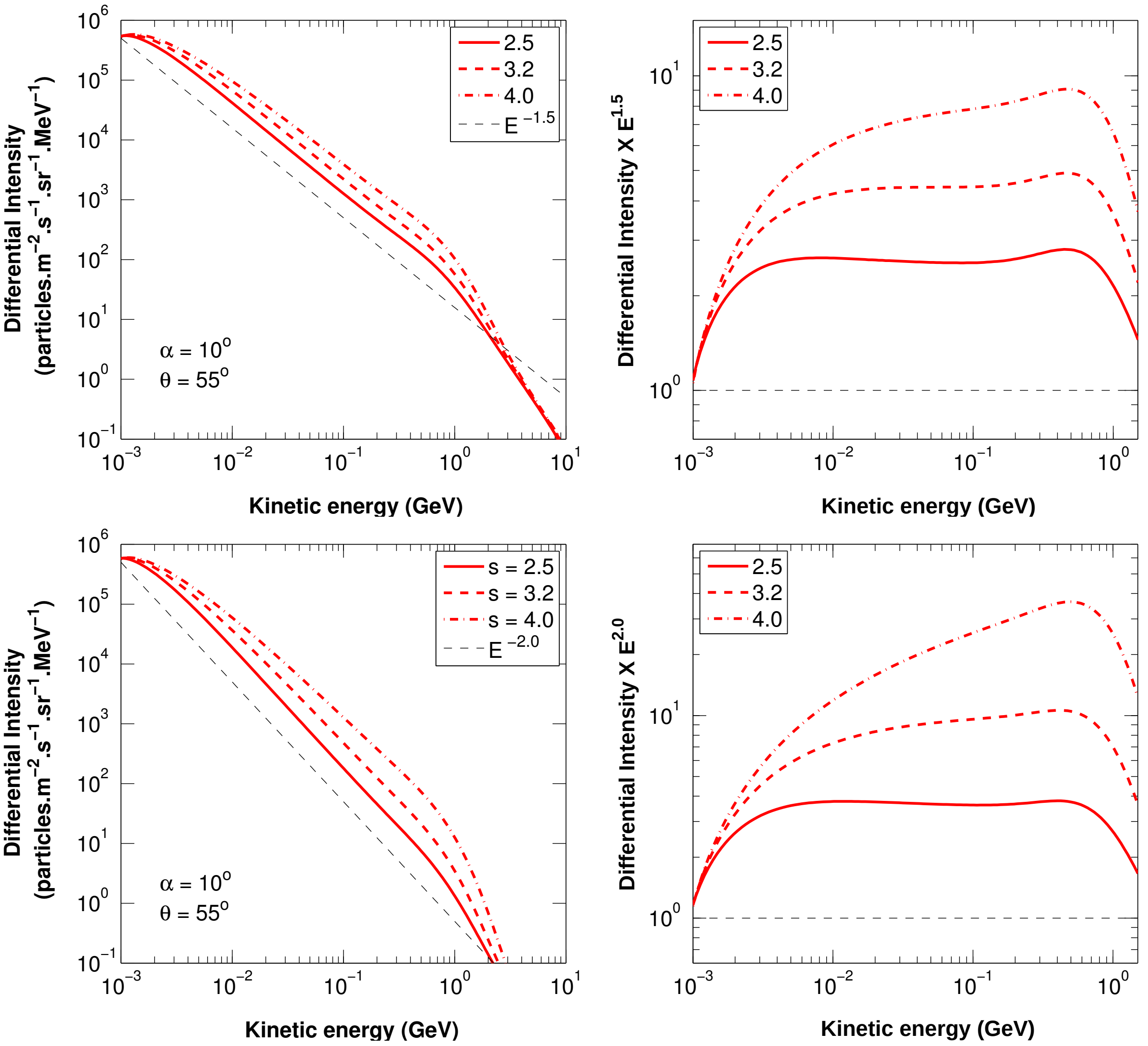

Figure 6.3: The modelled electron TS spectra shown on the left are accelerated from initial power-law distributions $E^{-1.5}$ (top panel) and $E^{-2.0}$ (bottom panel) for different compression ratios as indicated in the legend. Initial distributions are shown as black dashed lines. The solutions on the right are the same as those on the left, but are respectively multiplied by $E^{1.5}$ and $E^{2.0}$ and normalised to unity at $E = 10^{-3}$ GeV. The scale is chosen such that flattening out to a constant value signifies alignment with the initial power law, which is represented by a horizontal dashed line along unity.

in energy to yield a uniformly raised spectrum. The $E^{1.5}$-multiplied spectra remain constant across most of the considered energies, signifying that no hardening from the original spectrum occurs, with the exception of the spectrum for $s = 4.0$. Similarly, only a shock with $s = 4.0$ can produce a spectral index of -2.0 so that hardening is still marginal for weaker shocks if $\chi = -2.0$, although intensities are raised by larger factors. For an initial spectrum soft enough for a shock with $s = 2.5$ to produce, such as for $\chi = -3.0$, spectral intensities are raised by even greater amounts and significant hardening occurs for stronger shocks. Finally, for a very soft initial distribution, e.g. for $\chi = -4.0$, the accelerated spectra yield indices approximately equal to that calculated from Eq. 6.1. In this case intensities are raised from the injected spectrum with factors of a few hundred at 10 MeV, while nearer to 1 GeV spectra are raised by factors ranging from a few thousand for $s = 2.5$ to over a million for $s = 4.0$. This lopsided rise in spectral intensities, favouring the high-energy side of the spectrum, emerges as one of the most

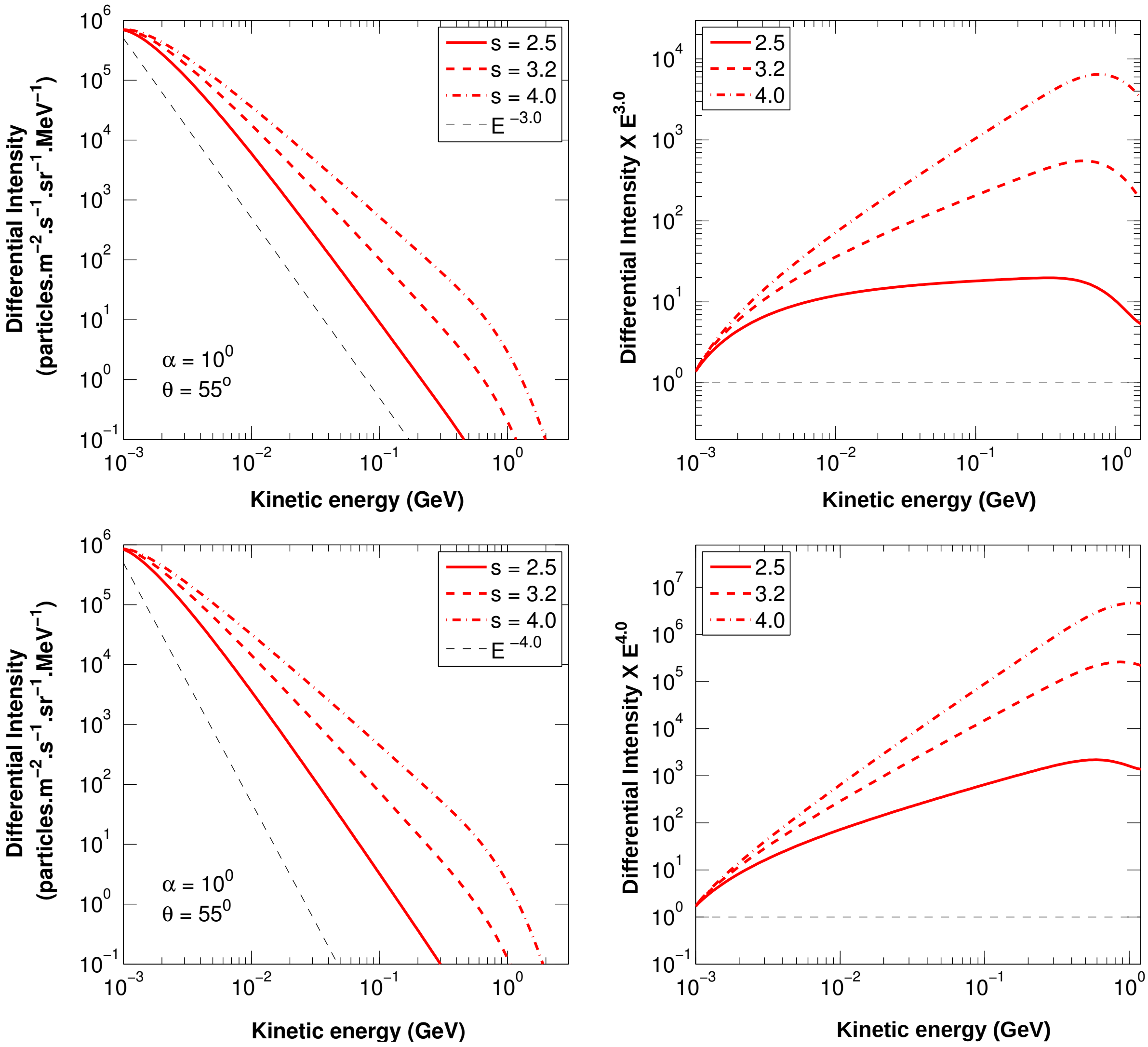

Figure 6.4: Similar to Figure 6.3, but for initial distributions $E^{-3.0}$ (top panel) and $E^{-4.0}$ (bottom panel).

revealing features of shock-accelerated electron distributions. Also note for future reference that the accelerated spectra consistently terminate above ~ 1 GeV, from where intensities begin to decrease exponentially.

Hence, to summarise, the effect DSA has on the energy distributions of particles injected at the TS is twofold: Firstly, should the initial distribution have a spectral index, χ, that is smaller than what the shock is expected to produce for monoenergetic injection, i.e. $\gamma(s)$ as per Eq. 6.1, the index, γ', observed for the accelerated distribution will be equal to the latter. That is,

$$\chi < \gamma(s) \implies \gamma' \approx \gamma(s). \tag{6.3}$$

If the initial distribution has a spectral index larger than what the shock is expected to produce, the former is retained. That is,

$$\chi > \gamma(s) \implies \gamma' \approx \chi. \tag{6.4}$$

In this second case, the initial spectrum is merely translated upward during acceleration by an amount depending on how similar χ and $\gamma(s)$ are. *Axford* [1981] and *Jones and Ellison* [1991] report similar findings. Note that these results are generally valid and applicable to any distribution (or part thereof) of CRs incident on the TS. This becomes especially relevant when interpreting the acceleration features for spectra arriving at the TS after being modulated from an initial spectrum, such as the HPS, specified further downstream. The dependence of acceleration effects on the hardness of spectra is a recurring concept in following sections.

6.3 Standard Features of Re-accelerated Galactic Electrons

In Chapter 5 the effects of various electron transport and modulation processes are studied with DSA at the TS suppressed, and hence the global characteristics that would arise from it are absent in the presented model solutions. It is however the purpose of the current chapter to demonstrate the effects of DSA on the modulated spectra incident at the TS, as well as to illustrate the transport of the consequently re-accelerated electrons. The restriction imposed in the previous chapter to suppress acceleration effects in the shock region is hence lifted to present *shocked* (or re-accelerated) solutions. That is, as described in Section 3.6, the negative divergence of the SW velocity in the shock region is allowed to translate into particle heating, which, subject to the matching condition, emulates the theoretically expected effects of DSA. Solutions without shock-acceleration effects are however still shown for comparison, and ratios of shocked to unshocked solutions are also used to accentuate the factors by which DSA increases electron intensities as functions of both position and energy. Note that all source functions are henceforth set equal to zero (as in Chapter 5), and that all spectral solutions are modulated and (where applicable) re-accelerated forms of the HPS.

6.3.1 Energy distributions of re-accelerated electrons

The standard model configuration of Section 5.2 with shock acceleration yields the energy spectra shown in Figure 6.5, which is accompanied for comparison by the DSA-suppressed solutions (shown in dashed lines) that are also illustrated in Figure 5.1. The acceleration appears from these spectra to be predominantly effective at energies lower than 100 MeV, although still visible up to a few GeV. Acceleration effects do not appear however to be substantially different for opposite magnetic polarities, and the more general spectral differences resemble that already attributed to drift-related modulation in Section 5.2. However, if the contribution of electrons accelerated at the TS is accentuated, and ratios of shocked to unshocked solutions are considered, the effects of drifts on the re-accelerated contribution are more evident. Figure 6.6 demonstrates that re-accelerated electrons may raise intensities at the TS with up to a factor of 2.5 from roughly 4 to 50 MeV for $A < 0$ and up to nearly 100 MeV for $A > 0$. This translates in turn to roughly doubled intensities at Earth up to 10 and 20 MeV for $A < 0$ and $A > 0$ respectively. Interestingly, a prominent feature that emerges for both polarities is a second energy region (aside from that already referenced above) with a relatively large re-accelerated contribution: The ratios plotted in Figure 6.6 attain a local maximum of ~ 1.5 near 1 GeV, preceded by a local minimum at roughly 200 MeV for $A < 0$ and 300 MeV for $A > 0$.

The insights garnered in Section 6.2 are essential in the interpretation of these features. Recall from Eq. 6.3 and 6.4 that DSA is unable to alter the indices of distributions that are larger

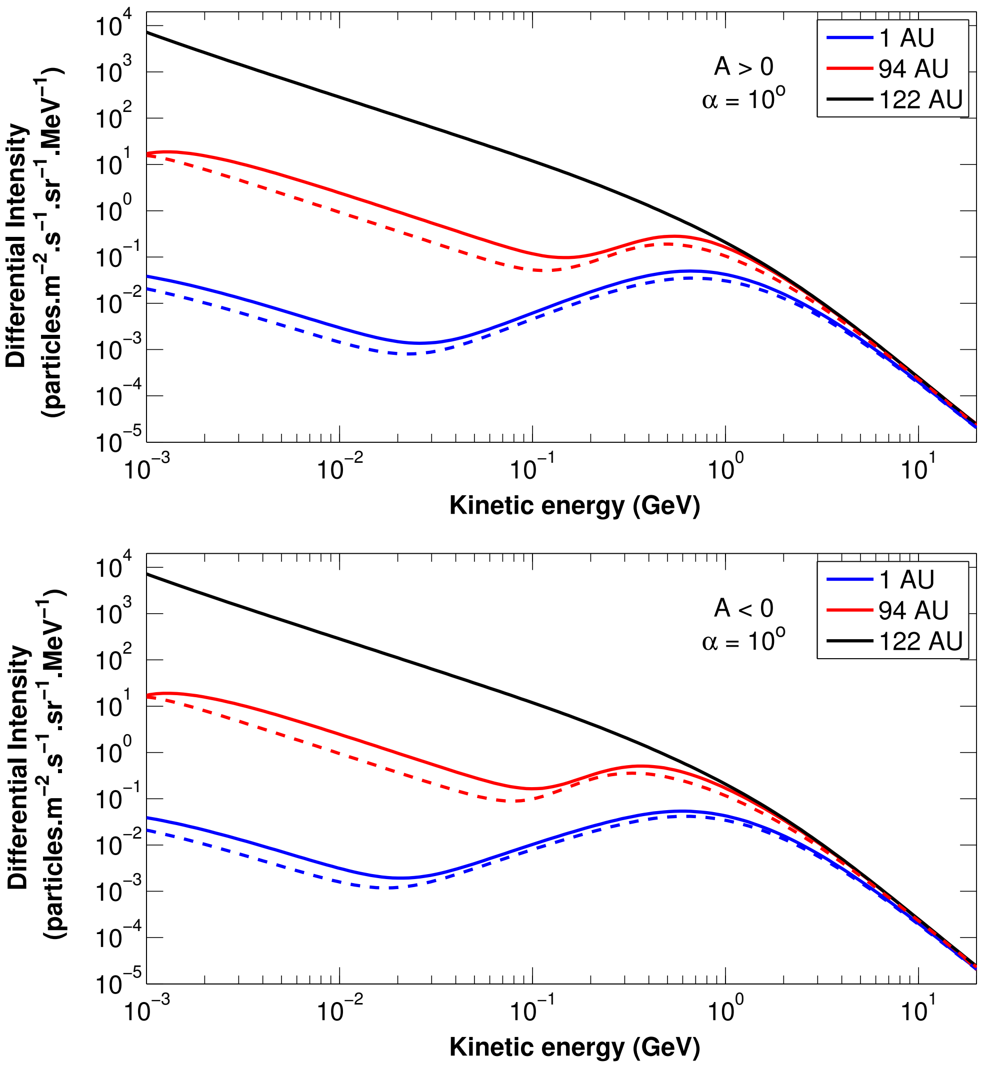

Figure 6.5: Modelled energy spectra for galactic electrons at the TS (94 AU, $\theta = 55°$) and Earth (1 AU, $\theta = 90°$) as modulated from the reference HPS (black line) at 122 AU. Line colours represent radial distances as indicated in the legend, while solutions with and without shock acceleration are shown in solid and dashed lines respectively. These solutions are shown for A > 0 (top panel) and A < 0 (bottom panel) during solar minimum conditions ($\alpha = 10°$).

than the index associated with the shock compression ratio, and uniformly raises the intensities instead. The factors by which the intensities are raised also depend on how similar the aforementioned indices are. Hence, the distribution up to nearly 100 MeV arriving at the TS, after having retained the power-law index of -1.35 during its modulation in the heliosheath, is too hard to be altered significantly by a shock with $s = 2.5$, which can at the very most yield an accelerated index of -3.0. As a result its intensity is raised uniformly with a factor of ~ 2.5 as mentioned before. The succeeding depression in acceleration effects, centred around 100 to 200 MeV, similarly follows because the spectrum incident at the TS becomes very hard due to decreasing modulation (as result of increasing MFPs) with increasing energy. Consequently, the intensities are raised by a barely noticeable factor on the scale of Figure 6.5. However, as modulation eventually diminishes toward 1 GeV due to very large MFPs, and the TS spectrum inherits the soft -3.18 power-law index from the HPS, acceleration effects are restored. Due to the similarity of the incident spectrum to that producible by the TS, intensities are raised by

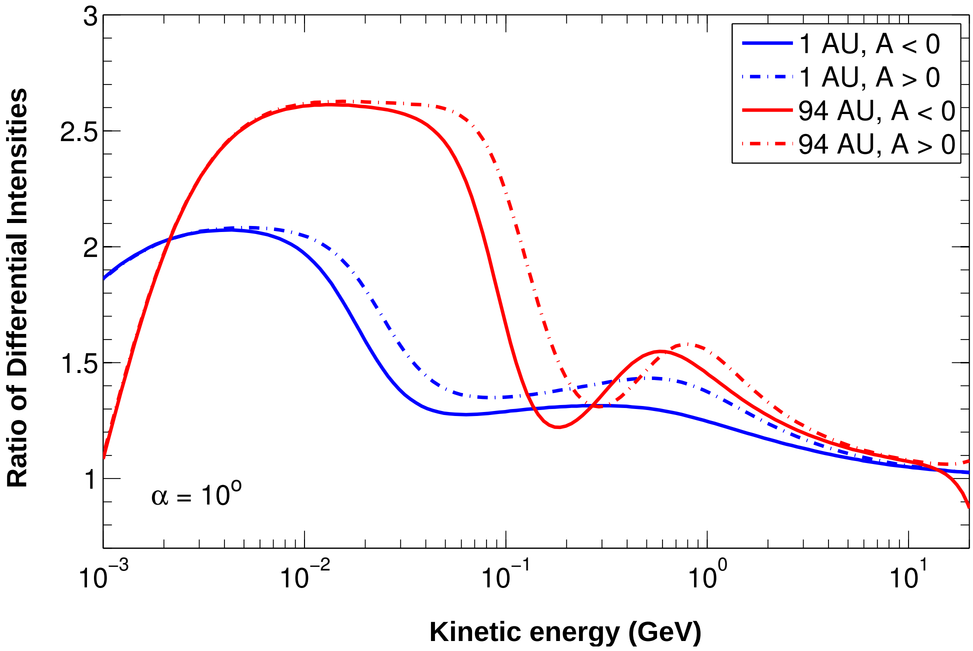

Figure 6.6: Ratios of the spectra shown in Figure 6.5 at the TS (94 AU, $\theta = 55°$) and at Earth (1 AU, $\theta = 90°$) with shock acceleration to those without. Line styles and colours respectively represent the magnetic polarities and radial distances as indicated in the legend.

a surprisingly large factor at such high energies of nearly 1.6. Figures 6.7 and 6.8 show radial profiles that are representative of electrons in each of the aforementioned spectral regions and reflect similar acceleration features at the TS position. Ultimately though, as in Section 6.2, acceleration effects wane due to the TS curvature limit (Eq. 3.55) at $E \gtrsim 1$ GeV. The higher energies obtained by re-accelerated electrons during the positive polarity cycle as shown in Figure 6.6 follows because the contribution of drifts to intensities manifests at higher energies during this cycle (see Figure 5.17). Drifts harden spectra between $\sim$ 100 and 400 MeV by raising intensities at the TS sharply between these energies; by the insights garnered earlier, DSA cannot raise the intensities of such hard distributions appreciably, and hence the re-accelerated contribution is diminished. From the ratios of Figure 6.6 it follows that the re-accelerated contribution is generally larger for A $>$ 0 than for A $<$ 0 (see also Figure 6.8), except for a narrow region between 300 and 700 MeV where the opposite is true. The discussion on drifts and their influence on the re-acceleration of electrons, and vice versa, is continued in Section 6.4.3.

6.3.2 Radial distributions of re-accelerated electrons

Though the spectral changes incurred due to DSA are revealed to be subtle, a further consideration to gauge the influence of this mechanism is the distribution of re-accelerated electrons throughout the heliosphere. Its largest contribution to electron intensities is of course expected at the shock itself, but subject to the various transport processes involved, intensities elsewhere may also be bolstered. Figure 6.7 shows the radial profiles of electrons at different energies both with and without the contribution of DSA. It is revealed, as in Figures 6.5 and 6.6, that re-acceleration is most prominent at lower energies, and that the contribution of these re-accelerated electrons is appreciable even in the deep heliospheric interior. Considering only

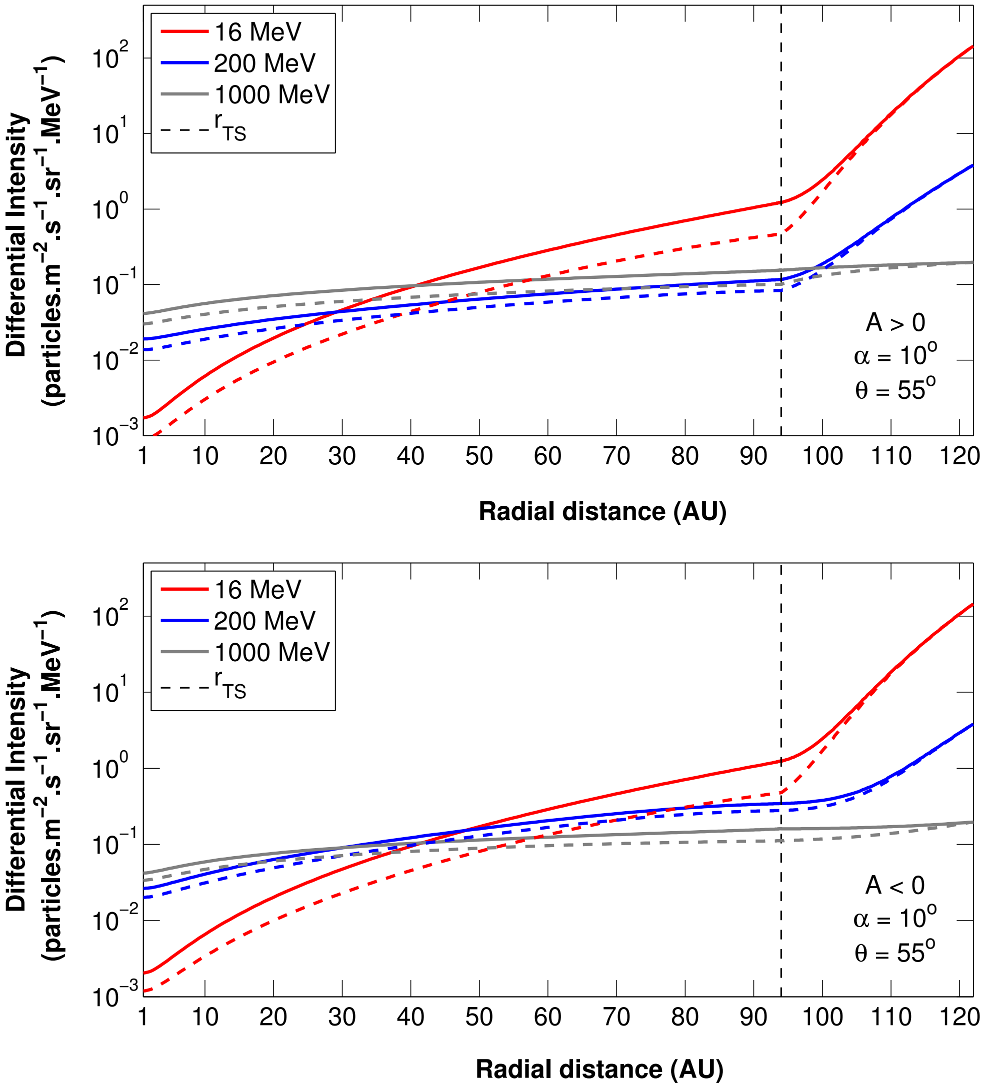

Figure 6.7: Modelled radial intensity profiles with DSA at the TS (solid lines) and without (dashed lines) for galactic electrons at sample energies of 16 MeV, 200 MeV and 1 GeV, represented by different line colours as indicated in the legend. Solutions are shown along $\theta = 55°$ for solar minimum conditions ($\alpha = 10°$) and both A > 0 and A < 0 as shown in the top and bottom panels respectively. The TS is marked at 94 AU with the vertical dashed line and the HP is at 122 AU.

these intensity profiles, the effects of DSA are not obvious aside from a general increase in intensities. Earlier studies [e.g. *Ferreira et al.*, 2004b; *Langner and Potgieter*, 2004; *Potgieter and Langner*, 2004] on the DSA of galactic electrons showed a more definitive intensity peak at the TS position, while the profiles in Figure 6.7 appear in contrast smooth across this boundary. The re-accelerated contribution does however peak at the TS, as illustrated by the ratios in Figure 6.8, and constitutes a factor increase in intensities there of at least 2.5 for 16 MeV electrons. By the same low-diffusion properties responsible for the massive decrease in galactic electron intensities across the heliosheath, the electrons re-accelerated at the TS do not diffuse far into the heliosheath either. In fact, under the current configuration, the model predicts that no re-accelerated electrons (for $E < 1$ GeV, at least) reach the HP. By contrast, the contribution inward from the TS is quite noticeable; the diffusion coefficients increase towards the TS inside the heliosphere so that re-accelerated electrons may permeate further into the heliosphere. The re-accelerated contribution in fact raises intensities throughout most of the interior by a factor

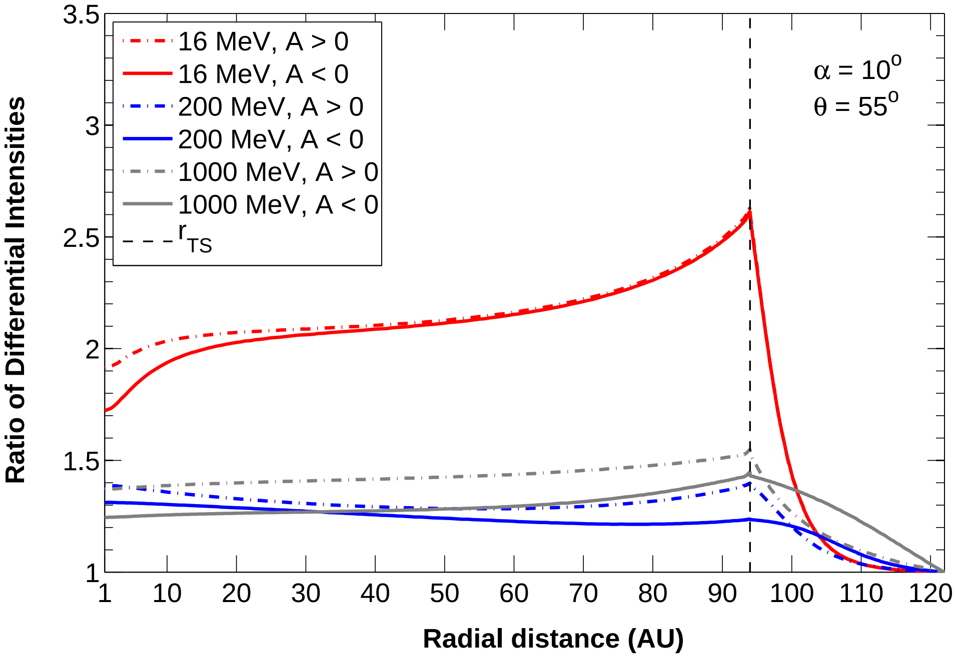

Figure 6.8: Ratios of the profiles shown in Figure 6.7 with shock acceleration to those without. Line styles and colours respectively represent the magnetic polarities and electron energies as indicated in the legend. The TS is marked at 94 AU with the vertical dashed line and the HP is at 122 AU.

of up to 2. This spread-out intensity profile upstream of the TS and the steep increase of intensities downstream in the heliosheath collectively serve to obscure intensity increases arising due to local acceleration, and hence a definitive peak-like structure is not observed at the shock in Figure 6.7. These profiles are shown at a polar angle of $\theta = 55°$; Section 6.6 illustrates the spatial distributions of re-accelerated electrons more globally and in greater detail.

6.4 Re-acceleration of Intermediate- and High-energy Electrons

Expanding on the review of Section 6.3 on the general properties of re-accelerated electrons, this section focuses particularly on the features and processes of which the effects appear predominantly at energies above ~ 10 MeV. For instance, it is discussed in this section how properties following from the high-energy rigidity profile of diffusion and electron drifts affect DSA. Explored first, however, is how the configuration of the HPS affects DSA at higher energies, and conversely whether and to what extent re-accelerated electrons are expected to influence intensities away from the TS.

6.4.1 Shock acceleration and the heliopause spectrum

Section 5.3 proposed a reference HPS that exhibits a power law at Voyager-observed energies with a spectral index between -1.35 and -1.55, based on spacecraft measurements of electron intensities [*Stone et al.*, 2013]. This power law is retained by the modulated energy spectrum incident at the TS as a result of rigidity-independent diffusion. As established in Section 6.2, a TS with a compression ratio of $s = 2.5$ is too weak to alter distributions with the aforementioned

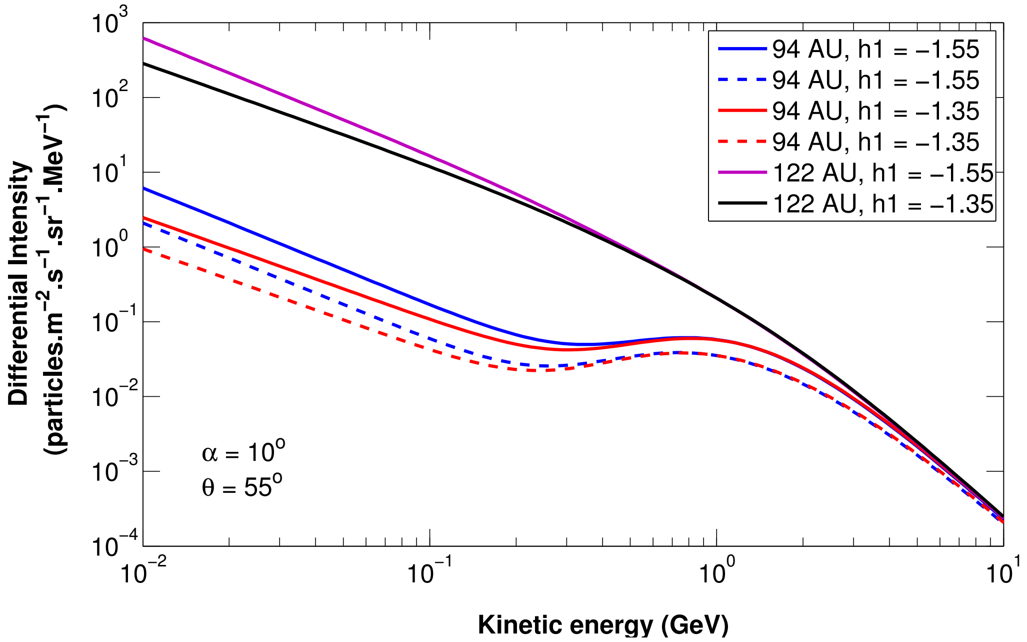

Figure 6.9: The modelled TS spectra in red and blue are respectively modulated from the HPS at 122 AU described by Eq. 5.1 with $h_1 = -1.35$ (in black) and -1.55 (in magenta). At the TS (94 AU, $\theta = 55°$), solid lines represent spectra with DSA effects and dashed lines represent spectra without. Drifts are disabled for these solutions.

spectral indices, but can raise their intensities. Indeed, Figure 6.9 shows that the intensities of the TS spectra are raised uniformly, and hence the power-law distributions are preserved not only during modulation, but also during the re-acceleration process. This holds for both the initial power-law distributions illustrated. While it is unclear from Figure 6.9 whether the amount by which DSA raises intensities differs substantially for the cases considered, Figure 6.10 creates a clear distinction: Intensities are raised up to 100 MeV by a factor of almost 3 for the incident distribution with index -1.55, as opposed to a factor increase of about 2.6 for -1.35. Thus, in accordance with earlier findings, the harder distribution once again proves more difficult to accelerate: The re-accelerated contribution can be more than 10 % larger when the lower limit on the Voyager-observed power-law index is used than for when the upper limit is employed. At higher energies the ratios converge for both initial distributions as the spectra adopt the softer power law with an index of -3.18. Note that since this high-energy index is similar to the -3.0 index attainable by accelerated spectra at the TS, the re-accelerated contribution might have been much larger had the curvature limit of the shock not also been attained at these energies. Intensities at high energies are nevertheless raised by an appreciable amount as also pointed out in Section 6.3. Evidently, the features of the HPS dictate to a large extent the features displayed by spectra incident at the TS; this, depending on how hard the distribution inherited from the HPS is, determines in turn the extent to which DSA raises spectral intensities at the TS.

When considering the converse – how DSA at the TS affects properties of the HPS or any distribution beyond – the low-diffusion barrier in the heliosheath is a great limiting factor. Under the standard configuration, particles with energies of up to a few hundred MeV are unable to penetrate far into the heliosheath, and it is unlikely that they will diffuse as far out as the HP. This is demonstrated in Figure 6.8. At higher energies MFPs increase so that the modulation

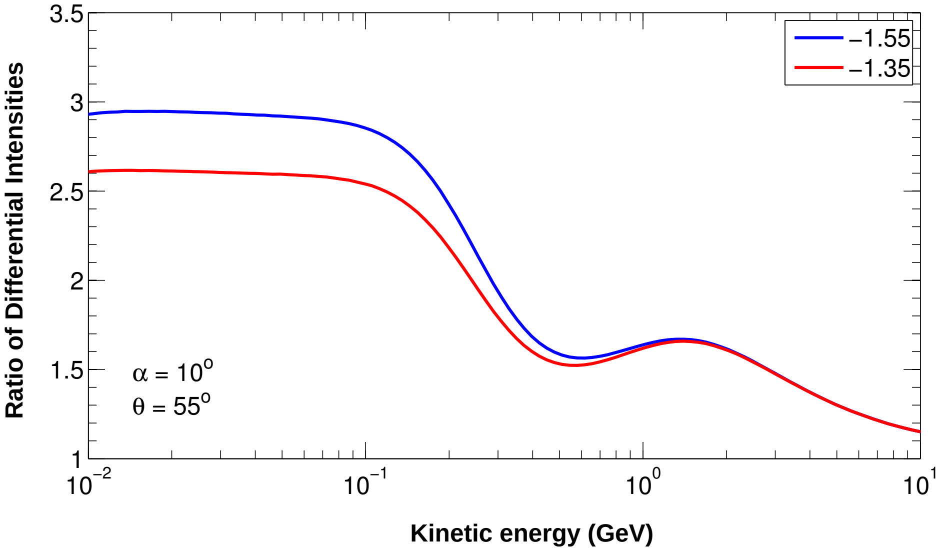

Figure 6.10: Ratios of the TS spectra presented in Figure 6.9 with DSA effects to those without. Legend values correspond to the spectral index h_1 of Eq. 5.1 according to which the HPS is configured.

barrier is lifted to an extent and particles pervade further into the heliosheath. This may suggest that local acceleration could have some influence on the HPS despite not being reflected in the modelled profiles; the numerical scheme forces the distribution function to adopt the fixed values specified as boundary conditions at the HP. Had the HPS been allowed to change dynamically during the solution of the TPE, the effects of DSA might have been visible at the HP at high energies. Indeed, earlier studies [e.g. *Potgieter and Ferreira*, 2002; *Langner and Potgieter*, 2004] predict that under certain conditions the TS spectra for electrons can actually exceed the intensity levels of the HPS between 0.1 and 1 GeV, albeit for overestimated shock compression ratios and lower input spectrum values. Under the standard model configuration, and with drifts neglected, Figure 6.10 illustrates that DSA raises spectral intensities at the TS with factors of up to 1.6 at energies exceeding 1 GeV. While it is conceivable that these high-energy re-accelerated electrons can enhance intensities at the HP, it can almost certainly do so at Earth. Figure 6.6 shows that intensities for electrons of a few hundred MeV are raised 30 to 40 % at Earth (depending on the polarity cycle) due to re-accelerated particles being transported there from the TS. This may easily contribute to the low-energy end of the intensity enhancement described by Eq. 5.2, drawing into question the extent to which this enhancement should be accounted for in the HPS; local acceleration may after all play a more substantive role in this regard than initially anticipated. This requires further investigation.

6.4.2 Dependence on the rigidity profile of diffusion

The form of the HPS is shown in the previous subsection to influence the re-acceleration of spectra at the TS, because it is largely preserved during modulation as a result of rigidity-independent diffusion. This is also the case at high energies, since very large MFPs phase out modulation. If the rigidity dependence of the diffusion coefficients is however altered such that modulated spectra do not necessarily reflect the characteristics of the original energy distribution, the properties of this new dependence would dictate the form of the distributions

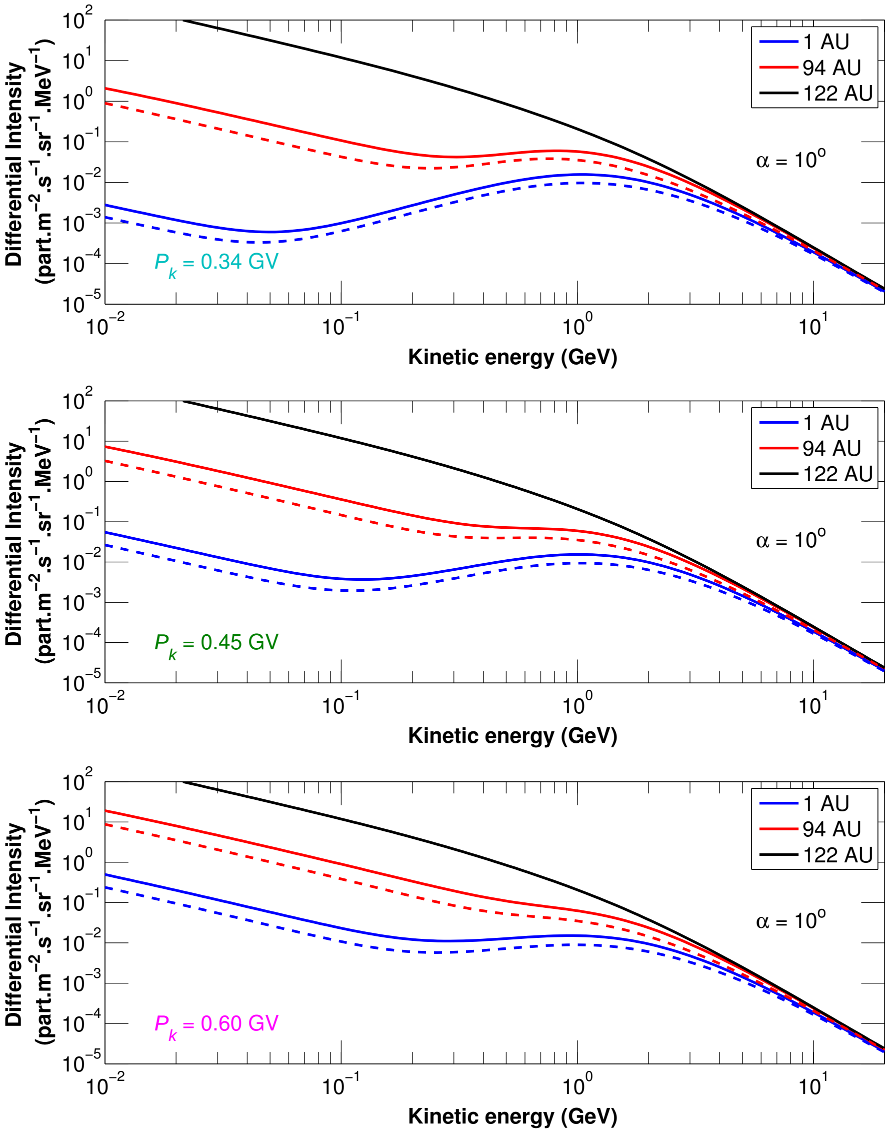

Figure 6.11: Modelled spectra at the TS (94 AU, $\theta = 55°$) and Earth (1 AU, $\theta = 90°$), respectively shown in red and blue, modulated from the HPS at 122 AU shown in black. Solid and dashed lines respectively represent solutions with and without DSA effects. Each panel corresponds to a configuration in Figure 5.8 for the indicated values of P_k (of Eq. 3.24). Drifts are neglected for these solutions.

incident at the TS and hence the extent by which they are modified during DSA. It is therefore worthwhile investigating the dependence of electron re-acceleration on the rigidity profile of diffusion. Section 5.4.1 demonstrates how varying P_k (of Eq. 3.24) alters the rigidity profile of the diffusion coefficients, and how this in turn affects the modulation of electron energy spectra; recall that P_k is the rigidity above which the energy range of the turbulence power spectrum becomes more prevalent in defining diffusion than the inertial range. It is shown in particular that increasing P_k reduces the segment of the rigidity profile along which MFPs increase with rigidity according to $P^{1.23}$, yielding rigidity-independent diffusion up to higher energies and larger MFPs at lower energies. This is furthermore limits the hardening of TS spectra in the region of 0.1 to 1 GeV, since the power law at lower energies transitions more directly into the softer power law retained from the HPS at high energies. This is shown in Figure 5.9.

The resultant spectra of the diffusion configurations explored in Section 5.4.1 are illustrated

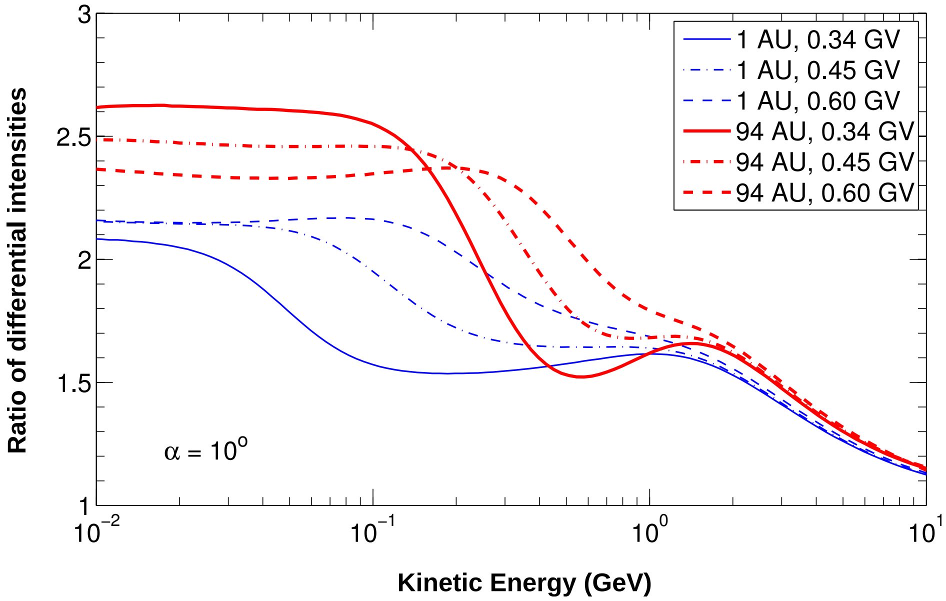

Figure 6.12: Ratios of the solutions in Figure 6.11 with DSA effects to those without, and shown for different values of P_k in different line styles as indicated in the legend. Ratios at Earth (1 AU, $\theta = 90°$) and the TS (94 AU, $\theta = 55°$) are shown in blue and red respectively.

again in Figure 6.11, but with the inclusion of shock-accelerated spectra. The accelerated intensities are higher by similar margins for all three diffusion configurations considered, but in the energy region of the power-law transition, where DSA effects seem to bottleneck, shock-accelerated intensities appear more pronounced for larger values of P_k. The TS spectrum being accelerated in case of $P_k = 0.60$ GV in Figure 6.11, for instance, is essentially distributed according to spectral indices of -1.35 and -3.18 at intermediate and high energies respectively, with somewhat harder spectra prevailing over a narrow energy region at the transition between these power laws. For smaller values of P_k this hardened spectral region is wider and the average spectral index thereof larger. DSA effects become more prominent in the transition region for larger values of P_k, because the hardening of spectra at these energies is largely circumvented by the diminishing of the segment of the rigidity profile increasing with P, and because the softer spectra that emerge are easier to accelerate. This ties in once again to the theme introduced in Section 6.2 that DSA raises the intensities of softer spectra by greater amounts than those of hard spectra. These amounts for each diffusion configuration are illustrated in Figure 6.12 by ratios of solutions with shock-acceleration to those without. The ratios demonstrate that the re-accelerated contribution at the TS declines less rapidly across the power-law transition from 100 MeV to just above 1 GeV for larger values of P_k, and that the large depression of acceleration effects visible for $P_k = 0.34$ GV (also pointed out in Section 6.3) at a few hundred MeV disappears. Similar effects are shown in Figure 6.12 for the contribution of re-accelerated electrons at Earth, although these extend to lower energies.

At the low-energy end of Figure 6.12, where ratios appear to remain constant with energy, the re-accelerated contribution is higher for the configurations where P_k is smaller - at the TS, $P_k = 0.34$ GV yields a factor increase below 100 MeV of at least 2.6 as opposed to a factor just short of 2.4 for $P_k = 0.60$ GV. This effect, which is hardly noticeable on the scale of Figure 6.11, follows likely as a result of more effective particle confinement; note that below 100 MeV the distributions incident at the TS as well the rigidity profiles of diffusion have the same form for the configurations considered, while only the values of MFPs differ for each. Recall from Chapter 4, and also Section 6.2, that impaired diffusion enhances acceleration. The larger MFPs ensuing at low energies when P_k is scaled up therefore causes DSA to raise spectral intensities by smaller amounts. Note however that above 100 MeV the re-accelerated contributions are greater for larger values of P_k (for reasons already explained above) despite the MFPs being larger in those cases. This suggests that the manner in which diffusion modifies energy spectra at the TS (or equivalently, the form of the rigidity dependence of diffusion) is more important than the level of diffusion in determining the amount by which DSA raises intensities. Hence, aside from the compression ratio, the form of energy distributions incident at the TS remains the predominant role player influencing the acceleration of these distributions. Finally, the ratios in Figure 6.12 converge toward high energies; since both the incident spectra and MFPs are identical there for each configuration, the associated acceleration effects are also the same.

6.4.3 The effects of electron drifts

Also influencing the form of modulated spectra in the same range of energies affected by varying the rigidity profile of diffusion as in Section 6.4.2 above, are electron drifts. Their effects on energy spectra and associated acceleration features are shown in Figure 6.13 for both polarities. Some drift-related features were also pointed out in the discussion of Section 6.3 and are noticeable from earlier-presented solutions: the ratios of e.g. Figure 6.10, for which drifts have been neglected, show larger re-accelerated intensity contributions at higher energies than for when drift effects are present such as in Figure 6.6.

Indeed, Section 5.5 illustrates that drifts raise 0.1 to 1 GeV electron intensities at the TS appreciably during both magnetic polarities and in doing so cause energy spectra to harden at the lower end of this affected range of energies. Hence, as per the recurring theme of spectral hardness and DSA, acceleration effects appear more subdued when drifts are enabled. This is illustrated in Figure 6.14, which shows the ratios of the solutions in Figures 6.11 and 6.13 with shock acceleration to those without at both the TS and Earth. While the no-drift acceleration effects are notably larger than those associated with drift solutions of either polarity, the latter do resemble the former: At the TS, both sets of ratios exhibit a notable decrease in the re-accelerated contribution from the low-energy global maximum to a local minimum, followed by a second maximum at higher energies above which acceleration effects gradually phase out. The aforementioned local minima occur at lower energies for drift-enabled solutions, because drifts harden TS spectra at these energies. The spectra do not soften again either until much higher energies where acceleration effects have already waned due to the attainment of the shock curvature limit. See also Figure 5.15 to aid in visualising the drift effects responsible for these acceleration features. The spectra at Earth, on the other hand, are just modulated forms of the re-accelerated spectra formed at the TS, and therefore display similar acceleration features, albeit smaller in magnitude. Moreover, the intensity increases due to DSA become generally more uniform for larger values of P_k, with the local minima and maxima in ratios at high energies becoming less prominent, because of the more direct transition of power laws brought about in the spectra incident at the shock.

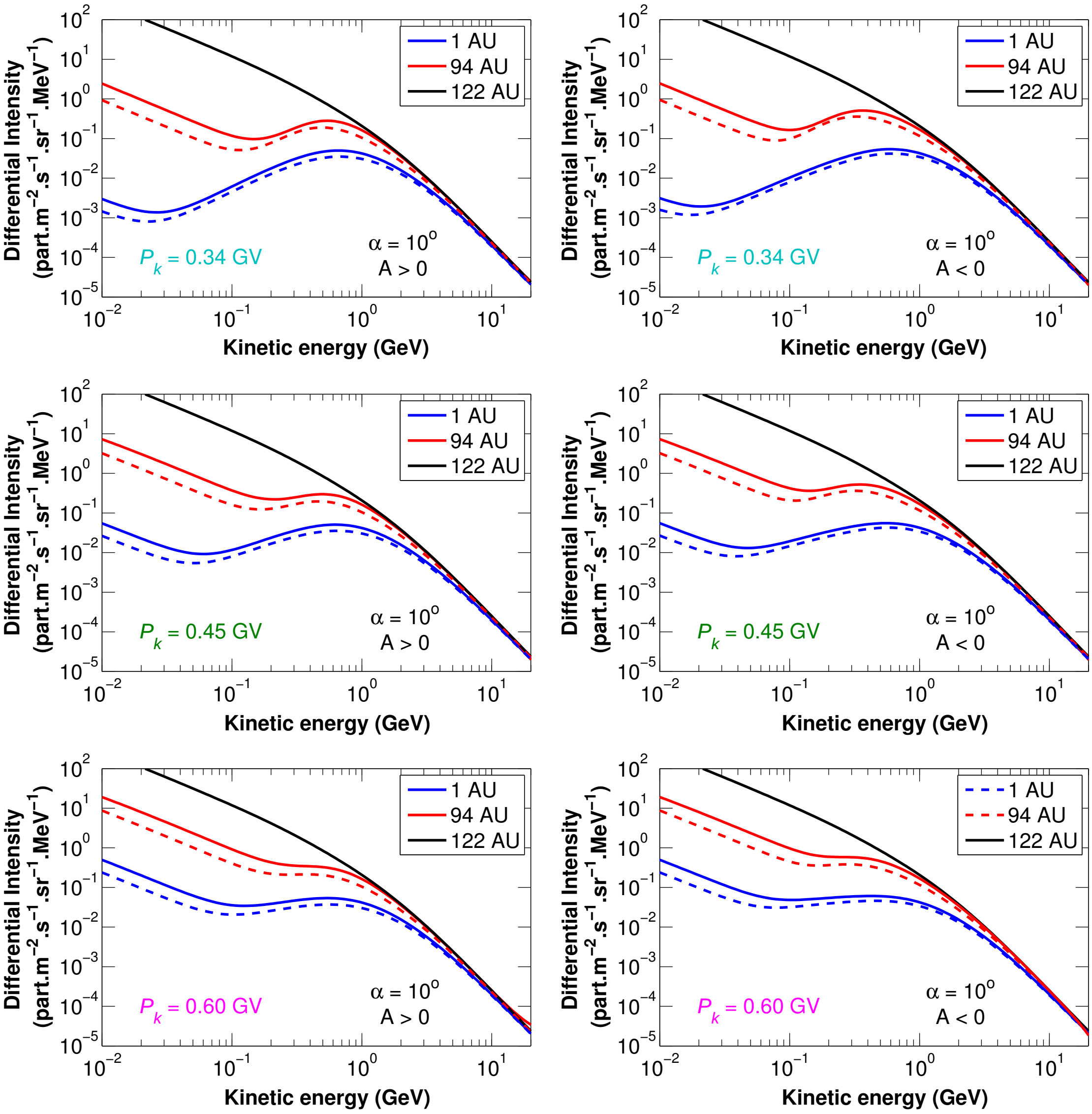

Figure 6.13: Similar to Figure 6.11, but with full drifts and shown for both the A $>$ 0 (left) and A $<$ 0 (right) cycles. Solid and dashed lines respectively represent solutions with and without DSA effects. The panels from top to bottom correspond to the different configurations of Eq. 3.24 shown in Figure 5.8 for $P_k = 0.34$ GV, 0.45 GV and 0.60 GV as indicated.

Considering Figure 6.13, which shows drift-enabled model solutions for both polarities and for each of the earlier considered diffusion configurations, the acceleration effects attributed to changes in the rigidity profile of diffusion are more obvious than those following from polarity-dependent changes. In each instance, the intensities are raised by a larger margin during the A $<$ 0 cycle (yielding harder spectra) than during the A $>$ 0 cycle, so that larger DSA effects are expected for the latter polarity. This is easier to discern from Figure 6.14. The re-accelerated contribution is shown to be consistently larger during the positive polarity cycle than during the negative. An exception is observed at the TS over an energy region between roughly 300 and 700 MeV wherein the opposite holds for $P_k = 0.34$ GV, and where the contributions during the two cycles are at least similar for the other diffusion configurations. Note from Figure 5.16 that drift effects diminish rapidly at the TS across this narrow energy interval so that the aforementioned features are to be expected. No such exception is visible in Figure 6.14 at Earth.

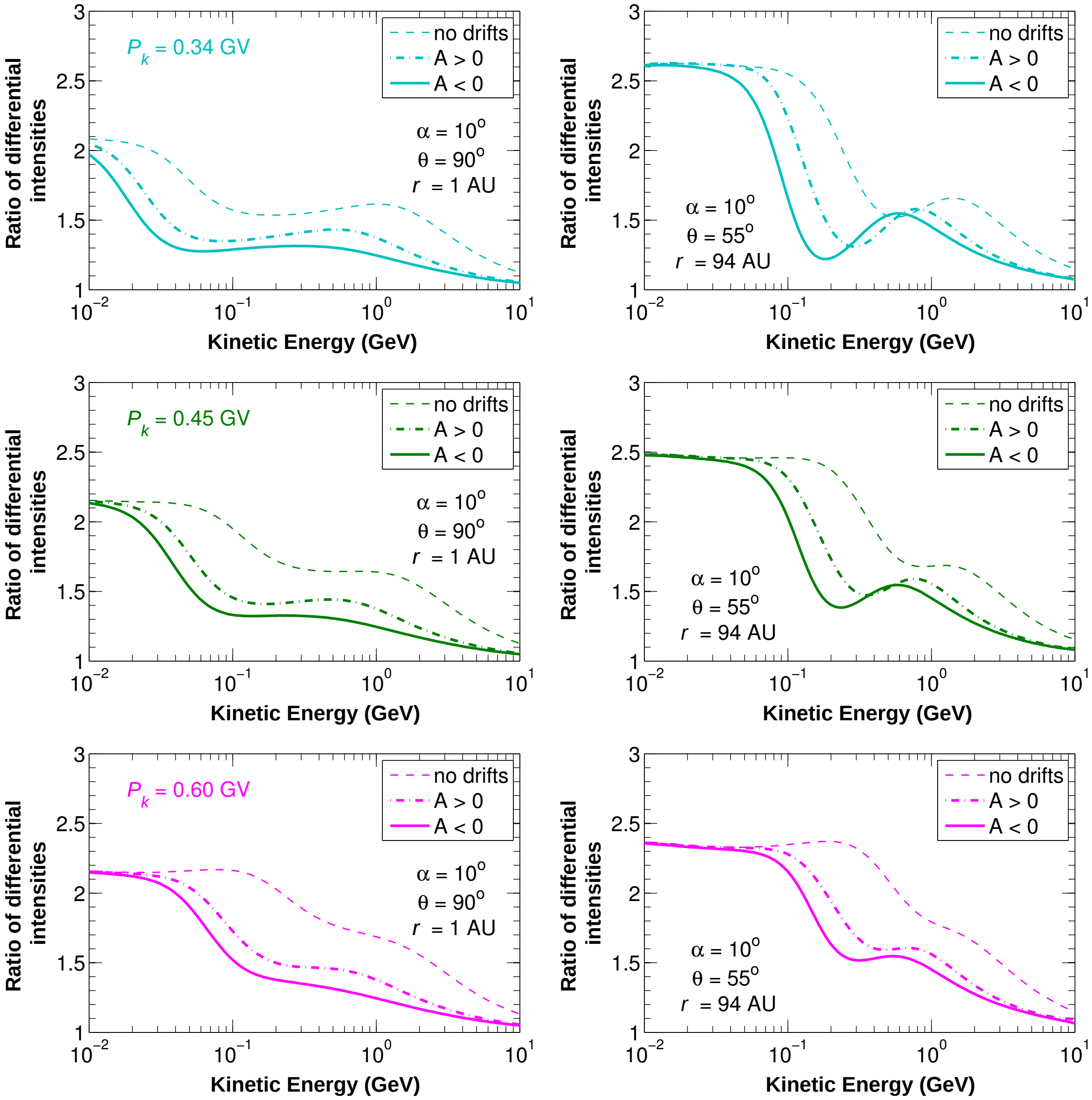

Figure 6.14: Ratios of the full-drift solutions in Figure 6.13 with DSA effects to those without for both polarities, along with the corresponding no-drift ratios of Figure 6.12. Panels from top to bottom correspond to the indicated values of P_k (of Eq. 3.24), with ratios shown at Earth (left) and the TS (right).

While drifts clearly influence the acceleration process of energy spectra at the TS by altering their form, the possible reciprocation of this interaction must also be considered. Section 5.5 demonstrates the magnitude of drift effects and the contribution of drifts to intensities during opposite magnetic polarities in conjunction with the effects of different rigidity profiles of diffusion. The discussion to follow explains how these effects and contributions differ when DSA is also present. First, it is considered how DSA affects the contribution of drifts to electron intensities: Figure 6.15 shows the ratios of shock-accelerated spectral intensities with drifts to those without; the ratios also presented in Figure 5.17 where DSA is suppressed are shown for comparison. Similar to the unshocked solutions, the drift contributions associated with shock-accelerated spectra are distributed over a wider range of energies at Earth than at the TS, and are larger during the A $<$ 0 cycle than during the A $>$ 0 cycle. As before, these contributions are also larger for the cases where diffusion levels are smaller, that is, for smaller values of P_k.

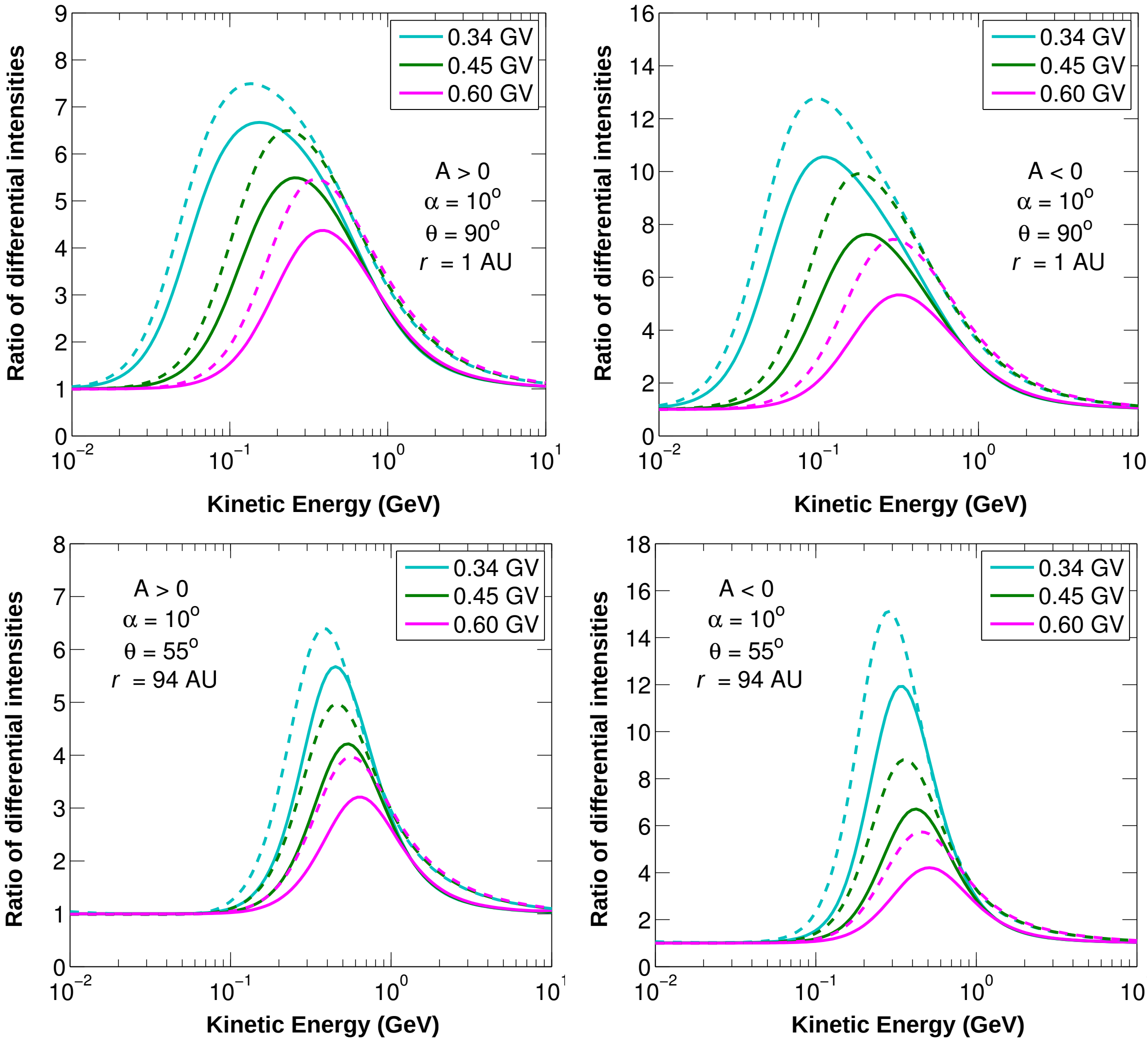

Figure 6.15: Ratios of the full-drift shock-accelerated solutions of Figure 6.13 to the no-drift shock-accelerated solutions of Figure 6.11. These are shown in solid lines for both A $>$ 0 (left) and A $<$ 0 (right) alongside the corresponding ratios in dashed lines (also presented in Figure 5.17) for which shock-acceleration is disabled. The ratios are displayed both at Earth and at the TS in the top and bottom panels respectively, with line colours representing the values of P_k indicated in the legend.

Aside from displaying the same qualitative features, however, the drift contributions associated to shock-accelerated solutions are shown to be notably smaller for both polarities. The same holds for drift effects as conventionally defined by ratios of intensities for drift-enabled solutions during the A $<$ 0 cycle to those of the A $>$ 0 cycle: These ratios, shown in Figure 6.16, also display qualitative features for shock-accelerated solutions that are similar to the ratios of solutions with no acceleration, although the ratios are again smaller where DSA is involved.

The explanation for these effects is relatively simple: Just as larger diffusion coefficients decrease modulation, resulting in larger intensities and smaller intensity gradients, DSA similarly raises intensities at the TS and thereby all intensities at smaller radial distances as well. The smaller intensity gradients that follow reduce the imprint of drifts on the distribution function in the TPE. Therefore, where DSA effects are present, drift effects and the contribution of drifts to intensities are diminished in the same way that larger MFPs would diminish them. While it appears from the above that particle drifts and DSA inhibit one another in terms of

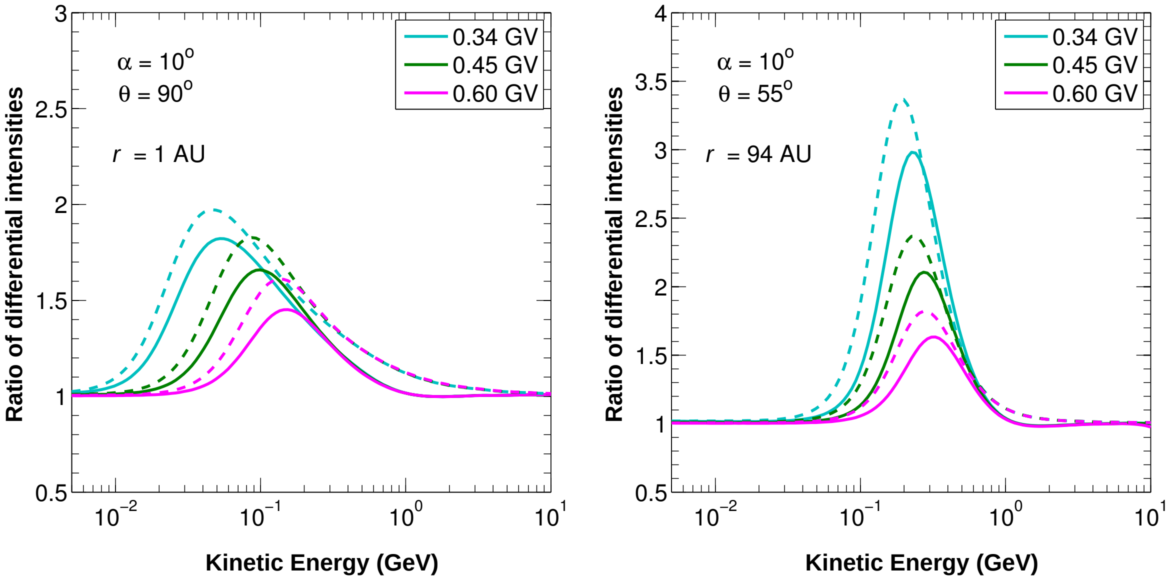

Figure 6.16: Ratios of the drift-enabled shock-accelerated solutions in Figure 6.13 with $A < 0$ to that for which $A > 0$. These are shown in solid lines, whereas the accompanying dashed lines represent the corresponding ratios (also shown in Figure 5.16) without DSA effects. The ratios are displayed both at Earth and at the TS in the panels on the left and right respectively, with line colours representing the values of P_k indicated in the legend.

global modulation, this does not imply (in physical terms, at least) that drifts are not involved in the acceleration process. When CRs drift along a shock and intermittently scatter across or off of it they gain energy in what is referred to as shock drift acceleration. These energy gains are similar to what is achieved through DSA and can be accounted for in the matching conditions at the TS [*Jokipii*, 1982], while the Parker TPE contains all the relevant physics to describe this process. This concept is yet to be developed further in the context of the current model and offers an intriguing subject for further research. See also the discussions by *Ball and Melrose* [2001] and *Moraal* [2001] for more on this topic.

6.5 Electron Re-acceleration at Very Low Energies

In contrast to the well-established process of high-energy electron modulation, the features of electrons at $E < 1$ MeV are relatively uncertain (especially in the outer heliosphere). Scenarios are hence presented in Chapter 5 for the low-energy HPS, and are revisited in this section with regards to the effects of each on the re-acceleration of galactic electrons. While the involvement of certain processes, such as drifts, can be neglected at low energies, other aspects are unique to electron modulation at these energies, e.g. the influence of the dissipation range of the turbulence power spectrum on diffusion properties, which in turn affects the DSA process. As before, the effects of input spectra are considered first.

6.5.1 Consequences of the form of input spectra

In Section 5.3.2 a number of possible low-energy distributions for the HPS are introduced, based on the results of galactic propagation modelling and available spacecraft measurements.

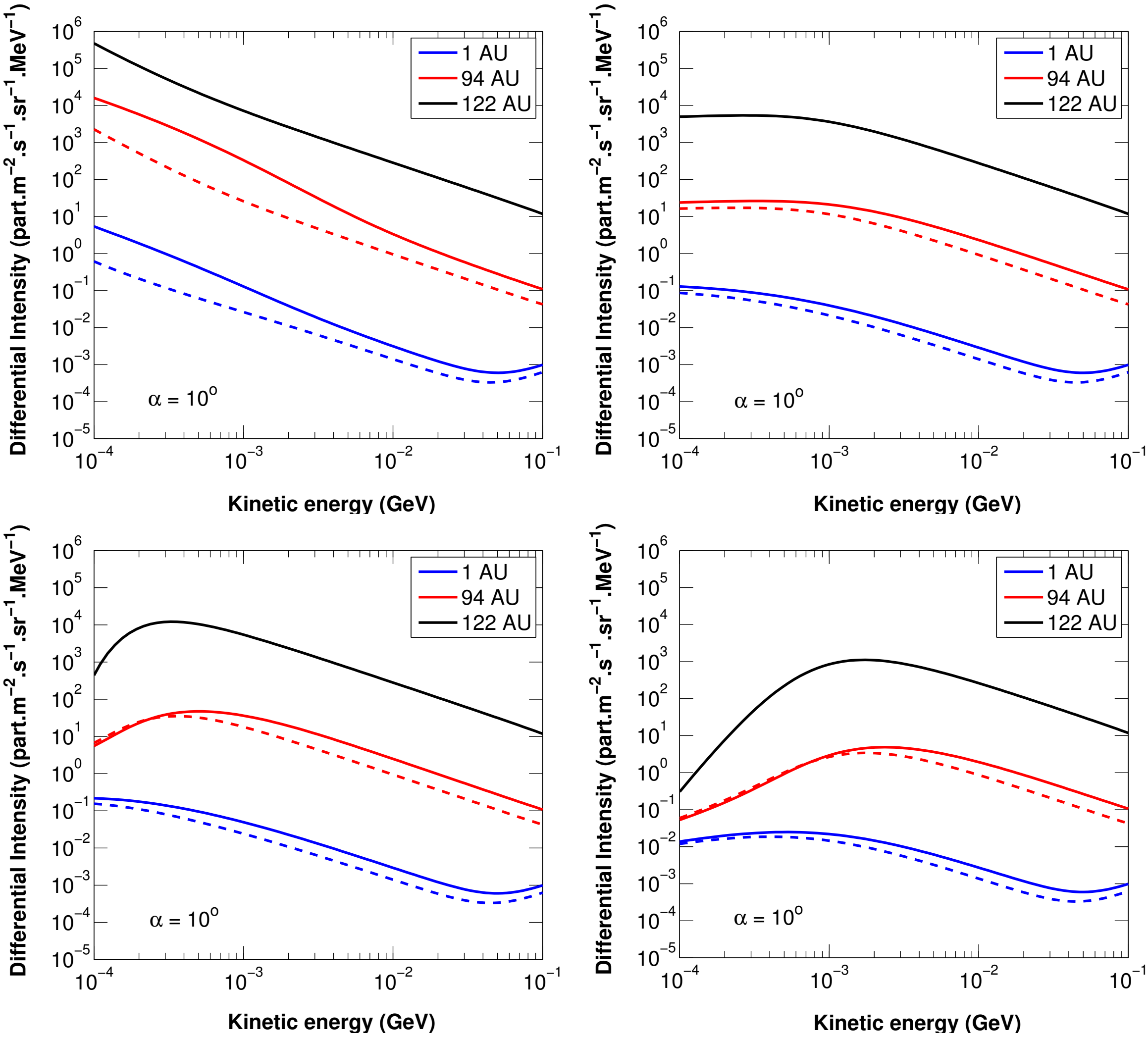

Figure 6.17: Modelled energy spectra at Earth (1 AU, $\theta = 90°$) and the TS (94 AU, $\theta = 55°$) with respect to different input spectra (black lines) at 122 AU. In the top-left panel the reference HPS is employed as input, in the bottom left Eq. 5.4 with $\Phi = 1.4$ is applied, while Eq. 5.3 is applied on the right with $h_0 =$ 1.0 and 6.0 for the top and bottom panels respectively. Solutions are shown for β-compensated rigidity-independent diffusion (as explained in Section 5.4.2). Solid and dashed lines respectively represent solutions with and without shock acceleration. Drifts are neglected for these solutions.

These scenarios are at best speculative, although the energy distribution of electrons at these low energies can possibly be inferred from the magnitude of observed intensity increases measured near the TS along the Voyager 1 trajectory [see *McDonald et al.*, 2003; *Decker et al.*, 2005; *Stone et al.*, 2005]. If these increases can indeed be attributed to the acceleration of electrons at the TS, the low-energy HPS can be approximated by the energy distribution that reproduces a similar magnitude intensity increase through DSA. Each of the aforementioned scenarios are investigated in this regard. In order to have the spectra incident at the TS directly reflect the features of the HPS, rigidity-independent diffusion is assumed for the following illustrations.

Figure 6.17 shows how spectra at Earth and the TS, as modulated from various forms of the HPS, are accelerated. Note that for each case the features of the HPS are mostly retained by the modulated spectra. Immediately noticeable is the large intensity increase in the case of the reference HPS; the softer spectrum induced by the deviation of β from unity in Eq. 5.1 provides a distribution that is easy to accelerate. Since the distribution incident at the TS has a spec-

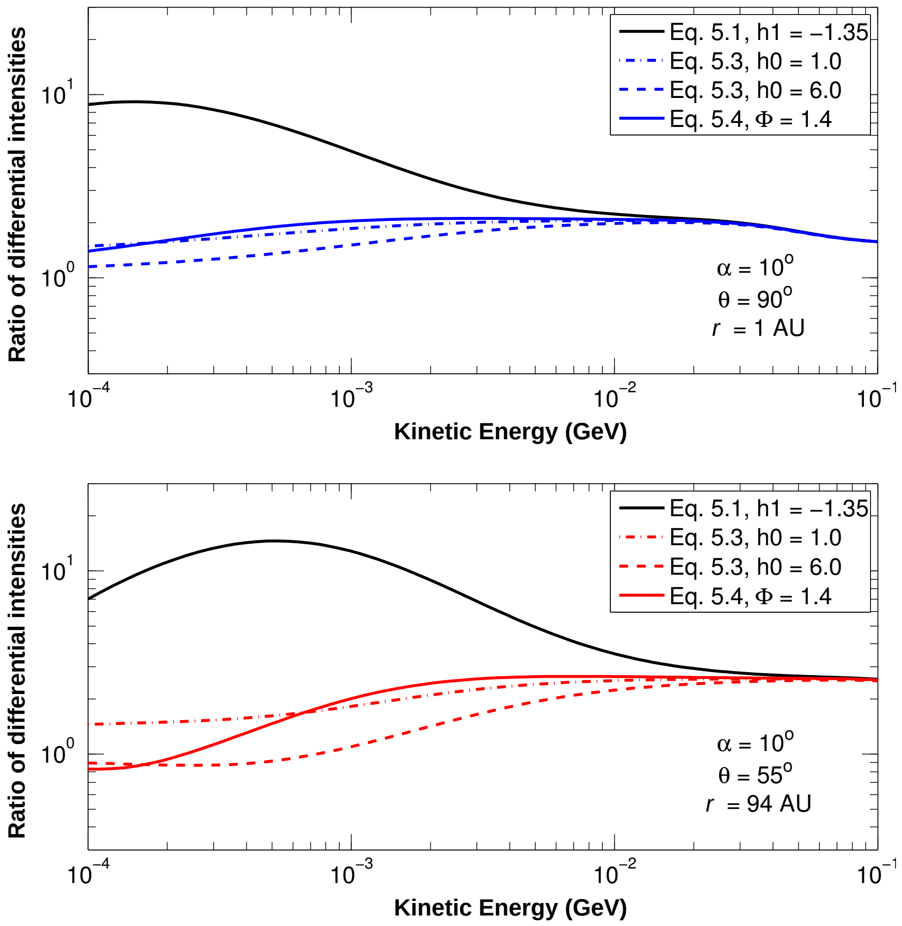

Figure 6.18: Ratios of the model solutions in Figure 6.17 with shock acceleration to those without. Each set of ratios are shown for one of the input spectra specified in the legend, and are shown both at Earth and the TS in the top and bottom panels respectively.

tral index that is similar to (or even slightly smaller than) that producible by the shock itself, DSA raises the intensities appreciably and even some hardening is observed in the shocked solutions. Figure 6.18 shows that the intensities are increased at the TS with an average factor larger than 10 below 1 MeV, which translates to a re-accelerated contribution of up to a factor of 9 at Earth for the same energies. This is a remarkably large effect, but in fact very similar to the magnitude of the peak-like intensity increases reported by *Decker et al.* [2005] near the shock for 0.35 to 1.5 MeV electrons. The acceleration effects in the cases where the other input spectra are employed are less spectacular, since the form of the spectra hardens toward lower energies; the factor by which the acceleration increases intensities both at the TS and Earth actually decreases from the factor achieved above 10 MeV. Of these cases, the HPS described by Eq. 5.4 and $\Phi = 1.4$ yields an intensity increase at the TS that declines from a factor of 2.5 at 10 MeV to about 2 at 1 MeV and is mostly diminished at 0.1 MeV. The input spectrum described by Eq. 5.3 with $h_0 = 1.0$ yields an intensity increase at the TS maintained at a factor of approximately 1.5 below 1 MeV, whereas, at the same energies, the intensities of the TS spectrum associated with the $h_0 = 6.0$ case are not raised at all. At Earth the same features are visible, but are translated to lower energies (likely as a result of adiabatic cooling). The findings presented here are again consistent with earlier results in that the hardness of spectra arriving at the TS determines the magnitude of the acceleration effects that follow.

While the reference HPS of Eq. 5.1 yields TS spectra that produce favourable acceleration features in the correct range of energies, its form is unlikely to be accurate. Recall from Section 5.3.2 that the intensities of galactic electrons arriving at the heliosphere are not expected to increase indefinitely toward low energies, but instead to eventually fall away. Note that the solutions in this subsection are shown only for rigidity-independent diffusion. Hence, if the other (possibly more realistic) forms suggested for the HPS are employed in conjunction with more appropriate low-energy diffusion properties, spectral forms at the TS that are more conducive to efficient acceleration may be attained.

6.5.2 The role of dissipation-range turbulence in electron acceleration

Just as the inertial and energy ranges of the turbulence power spectrum characterise diffusion for higher-energy electrons, low-energy diffusion properties is predominantly characterised by the dissipation range. This turbulence is often shown to manifest as an up-turn in low-energy electron MFPs, which is shown in Section 5.4.3 to have one of two effects on modulated spectra: Firstly, spectra become softer during modulation when MFPs decrease with increasing rigidity, which is expected to enhance their acceleration. Secondly, if the up-turn is particularly pronounced, MFPs may be large enough at low energies that modulated spectra coincide with the HPS. In this case the acceleration effects will adopt a magnitude similar to that seen in Figures 6.17 and 6.18 for each HPS. Only the model solutions for the less-steep input spectra (that is, those also presented in e.g. Figure 5.14) are considered in the following discussion; modulated spectra will at best retain the form of the employed HPS, which in the case of Eq. 5.3 with $h_0 = 6.0$ and Eq. 5.4 with $\Phi = 1.4$ is too hard for the shock to accelerate appreciably.

Figure 6.19 illustrates the acceleration of spectra modulated subject to the diffusion configurations of Figure 5.13 with respect to the reference HPS and the input spectrum of Eq. 5.3 with $h_0 = 1.0$. The solutions presented in Figure 6.17 for these input spectra represent the rigidity-independent diffusion configuration, and are already discussed. The intensity increases due to DSA are also illustrated in Figure 6.20 in terms of ratios of solutions with shock acceleration to those without. When the reference HPS is employed, intensity increases are larger toward smaller energies if g_0 is set to 0.5 in Eq. 5.5 than for $g_0 = -1.0$. The re-accelerated contributions are also significantly smaller below 1 MeV when a MFP up-turn is present than for when standard rigidity-independent diffusion is applied. At somewhat higher energies, nearer to where the MFPs transition from decreasing with P to being rigidity-independent, the acceleration effects appear to be at their greatest for both up-turn configurations. The re-accelerated contribution emerging at the TS when the reference HPS is employed peaks in the vicinity of 4 to 7 MeV, representing a factor increase of nearly 10 for both $g_0 = -0.5$ and -1.0. When Eq. 5.3 with $h_0 = 1.0$ is applied as HPS, DSA increases intensities by similar amounts toward lower energies for the two configurations, and in each case the most prominent acceleration also appears at the bend where the rigidity dependence of MFPs changes. In this case acceleration increases intensities near the bend with factors of up to 6 for $g_0 = -1.0$ and up to 4 for $g_0 = -0.5$. Since the spectra at Earth are modulated from shock-accelerated spectra at the TS, the features of the re-accelerated contribution to intensities in the inner heliosphere are similar to those at the shock, although smaller in magnitude and translated to lower energies.

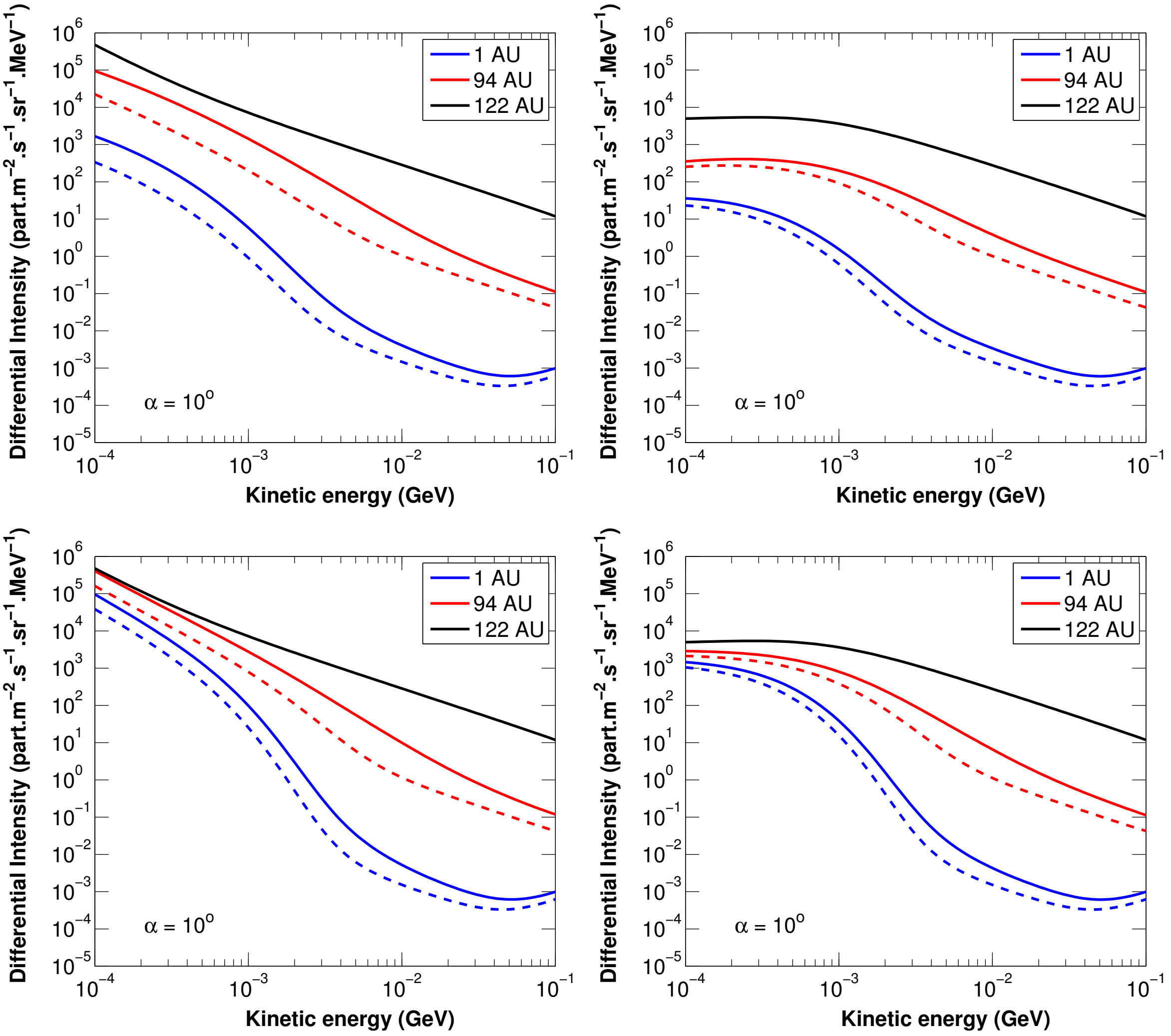

Figure 6.19: Modelled energy spectra at Earth (1 AU, $\theta = 90°$) and the TS (94 AU, $\theta = 55°$) with respect to the HPS (black lines) at 122 AU. The reference HPS is employed as input spectrum on the left, while Eq. 5.3 is applied on the right with $h_0 = 1.0$. Solutions in the top and bottom panels respectively correspond to the diffusion configurations described by Eq. 5.5 with $g_0 = -0.5$ and -1.0. Solid and dashed lines respectively represent solutions with and without shock acceleration. Drifts are neglected.

From the results above, the largest acceleration consistently occurs in proximity to where the rigidity dependence of diffusion changes and thus where energy distributions change in response. Particularly, the most pronounced re-accelerated contributions occur at the transitions where softer distributions are succeeded by hard distributions. This effect is visible near the energy equivalent to P_{k1} (of Eq. 5.5) for all solutions with up-turns in their low-energy diffusion coefficients. Larger values of g_0 lead to greater intensity increases at the transition near 10 MeV, because larger up-turns in low-energy MFPs yield softer spectra at energies preceding the transition. When the reference input spectrum of Eq. 5.1 is applied (see the top panel of Figure 6.20), the aforementioned effect also surfaces for rigidity-independent diffusion ($g_0 = 0$) at $\sim$ 0.5 MeV, where β begins to decline appreciably toward lower energies, causing the intensities there to increase more rapidly and the spectrum to soften. When a low-energy MFP up-turn is present, however, the acceleration effects associated with the β-induced bend become progressively smaller for larger values of g_0 and intensities are instead increased more at the diffusion-induced transition near 10 MeV. This is because for larger values of g_0 the spec-

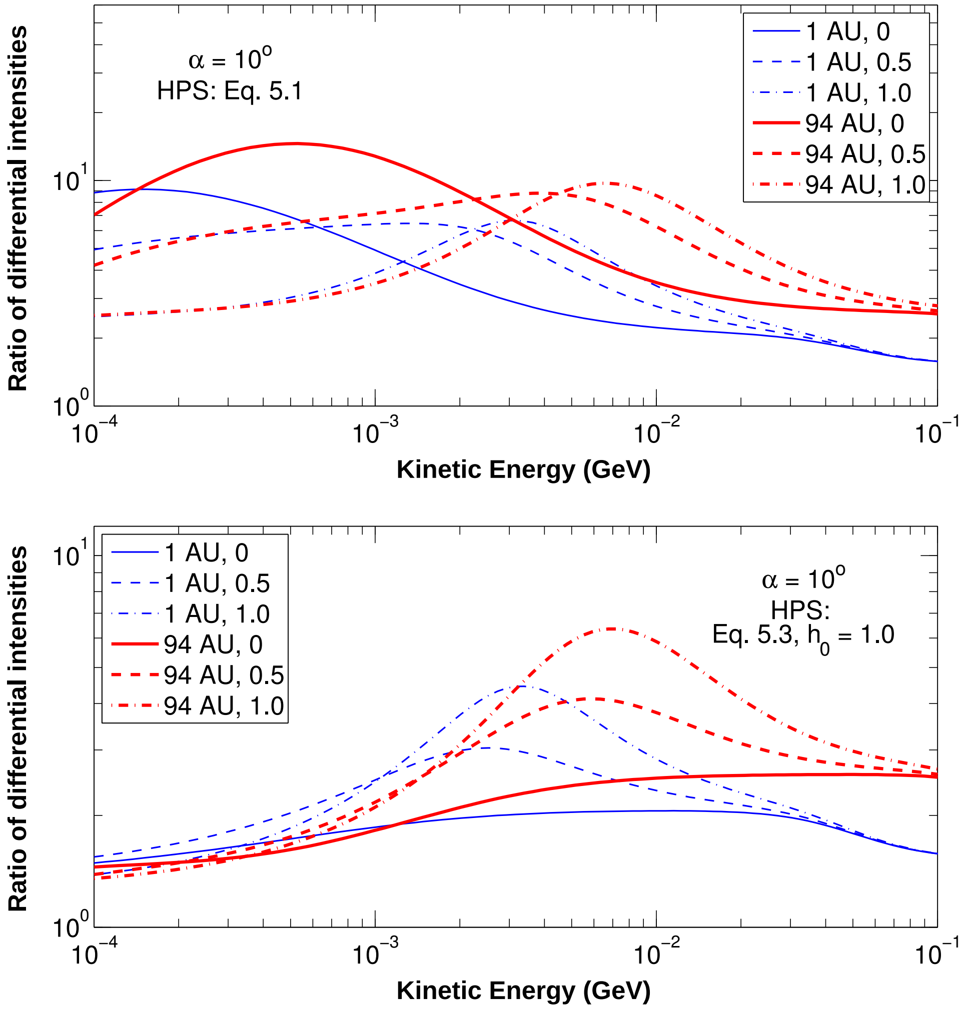

Figure 6.20: Ratios of the solutions in Figure 6.19 with shock acceleration to those without for the input spectra as indicated in each panel. Line styles correspond to the values for g_0 (of Eq. 5.5) indicated in the legend; $g_0 = 0$ refers to the rigidity-independent cases presented for the same input spectra in Figure 6.17. The ratios are shown in blue at Earth (1 AU, $\theta = 90°$) and in red at the TS (94 AU, $\theta = 55°$).

trum above 0.5 MeV softens more, which in physical terms implies that electrons accelerated up until energies at the bend can more easily be accelerated further, and consequently the peak in the re-accelerated contribution moves to larger energies (or in this case, to the next spectral bend at 10 MeV). A hard distribution following a transition, by contrast, impairs further acceleration of electrons; the re-accelerated contribution is therefore not distributed to higher energies, but instead peaks at the transition itself.

In summary, the results of this section not only reaffirms the expected result of larger acceleration where modulated spectra soften, but also reveals insight pertaining to transitions between different energy distributions: Acceleration is more pronounced at spectral transitions where the distribution preceding the transition is softer and the distribution succeeding it is harder. Moreover, by virtue of the aforementioned mechanisms, it is shown that a low-energy MFP upturn can indeed facilitate greater acceleration effects in cases where the distribution supplied by the HPS is too hard to accelerate. Comment on what combinations of input spectra and diffusion configurations are most realistic is reserved for Chapter 7.

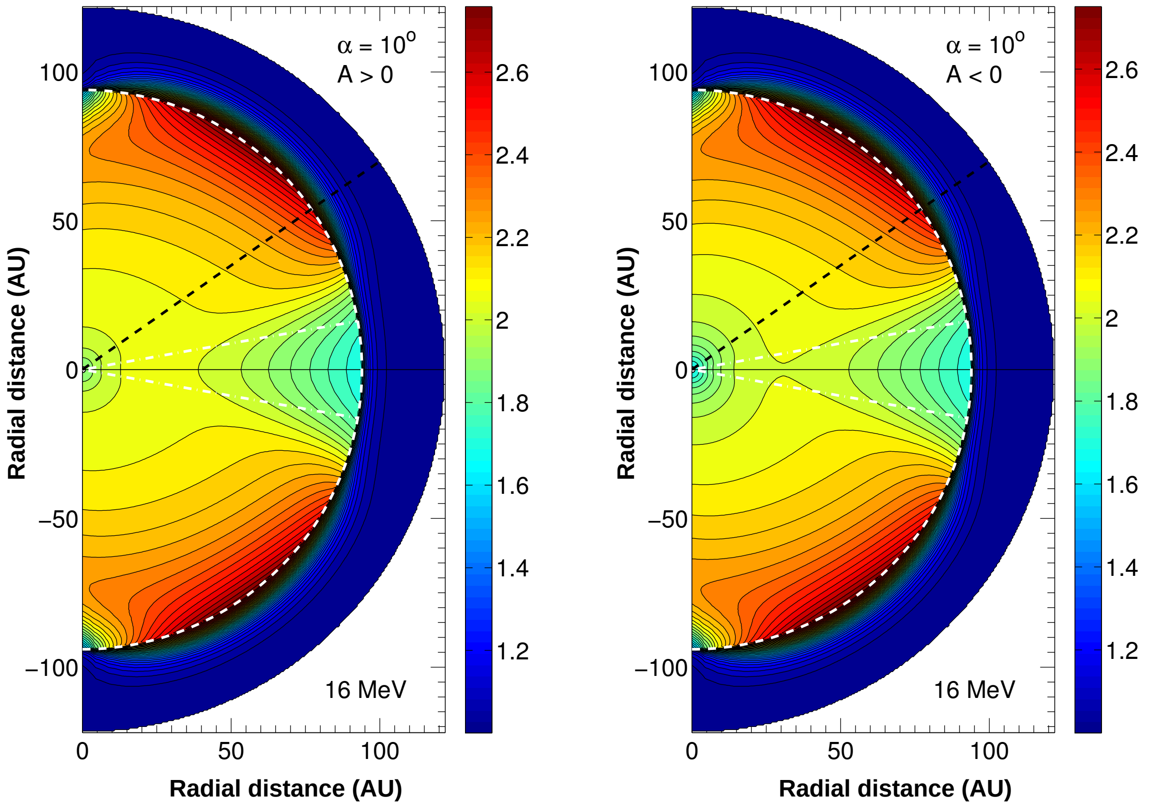

Figure 6.21: Contour plots for 16 MeV electron intensity ratios, illustrating the factor by which solutions with shock acceleration at the TS increases the intensities of solutions where shock acceleration is suppressed. The plots are shown in the meridional plane of the heliosphere for A $>$ 0 (left) and A $<$ 0 (right). The dashed white halfcircle indicates the TS position at 94 AU, the dash-dotted lines indicate the polar extent of the HCS for $\alpha = 10^\circ$, and the dashed black line shows the trajectory along $\theta = 55^\circ$ at which the corresponding ratios in Figures 6.6 and 6.8 are shown. The Sun is located at the origin.

6.6 Global Spatial Distributions of Re-accelerated Electrons

Earlier sections reviewed a great deal of spectral features of DSA and re-accelerated electrons, with solutions predominantly displayed at Earth in the equatorial plane of the heliosphere and at the TS along the approximate Voyager trajectory. This section endeavours to place the spectral features encountered in this chapter into a more global spatial context. The contributions of re-accelerated electrons to global intensities are to this end best expressed as the factors by which shock acceleration raises the intensities of solutions where DSA is suppressed. This is illustrated across all latitudes using coloured contour plots, which are shown in Figures 6.21, 6.22 and 6.23 for the sample energies of 16 MeV, 200 MeV and 1 GeV. The modulated spatial features of 200 MeV electrons are shown in Figure 5.3, while similar plots are shown for reference purposes in Figures 6.24 and 6.25 for 16 MeV and 1 GeV electrons.

Considering 16 MeV electrons first, Figure 6.24 illustrates that their spatial features during the two polarity cycles are virtually indistinguishable. The uniformity of their modulation and the modulation barrier in the heliosheath emerge as the most notable features. The re-accelerated contribution is similarly shown in Figure 6.21 to differ only slightly near Earth and along the equatorial plane during opposite polarities; earlier figures often show that features exhibited by spectra at larger radial distances are translated to lower energies at Earth so that the slight

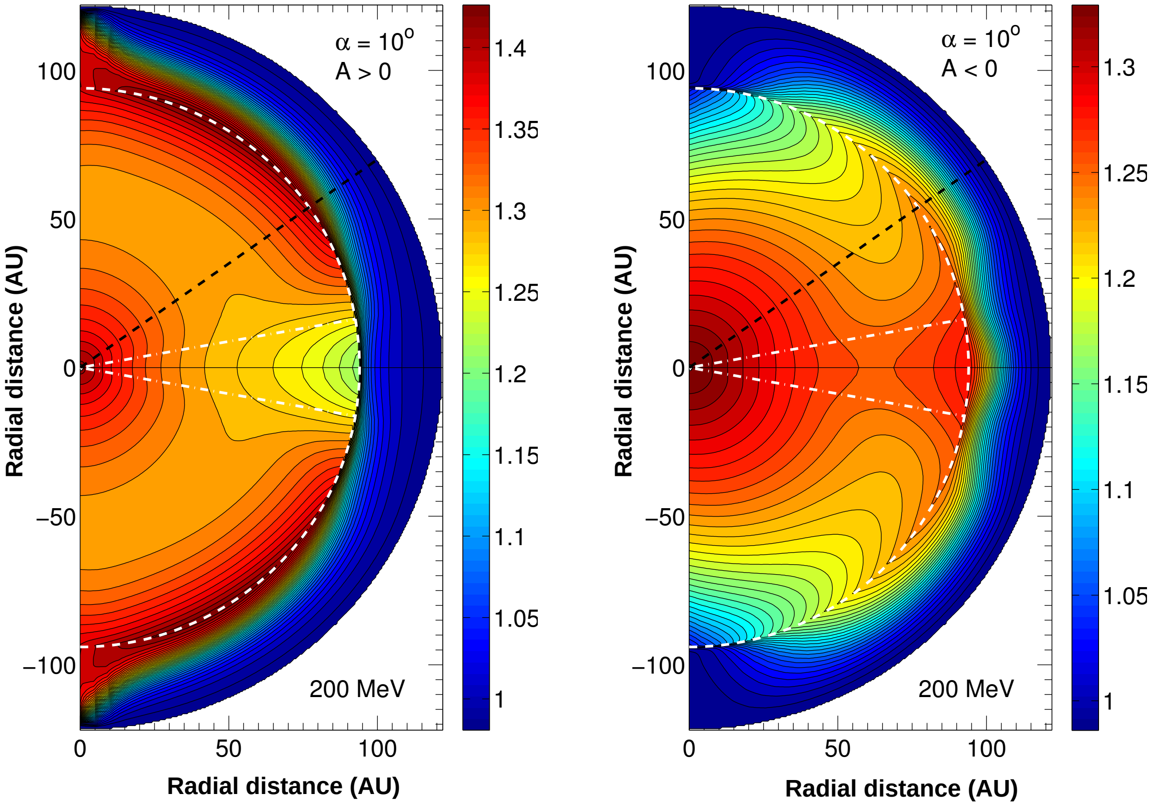

Figure 6.22: Similar to Figure 6.21, but for 200 MeV electron intensity ratios. Note that the colour scales of the two plots are not the same and are instead specified as most appropriate in each instance.

polarity dependence in Figure 6.21 is not entirely unexpected. Another notable feature is a region of enhanced TS acceleration (with factor increases of up to 2.6) visible from about 25° above the equatorial plane. While the factors by which intensities are increased are not necessarily small near the TS in the equatorial plane, acceleration effects do seem subdued there relative to the factors achieved at higher latitudes. There is also a similar but less prominent depression at the poles. This latitude dependence likely stems from a combination of a number of factors accounted for in the model: The emergence of a fast SW stream and enhanced polar diffusion higher than 25° above the equatorial plane, residual drift effects along the HCS, and HMF modifications at the poles may all influence acceleration at the TS. Note that the compression ratio is not latitude-dependent in this chapter and therefore not involved in creating the aforementioned features. Consider though the diffusion length scale, κ_{rr}/V_{sw}, which is an important quantity for shock acceleration and governs the extent of particle movement toward and away from the TS: Due to the SW speed, V_{sw}, emulating the fast SW stream at $\theta < 65^\circ$ during solar minimum conditions, its value doubles at these angles with respect to that in the equatorial plane, and as a result κ_{rr}/V_{sw} is smaller at higher latitudes. This creates more conducive conditions for acceleration, and the factors by which DSA increases intensities for $\theta < 65^\circ$ are thus larger. It remains however to be investigated further within the context of the model how transport of CRs along the shock (as opposed to transverse to it), especially via drifts, influences their acceleration.

With regards to the re-accelerated contributions shown in Figures 6.22 and 6.23 for higher energies, the imprints of drift effects are obvious in their spatial distributions and clear changes

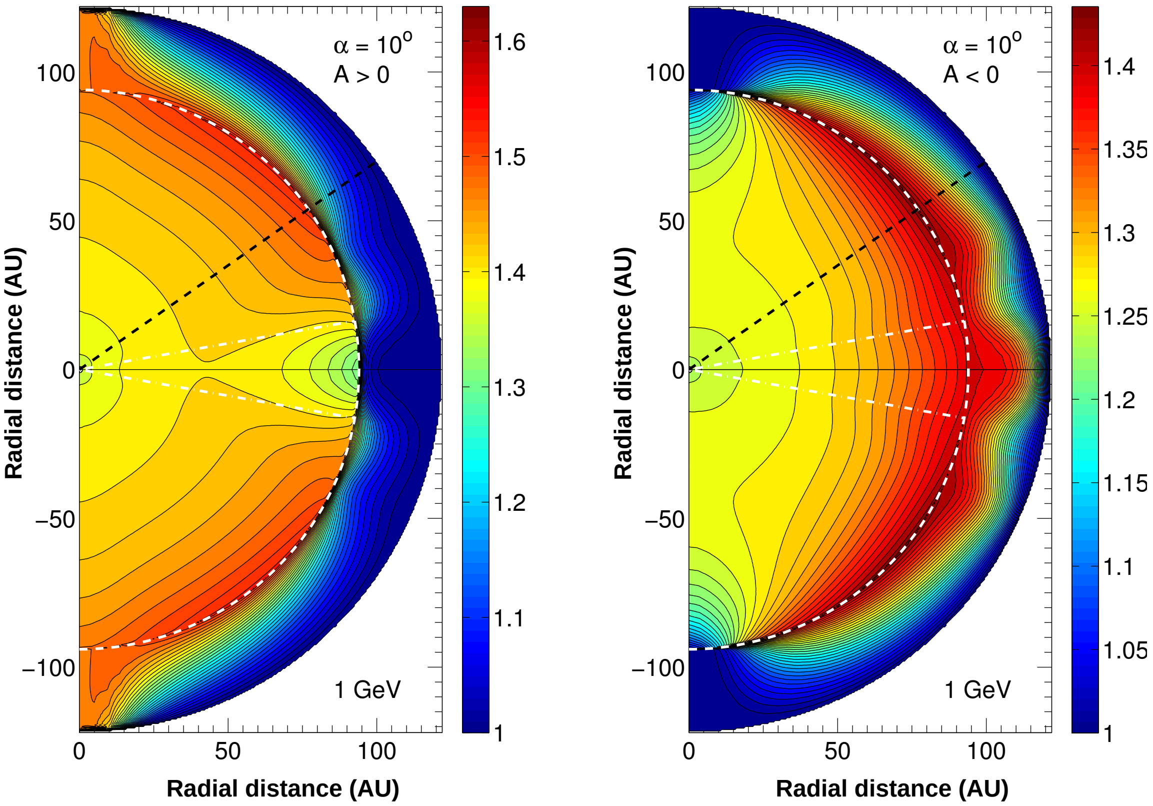

Figure 6.23: Similar to Figure 6.21, but for 1 GeV electron intensity ratios. Note that the colour scales of the two plots are not the same and are instead specified as most appropriate in each instance.

emerge during opposite polarities. Due to global drift patterns, re-accelerated electrons are predominantly concentrated toward higher latitudes and particularly at the poles during the A > 0 cycle, whereas contributions are more prominent in the equatorial regions for the A < 0 cycle. Although the low-diffusion barrier does limit the passage of re-accelerated particles downstream of the TS, drifts allow higher-energy particles to penetrate deeper into the heliosheath. The modulation barrier does appear from Figure 6.25 to be somewhat lifted for 1 GeV electrons, since intensities remain high throughout the heliosheath and some way into the interior as well. Also note that the large contributions of re-accelerated 200 MeV electrons to the intensities in the heliospheric interior follow as a result of the spectral features around those energies; the ratios in Figure 6.6 are in fact smaller at the TS than at Earth for energies in the region of 200 MeV. There are a number of features visible in Figures 6.21 to 6.23 that relate to spectral features pointed out earlier. At drift-sensitive energies the acceleration effects in the contour plots are generally larger for A > 0 than for A < 0, corroborating the same observation that is explained in previous sections to follow because distributions are harder at the involved energies during the latter cycle than during the former. Similarly, the plots for 16 MeV electrons show the largest acceleration effects, followed by that for 1 GeV electrons, while 200 MeV electrons are accelerated the least; Figures 6.6 and 6.8 convey the same trend based on the hardness of distributions at each energy.

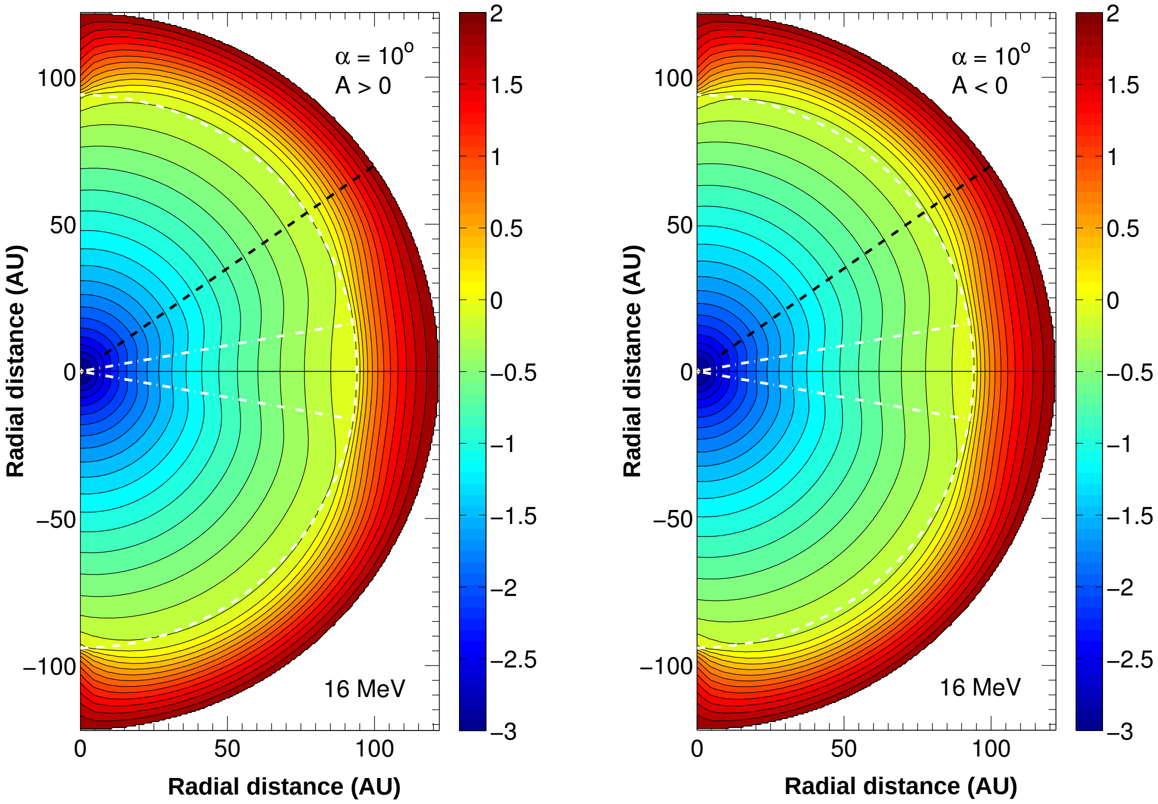

Figure 6.24: Similar to Figure 5.3, but for 16 MeV electrons.

6.7 Summary and Conclusions

Chapter 6 expands upon and ties together the groundwork provided in preceding chapters by application of the model to the study of electron acceleration at the TS. The chief aim of the chapter is to provide a comprehensive review of the features arising from the DSA of galactic electrons, and the interaction of this acceleration mechanism with the other processes accounted for in the TPE. Since shock acceleration primarily entails changes in the energies of electrons, this study especially focuses on the energy distributions of these particles.

In Section 6.2, mimicking the process of Chapter 4 where a source function is used to emulate a seed population of PUIs injected at the shock, the spectral features arising directly from the acceleration of monoenergetic electrons are shown to be similar to the features observed earlier for ACRs. They differ however in that the accelerated spectra of electrons extend to relativistic energies, where the values of the spectral indices of these spectra for any given shock compression ratio are about half of that typically expected for accelerated ion spectra. Exploiting the aforementioned technique further, the imprint of DSA on existing distributions of electrons with energy is evaluated for different shock strengths. The following central recurring outcomes are revealed:

> Should the incident energy distribution of electrons be softer than what the shock is able to produce when accelerating a monoenergetic population of electrons, this distribution hardens to adopt the spectral index associated with the shock compression ratio.

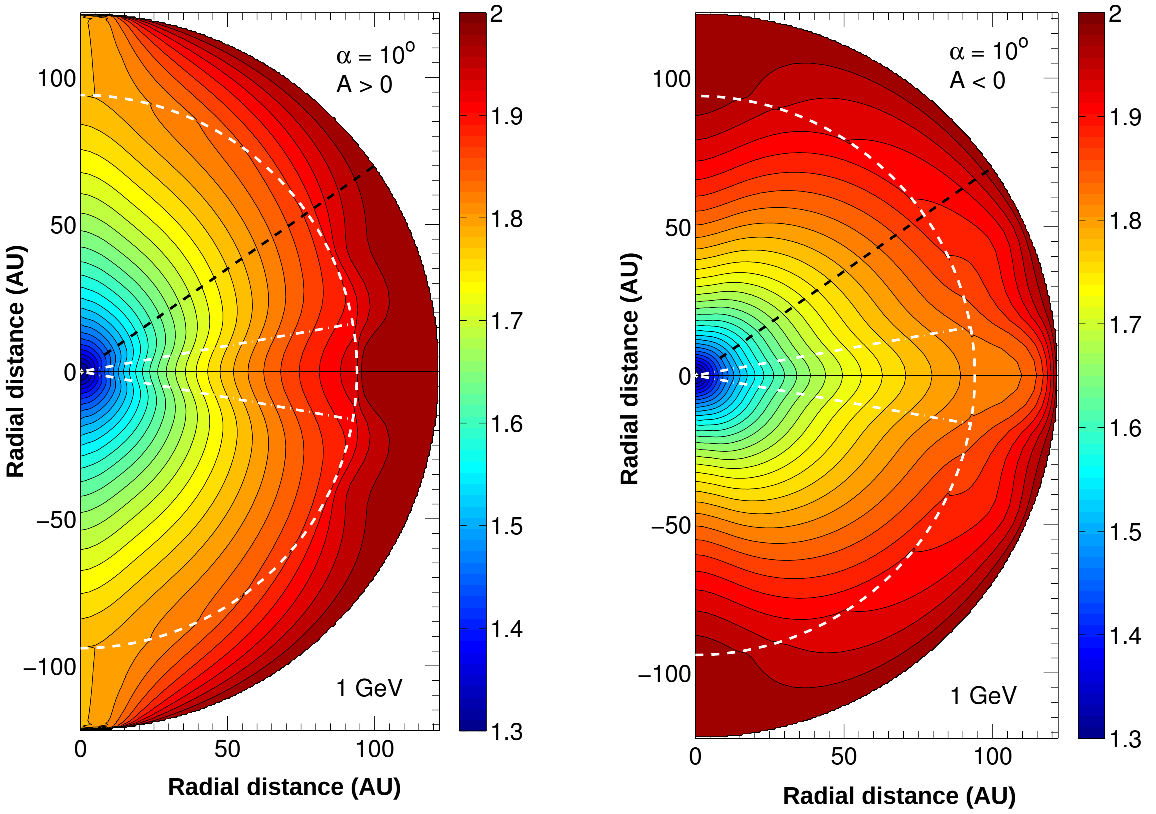

Figure 6.25: Similar to Figure 5.3, but for 1 GeV electrons.

Otherwise, if the incident distribution is harder than what the shock is able to produce, it is uniformly shifted to higher energies so that its intensities are raised by an amount depending on the similarity of its spectral index to that associated with the compression ratio.

The implications of these outcomes are far-reaching in the context of the acceleration of galactic electrons. Acceleration features shown in Section 6.3, emerging from the reference model configuration, reveal that intensities are raised by distinct amounts in different energy regions, depending on the hardness of the spectral form retained from the HPS or attained during modulation. No hardening of spectra occurs as a result of DSA, because the incident spectral forms are already harder than what the shock is able to produce. The intensities of softer distributions, with indices more similar to that associated with the compression ratio of 2.5 at the TS, are hence raised by greater amounts during acceleration. The fact that the accelerated intensity increase is 10% larger when the HPS exhibits a -1.55 power law index at Voyager-observed energies instead of an index of -1.35 illustrates this. It is hence worth stressing from the above that DSA of electron spectra in the outer heliosphere cannot necessarily be detected from observations by evaluating changes in spectral slopes across the TS, because its compression ratio is likely too small and the incident spectrum too hard to induce them. The effects of DSA at the TS, though subtle, are nevertheless present as evidenced by the intensity increases they induce. It is also visible from the modelled solutions of Section 6.3 that acceleration effects are largest at the TS, however a peak-like structure is not observed at its position in radial intensity profiles. This concealment of a peak-like increase follows both because of the steep intensity gradients caused by the low-diffusion barrier downstream of the shock, which also prevents re-accelerated particles from travelling far into the heliosheath, and the contrastingly large diffusion that allows re-accelerated particles to be transported further upstream of the shock. Indeed, the latter leads to doubled intensities at Earth, which raises doubts about whether the slight intensity enhancement observed at 0.5 to 20 GeV in near-Earth electron measurements should be accounted for in the HPS, since it is conceivably a result of TS acceleration.

The influence of other processes on DSA, as respectively explored in Sections 6.4 and 6.5 at opposite ends of the energy spectrum, depends mostly on how they alter the form of TS spectra. The rigidity profile of diffusion, for instance, can be modified in a manner that causes acceleration at certain energies to be enhanced: If segments of the rigidity dependence where MFPs increase with rigidity are diminished in favour of rigidity-independent segments, spectral hardening is limited during modulation, while if either of the aforementioned are diminished in favour of MFPs that decrease with increasing rigidity, spectra soften instead. Both cases yield more favourable spectral forms for acceleration, while the latter could allow for the implementation of (potentially) more realistic input spectra at low energies that would otherwise have supplied spectra at the TS that are too hard to accelerate appreciably. DSA-induced intensity increases are especially pronounced at energies corresponding to transitions in the diffusion rigidity profile that yield soft energy distributions followed by harder ones. Another important revelation is that even though impaired diffusion is conducive to acceleration, the level of diffusion is less prevalent in determining the efficiency of acceleration than its rigidity dependence, which largely governs the form of modulated spectra incident at the TS.

Furthermore, due to the hardening of spectra brought about at affected energies, drifts are shown in Section 6.4 to inhibit acceleration; this is especially notable during the negative magnetic polarity, since TS spectra are harder during this cycle. This inhibition is also reciprocated though, because the higher spectral intensities ensuing from DSA reduces intensity gradients, which in turn implicitly diminishes drift effects and the contribution of drifts to global electron intensities. Finally, Section 6.6 demonstrates that acceleration is especially efficient at smaller polar angles for drift-insensitive energies, because the fast SW speed that emerges during solar minimum conditions reduces the length scales of diffusion at these latitudes. At higher energies, drifts during the positive and negative polarity cycles are shown to direct re-accelerated electrons to the polar and equatorial regions respectively.

The collective insights garnered in the current and preceding chapters are sufficient to inform the application of the model to reproduce electron observations in the outer heliosphere. These observations include their energy distributions, intensity profiles and effects thought to be related to their acceleration at the TS.

Chapter 7

Modelling Low-energy Galactic Electrons in the Outer Heliosphere

7.1 Introduction

Upon their outbound journey, the Voyager spacecraft have made a number of notable discoveries, with the crossing of the TS certainly being among them. Measurements of electron intensities [e.g. *McDonald et al.*, 2003; *Decker et al.*, 2005; *Stone et al.*, 2005] in the proximity of the TS show narrow peak-like increases, which are thought to result, at least in part, due to DSA [see e.g. *Stone et al.*, 2005]. Other significant features, such as the steep increase of electron intensities in the inner heliosheath [e.g. *Webber et al.*, 2012], have also since been recorded up to the probable detection of the HP itself [see *Gurnett et al.*, 2013; *Stone et al.*, 2013; *Webber and McDonald*, 2013]. Drawing upon the insights of earlier chapters, the model is applied in the following sections in an attempt to account, through DSA, for intensity increases at the TS that are similar in magnitude to that seen in observations, while simultaneously reproducing significant global modulation features as well.

First, the observational features that modelled results are desired to reproduce are identified and the configuration required to achieve this is discussed. Modelled energy distributions and radial intensity profiles are consequently illustrated and compared to observational data from Voyager 1 and PAMELA. Following the analysis of observed and modelled features, conclusions are drawn with regards to the acceleration features displayed by model solutions.

7.2 Configuration to Reproduce Electron Observations

In this chapter, two sets of observational features are of interest: Firstly, it is required that modelled radial and energy distributions reflect global modulation features of galactic electrons that are similar to those revealed by the Voyager 1 observations initially presented in Figures 2.17 and 2.18. It is also aimed to attain the intensity levels measured by PAMELA for high-energy electrons at Earth. Secondly, the model must show that by including the effects of DSA in solutions, intensity increases are produced at the TS with magnitudes comparable to that of the

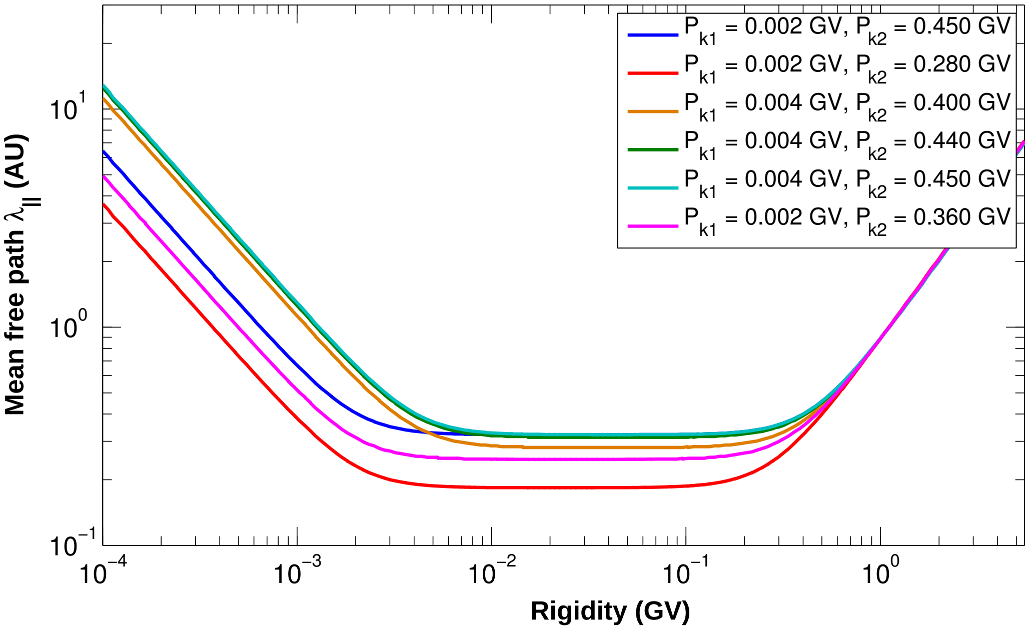

Figure 7.1: Rigidity profiles of MFPs for different values of P_{k1} and P_{k2} of Eq. 5.5 as indicated in the legend and summarised in Table 7.1 as part of configurations to reproduce observations at the radial distances listed therein. The segments from the lowest to highest rigidities have dependences of P^{-1}, P^{0} and $P^{1.23}$. Each profile corresponds to solutions shown in the same colour in Figures 7.3 and 7.6.

peak-like intensity increases measured for electrons near the TS. These increases are observed from energies as low as 0.35 MeV up to roughly 14 MeV [see e.g. *Decker et al.*, 2005; *Stone et al.*, 2005, 2008]. Should the latter aim be achieved it would reaffirm the notion that these intensity increases can indeed be attributed to DSA, while the simultaneous reproduction of modulation features would verify that the shock-acceleration effects are obtained under realistic conditions. The model configuration required to attain the desired results is subsequently discussed.

As usual, the input spectrum is considered first. Of the HPS scenarios introduced in Chapter 5 for electrons, the reference HPS of Eq. 5.1 yields the most pronounced acceleration effects at lower energies. Although large acceleration effects are desirable, it is not a realistic expectation that HPS intensities should grow indefinitely toward lower energies - to the contrary, the very limited available measurements of electrons below 0.1 MeV show much smaller intensities than those typically registered by the Voyager detectors. See e.g. the 50 keV electron profiles of *Hill et al.* [2014]. However, for the purposes of this chapter, these measurements are merely considered to suggest that electron intensities do indeed fall away toward lower energies without providing bounding constraints on how rapidly they fall away or at which particular energies. If a HPS is hence applied with an exponential decrease of intensities that is less rapid and initiates at lower energies than previously specified, a larger segment of the spectrum remains soft and is hence more conducive to acceleration. The input spectrum described by Eq. 5.4 is therefore applied in this chapter with $h_1 = -1.35$, $E_c = 0.1$ MeV and $\Phi = 1.0$. Where modulation is concerned, the levels of diffusion in the inner heliosphere is difficult to establish since it remains unclear what the contribution of galactic electrons is to intensities at Earth, which is dominated by Jovian electrons out to at least 10 AU [*Strauss et al.*, 2013a]. See also the scenarios explored by *Potgieter and Nndanganeni* [2013a]. The radial dependence of the diffusion coefficients is specified in this chapter such that the total modulation of electron intensities from the

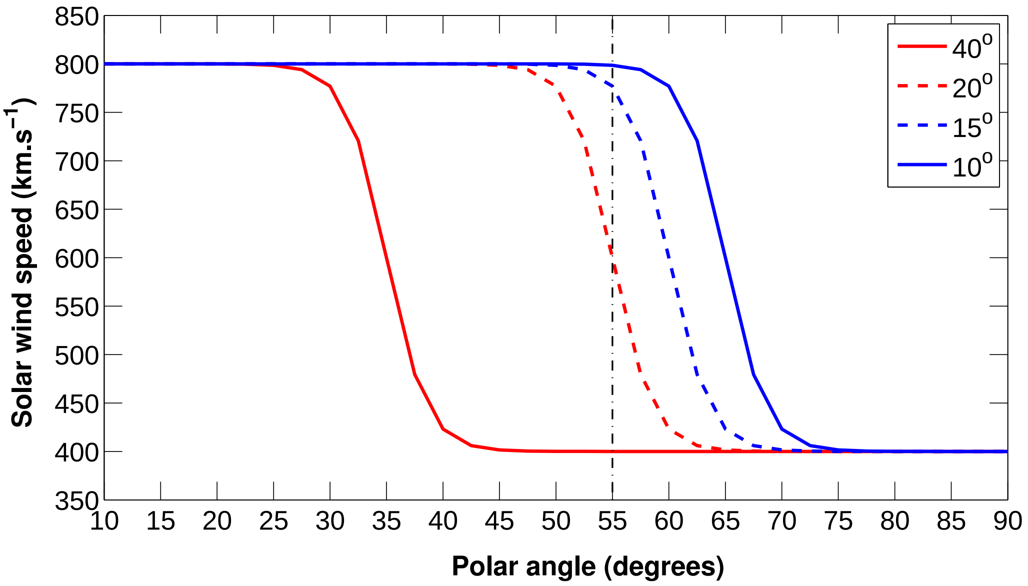

Figure 7.2: Modelled heliographic latitude profiles for the upstream SW speed (according to Eq. 2.2) for different stages of solar activity as represented by the HCS tilt angle values shown in the legend. The approximate polar position of Voyager 1 is indicated with a vertical dash-dotted line at $\theta = 55°$, where the SW speed is estimated at 400, 600, 775 and 800 km.s^{-1} for tilt angles of 40°, 20°, 15° and 10° respectively. The equatorial plane is at $\theta = 90°$.

HP to Earth is similar to that reported by earlier studies [e.g *Vos*, 2012], but with the modulation in the heliosheath proportionally larger in order to reproduce Voyager observations in the outer heliosphere. Hence, $\lambda_{r,0}$ and λ_{r,TS^+} in Eq. 3.25 are chosen as 1 AU and 0.243 AU respectively, with Λ_{IH} adapted to 0.45 to yield a dependence of $\sim r^{0.8}$ for $\lambda_{||}$ in the inner heliosphere. The rigidity profile of diffusion furthermore includes a low-energy up-turn in MFPs, which is accounted for in Eq. 5.5 with $g_0 = -1.0$; the rigidities P_{k1} and P_{k2} at which the dependence changes are varied as needed to reproduce observed energy spectra, with the resultant rigidity profiles of MFPs illustrated in Figure 7.1. More on this follows in the discussion below. The drift efficiency is scaled down so that $\kappa_{D,0} = 0.55$. The TS compression ratio is kept fixed at $s = 2.5$ for all latitudes, with $r_{TS} = 94$ AU and $r_{HP} = 122$ AU as detected by Voyager 1.

Note however that since the Voyager observations that model solutions are aimed to reproduce were collected over a period of almost 8 years, it is inadequate to assume constant levels of solar activity: The detection of the TS by Voyager 1 in late 2004 follows a period of moderate solar activity conditions, while subsequent measurements of heliosheath intensities concur with the decline of solar activity to remarkably low levels during 2009. From this time, solar activity increases again up to the detection of the HP in 2012. Note that this period of observation coincides with the A $<$ 0 polarity cycle. Although the model yields steady-state solutions and cannot explicitly describe time-dependent changes, the necessary solar-cycle dependences are accounted for in the model using the HCS tilt angle, α, as a proxy [see also *Ferreira and Potgieter*, 2003]; recall that α not only indicates the polar extent of the HCS along which CRs drift, but is also used in the model to describe the latitude dependence of the SW speed (see e.g. Figure 7.2) and scale diffusion coefficients according to solar activity. Hence, in order to reproduce observations recorded at different stages of solar activity, the TPE is solved for different tilt angles. Consider though that the magnetic or current sheet properties that are measured at

Earth take a significant amount of time to propagate out to larger radial distances, and that the values of the tilt angle to be considered for modelling electron intensities at e.g. the TS should typically be taken as those measured at the Sun (see Figure 2.11) roughly 13 months prior to the date of observation when assuming a SW convection speed of 400 km.s^{-1}. The matter becomes more complicated when considering the propagation of SW-related conditions further into the heliosheath, because the radial component of the SW speed diminishes with increasing distance, while the polar and azimuthal components become more pronounced [see e.g. *Richardson et al.*, 2009]. Under the assumption of incompressible flow in the heliosheath, the SW speed decreases as r^{-2}, which implies that up to $\sim$ 4 years may elapse, if the slow SW stream is considered, before modulation conditions have propagated from the TS to the HP. This time delay only lengthens should the decrease of the radial SW speed in the heliosheath be assumed to be steeper than r^{-2} as some studies suggest [e.g. *Florinski et al.*, 2004; *Ferreira et al.*, 2007a]. See also the review by *Richardson and Burlaga* [2013] on the SW and related properties in the outer heliosphere and heliosheath. The implication of the above is that plasma and magnetic properties relating to earlier phases of the solar cycle may be encountered in different regions within the heliosheath. See also the comments of *Hill et al.* [2014] in this regard. Solar variability provides a global context in which measurements and model results alike may be interpreted, and it would be insightful to gauge the response of electron modulation to an emulated solar cycle dependence in the heliosheath.

If the time of travel of the SW is considered at least up to the TS, and the values of the magnetic field at Earth and the tilt angles (see Figures 2.6 and 2.11) measured at least 13 months prior to the time of observations adopted, the model configuration can be constructed as summarised in Table 7.1. Note that the tilt angles used are those estimated by the more recent radial model [e.g *Wang and Sheeley*, 1992]. Included in the table are values for P_{k1} and P_{k2}, which define the rigidity profiles of diffusion needed to reproduce heliosheath observations for the assumed conditions. It follows that P_{k2} is scaled to adjust diffusion levels, while P_{k1}, on the other hand, is adjusted for better correspondence of solutions to the lowest-energy observations and to control the range of acceleration effects. Recall that acceleration is enhanced at the energy corresponding to P_{k1}, since it is where soft spectra transitions to harder spectra if a pronounced MFP up-turn is present. Also in Table 7.1 is the configuration to reproduce the PAMELA spectrum at Earth for the second semester of 2009, for which the magnetic field and tilt angle are inferred directly from Figures 2.6 and 2.11 at the time of observation. All other parameters not mentioned in the discussion above are as defined for Chapters 5 and 6.

7.3 Model Results for Electron Modulation and Acceleration

Applying the configuration(s) described in the previous section to reproduce observations, the energy spectra and radial distributions of galactic electrons are modelled in the outer heliosphere and heliosheath. Features pertaining to the general modulation of electrons and also their re-acceleration are subsequently discussed. Solutions are presented along Voyager 1's approximate trajectory at a polar angle of $\theta = 55^\circ$ for comparison with the observations of this spacecraft. It should be borne in mind that the energy spectra presented in the following

	r_{obs}	t_{obs}	α	B_e	P_{k1}	P_{k2}
a	94 AU	2004.9	40°	7.0 nT	$2{\cdot}10^{-3}$ GV	0.28 GV
b	100 AU	2006.6	15°	5.0 nT	$4{\cdot}10^{-3}$ GV	0.40 GV
c	106 AU	2008.3	15°	4.3 nT	$4{\cdot}10^{-3}$ GV	0.44 GV
d	112 AU	2009.9	10°	3.9 nT	$4{\cdot}10^{-3}$ GV	0.45 GV
e	118 AU	2011.6	20°	5.0 nT	$2{\cdot}10^{-3}$ GV	0.36 GV
	1 AU	2009.5-2010.0	10°	3.9 nT	$2{\cdot}10^{-3}$ GV	0.45 GV

Table 7.1: Configuration of dynamic variables to reproduce observations at the indicated dates (t_{obs}) and radial distances (r_{obs}). The values of the HCS tilt angle, α, and magnetic field magnitude at Earth, B_e, are inferred from measured data at Earth roughly 13 months prior to t_{obs} for the Voyager 1 observations at the distances in the heliosheath labelled (a) to (e); these quantities are however inferred directly at t_{obs} from measurements at Earth (1 AU) to fit the PAMELA observations. The transition rigidities, P_{k1} and P_{k2} (of Eq. 5.5), are adjusted in each case for the optimum data reproduction; the associated rigidity profiles are illustrated in Figure 7.1.

subsection are steady-state solutions that are attained independently at each radial distance according to the configurations presented in Table 7.1; e.g. the TS spectrum is not modulated from the spectrum shown at 100 AU, nor that at 100 AU from 106 AU, and so forth.

7.3.1 Reproduction of electron energy distributions

Figure 7.3 presents modelled energy spectra at a number of radial distances in the heliosheath, at the TS, and at Earth. Accompanying each of these computed spectra in the heliosheath and at the TS is a set of intensity measurements for ~4 to 40 MeV electrons from the Voyager 1 spacecraft as provided by *Webber* [2014]. As is also shown in Chapter 5, the modelled spectra demonstrate that the power-law distribution of the HPS, which itself provides a satisfactory fit to observations at 122 AU, is mostly retained during modulation in the heliosheath. The Voyager measurements also reflect this. However, the lowest-energy measurements at about 4 and 8 MeV increasingly deviate from the power-law distribution with decreasing radial distances. This indicates that the assumption of rigidity-independent diffusion is only valid down to a particular energy corresponding to the rigidity P_{k1}. Below this rigidity MFPs increase and thereby decreases modulation, which allows spectral intensities to be raised and coincide with the spacecraft measurements. If the values of P_{k1} that were used to reproduce each set of observations are considered (see Table 7.1), it is revealed that the MFP up-turn is initiated at lower rigidities at 94 and 118 AU than at the radial distances in between. Coincidentally, the spectra at 100, 106 and 112 AU were also reproduced for smaller tilt angles and hence for less active solar conditions. This may suggest that the MFP up-turn has a solar-cycle dependence, which would also imply a dependence of the underlying dissipation-range turbulence, but there are also other factors that may account for this: Consider for instance that the 118 AU spectrum might have been reproduced with similar accuracy should P_{k1} have been adjusted to $4{\cdot}10^{-3}$ GV, because however rapidly MFPs increase, the spectral intensities cannot be raised much before adopting HPS values. On the other hand, the TS spectrum might also have been modelled using $P_{k1} = 4{\cdot}10^{-3}$ GV if DSA was suppressed, considering that the Voyager measurements

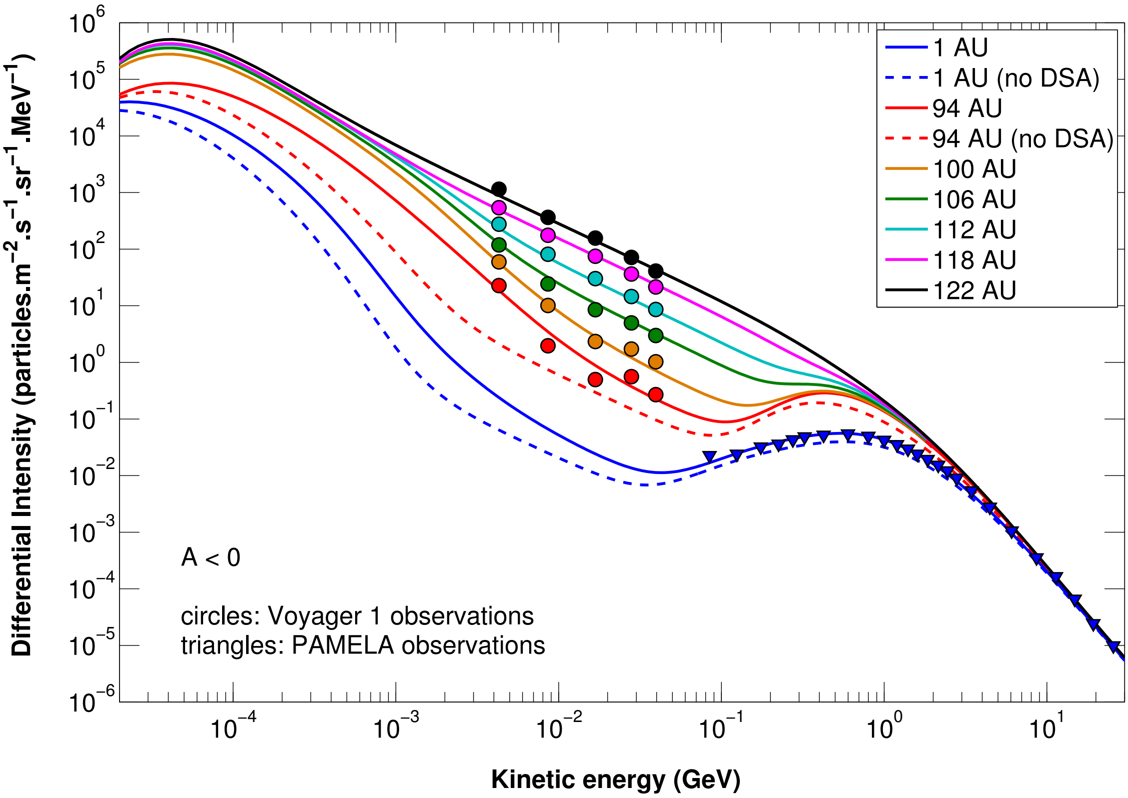

Figure 7.3: Modelled energy spectra for galactic electrons, with accompanying observations from Voyager 1 [*Webber*, 2014] and PAMELA [*Adriani et al.*, 2011] respectively presented using circular and triangular markers. The HPS is shown as a solid black line at 122 AU. Different colours represent radial distances as indicated in the legend, with spectra at 94 to 122 AU shown at $\theta = 55°$ and 1 AU at $\theta = 90°$. The computed spectra are shown for the A < 0 cycle and are generated for the model configuration discussed in Section 7.2 and the parameters specified at each distance in Table 7.1. Solid and dashed lines respectively represent solutions with and without DSA effects.

at 94 AU are fitted more because of acceleration effects than due to the spectral shape brought about by modulation. Note that the unshocked TS spectrum (shown as a dashed red line in Figure 7.3) does not fit the observational points, while the spectrum with DSA effects does so quite accurately. Moreover, the Voyager measurements may also suggest that the underlying turbulence displays a radial dependence, since the MFP up-turn becomes less pronounced with increasing distance from the TS. Ultimately, the chosen rigidity profiles of diffusion and TS acceleration collectively reproduce the presented heliosheath observations, as well as their radial distribution, with reasonable accuracy.

Also shown in Figure 7.3 are modelled spectra at Earth, which closely follows the accompanying PAMELA measurements [*Adriani et al.*, 2011] at high energies ($E \gtrsim$ 100 MeV). This confirms that in addition to the correct levels of modulation achieved in the heliosheath, the total global modulation at these energies is also accurately reproduced. As intended, the heliosheath modulation is larger than that occurring between the TS and Earth under the current configuration. The properties of the diffusion rigidity profile implemented at Earth are similar to that used by *Vos* [2012], while the heliospheric conditions assumed are also alike - the referenced study implements $\alpha = 10°$, $B_e =$ 3.94 nT and $P_{k2} =$ 0.45 GV to fit PAMELA observations from 2009, which are indeed very similar to the values listed for the same period in Table 7.1. Also note that the parameters used to reproduce the spectrum at Earth are similar to those used to repro-

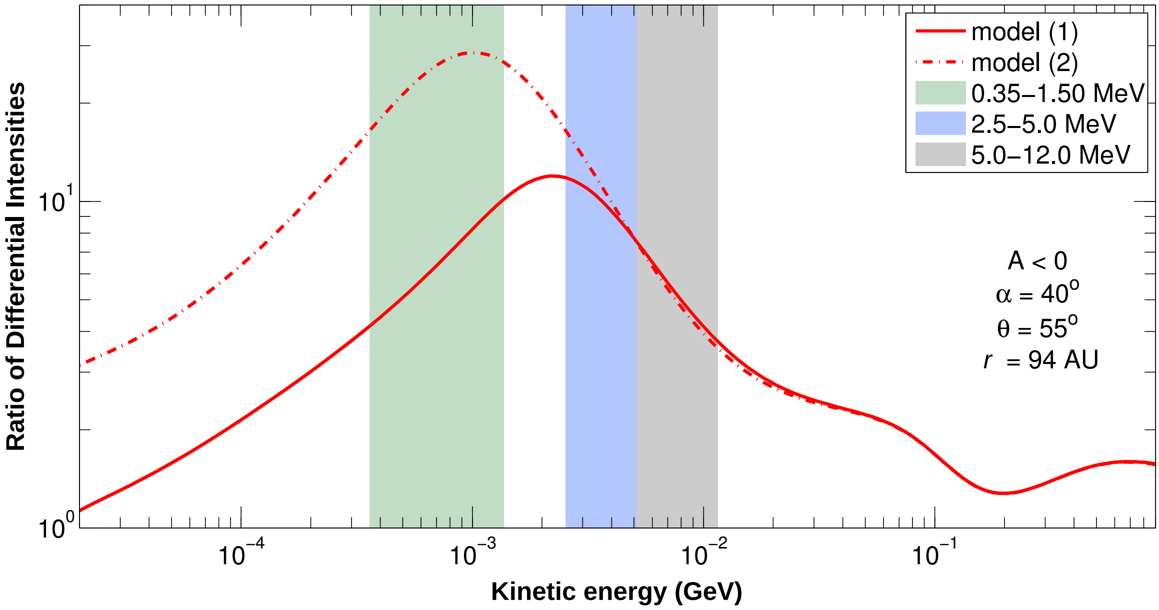

Figure 7.4: Ratios of modelled TS spectra with DSA effects to those without for two different configurations of the low-energy diffusion profile. The ratios representing the first configuration (model (1): $P_{k1} = 2.0 \cdot 10^{-3}$ GV, $g_0 = -1.0$) is shown as a solid red line, while those representing the second (model (2): $P_{k1} = 1.5 \cdot 10^{-3}$ GV, $g_0 = -1.2$) is shown as a dash-dotted line. The shaded regions, from lowest to highest energies, respectively indicate the energy intervals for which *Decker et al.* [2005], *Stone et al.* [2008] and *Webber* [2014] present intensity profiles with possible DSA effects near the TS.

duce the spectrum at 112 AU, which was observed within the same period that the PAMELA measurements were made. The only difference is the values of P_{k1}; had the same values been applied, the intensities at Earth would have exceeded the TS intensities toward lower energies. Since the position of the low-energy up-turn is the only difference between the configurations applied at the two distances, it is again indicative of a radial dependence of the underlying turbulence. See also *Engelbrecht and Burger* [2013a] for examples of how features of the turbulence spectrum and associated electron MFPs may vary with radial distance for $r < r_{TS}$.

7.3.2 The features of electron re-acceleration

With regards to DSA at the TS, the contribution of re-accelerated electrons to intensities is emphasised using the ratio of the TS spectrum (of Figure 7.3) with DSA to that without; see the solid red line in Figure 7.4. What emerges is a clear peak in acceleration effects near 2 MeV, with the amount by which DSA raises intensities at the TS diminishing rapidly both toward lower and higher energies. The reason for the pronounced intensity increase of more than a factor of 10 at 2 MeV is because of the corresponding transition in the rigidity profile of diffusion: The low-energy MFP up-turn softens the TS spectrum at energies preceding 2 MeV, while at higher energies the -1.35 power law is retained from the input spectrum due to diffusion becoming rigidity independent. As explained in Section 6.5, a soft energy spectrum followed by a harder one gives rise to an especially large DSA-induced intensity increase at the transition between them. Above roughly 10 MeV the re-accelerated contribution begins to show the same features encountered at high energies in the reference solutions of Section 6.3.

	Observations			**Model (1)**			**Model (2)**		
	min	max	average	min	max	average	min	max	average
0.35 - 1.50 MeV[†]	7	30	13.8	4.2	9.7	6.6	16.5	28.6	24.5
2.50 - 5.00 MeV[††]	–	5*	–	7.5	11.8	9.9	7.5	16.5	11.5
5.00 - 12.0 MeV[‡]	2.4*	2.5*	–	3.9	7.5	5.5	3.7	7.5	5.3

Table 7.2: This table presents the factors by which DSA is estimated to raise intensities at the TS. The second column shows the magnitudes of acceleration effects as deduced from the observations of [†]*Decker et al.* [2005], [††]*Stone et al.* [2008] and [‡]*Webber* [2014] in the energy intervals given in the first column. The third and fourth columns show the factors estimated from the model using two different diffusion configurations, namely model (1), with $P_{k1} = 2.0 \cdot 10^{-3}$ GV and $g_0 = -1.0$, and model (2), with $P_{k1} = 1.5 \cdot 10^{-3}$ GV and $g_0 = -1.2$; see Eq. 5.5. In the case of observations, "min","max" and "average" refer to the smallest, largest and average size of intensity peaks, while for the models they refer to the smallest, largest and average factor increases estimated (from Figure 7.4) within the corresponding energy range. *These values are lower-limit estimates.

To establish how these acceleration features compare to observations, the re-accelerated ratio is considered in the energy intervals marked by the shaded regions in Figure 7.4. These intervals correspond to the energy channels of the LECP instrument aboard Voyager 1, which measured radial intensity profiles that display peak-like increases (tentatively) attributed to DSA at the TS; the 0.35 to 1.5 MeV intensity profile is presented by *Decker et al.* [2005], the 2.5 to 5 MeV profile by *Stone et al.* [2008], and the 5 to 12 MeV profile, provided by *Webber* [2014], are shown in Section 7.3.3. See also 6 to 14 MeV profiles [e.g. *Stone et al.*, 2005, 2008] for comparison. For the purposes of this discussion, the magnitude of acceleration effects refers to the factor by which intensities are raised during these supposed DSA events from the background intensity level of the observed profiles. These intensities are however thought to be contaminated by electrons produced within the detector on Voyager 1 so that the background may be artificially raised [*Webber*, 2014]. Note that the *Decker et al.* [2005] intensities have been corrected for additional background; see also *Zhang* [2005] for the handling of CR background levels in Voyager 1 observations. Hence, because the peak-like intensity increases are likely larger than can be deduced from observations, the aforementioned magnitude of acceleration effects can therefore be regarded as a lower limit for the higher energy intervals. The observed magnitudes are presented in Table 7.2 alongside that predicted by the model (from Figure 7.4) for each energy interval. Since the 0.35 to 1.5 MeV intensities of *Decker et al.* [2005] are of a higher resolution so that multiple peaks can be discerned during each intensity-raising event, an average magnitude of acceleration effects is also included for this energy interval. This is not meaningful for the other energies, where only one or two distinct peaks can be discerned.

Note from Table 7.2 that the model-predicted factors ensuing from the 94 AU configuration of Table 7.1, referred to as model (1), underestimate observed acceleration effects for 0.35 to 1.5 MeV electrons, but overshoots the observed lower-limit magnitudes for the higher-energy intervals. Since the factors for 2.5 to 12 MeV electrons may yet be larger than can be deduced from the observations, the need to dampen modelled acceleration effects at these energies is not too compelling. For the lower-energy interval, however, it is desirable that the model can attain factors as large as the observed magnitude of acceleration effects (or larger). The modelled acceleration effects must hence be enhanced between 0.35 and 1.5 MeV without altering the re-accelerated contribution appreciably at higher energies. In the context of the model this can be

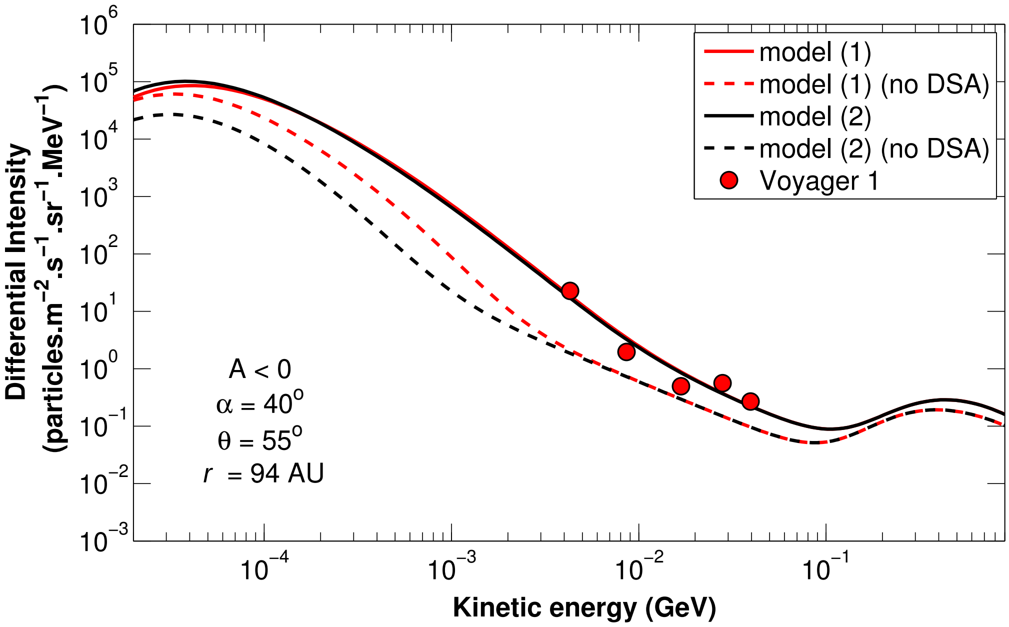

Figure 7.5: Computed TS spectra with DSA effects (solid lines) and without (dashed lines) following from model (1) and (2) as indicated in the legend; the details of the two configurations are provided in the captions of Figure 7.4 and Table 7.2. The circular markers in red are Voyager 1 measurements at the TS as provided by *Webber* [2014].

achieved by shifting the MFP up-turn to lower energies, that is, by lowering the value of P_{k1} in Eq. 5.5 to approximately $1.5 \cdot 10^{-3}$ GV. To compensate for this modification, however, a stronger negative rigidity dependence of MFPs at lower energies is employed by specifying $g_0 = -1.2$ to soften the resultant distribution. This is to enhance acceleration at the spectral transition associated with P_{k1} and in doing so raise spectral intensities enough to still reproduce the lower-energy Voyager measurements at the TS.

The re-accelerated contribution following from this adapted configuration, referred to as model (2), is illustrated in Figure 7.4 as a dash-dotted line. The model (2) estimates for acceleration effects are shown in Table 7.2 to be much larger than the corresponding model (1) estimates for the 0.35 to 1.5 MeV interval. This modified configuration also overestimates the average observed magnitude, but comes closer to accounting for the largest observed intensity increase of about a factor of 30. It follows that the optimum configuration to reproduce acceleration effects consists of a combination of P_{k1} valued between $1.5 \cdot 10^{-3}$ and $2.0 \cdot 10^{-3}$ GV and g_0 between -1.0 and -1.2. Remarkably, both configurations are shown in Figure 7.5 to yield nearly indistinguishable shocked spectra and reproduce the Voyager-observed measurements at the TS, while the effects of the different rigidity profiles of diffusion are clearly visible for the spectra without DSA. It is therefore possible using the model with different parameter configurations to account through DSA for the magnitudes of observed intensity peaks at the TS, while simultaneously reproducing the energy spectra measured at the TS by Voyager 1.

7.3.3 Reproducing radial electron intensity profiles

For the sake of discernibility, only the solutions with shock-acceleration effects are shown in Figure 7.3 in the heliosheath, while the transport of re-accelerated electrons into this region is

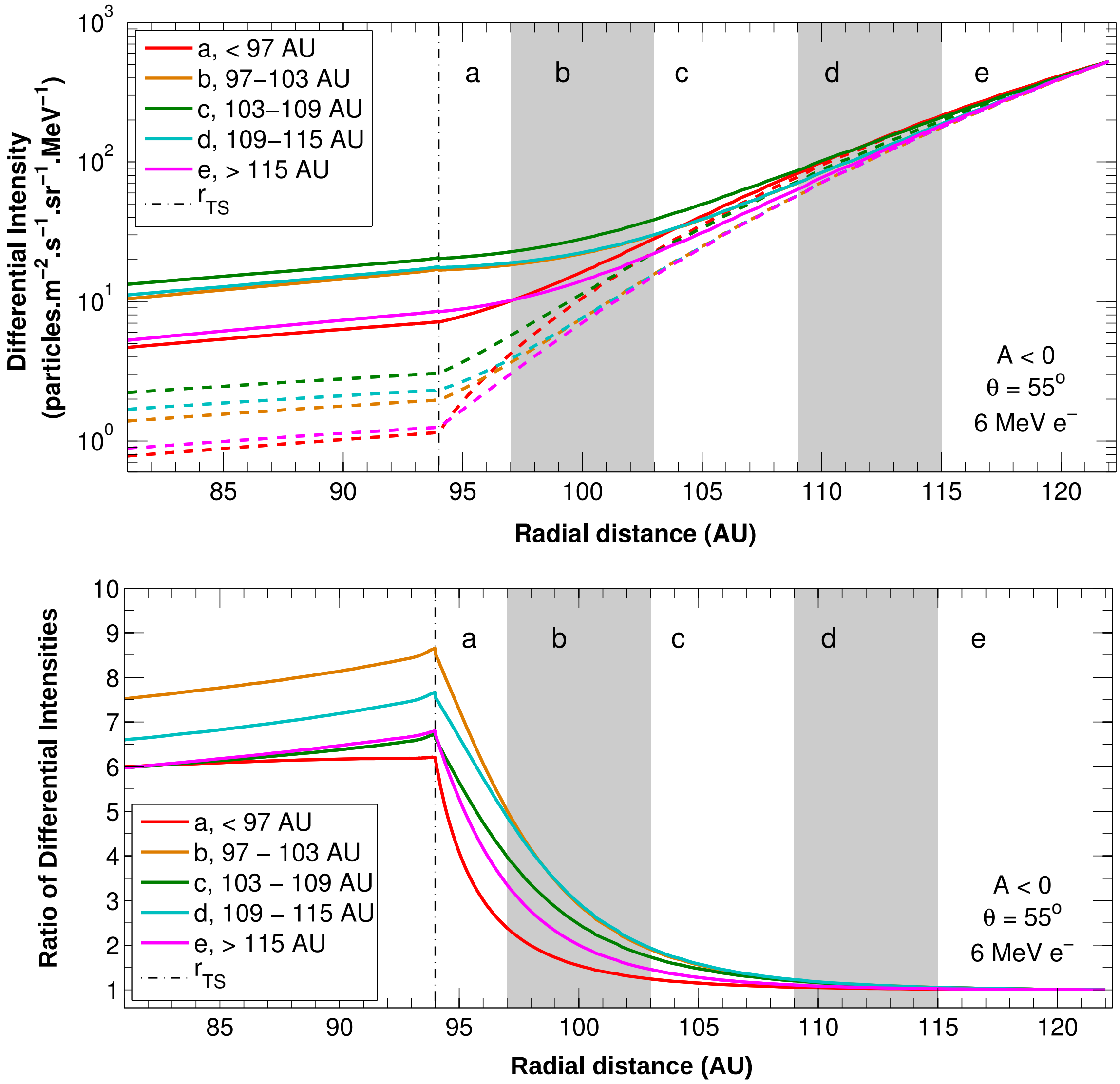

Figure 7.6: TOP: Modelled radial intensity profiles for 6 MeV electrons for the configurations (a) to (e) as defined in Table 7.1. The profiles are estimated to be valid only in the accordingly labelled regions specified in the legend. Profiles with and without DSA effects are shown in solid and dashed lines respectively. The TS position is indicated with a vertical dash-dotted line. BOTTOM: Similar to the top panel, but illustrating the ratios of profiles with DSA effects to those without for each configuration.

instead illustrated using radial intensity profiles. Distributions of 6 MeV electron intensities in the heliosheath are presented in Figure 7.6 for each of the configurations presented in Table 7.1. Note however that each configuration, labelled (a) to (e), is technically only estimated to be valid roughly within the regions described for each profile in the figure legend, because they are meant to emulate different instances in time (or equivalently, in the solar activity cycle). These regions are shown as consecutively shaded and unshaded areas. From these profiles it is possible to compare the modulation and acceleration effects following from the different configurations. The total heliosheath modulation is greater for configurations (a) and (e) than for (b) to (d), which follows largely as a result of the tilt angle for which they are solved; consider e.g. that the levels of the profiles for (b) to (c), attained using similar tilt angles, are alike, while configurations (b) and (e) with similar magnetic fields at Earth yield noticeably different intensity levels. The tilt angle, as a proxy for solar activity, is hence the most prevalent parameter of those listed in Table 7.1 in determining modulation effects in the model: it controls the scaling constants of the diffusion coefficients as well as the latitude dependence of the SW speed (see e.g. Figure 7.2), which in turn affects both the diffusion length scales and global HMF magnitudes. Consequently, the smaller diffusion length scales following from the fast SW stream at $\theta = 55^o$ enhances the acceleration of electrons at the TS, and hence the ratios in the bottom panel of Figure 7.6 are generally larger for solutions associated with minimum solar activity. It is important not to confuse the tilt angle's role as proxy for solar activity with its physical role of defining the HCS inclination; the aforementioned effects follow as a result of the former.

In order to reproduce the observed intensities for 5 to 12 MeV electrons in the heliosheath, the appropriate conditions must be simulated in the model throughout the region. Since the distribution of observed spectra with radial distance has already been successfully reproduced in Figure 7.3, the configurations of Table 7.1 that were used to do so provide a convenient starting point. If each configuration is assumed to be roughly valid in a limited region around the radial distance it is associated with, the segments of the profiles of Figure 7.6 within these regions can be combined to construct realistic radial intensity profiles (both with and without DSA effects) for the entire heliosheath; the transitions of profiles between different regions are smoothed by means of taking a moving average. These profiles are shown in Figure 7.7 at a representative energy of 6 MeV alongside intensities measured by Voyager 1 in the 5 to 12 MeV interval. The model reproduces the observed radial distribution of intensities quite accurately, especially in the respective proximities of the TS and HP: From the TS out to at least 100 AU the effects of DSA are essential to account for the shape of the first large incline in intensities, while modelled and observed intensities are also similar for $r > 109$ AU, where acceleration effects have mostly diminished; see also the bottom panel of Figure 7.7. At intermediate distances (100–109 AU), the observations are better represented without DSA effects, since the re-accelerated contribution causes the model to overestimate intensities in this region. At $r < r_{TS}$, the model predicts intensities at roughly the same level of the highest points of the observed intensity peaks. The factor of about 6 by which these intensities are raised from levels without shock effects is much larger than the magnitudes of the peaks shown in Figure 7.7, however these might in fact be larger if the background intensities (shown in red) are indeed artificially raised as discussed in Section 7.3.2. As also concluded in the previous subsection, DSA as implemented in the model is efficient enough to produce intensity increases of the magnitude of these peaks and larger.

A final issue to consider is what causes the peak-like shapes of the observed intensity increases near the TS if DSA is indeed assumed to be an involved mechanism. A simple explanation involves a magnetic connection between the TS and the spacecraft at the time of observation, which would allow particles re-accelerated at the shock to be transported along field lines to the spacecraft for as long as the two are connected. If this is assumed not to be the cause, the following mechanisms are considered: In the model, diffusion levels are too high upstream of the shock to limit the passage of re-accelerated electrons to such narrow spatial intervals. In this context one might expect any event creating local low-diffusion conditions to be able to account for their narrow shape. Its cause may however be spatial as well as temporal, e.g. the relative movement of the spacecraft and TS, or the movement of either of these in and out of different magnetic sectors [*Hill et al.*, 2014]. It is suggested by *Stone et al.* [2005] that

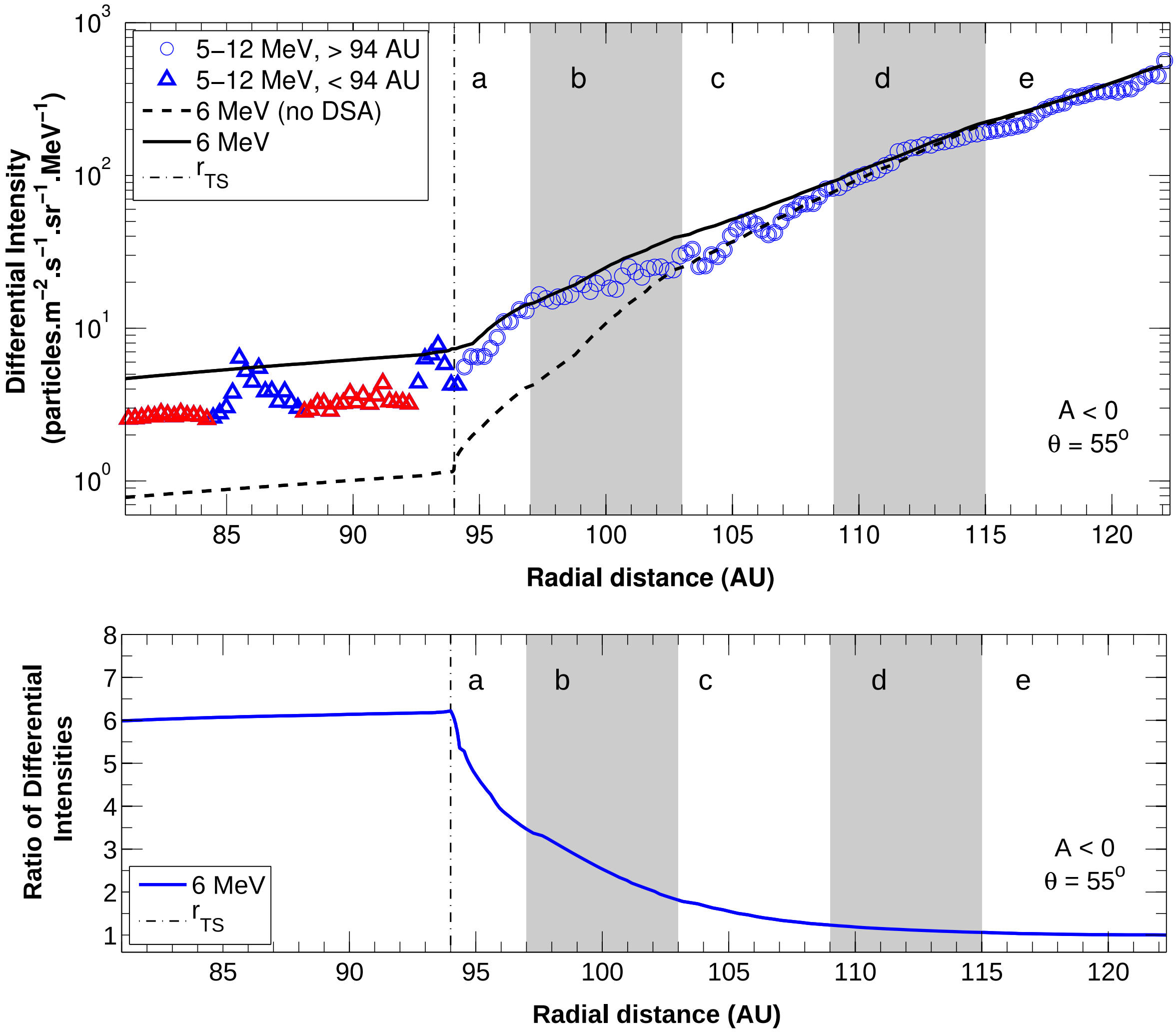

Figure 7.7: Similar to Figure 7.6, this figure shows 6 MeV electron intensities modelled by combining the segments of profiles valid in each labelled region. Computed profiles with and without DSA are respectively shown in solid and dashed black lines. Triangular and circular markers denote Voyager 1 observations [*Webber*, 2014] for $r < r_{TS}$ and $r > r_{TS}$, while the red markers represent background intensities. The bottom panel shows the ratio of the computed profile with DSA to that without.

these peaks may result because of the interaction of particles accelerated at the TS with large-scale disturbances, e.g. merged interaction regions, forming in interplanetary space due to the coalescence of coronal mass ejections, that are convected outward by high SW speeds. Such temporal effects may be studied more effectively using time-dependent models [e.g. *Ferreira and Potgieter*, 2004; *Manuel et al.*, 2011, 2014].

7.4 Summary and Conclusions

This chapter applies the insights from previous chapters to model the features of galactic electrons throughout the outer heliosphere, and finally compares these modelling results with observations from Voyager 1 and PAMELA. Two sets of features are singled out: It is firstly aimed to reproduce the more global modulation features of electrons, including the correct decrease of intensities in the heliosheath and the total modulation to the Earth. Secondly, it is aimed to apply the model to simulate observational features that are associated with DSA at the TS to confirm the involvement of this mechanism. To achieve this, the model configuration is chosen such that it is conducive to acceleration while still being able to account for known features of electron modulation and the heliosphere; see Section 7.2. Notable features of the configuration include a HPS with intensities increasing toward lower energies, but that eventually falls away exponentially, and a rigidity dependence of diffusion that includes a low-energy up-turn, followed by segments of rigidity-independent diffusion and of MFPs growing proportional to rigidity at the high-energy end. Furthermore, a solar activity dependence is emulated using the HCS tilt angle and magnetic fields, which are inferred appropriately for the time and distance at which Voyager observations were made. The rigidity profile of diffusion is adapted in each instance to optimise the reproduction of observational features.

The energy spectra observed by Voyager 1 in the heliosheath are reproduced satisfactorily, along with the level of total modulation at higher energies able to reproduce the PAMELA spectrum at Earth. The results and parameters used are similar to those of earlier related studies. While rigidity-independent diffusion reproduces observations at intermediate energies, it is revealed that the up-turn in MFPs at $E < 4$ MeV is crucial to account for the form of observed spectra at lower energies, both by reducing modulation at those energies and by enhancing acceleration to raise intensities. To reproduce observations it is also necessary that the rigidity profile of diffusion is changed at different radial distances, which is highly suggestive of a radial dependence of the underlying turbulence. A possible solar-cycle dependence is also implied. Furthermore, the radial distribution of intensities in the heliosheath as observed by Voyager 1 is also reproduced by the model using an emulated solar cycle dependence. DSA effects are shown to be essential to account for observed intensities out to at least 100 AU, or 6 AU into the heliosheath as measured from the TS.

In terms of the magnitude of acceleration effects, the largest intensity increases consistently occur where soft spectra are succeeded by harder spectra, which is mostly induced by the transition of up-turned MFPs at lower energies to the rigidity-independent MFPs that follow at higher energies. Observed radial profiles with peak-like intensity increases in the vicinity of the TS suggest that should these increases indeed be attributable to DSA, the acceleration is more pronounced at lower energies, typically below 1.5 MeV, than toward higher energies, where increases are registered to be of magnitudes of at least a factor of 2. The modelled intensity increases at the TS, resulting from DSA, exceeds the lower-limit estimates of the observed intensity increases at higher energies, while a parameter space is constrained for the exact reproduction of the observed magnitudes of acceleration effects at lower energies. It is also demonstrated that acceleration effects are enhanced during minimum solar activity conditions, possibly because of the faster SW streams along the Voyager trajectory that diminish diffusion length scales at the TS.

Ultimately, the intensity increases attainable through DSA are large enough to account for the observed intensity peaks, and thus the notion that DSA is involved in their production is reinforced. Their narrow structure (if assumed not to follow from a temporary magnetic connection between the TS and the spacecraft) can only be accounted for in conjunction with other events, possibly temporal in nature, that create local low-diffusion conditions at the TS.

Chapter 8

Summary and Conclusions

The heliosphere was introduced in this study as a region of interstellar space containing solar material, and is largely characterised by the SW outflow and its embedded magnetic field. Near the TS, where the initially radial supersonic SW speed decreases abruptly with a factor referred to as the compression ratio, the Voyager spacecraft detected peak-like intensity increases for low-energy electrons up to about 14 MeV. With the TS being a known site for DSA, these intensity peaks are thought to arise as a result of this acceleration mechanism. Prompted by these observations, the features of the DSA of CRs were investigated comprehensively in this study. This was done by numerically solving a TPE that accommodates the DSA process through a term simulating adiabatic energy changes in terms of the SW velocity divergence, along with a matching condition which relates the CR flux on either side of the TS. This study endeavoured to illustrate the extent of DSA effects, especially as pertaining to electron re-acceleration, with the more general aim of revitalising interest in this acceleration mechanism.

Modelling the acceleration of ACR Oxygen from a monoenergetic source function, representing a population of PUIs injected at the TS, explicitly demonstrates the features of shock-accelerated spectra. The primary feature is a power-law distribution with a spectral index dependent on the shock compression ratio. This power law terminates in an exponential decrease at energies of 30 to 100 MeV. nuc^{-1} where the diffusion length scales of particles become comparable with the shock radius. It follows that smaller diffusion coefficients result in DSA to higher energies, with the position of the spectral cut-off being especially sensitive to perpendicular diffusion. In the presence of drift effects the shock-accelerated spectra terminate at lower energies than when drifts are neglected. Toward lower energies, typically below 0.3 MeV. nuc^{-1}, the diffusion length scales of ACR Oxygen become smaller than the width of the TS precursor. The energy distributions displayed by accelerated particles are softer as a result (that is, their spectral indices are smaller), because the factor decrease in the SW speed observed within the precursor structure is only a fraction of the compression ratio. In the absence of a precursor, or stated otherwise, for a fully discontinuous SW decrease across the TS, shock-accelerated distributions display spectral indices associated with the full compression ratio.

Applying a similar technique, the DSA of a monoenergetic electron source was investigated, revealing accelerated spectra with similar features to those of the ACRs. A notable difference is that the accelerated electron energy distributions extend to relativistic energies, where their spectral indices are about double in absolute value of those displayed at non-relativistic energies. This follows because $P \propto E$ above the rest-mass energy, which is only 0.511 MeV for electrons, while $P \propto E^{1/2}$ below it; note that these spectral indices are negative for all admissible values of the compression ratio. Hence, while the shock-accelerated spectral index still depends only on the compression ratio, the nature of this dependence varies with kinetic energy. The source function was furthermore specified to represent an electron seed population that is already distributed with energy. This revealed that should an energy distribution incident at the shock be softer than what the shock is able to produce when accelerating a monoenergetic source, the accelerated spectrum will harden to adopt the spectral index associated with the compression ratio. Otherwise, if the incident distribution is harder than what the shock is able to produce, its intensities are merely raised by an amount depending on how similar its spectral index and that associated with the compression ratio are. Note that the effects of DSA on electrons at Voyager-observed energies cannot necessarily be discerned from changes in their spectral slopes across the TS, because their spectra are already too hard and the compression ratio of the shock too small to induce them.

Since galactic electrons are modelled in this study by specifying an input energy spectrum at the HP, whereupon this spectrum is modulated in the heliosheath, the re-acceleration of these electrons at the TS depends on both the spectral features retained from the HPS and those obtained during modulation. The features of the electron HPS were hence investigated, and while these are fairly well-established at energies higher than ~ 5 MeV due to the availability of spacecraft observations, the lower-energy features are still uncertain. It is argued that its intensities are unlikely to increase indefinitely toward lower energies, but that they could fall away instead; in subsequent modelling, different scenarios for this low-energy spectrum were explored. In terms of modulation, diffusion appears to be the most prevalent transport process influencing the features of spectra at the TS. Although the MFPs of electrons and ions become increasingly similar toward higher energies, at low energies the sensitivity of electrons to dissipation-range turbulence gives rise to larger MFPs. Not only does this result in less modulation at lower energies, but it also obscures the effects of other modulation processes, e.g. adiabatic cooling, which would have forced modulated spectra in the inner heliosphere into positively distributed power laws. Also, because pronounced diffusion results in less modulation, the extinguished intensity gradients that follow reduce drift effects in the TPE.

As mentioned above, the hardness of a spectrum incident at the TS affects the extent to which DSA will raise its intensities if it is already harder than what the shock can produce. The manner in which the energy spectra of particles incident at the shock are altered depends mainly on the rigidity profile of the diffusion coefficients. Thus, this rigidity dependence has great bearing on the efficiency of acceleration. It was revealed that MFPs increasing with rigidity generally yield harder spectra and consequently smaller DSA-induced intensity increases. On the other hand, MFPs that decrease with increasing rigidity soften spectra, and hence greater intensity increases follow as a result of DSA. This effect is furthermore amplified if a soft spectrum is succeeded by a hard spectrum at higher energies. Ultimately, even though impaired diffusion is conducive to acceleration, the level of diffusion was shown to be less important in determining the magnitude of DSA-induced intensity increases than its rigidity dependence.

Note that electron drifts tend to inhibit acceleration due to the spectral hardening they induce at the TS in the approximate region of 100 MeV to just short of 1 GeV. DSA, on the other hand, diminishes intensity gradients by raising intensities, which in turn reduces drift effects.

The same processes and modulation parameters influencing the spectral effects of DSA also affects the spatial distribution of re-accelerated electrons. Due to the large upstream diffusion coefficients, re-accelerated electrons may be transported far into the heliospheric interior and can raise intensities by a factor of at least 2 at the Earth. In contrast, the downstream coefficients are small in order to account for the large modulation observed in the heliosheath, and as a result re-accelerated electrons do not pervade far into this region. None but the highest-energy re-accelerated electrons ($E \gtrsim 1$ GeV) are able to reach the HP. Moreover, at drift-insensitive energies, the re-accelerated contribution is larger at higher heliolatitudes (or smaller polar angles) than in the equatorial regions. This follows because the fast SW stream that forms at higher latitudes reduces diffusion length scales. This latitude dependence is obscured at energies where drift effects dominate, since the re-accelerated electrons are redirected to the poles and equatorial regions during the positive and negative polarity cycles respectively.

Further conclusions can be drawn from the model configuration applied to reproduce observations, both at Voyager-observed energies (4 MeV $< E <$ 40 MeV) and at the high-energy end of the spectrum ($E \gtrsim 100$ MeV) as observed by PAMELA. With regards to the HPS, intensities are assumed to continue increasing towards lower energies until an exponential decrease ensues below $\sim$ 0.1 MeV. This provides a spectrum in the range of about 0.3 to 2 MeV that is soft enough, after modulation, for DSA to raise intensities at the TS to match the magnitude of observed intensity increases near this boundary. While the power-law form retained from the HPS by virtue of rigidity-independent diffusion is sufficient to account for observations at $E > 4$ MeV, and MFPs increasing with rigidity reproduce the observations above 100 MeV, the lowest-energy observations, at $E \leq 4$ MeV, can only be reproduced if MFPs increase toward lower energies. This up-turn in MFPs, associated with dissipation-range turbulence, has an onset at 1.5 to 2 MeV, below which $\lambda \propto P^{g_0}$ with $g_0 = [-1.2, -1.0]$, and its effect is twofold: The larger MFPs give rise to less modulation and higher intensities, but intensities are also raised due to enhanced DSA at the soft-to-hard spectral transition the up-turn creates at its onset. The MFP up-turn, and by extension, the underlying turbulence, appear to have both a radial and a solar-cycle dependence.

The intensity increases attributed to the DSA of electrons at the TS ranges from factors in excess of 10 at energies of up to 2 MeV to an average factor of 2.5 between 10 and 100 MeV - this rapid decrease is due to the hardening of spectra. This factor is furthermore briefly depressed at $\sim$ 200 MeV, where spectra are severely hardened as a result of MFPs increasing with rigidity, but are restored to about 1.6 where the softer form of the HPS is adopted at higher energies. DSA effects diminish entirely above 1 GeV due to the TS curvature limit. In terms of their spatial distribution, the contribution of re-accelerated electrons is essential to account for the radial intensity profile of 5 to 12 MeV electrons out to at least 100 AU, or 6 AU into the heliosheath as measured from the TS at 94 AU. It can be ultimately concluded that the intensity increases attainable through DSA are large enough to account for the intensity peaks observed by Voyager 1 for 0.35 to 14 MeV electrons in the proximity of the TS. Their narrow structures can be explained as a temporary magnetic connection between the TS and the spacecraft at the time of observation, but can also be accounted for in conjunction with possibly temporal processes that create local low-diffusion conditions.

Avenues of further research identified throughout this exploratory study include:

- Expansion of the current study to include other GCR species.
- A study of the DSA of CRs at shocks within polyatomic and relativistic media, where larger compression ratios may be expected. This may yield insights with regards to the spectral indices displayed by the local interstellar spectra of GCRs.
- A study of the contribution of CR acceleration within the confines of the heliosphere to the features of local interstellar spectra of GCRs.
- Studying in particular the features of the HPS (and spectra at other remote locations) at energies below 1 MeV. These features were shown in this study to have a substantial effect on electron re-acceleration.
- Studying the causes of unexplained spectral features of accelerated ACRs, such as the intensity enhancement preceding the roll-over energy.
- A study of the radial and solar cycle dependences of the individual parts of the rigidity dependence of the diffusion coefficients, e.g. the radial dependence of the low-energy MFP up-turn (and the underlying dissipation-range turbulence).
- Investigating the appropriate characterisation of diffusion and drifts in the heliosheath, and studying the effects of shock drift acceleration.
- A study of the role of the HCS and associated magnetic sectoring in the production of the peak-like intensity increases that were posited in this study to result from DSA.
- Probing the effects of adiabatic heating and stochastic acceleration in the heliosheath on CR electrons.
- A formal study comparing the prevalence of different acceleration mechanisms, e.g. magnetic reconnection, stochastic acceleration, DSA, etc. in different parts of the heliosphere.
- An expansion of the current study to three spatial dimensions, where CR transport and DSA are modelled by the solving stochastic differential equations.

References

Adriani, O., et al., Cosmic-ray electron flux measured by the PAMELA experiment between 1 and 625 GeV, *Phys. Rev. Lett.*, *106*, 201101, 2011.

Arthur, A. D., and J. A. le Roux, Particle acceleration at the heliospheric termination shock with a stochastic shock obliquity approach, *Astrophys. J. Lett.*, *772*, L26, 2013.

Axford, W. I., Acceleration of cosmic rays by shock waves, in *International Cosmic Ray Conference*, *Inter. Cosmic Ray Conf. Ser.*, vol. 12, pp. 155–203, 1981.

Axford, W. I., E. Leer, and G. Skadron, The acceleration of cosmic rays by shock waves, in *International Cosmic Ray Conference*, *Inter. Cosmic Ray Conf. Ser.*, vol. 11, pp. 132–137, 1977.

Ball, L., and D. B. Melrose, Shock drift acceleration of electrons, *Publ. Astron. Soc. Aus.*, *18*, 361–373, 2001.

Balogh, A., and G. Erdös, The heliospheric magnetic field, *Space Sci. Rev.*, *176*, 177–215, 2013.

Balogh, A., and J. R. Jokipii, The heliospheric magnetic field and its extension to the inner heliosheath, *Space Sci. Rev.*, *143*, 85–110, 2009.

Baranov, V. B., Possible physical properties of the flow in the vicinity of the heliopause, *Adv. Space Res.*, *44*, 471–477, 2009.

Bazilevskaya, G. A., E. W. Cliver, G. A. Kovaltsov, A. G. Ling, M. A. Shea, D. F. Smart, and I. G. Usoskin, Solar cycle in the heliosphere and cosmic rays, *Space Sci. Rev.*, *186*, 409–435, 2014.

Bieber, J. W., W. H. Matthaeus, C. W. Smith, W. Wanner, M.-B. Kallenrode, and G. Wibberenz, Proton and electron mean free paths: The Palmer consensus revisited, *Astrophys. J*, *420*, 294–306, 1994.

Bieber, J. W., W. H. Matthaeus, A. Shalchi, and G. Qin, Nonlinear guiding center theory of perpendicular diffusion: General properties and comparison with observation, *Geophys. Res. Lett.*, *31*, L10805, 2004.

Biermann, L., The solar wind and interplanetary media, in *Space Astrophysics*, edited by W. Liller, pp. 150–156, New York: McGraw-Hill, 1961.

Bisschoff, D., Private communication, 2014.

Bisschoff, D., and M. S. Potgieter, Implications of Voyager 1 observations beyond the heliopause for the local interstellar electron spectrum, *Astrophys. J.*, *794*, 166, 2014.

Borovikov, S. N., and N. V. Pogorelov, Voyager 1 near the heliopause, *Astrophys. J. Lett.*, *783*, L16, 2014.

Borovikov, S. N., N. V. Pogorelov, and R. W. Ebert, Solar rotation effects on the heliosheath flow near solar minima, *Astrophys. J.*, *750*, 42, 2012.

Burger, R. A., Cosmic-ray modulation and the heliospheric magnetic field, *Adv. Space Res.*, *35*, 636–642, 2005.

Burger, R. A., and M. Hattingh, Effect of Fisk-type heliospheric magnetic fields on the latitudinal transport of cosmic rays, in *International Cosmic Ray Conference*, *Inter. Cosmic Ray Conf. Ser.*, vol. 9, pp. 3698–3701, 2001.

Burger, R. A., and M. S. Potgieter, The calculation of neutral sheet drift in two-dimensional cosmic-ray modulation models, *Astrophys. J.*, *339*, 501–511, 1989.

Burger, R. A., and D. J. Visser, Reduction of drift effects due to solar wind turbulence, *Astrophys. J.*, *725*, 1366–1372, 2010.

Burger, R. A., M. S. Potgieter, and B. Heber, Rigidity dependence of cosmic ray proton latitudinal gradients measured by the Ulysses spacecraft: Implications for the diffusion tensor, *J. Geophys. Res.*, *105*, 27,447–27,456, 2000.

Burger, R. A., T. P. J. Kruger, M. Hitge, and N. E. Engelbrecht, A Fisk-Parker hybrid heliospheric magnetic field with a solar-cycle dependence, *Astrophys. J*, *674*, 511–519, 2008.

Burlaga, L. F., and N. F. Ness, Global patterns of heliospheric magnetic field polarities and elevation angles: 1990 through 1995, *J. Geophys. Res.*, *102*, 19,731–19,742, 1997.

Burlaga, L. F., and N. F. Ness, Heliosheath magnetic fields between 104 and 113 AU in a region of declining speeds and a stagnation region, *Astrophys. J*, *749*, 13, 2012.

Burlaga, L. F., N. F. Ness, M. H. Acuña, R. P. Lepping, J. E. P. Connerney, E. C. Stone, and F. B. McDonald, Crossing the termination shock into the heliosheath: Magnetic fields, *Science*, *309*, 2027–2029, 2005.

Burlaga, L. F., N. F. Ness, M. H. Acuña, R. P. Lepping, J. E. P. Connerney, and J. D. Richardson, Magnetic fields at the solar wind termination shock, *Nature*, *454*, 75–77, 2008.

Burlaga, L. F., N. F. Ness, V. Florinski, and J. Heerikhuisen, Magnetic field fluctuations observed in the heliosheath and interstellar magnetic field by Voyager 1 at 115.7-124.9 AU during 2011-2013, *Astrophys. J*, *792*, 134, 2014.

Büsching, I., O. C. de Jager, M. S. Potgieter, and C. Venter, A cosmic-ray positron anisotropy due to two middle-aged, nearby pulsars?, *Astrophys. J. Lett.*, *678*, L39–L42, 2008a.

Büsching, I., C. Venter, and O. C. de Jager, Contributions from nearby pulsars to the local cosmic ray electron spectrum, *Adv. Space Res.*, *42*, 497–503, 2008b.

Caballero-Lopez, R. A., H. Moraal, and F. B. McDonald, The modulation of galactic cosmic-ray electrons in the heliosheath, *Astrophys. J.*, *725*, 121–127, 2010.

Carlson, P., A century of cosmic rays, *Phys. Today*, *65*, 30–36, 2012.

Chalov, S. V., and H. J. Fahr, Spatial variation of the supersonic thermal plasma flow downstream of the termination shock, *Adv. Space Res.*, *47*, 1523–1528, 2011.

Choudhuri, A., *The Physics of Fluids and Plasmas: An Introduction for Astrophysicists*, Cambridge University Press, 1998.

Clette, F., L. Svalgaard, J. M. Vaquero, and E. W. Cliver, Revisiting the sunspot number. A 400-year perspective on the solar cycle, *Space Sci. Rev.*, *186*, 35–103, 2014.

Cliver, E. W., Solar energetic particles: Acceleration and transport, in *26th Int. Cosmic Ray Conf.*, *AIP Conf. Ser.*, vol. 516, edited by B. L. Dingus, D. B. Kieda, and M. H. Salamon, pp. 103–119, 2000.

Decker, R. B., S. M. Krimigis, E. C. Roelof, M. E. Hill, T. P. Armstrong, G. Gloeckler, D. C. Hamilton, and L. J. Lanzerotti, Voyager 1 in the foreshock, termination shock, and heliosheath, *Science*, *309*, 2020–2024, 2005.

Decker, R. B., S. M. Krimigis, E. C. Roelof, M. E. Hill, T. P. Armstrong, G. Gloeckler, D. C. Hamilton, and L. J. Lanzerotti, Mediation of the solar wind termination shock by non-thermal ions, *Nature*, *454*, 67–70, 2008.

Decker, R. B., S. M. Krimigis, E. C. Roelof, and M. E. Hill, No meridional plasma flow in the heliosheath transition region, *Nature*, *489*, 124–127, 2012.

Dosch, A., A. Shalchi, and B. Weinhorst, Relation between different theories for cosmic ray cross field diffusion, *Adv. Space Res.*, *44*, 1326–1336, 2009.

Dröge, W., Particle scattering by magnetic fields, *Space Sci. Rev.*, *93*, 121–151, 2000a.

Dröge, W., The rigidity dependence of solar particle scattering mean free paths, *Astrophys. J.*, *537*, 1073–1079, 2000b.

Drury, L., On particle acceleration in supernova remnants, *Space Sci. Rev.*, *36*, 57–60, 1983.

Engelbrecht, N. E., On the heliospheric diffusion tensor and its effect on 26-day recurrent cosmic ray variations, Master's thesis, North-West University, South Africa, Potchefstroom, 2008.

Engelbrecht, N. E., On the development and applications of a three-dimensional ab initio cosmic-ray modulation model, Ph.D. thesis, North-West University, South Africa, Potchefstroom, 2013.

Engelbrecht, N. E., and R. A. Burger, Effects of various dissipation range onset models on the 26-day variations of low-energy galactic cosmic-ray electrons, *Adv. Space Res.*, *45*, 1015–1025, 2010.

Engelbrecht, N. E., and R. A. Burger, An ab initio model for the modulation of galactic cosmic-ray electrons, *Astrophys. J.*, *779*, 158, 2013a.

Engelbrecht, N. E., and R. A. Burger, An ab initio model for cosmic-ray modulation, *Astrophys. J.*, *772*, 46, 2013b.

Engelbrecht, N. E., and R. A. Burger, A comparison of turbulence-reduced drift coefficients of importance for the modulation of galactic cosmic-ray protons in the supersonic solar wind, *Adv. Space Res.*, *55*, 390–400, 2015.

Fahr, H. J., T. Kausch, and H. Scherer, A 5-fluid hydrodynamic approach to model the solar system-interstellar medium interaction, *Astron. Astrophys.*, *357*, 268–282, 2000.

Fahr, H. J., K. Scherer, M. S. Potgieter, and S. E. S. Ferreira, Longitudinal variation of the pickup-proton-injection efficiency and rate at the heliospheric termination shock, *Astron. Astrophys.*, *486*, L1–L4, 2008.

Ferreira, S. E. S., The heliospheric transport of cosmic rays and jovian electrons, Ph.D. thesis, Potchefstroom University for CHE, South Africa, Potchefstroom, 2002.

Ferreira, S. E. S., and M. S. Potgieter, The modulation of 4- to 16-MeV electrons in the outer heliosphere: Implications of different local interstellar spectra, *J. Geophys. Res.*, *107*, 1221, 2002.

Ferreira, S. E. S., and M. S. Potgieter, Modulation over a 22-year cosmic ray cycle: On the tilt angles of the heliospheric current sheet, *Adv. Space Res.*, *32*, 657–662, 2003.

Ferreira, S. E. S., and M. S. Potgieter, Long-term cosmic-ray modulation in the heliosphere, *Astrophys. J.*, *603*, 744–752, 2004.

Ferreira, S. E. S., and K. Scherer, Modulation of cosmic-ray electrons in the outer heliosphere, *Astrophys. J.*, *616*, 1215–1223, 2004.

Ferreira, S. E. S., M. S. Potgieter, R. A. Burger, and B. Heber, Modulation effects of anisotropic perpendicular diffusion on cosmic ray electron intensities in the heliosphere, *J. Geophys. Res.*, *105*, 18,305–18,314, 2000.

Ferreira, S. E. S., M. S. Potgieter, R. A. Burger, B. Heber, and H. Fichtner, Modulation of Jovian and galactic electrons in the heliosphere: 1. Latitudinal transport of a few MeV electrons, *J. Geophys. Res.*, *106*, 24,979–24,987, 2001a.

Ferreira, S. E. S., M. S. Potgieter, R. A. Burger, B. Heber, H. Fichtner, and C. Lopate, Modulation of Jovian and galactic electrons in the heliosphere: 2. Radial transport of a few MeV electrons, *J. Geophys. Res.*, *106*, 29,313–29,321, 2001b.

Ferreira, S. E. S., M. S. Potgieter, and K. Scherer, Modulation of cosmic-ray electrons in a non-spherical and irregular heliosphere, *Astrophys. J.*, *607*, 1014–1023, 2004a.

Ferreira, S. E. S., M. S. Potgieter, and W. R. Webber, Modulation of low-energy cosmic ray electrons in the outer heliosphere, *Adv. Space Res.*, *34*, 126–131, 2004b.

Ferreira, S. E. S., M. S. Potgieter, and K. Scherer, Transport and acceleration of anomalous cosmic rays in the inner heliosheath, *J. Geophys. Res.*, *112*, A11,101, 2007a.

Ferreira, S. E. S., M. S. Potgieter, and K. Scherer, Modeling of the heliospheric interface, magnetic field, and cosmic-ray transport, *Astrophys. J.*, *659*, 1777–1783, 2007b.

Fichtner, H., Anomalous cosmic rays: Messengers from the outer heliosphere, *Space Sci. Rev.*, *95*, 639–754, 2001.

Fisk, L. A., Motion of the footpoints of heliospheric magnetic field lines at the Sun: Implications for recurrent energetic particle events at high heliographic latitudes, *J. Geophys. Res.*, *101*, 15,547–15,554, 1996.

Fisk, L. A., An overview of the transport of galactic and anomalous cosmic rays in the heliosphere: theory, *Advances in Space Research*, *23*, 415–423, 1999.

Fisk, L. A., and G. Gloeckler, The global configuration of the heliosheath inferred from recent Voyager 1 observations, *Astrophys. J.*, *776*, 79, 2013.

Fisk, L. A., B. Kozlovsky, and R. Ramaty, An interpretation of the observed oxygen and nitrogen enhancements in low-energy cosmic rays, *Astrophys. J. Lett.*, *190*, L35, 1974.

Florinski, V., and J. R. Jokipii, Cosmic-ray spectra at spherical termination shocks, *Astrophys. J.*, *591*, 454–460, 2003.

Florinski, V., G. P. Zank, J. R. Jokipii, E. C. Stone, and A. C. Cummings, Do anomalous cosmic rays modify the termination shock?, *Astrophys. J.*, *610*, 1169–1181, 2004.

Florinski, V., R. B. Decker, J. A. le Roux, and G. P. Zank, An energetic-particle-mediated termination shock observed by Voyager 2, *Geophys. Res. Lett.*, *36*, L12101, 2009.

Florinski, V., S. E. S. Ferreira, and N. V. Pogorelov, Galactic cosmic rays in the outer heliosphere: Theory and models, *Space Sci. Rev.*, *176*, 147–163, 2013.

Fraschetti, F., On the acceleration of ultra-high-energy cosmic rays, *Royal Society of London Philosophical Transactions Series A*, *366*, 4417–4428, 2008.

Frisch, P. C., and D. J. McComas, The interstellar boundary explorer (IBEX): Tracing the interaction between the heliosphere and surrounding interstellar material with energetic neutral atoms, *Space Sci. Rev.*, *176*, 101–113, 2013.

Garcia-Munoz, M., G. M. Mason, and J. A. Simpson, A new test for solar modulation theory: The 1972 May-July low-energy galactic cosmic-ray proton and helium spectra, *Astrophys. J. Letters*, *182*, L81, 1973.

Giacalone, J., and J. R. Jokipii, The transport of cosmic rays across a turbulent magnetic field, *Astrophys. J.*, *520*, 204–214, 1999.

Giacalone, J., J. F. Drake, and J. R. Jokipii, The acceleration mechanism of anomalous cosmic rays, *Space Sci. Rev.*, *173*, 283–307, 2012.

Gil, A., I. G. Usoskin, G. A. Kovaltsov, A. L. Mishev, C. Corti, and V. Bindi, Can we properly model the neutron monitor count rate?, *J. Geophys. Res.*, *120*, 7172–7178, 2015.

Gleeson, L. J., and W. I. Axford, Cosmic rays in the interplanetary medium, *Astrpohys. J. Lett.*, *149*, L115–L118, 1967.

Gleeson, L. J., and W. I. Axford, The Compton-Getting effect, *Astrophy. Space Sci.*, *2*, 431–437, 1968.

Gurnett, D. A., W. S. Kurth, L. F. Burlaga, and N. F. Ness, In situ observations of interstellar plasma with Voyager 1, *Science*, *341*, 1489–1492, 2013.

Haasbroek, L. J., The transport and acceleration of charged particles in the heliosphere, Ph.D. thesis, Potchefstroom University for CHE, South Africa, Potchefstroom, 1997.

Haasbroek, L. J., M. S. Potgieter, and J. A. Le Roux, The time-dependent recovery after the large cosmic-ray decrease in 1991, in *International Cosmic Ray Conference*, *Inter. Cosmic Ray Conf. Ser.*, vol. 4, pp. 710–713, 1995.

Hathaway, D. H., The solar cycle, *Living Rev. Solar Phys.*, *7*, 1, 2010.

Hattingh, M., The modulation of galactic cosmic rays in a three dimensional heliosphere, Ph.D. thesis, Potchefstroom University for CHE, South Africa, Potchefstroom, 1998.

Hattingh, M., and R. A. Burger, A new simulated wavy neutral sheet drift model, *Adv. Space Res.*, *16*, 213–216, 1995.

Heber, B., Cosmic rays through the solar hale cycle, *Space Sci. Rev.*, *176*, 256–278, 2011.

Heber, B., and M. S. Potgieter, Cosmic rays at high heliolatitudes, *Space Sci. Rev.*, *127*, 117–194, 2006.

Hill, M. E., R. B. Decker, L. E. Brown, J. F. Drake, D. C. Hamilton, S. M. Krimigis, and M. Opher, Dependence of energetic ion and electron intensities on proximity to the magnetically sectored heliosheath: Voyager 1 and 2 observations, *Astrophys. J.*, *781*, 94, 2014.

Hillas, A. M., The cosmic-ray knee and ensuing spectrum seen as a consequence of Bell's self-magnetized SNR shock acceleration process, *J. Phys. Conf. Ser.*, *47*, 168–177, 2006.

Hoeksema, J. T., Large-scale solar and heliospheric magnetic fields, *Adv. Space Res.*, *11*, 15–24, 1991.

Hovestadt, D., O. Vollmer, G. Gloeckler, and C. Y. Fan, Differential energy spectra of low-energy (less than 8.5 MeV per mucleon) heavy cosmic rays during solar quiet times, *Phys. Rev. Lett.*, *31*, 650–653, 1973.

Hoyt, D. V., and K. H. Schatten, Group sunspot numbers: A new solar activity reconstruction, *Sol. Phys.*, *179*, 189–219, 1998.

Hundhausen, A., *Coronal expansion and solar wind*, Physics and chemistry in space, Springer-Verlag, 1972.

Jokipii, J. R., Cosmic-ray propagation. I. Charged particles in a random magnetic field, *Astrophys. J.*, *146*, 480–487, 1966.

Jokipii, J. R., Particle drift, diffusion, and acceleration at shocks, *Astrophys. J.*, *255*, 716–720, 1982.

Jokipii, J. R., Particle acceleration at a termination shock. I - Application to the solar wind and the anomalous component, *J. Geophys. Res.*, *91*, 2929–2932, 1986.

Jokipii, J. R., Diffusive shock acceleration - Acceleration rate, magnetic-field direction and the diffusion limit, in *Particle Acceleration in Cosmic Plasmas, AIP Conf. Ser.*, vol. 264, edited by G. P. Zank and T. K. Gaisser, pp. 137–147, 1992.

Jokipii, J. R., The heliospheric termination shock, *Space Sci. Rev.*, *176*, 115–124, 2013.

Jokipii, J. R., and J. Kota, The polar heliospheric magnetic field, *Geophys. Res. Lett.*, *16*, 1–4, 1989.

Jokipii, J. R., and J. Kota, A strong constraint on the anomalous-cosmic-ray source location, *AGU Fall Meeting Abstracts*, p. A1913, 2011.

Jokipii, J. R., and B. Thomas, Effects of drift on the transport of cosmic rays. IV - Modulation by a wavy interplanetary current sheet, *Astrophys. J.*, *243*, 1115–1122, 1981.

Jokipii, J. R., E. H. Levy, and W. B. Hubbard, Effects of particle drift on cosmic-ray transport. I - General properties, application to solar modulation, *Astrophys. J.*, *213*, 861–868, 1977.

Jones, F. C., and D. C. Ellison, The plasma physics of shock acceleration, *Space Sci. Rev.*, *58*, 259–346, 1991.

Kallenrode, M.-B., *Space physics : an introduction to plasmas and particles in the heliosphere and magnetospheres*, xv, 2nd ed., 365 pp., Springer, 2001.

Khül, P., et al., Spectrum of galactic and Jovian electrons, *Proc. 33rd Int. Cosmic Ray Conf., Rio de Janeiro, Brazil*, *0072*, 2013.

Kota, J., and J. R. Jokipii, Diffusive shock acceleration in the presence of current sheets, *Astrophys. J*, *429*, 385–390, 1994.

Krieger, A. S., A. F. Timothy, and E. C. Roelof, A Coronal hole and its identification as the source of a high velocity solar wind stream, *Sol. Phys.*, *29*, 505–525, 1973.

Kruells, W. M., and A. Achterberg, Computation of cosmic-ray acceleration by Ito's stochastic differential equations, *Astron. Astrophys.*, *286*, 314–327, 1994.

Lagage, P. O., and C. J. Cesarsky, The maximum energy of cosmic rays accelerated by supernova shocks, *Astron. Astrophys.*, *125*, 249–257, 1983.

Langner, U. W., Effects of termination shock acceleration on cosmic rays in the heliosphere, Ph.D. thesis, Potchefstroom University for CHE, South Africa, Potchefstroom, 2004.

Langner, U. W., and M. S. Potgieter, Effects of the solar wind termination shock on charge-sign dependent cosmic ray modulation, *Adv. Space Res.*, *34*, 144–149, 2004.

Langner, U. W., and M. S. Potgieter, Modulation of galactic protons in an asymmetrical heliosphere, *Astrophys. J*, *630*, 1114–1124, 2005.

Langner, U. W., and M. S. Potgieter, Possible explanations of anomalous spectra observed with Voyager 1 crossing the solar wind termination shock, in *Physics of the Inner Heliosheath*, *AIP Conf. Ser.*, vol. 858, edited by J. Heerikhuisen, V. Florinski, G. P. Zank, and N. V. Pogorelov, pp. 233–238, 2006.

Langner, U. W., and M. S. Potgieter, The role of radial perpendicular diffusion and latitude dependent acceleration along the solar wind termination shock, *Adv. Space Res.*, *41*, 368–372, 2008.

Langner, U. W., O. C. de Jager, and M. S. Potgieter, On the local interstellar spectrum for cosmic ray electrons, *Adv. Space Res.*, *27*, 517–522, 2001.

Langner, U. W., M. S. Potgieter, and W. R. Webber, Modulation of cosmic ray protons in the heliosheath, *J. Geophys. Res.*, *108*, 8039, 2003.

Langner, U. W., M. S. Potgieter, and W. R. Webber, Modelling of 'barrier' modulation for cosmic ray protons in the outer heliosphere, *Adv. Space Res.*, *34*, 138–143, 2004.

Langner, U. W., M. S. Potgieter, H. Fichtner, and T. Borrmann, Effects of different solar wind speed profiles in the heliosheath on the modulation of cosmic-ray protons, *Astrophys. J.*, *640*, 1119–1134, 2006a.

Langner, U. W., M. S. Potgieter, H. Fichtner, and T. Borrmann, Modulation of anomalous protons: Effects of different solar wind profiles in the heliosheath, *J. Geophys. Res.*, *111*, A10,106, 2006b.

Lazarian, A., and M. Opher, A model of acceleration of anomalous cosmic rays by reconnection in the heliosheath, *Astrophys. J.*, *703*, 8–21, 2009.

le Roux, J. A., and H. Fichtner, A self-consistent determination of the heliospheric termination shock structure in the presence of pickup, anomalous, and galactic cosmic ray protons, *J. Geophys. Res.*, *102*, 17,365–17,380, 1997.

le Roux, J. A., and M. S. Potgieter, The simulation of complete 11 and 12 year modulation cycles for cosmic rays in the heliosphere using a drift model with global merged interaction regions, *Astrophys. J*, *442*, 847–851, 1995.

le Roux, J. A., M. S. Potgieter, and V. S. Ptuskin, A transport model for the diffusive shock acceleration and modulation of anomalous cosmic rays in the heliosphere, *J. Geophys. Res.*, *101*, 4791–4804, 1996.

le Roux, J. A., G. P. Zank, and V. S. Ptuskin, An evaluation of perpendicular diffusion models regarding cosmic ray modulation on the basis of a hydromagnetic description for solar wind turbulence, *J. Geophys. Res.*, *104*, 24,845–24,862, 1999.

Leamon, R. J., W. H. Matthaeus, C. W. Smith, G. P. Zank, D. J. Mullan, and S. Oughton, MHD-driven kinetic dissipation in the solar wind and corona, *Astrophys. J.*, *537*, 1054–1062, 2000.

Lee, M. A., H. J. Fahr, H. Kucharek, E. Moebius, C. Prested, N. A. Schwadron, and P. Wu, Physical processes in the outer heliosphere, *Space Sci. Rev.*, *146*, 275–294, 2009.

Leske, R. A., A. C. Cummings, R. A. Mewaldt, and E. C. Stone, Anomalous and galactic cosmic rays at 1 AU during the cycle 23/24 solar minimum, *Space Sci. Rev.*, *176*, 253–263, 2013.

Li, H., C. Wang, and J. D. Richardson, Properties of the termination shock observed by Voyager 2, *Geophys. Res. Lett.*, *35*, L19107, 2008.

Luo, X., M. Zhang, M. Potgieter, X. Feng, and N. V. Pogorelov, A numerical simulation of cosmic-ray modulation near the heliopause, *Astrophys. J.*, *808*, 82, 2015.

Manuel, R., S. E. S. Ferreira, M. S. Potgieter, R. D. Strauss, and N. E. Engelbrecht, Time-dependent cosmic ray modulation, *Adv. Space Res.*, *47*, 1529–1537, 2011.

Manuel, R., S. E. S. Ferreira, and M. S. Potgieter, Time-dependent modulation of cosmic rays in the heliosphere, *Sol. Phys.*, *289*, 2207–2231, 2014.

Marsch, E., Kinetic physics of the solar wind plasma, in *Physics of the Inner Heliosphere II*, *Physics and Chemistry in Space - Space and Solar Physics*, vol. 21, edited by R. Schwenn and E. Marsch, pp. 45–133, Springer-Verlag, 1991.

Matthaeus, W. H., P. C. Gray, J. D. H. Pontius, and J. W. Bieber, Spatial structure and field-Line diffusion in transverse magnetic turbulence, *Phys. Rev. Lett.*, *75*, 2136–2139, 1995.

Matthaeus, W. H., G. Qin, J. W. Bieber, and G. P. Zank, Nonlinear collisionless perpendicular diffusion of charged particles, *Astrophys. J. Lett.*, *590*, L53–L56, 2003.

McComas, D. J., and N. A. Schwadron, An explanation of the Voyager paradox: Particle acceleration at a blunt termination shock, *Geophys. Res. Lett.*, *33*, L04102, 2006.

McComas, D. J., et al., Global observations of the interstellar interaction from the interstellar boundary explorer (IBEX), *Science*, *326*, 959–962, 2009.

McComas, D. J., et al., The heliosphere's interstellar interaction: No bow shock, *Science*, *336*, 1291–1293, 2012.

McDonald, F. B., B. J. Teegarden, J. H. Trainor, and W. R. Webber, The anomalous abundance of cosmic-ray itrogen and oxygen nuclei at low energies, *Astrophys. J. Lett.*, *187*, L105, 1974.

McDonald, F. B., E. C. Stone, A. C. Cummings, B. Heikkila, N. Lal, and W. R. Webber, Enhancements of energetic particles near the heliospheric termination shock, *Nature*, *426*, 48–51, 2003.

McDonald, F. B., E. C. Stone, A. C. Cummings, W. R. Webber, B. C. Heikkila, and N. Lal, Anomalous cosmic rays in the distant heliosphere and the reversal of the Sun's magnetic polarity in Cycle 23, *Geophys. Res. Lett.*, *34*, L05105, 2007.

Menn, W., et al., The PAMELA space experiment, *Adv. Space Res.*, *51*, 209–218, 2013.

Mewaldt, R. A., R. S. Selesnick, J. R. Cummings, E. C. Stone, and T. T. von Rosenvinge, Evidence for multiply charged anomalous cosmic rays, *Astrophys. J. Lett.*, *466*, L43, 1996.

Minnie, J., J. W. Bieber, W. H. Matthaeus, and R. A. Burger, Suppression of particle drifts by turbulence, *Astrophys. J.*, *670*, 1149–1158, 2007.

Moebius, E., B. Klecker, D. Hovestadt, and M. Scholer, Interaction of interstellar pick-up ions with the solar wind, *Astrophys. Space Sci.*, *144*, 487–505, 1988.

Moeketsi, D. M., M. S. Potgieter, S. E. S. Ferreira, B. Heber, H. Fichtner, and V. K. Henize, The heliospheric modulation of 3 to 10 MeV electrons: Modeling of changes in the solar wind speed in relation to perpendicular polar diffusion, *Adv. Space Res.*, *35*, 597–604, 2005.

Moraal, H., Proton modulation near solar minimim periods in consecutive solar cycles, in *International Cosmic Ray Conference*, *Inter. Cosmic Ray Conf. Ser.*, vol. 6, p. 140, 1990.

Moraal, H., The discovery and early development of the field of anomalous cosmic rays, in *The Outer Heliosphere: The Next Frontiers*, edited by K. Scherer, H. Fichtner, H. J. Fahr, and E. Marsch, p. 147, 2001.

Moraal, H., Cosmic-ray modulation equations, *Space Sci. Rev.*, *176*, 299–319, 2013.

Moraal, H., and M. S. Potgieter, Solutions of the spherically-symmetric cosmic-ray transport equation in interplanetary space, *Astrophys. Space Sci.*, *84*, 519–533, 1982.

Moraal, H., and P. H. Stoker, Long-term neutron monitor observations and the 2009 cosmic ray maximum, *J. Geophys. Res.*, *115*, A12109, 2010.

Moraal, H., R. A. Caballero-Lopez, and V. Ptuskin, Stochastic acceleration in the heliosheath: effect on anomalous cosmic ray spectra, in *International Cosmic Ray Conference*, *Inter. Cosmic Ray Conf. Ser.*, vol. 1, pp. 865–868, 2008.

Moskalenko, I. V., A. W. Strong, J. F. Ormes, and M. S. Potgieter, Secondary antiprotons and propagation of cosmic rays in the galaxy and heliosphere, *Astrophys. J*, *565*, 280–296, 2002.

Ness, N. F., and J. M. Wilcox, Sector structure of the quiet interplanetary magnetic field, *Science*, *148*, 1592–1594, 1965.

Neugebauer, M., and C. W. Snyder, Solar plasma experiment, *Science*, *138*, 1095–1097, 1962.

Ngobeni, M. D., Aspects of the modulation of cosmic rays in the outer heliosphere, Master's thesis, (Centre for Space Research) North West University, South Africa, Potchefstroom, 2006.

Ngobeni, M. D., Modelling of galactic cosmic rays in the heliosphere, Ph.D. thesis, (Centre for Space Research) North West University, South Africa, Potchefstroom, 2015.

Ngobeni, M. D., and M. S. Potgieter, Cosmic ray anisotropies in the outer heliosphere, *Adv. Space Res.*, *41*, 373–380, 2008.

Ngobeni, M. D., and M. S. Potgieter, Modulation of galactic cosmic rays in a north-south asymmetrical heliosphere, *Adv. Space Res.*, *48*, 300–307, 2011.

Ngobeni, M. D., and M. S. Potgieter, Modelling of galactic Carbon in an asymmetrical heliosphere: Effects of asymmetrical modulation conditions, *Adv. Space Res.*, *49*, 1660–1669, 2012.

Ngobeni, M. D., and M. S. Potgieter, Modelling the effects of scattering parameters on particle-drift in the solar modulation of galactic cosmic rays, *Adv. Space Res.*, *56*, 1525–1537, 2015.

Nkosi, G. S., M. S. Potgieter, and W. R. Webber, Modelling of low-energy galactic electrons in the heliosheath, *Adv. Space Res.*, *48*(9), 1480–1489, 2011.

Nndanganeni, R. R., Modelling of galactic cosmic ray electrons in the heliosphere, Master's thesis, (Centre for Space Research) North West University, South Africa, Potchefstroom, 2012.

Nndanganeni, R. R., Modelling of electrons in the heliosphere, Ph.D. thesis, (Centre for Space Research) North West University, South Africa, Potchefstroom, 2015.

Opher, M., E. C. Stone, and P. C. Liewer, The Effects of a local interstellar magnetic field on Voyager 1 and 2 observations, *Astrophys. J. Lett.*, *640*, L71–L74, 2006.

Opher, M., J. D. Richardson, G. Toth, and T. I. Gombosi, Confronting observations and modeling: The role of the interstellar magnetic field in Voyager 1 and 2 asymmetries, *Space Sci. Rev.*, *143*, 43–55, 2009.

Opher, M., J. F. Drake, M. Velli, R. B. Decker, and G. Toth, Near the boundary of the heliosphere: A flow transition region, *Astrophys. J.*, *751*, 80, 2012.

Palmer, I. D., Transport coefficients of low-energy cosmic rays in interplanetary space, *Rev. Geoph. Space Phys.*, *20*, 335–351, 1982.

Parker, E. N., Dynamics of the interplanetary gas and magnetic fields., *Astrophys. J*, *128*, 664–675, 1958.

Parker, E. N., The stellar-wind regions., *Astrophys. J*, *134*, 20–27, 1961.

Parker, E. N., Dynamical theory of the solar wind, *Space Sci. Rev.*, *4*, 666–708, 1965a.

Parker, E. N., The passage of energetic charged particles through interplanetary space, *Planet. Space Sci.*, *13*, 9–49, 1965b.

Parker, E. N., A history of early work on the heliospheric magnetic field, *J. Geophys. Res.*, *106*, 15,797–15,802, 2001.

Pesses, M. E., D. Eichler, and J. R. Jokipii, Cosmic ray drift, shock wave acceleration, and the anomalous component of cosmic rays, *Astrophys. J. Lett.*, *246*, L85–L88, 1981.

Phillips, J. L., et al., Ulysses solar wind plasma observations from pole to pole, *Geophys. Res. Lett.*, *22*, 3301–3304, 1995.

Pogorelov, N. V., E. C. Stone, V. Florinski, and G. P. Zank, Termination shock asymmetries as seen by the Voyager spacecraft: The role of the interstellar magnetic field and neutral hydrogen, *Astrophys. J.*, *668*, 611–624, 2007.

Pogorelov, N. V., J. Heerikhuisen, and G. P. Zank, Probing heliospheric asymmetries with an MHD-kinetic model, *Astrophys. J. Lett.*, *675*, L41–L44, 2008.

Pogorelov, N. V., J. Heerikhuisen, G. P. Zank, and S. N. Borovikov, Influence of the interstellar magnetic field and neutrals on the shape of the outer heliosphere, *Space Sci. Rev.*, *143*, 31–42, 2009.

Pogorelov, N. V., S. N. Borovikov, G. P. Zank, L. F. Burlaga, R. A. Decker, and E. C. Stone, Radial velocity along the Voyager 1 trajectory: The effect of solar cycle, *Astrophys. J. Lett.*, *750*, L4, 2012.

Pogorelov, N. V., S. N. Borovikov, J. Heerikhuisen, and M. Zhang, The heliotail, *Astrophys. J. Lett.*, *812*, L6, 2015.

Potgieter, M., Solar modulation of cosmic rays, *Living Rev. Solar Phys.*, *10*, 2013.

Potgieter, M. S., The modulation of galactic comic rays as described by a three-dimensional drift model, Ph.D. thesis, Potchefstroom University for CHE, South Africa, Potchefstroom, 1984.

Potgieter, M. S., Heliospheric terminal shock acceleration and modulation of the anomalous cosmic-ray component, *Adv. Space Res.*, *9*, 21–24, 1989.

Potgieter, M. S., Heliospheric modulation of galactic electrons: Consequences of new calculations for the mean free path of electrons between 1 MeV and ˜10 GeV, *J. Geophys. Res.*, *101*, 24,411–24,422, 1996.

Potgieter, M. S., Heliospheric modulation of cosmic ray protons: Role of enhanced perpendicular diffusion during periods of minimum solar modulation, *J. Geophys. Res.*, *105*, 18,295–18,304, 2000.

Potgieter, M. S., Solar cycle variations and cosmic rays, *J. Atmos. Sol. Terr. Phys.*, *70*, 207–218, 2008.

Potgieter, M. S., The dynamic heliosphere, solar activity, and cosmic rays, *Adv. Space Res.*, *46*, 402–412, 2010.

Potgieter, M. S., Very local interstellar spectra for galactic electrons, protons and helium, *Braz. J. Phys.*, *44*, 581–588, 2014a.

Potgieter, M. S., The charge-sign dependent effect in the solar modulation of cosmic rays, *Adv. Space Res.*, *53*, 1415–1425, 2014b.

Potgieter, M. S., and S. E. S. Ferreira, Effects of the solar wind termination shock on the modulation of Jovian and galactic electrons in the heliosphere, *J. Geophys. Res.*, *107*, 1089, 2002.

Potgieter, M. S., and U. W. Langner, Heliospheric modulation of cosmic-ray positrons and electrons: Effects of the heliosheath and the solar wind termination shock, *Astrophys. J.*, *602*, 993–1001, 2004.

Potgieter, M. S., and J. A. Le Roux, A numerical model for a cosmic ray modulation barrier in the outer heliosphere, *Astron. Astrophys.*, *209*, 406–410, 1989.

Potgieter, M. S., and H. Moraal, A drift model for the modulation of galactic cosmic rays, *Astrophys. J.*, *294*, 425–440, 1985.

Potgieter, M. S., and H. Moraal, Acceleration of cosmic rays in the solar wind termination shock. I - A steady state technique in a spherically symmetric model, *Astrophys. J.*, *330*, 445–455, 1988.

Potgieter, M. S., and R. R. Nndanganeni, The solar modulation of electrons in the heliosphere, *Astrophys. Space Sci.*, *345*, 33–40, 2013a.

Potgieter, M. S., and R. R. Nndanganeni, A local interstellar spectrum for galactic electrons, *Astropart. Phys.*, *48*, 25–29, 2013b.

Potgieter, M. S., E. E. Vos, R. R. Nndanganeni, M. Boezio, and R. Munini, A very local interstellar spectrum for Galactic electrons, *Proc. 33rd Int. Cosmic Ray Conf., Rio de Janeiro, Brazil*, 2013.

Potgieter, M. S., E. E. Vos, M. Boezio, N. De Simone, V. Di Felice, and V. Formato, Modulation of galactic protons in the heliosphere during the unusual solar minimum of 2006 to 2009, *Sol. Phys.*, *289*, 391–406, 2014a.

Potgieter, M. S., E. E. Vos, and R. R. Nndanganeni, The first very local interstellar spectra for galactic protons, helium and electrons, in *Astroparticle, Particle, Space Physics and Detectors for Physics Applications - Proceedings of the 14th ICATPP Conference*, edited by S. Giani et al., pp. 204–211, 2014b.

Potgieter, M. S., E. E. Vos, R. Munini, M. Boezio, and V. Di Felice, Modulation of galactic electrons in the heliosphere during the unusual solar minimum of 2006-2009: A modeling approach, *Astrophys. J.*, *810*, 1–10, 2015.

Ptuskin, V. S., I. V. Moskalenko, F. C. Jones, A. W. Strong, and V. N. Zirakashvili, Dissipation of magnetohydrodynamic waves on energetic particles: Impact on interstellar turbulence and cosmic-ray transport, *Astrophys. J*, *642*, 902–916, 2006.

Raath, J. L., A comparative study of cosmic ray modulation models, Master's thesis, (Centre for Space Research) North West University, South Africa, Potchefstroom, 2015.

Richardson, J. D., and L. F. Burlaga, The solar wind in the outer heliosphere and heliosheath, *Space Sci. Rev.*, *176*, 217–235, 2013.

Richardson, J. D., and E. C. Stone, The solar wind in the outer heliosphere, *Space Sci. Rev.*, *143*, 7–20, 2009.

Richardson, J. D., C. Wang, and K. I. Paularena, The solar wind: from solar minimum to solar maximum, *Adv. Space Res.*, *27*, 471–479, 2001.

Richardson, J. D., J. C. Kasper, C. Wang, J. W. Belcher, and A. J. Lazarus, Cool heliosheath plasma and deceleration of the upstream solar wind at the termination shock, *Nature*, *454*, 63–66, 2008.

Richardson, J. D., E. C. Stone, J. C. Kasper, J. W. Belcher, and R. B. Decker, Plasma flows in the heliosheath, *Geophys. Res. Lett.*, *36*, L10102, 2009.

Scherer, K., and H. J. Fahr, Breathing of heliospheric structures triggered by the solar-cycle activity, *Ann. Geophys.*, *21*, 1303–1313, 2003.

Scherer, K., and H.-J. Fahr, Spatial variation of the pickup-proton-injection rate into the ACR regime at the 3D-heliospheric termination shock, *Astron. Astrophys.*, *495*, 631–638, 2009.

Scherer, K., and S. E. S. Ferreira, A heliospheric hybrid model: hydrodynamic plasma flow and kinetic cosmic ray transport, *Astrophys. Space Sci. Trns.*, *1*, 17–27, 2005.

Scherer, K., and H. Fichtner, The return of the bow shock, *Astrophys. J.*, *782*, 25, 2014.

Scherer, K., S. E. S. Ferreira, M. S. Potgieter, and H. Fichtner, Time- and latitude-dependence of the compression ratio and the injection rate at the heliospheric termination shock, in *Physics of the Inner Heliosheath*, *AIP Conf. Ser.*, vol. 858, edited by J. Heerikhuisen, V. Florinski, G. P. Zank, and N. V. Pogorelov, pp. 20–26, 2006.

Scherer, K., H. Fichtner, R. D. Strauss, S. E. S. Ferreira, M. S. Potgieter, and H.-J. Fahr, On cosmic ray modulation beyond the heliopause: Where is the modulation boundary?, *Astrophys. J*, *735*, 128, 2011.

Schlickeiser, R., *Cosmic Ray Astrophysics*, Springer, Germany, 2002.

Schwenn, R., The average solar wind in the inner heliosphere: Structures and slow variations, in *NASA Conference Publication*, vol. 228, pp. 489–507, 1983.

Shalchi, A., Extended nonlinear guiding center theory of perpendicular diffusion, *Astron. Astrophys.*, *453*, L43–L46, 2006.

Shalchi, A. (Ed.), *Nonlinear Cosmic Ray Diffusion Theories*, *Astrophysics and Space Science Library*, vol. 362, Springer, 2009.

Sheeley, J. N. R., et al., Measurements of flow speeds in the corona between 2 and 30 $R_\odot$, *Astrophys. J.*, *484*, 472–78, 1997.

Smith, C. W., and J. W. Bieber, Solar cycle variation of the interplanetary magnetic field spiral, *Astrophys. J.*, *370*, 435–441, 1991.

Smith, C. W., K. Hamilton, B. J. Vasquez, and R. J. Leamon, Dependence of the dissipation range spectrum of interplanetary magnetic fluctuationson the rate of energy cascade, *Astrophys. J. Lett.*, *645*, L85–L88, 2006.

Smith, E. J., The heliospheric current sheet, *J. Geophys. Res.*, *106*, 15,819–15,832, 2001.

Smith, E. J., The global heliospheric magnetic field, in *The Heliosphere through the Solar Activity Cycle*, edited by A. Balogh, L. J. Lanzerotti, and S. T. Suess, pp. 79–150, 2008.

Smith, E. J., and R. G. Marsden, Ulysses observations at solar maximum: Introduction, *Geophys. Res. Lett.*, *30*, 8027, 2003.

Snodgrass, H. B., Magnetic rotation of the solar photosphere, *Astrophys. J.*, *270*, 288–299, 1983.

Steenberg, C. D., Modelling of anomalous and galactic cosmic ray modulation in the outer heliosphere., Ph.D. thesis, Potchefstroom University for CHE, South Africa, Potchefstroom, 1998.

Steenberg, C. D., and H. Moraal, An acceleration/modulation model for anomalous cosmic-ray hydrogen in the heliosphere, *Astrophys. J.*, *463*, 776–783, 1996.

Steenberg, C. D., and H. Moraal, Form of the anomalous cosmic ray spectrum at the solar wind termination shock, *J. Geophys. Res.*, *104*, 24,879–24,884, 1999.

Steenkamp, R., Shock acceleration as source of the anomalous cosmic ray spectrum at the solar wind termination shock, Ph.D. thesis, Potchefstroom University for CHE, South Africa, Potchefstroom, 1995.

Steinolfson, R. S., and D. A. Gurnett, Distances to the termination shock and heliopause from a simulation analysis of the 1992-93 heliospheric radio emission event, *Geophys. Res. Lett.*, *22*, 651–654, 1995.

Stix, M., *The Sun: An Introduction*, Astronomy and Astrophysics Library, Springer Berlin Heidelberg, 2012.

Stone, E. C., A. C. Cummings, F. B. McDonald, B. C. Heikkila, N. Lal, and W. R. Webber, Voyager 1 explores the termination shock region and the heliosheath beyond, *Science*, *309*, 2017–2020, 2005.

Stone, E. C., A. C. Cummings, F. B. McDonald, B. C. Heikkila, N. Lal, and W. R. Webber, An asymmetric solar wind termination shock, *Nature*, *454*, 71–74, 2008.

Stone, E. C., A. C. Cummings, F. B. McDonald, B. C. Heikkila, N. Lal, and W. R. Webber, Changes in the Solar Modulation of Anomalous Cosmic Rays in the Heliosheath, *AGU Fall Meeting Abstracts*, p. C3, 2009.

Stone, E. C., A. C. Cummings, F. B. McDonald, B. C. Heikkila, N. Lal, and W. R. Webber, Voyager 1 observes low-energy galactic cosmic rays in a region depleted of heliospheric ions, *Science*, *341*, 150–153, 2013.

Strauss, R. D., Modelling of anomalous cosmic rays, Master's thesis, (Centre for Space Research) North West University, South Africa, Potchefstroom, 2010.

Strauss, R. D., Modelling of cosmic ray modulation in the heliosphere by stochastic processes , Ph.D. thesis, (Centre for Space Research) North West University, South Africa, Potchefstroom, 2013.

Strauss, R. D., and M. S. Potgieter, Modeling anomalous cosmic ray oxygen gradients over successive solar cycles, *J. Geophys. Res.*, *115*, 12,111, 2010.

Strauss, R. D., and M. S. Potgieter, Where does the heliospheric modulation of galactic cosmic rays start?, *Adv. Space Res.*, *53*, 1015–1023, 2014.

Strauss, R. D., M. S. Potgieter, and S. E. S. Ferreira, The heliospheric transport and modulation of multiple charged anomalous oxygen revisited, *Astron. Astrophys.*, *513*, A24, 2010a.

Strauss, R. D., M. S. Potgieter, S. E. S. Ferreira, and M. E. Hill, Modelling anomalous cosmic ray oxygen in the heliosheath, *Astron. Astrophys.*, *522*, A35, 2010b.

Strauss, R. D., M. S. Potgieter, and S. E. S. Ferreira, Modeling the acceleration and modulation of anomalous cosmic ray oxygen, *Adv. Space Res.*, *48*(1), 65–75, 2011a.

Strauss, R. D., M. S. Potgieter, A. Kopp, and I. Büsching, On the propagation times and energy losses of cosmic rays in the heliosphere, *J. Geophys. Res.*, *116*, A12105, 2011b.

Strauss, R. D., M. S. Potgieter, I. Büsching, and A. Kopp, Modelling heliospheric current sheet drift in stochastic cosmic ray transport models, *Astrophys. Space Sci.*, *339*, 223–236, 2012.

Strauss, R. D., M. S. Potgieter, and S. E. S. Ferreira, Modelling and observing Jovian electron propagation times in the inner heliosphere, *Adv. Space Res.*, *51*, 339–349, 2013a.

Strauss, R. D., M. S. Potgieter, S. E. S. Ferreira, H. Fichtner, and K. Scherer, Cosmic ray modulation beyond the heliopause: A hybrid modeling approach, *Astrophys. J. Lett.*, *765*, L18, 2013b.

Strong, A. W., I. V. Moskalenko, and O. Reimer, Diffuse continuum gamma rays from the galaxy, *Astrophys. J.*, *537*, 763–784, 2000.

Strong, A. W., I. V. Moskalenko, and V. S. Ptuskin, Cosmic-ray propagation and interactions in the galaxy, *Annu. Rev. Nucl. Part. Sci.*, *57*, 285–327, 2007.

Strong, A. W., E. Orlando, and T. R. Jaffe, The interstellar cosmic-ray electron spectrum from synchrotron radiation and direct measurements, *Astron. Astrophys.*, *534*, A54, 2011.

Strong, A. W., et al., Diffuse continuum gamma rays from the Galaxy observed by COMPTEL, *Astron. Astrophys.*, *292*, 82–91, 1994.

Swordy, S. P., The energy spectra and anisotropies of cosmic rays, *Space Sci. Rev.*, *99*, 85–94, 2001.

Tautz, R. C., I. Lerche, and F. Kruse, Modification of cosmic-ray energy spectra by stochastic acceleration, *Astron. Astrophys.*, *555*, A101, 2013.

Tayler, R. J., *The Stars: Their Structure and Evolution*, Cambridge University Press, 1994.

Teufel, A., and R. Schlickeiser, Analytic calculation of the parallel mean free path of heliospheric cosmic rays. I. Dynamical magnetic slab turbulence and random sweeping slab turbulence, *Astron. Astrophys.*, *393*, 703–715, 2002.

Teufel, A., and R. Schlickeiser, Analytic calculation of the parallel mean free path of heliospheric cosmic rays. II. Dynamical magnetic slab turbulence and random sweeping slab turbulence with finite wave power at small wavenumbers, *Astron. Astrophys.*, *397*, 15–25, 2003.

Vaquero, J. M., Historical sunspot observations: A review, *Adv. Space Res.*, *40*, 929–941, 2007.

von Steiger, R., N. A. Schwadron, L. A. Fisk, J. Geiss, G. Gloeckler, S. Hefti, B. Wilken, R. F. Wimmer-Schweingruber, and T. H. Zurbuchen, Composition of quasi-stationary solar wind flows from Ulysses/Solar wind ion composition spectrometer, *J. Geophys. Res.*, *105*, 27,217–27,238, 2000.

Vos, E. E., Cosmic ray modulation processes in the heliosphere, Master's thesis, (Centre for Space Research) North West University, South Africa, Potchefstroom, 2012.

Wang, Y.-M., and J. N. R. Sheeley, On potential field models of the solar corona, *Astrophys.J.*, *392*, 310–319, 1992.

Webber, W. R., Private communication, 2014.

Webber, W. R., and P. R. Higbie, Limits on the interstellar cosmic ray electron spectrum below 1-2 GeV derived from the galactic polar radio spectrum and constrained by new Voyager 1 measurements, *J. Geophys. Res.*, *113*, A11106, 2008.

Webber, W. R., and P. R. Higbie, Calculations of the propagated LIS electron spectrum which describe the cosmic ray electron spectrum below 100 MeV measured beyond 122 AU at Voyager 1 and its relationship to the PAMELA electron spectrum above 200 MeV, *ArXiv e-prints*, *1308.6598*, 2013.

Webber, W. R., and F. B. McDonald, Recent Voyager 1 data indicate that on 25 August 2012 at a distance of 121.7 AU from the Sun, sudden and unprecedented intensity changes were observed in anomalous and galactic cosmic rays, *Geophys. Res. Lett.*, *40*, 1665–1668, 2013.

Webber, W. R., A. C. Cummings, F. B. McDonald, E. C. Stone, B. Heikkila, and N. Lal, Temporal and spectral variations of anomalous oxygen nuclei measured by Voyager 1 and Voyager 2 in the outer heliosphere, *J. Geophys. Res.*, *112*, A06105, 2007.

Webber, W. R., F. B. McDonald, A. C. Cummings, E. C. Stone, B. Heikkila, and N. Lal, Sudden intensity increases and radial gradient changes of cosmic ray MeV electrons and protons observed at Voyager 1 beyond 111 AU in the heliosheath, *Geophys. Res. Lett.*, *39*, L06107, 2012.

Weiss, N. O., and S. M. Tobias, Physical causes of solar activity, *Space Sci. Rev.*, *94*, 99–112, 2000.

Wilcox, J. M., and N. F. Ness, Quasi-stationary corotating structure in the interplanetary medium, *J. Geophys. Res.*, *70*, 5793–5805, 1965.

Zank, G. P., J. Heerikhuisen, B. E. Wood, N. V. Pogorelov, E. Zirnstein, and D. J. McComas, Heliospheric structure: The bow wave and the hydrogen wall, *Astrophys. J.*, *763*, 20, 2013.

Zhang, M., The Compton-Getting effect of energetic particles with an anisotropic pitch-angle distribution: An application to Voyager 1 results at 85 AU, *Astrophys. J.*, *624*, 1038–1048, 2005.

Zhang, M., Acceleration of galactic and anomalous cosmic rays in the heliosheath, in *Physics of the Inner Heliosheath*, *AIP Conf. Ser.*, vol. 858, edited by J. Heerikhuisen, V. Florinski, G. P. Zank, and N. V. Pogorelov, pp. 226–232, 2006.

Acknowledgements

I hereby express my gratitude to the following persons and institutions for their support:

- Prof MS Potgieter, my supervisor, for his guidance, academic and otherwise, and for his unfailing commitment throughout this study.
- Dr RD Strauss, my co-supervisor, for the many helpful hints and discussions, and much-appreciated technical advice.
- Prof SES Ferreira and Drs NE Engelbrecht and ND Ngobeni for useful discussions. I also thank my colleagues, Mr D Bisschoff, Ms RR Nndanganeni, and Mr EE Vos, for their assistance.
- Prof H Moraal, who sadly passed away during the final stages of this study, not only for his contribution to my education in physics, but for all the knowledge he imparted unto the world.
- Prof WR Webber for providing Voyager 1 data.
- Prof JA le Roux and Dr H Fichtner for useful discussions during their respective visits.
- Mrs MP Sieberhagen, Mrs E van Rooyen, and Mrs L van Wyk for handling administrative queries.
- Mr M Holleran for technical support and computer maintenance.
- The National Research Foundation, the South African National Space Agency, and the Centre for Space Research, NWU, for financial support throughout my studies.
- My parents and my brother, for their love, prayers, and support from afar.
- Ms LP Sumbane, firstly for her help in proofreading and typesetting this lofty document, but especially for her constant love, encouragement, and no small amount of *patience*, during this study.

Soli Deo Gloria

Phillip Lourens Prinsloo
Centre for Space Research
North-West University
December 2015.